



รายงานวิจัยฉบับสมบูรณ์

โครงการ การออกแบบพอลิเมอร์ลอกแบบโมเลกุลด้วยวิธีคอมพิวเตอร์ สำหรับใช้วิเคราะห์ยาต้านไวรัส เอช-ไอ-วี

โดย ผศ.ดร.ปิยรัตน์ นิมมานพิภักดิ์ และคณะ

รายงานวิจัยฉบับสมบูรณ์

โครงการ การออกแบบพอลิเมอร์ลอกแบบโมเลกุลด้วยวิธีคอมพิวเตอร์ สำหรับใช้วิเคราะห์ยาต้านไวรัส เอช-ไอ-วี

ผศ.ดร.ปิยรัตน์ นิมมานพิภักดิ์ ดร.วรรณจันทร์ แลงหิรัญ ลี ภาควิชาเคมี คณะวิทยาศาสตร์ มหาวิทยาลัยเชียงใหม่ ภาควิชาเคมี คณะวิทยาศาสตร์ มหาวิทยาลัยเชียงใหม่

สนับสนุนโดยสำนักงานคณะกรรมการการอุดมศึกษา และสำนักงานกองทุนสนับสนุนการวิจัย

(ความเห็นในรายงานนี้เป็นของผู้วิจัย สกอ. และ สกว. ไม่จำเป็นต้องเห็นด้วยเสมอไป)

กิตติกรรมประกาศ

รายงานการวิจัยเรื่อง "การออกแบบพอลิเมอร์ลอกแบบโมเลกุลด้วยวิธีคอมพิวเตอร์สำหรับใช้ วิเคราะห์ยาต้านไวรัส เอช-ไอ-วี" เป็นโครงการที่จัดทำขึ้นโดยได้รับการสนับสนุนจากสำนักงานคณะกรรมการ การศึกษาแห่งชาติและสำนักงานกองทุนสนับสนุนการวิจัย เพื่อพัฒนาศักยภาพในการวิจัยของอาจารย์ ระดับอุดมศึกษารุ่นใหม่

ผู้วิจัยขอขอบคุณ ดร.วรรณจันทร์ แสงหิรัญ ลี นักวิจัยที่ปรึกษาที่ได้กรุณาให้ข้อคิดเห็น ข้อเสนอแนะที่เป็นประโยชน์ยิ่งต่อการวิจัย รวมถึงได้ให้โอกาสในการพบปะ ทำงานร่วมกับนักวิจัยที่ เกี่ยวข้อง พร้อมกันนี้ ขอขอบคุณ ดร.มุกดา ภัทราวราพันธ์ ที่ช่วยให้ข้อคิดเห็นในงานวิจัยในทางปฏิบัติการที่ มีความจำเป็นเป็นอย่างดี

ขอขอบคุณสำนักงานคณะกรรมการการศึกษาแห่งชาติ และสำนักงานกองทุนสนับสนุนการวิจัยที่ อนุมัติงบประมาณอุดหนุนวิจัยเป็นค่าใช้จ่ายของโครงการวิจัยนี้ และขอขอบคุณห้อง ปฏิบัติการเพื่อออกแบบ โมเดล และการจำลองโดยวิธีคอมพิวเตอร์ มหาวิทยาลัยเชียงใหม่ และ ศูนย์นาโนเทคโนโลยีแห่งชาติ สำหรับ คอมพิวเตอร์แม่ข่ายและโปรแกรมสำหรับการคำนวณที่เป็นประโยชน์ยิ่งต่องานวิจัยชิ้นนี้

ผศ.ดร.ปิยรัตน์ นิมมานพิภักดิ์ มหาวิทยาลัยเชียงใหม่ พฤษภาคม 2553

Abstract

Project Code: MRG5180003

Project Title: Computational Design of Molecular Imprinting Polymer for Determination of an

Anti-HIV Drug

Investigator: Asst.Prof.Dr. Piyarat Nimmanpipug

E-mail Address: piyaratn@gmail.com, npiyarat@chiangmai.ac.th

Project Period: 15 May 2008 – 15 May 2010

In this study, Monte Carlo simulation and density functional calculations for the design of molecularly imprinted polymers (MIPs) are intestigated. Molecular template, indinavir, using the rational choice of suitable monomer set used in MIP was designed. Monte Carlo simulations were performed for four difference groups based on their functional group: nitrogen containing hydrocarbon (amine), aromatic hydrocarbon, oxygen containing hydrocarbon (acid and ester), and amino-like hydrocarbon. The prepolymerization adducts of the template at different functional monomers were discovered in this study. The binding energy and hydrogen bond networks were analyzed and compared with experimental results to clarify the preferably imprinting complex forming the selective polymer with nanopore structure.

Keywords: Molecular Imprinting Polymer, Indinavir, DFT, MC simulation, hydrogen bond

network

บทคัดย่อ

รหัสโครงการ MRG5180003

ชื่อโครงการ การออกแบบพอลิเมอร์ลอกแบบโมเลกุลด้วยวิธีคอมพิวเตอร์สำหรับใช้วิเคราะห์ยาต้าน

ไวรัส เอช-ไอ-วี

ชื่อนักวิจัย ผศ.ดร.ปิยรัตน์ นิมมานพิภักดิ์

อีเมลล์ piyaratn@gmail.com, npiyarat@chiangmai.ac.th

ระยะเวลาโครงการ 15 พฤษภาคม 2551 – 15 พฤษภาคม 2553

ในการศึกษานี้ ได้ใช้การจำลองด้วยมอนติ คาร์โล และการคำนวณด้วยทฤษฎีเดนซิตี้ฟังก์ชันในการ ติดตามการออกแบบพอลิเมอร์ลอกแบบ (MIPs) ทั้งนี้ เลือกเซตของมอนอเมอร์สำหรับโมเลกุลต้นแบบ อินดินาเวียร์ โดยได้ทำการจำลองมอนติ คาร์โล สำหรับสี่กลุ่มที่แตกต่างกันพิจารณาจากหมู่ฟังก์ชัน อันได้แก่ สารประกอบไฮโดรคาร์บอนที่มีในโตรเจน (เอมีน) สารประกอบไฮโดรคาร์บอนแบบอะโรมาติก สารประกอบไฮโดรคาร์บอนที่มีออกซิเจน (กรดและเอสเทอร์) สารประกอบไฮโดรคาร์บอนที่คล้ายอะมิโน ในการศึกษานี้ ได้พบผลก่อนการเกิดพอลิเมอร์ไรเซชันจากปฏิกิริยาการเติมโดยอาศัยมอนอเมอร์ที่มีหมู่ฟังก์ชันต่างๆกัน โดยได้วิเคราะห์พลังงานการยึดจับและโครงข่ายพันธะไฮโดรเจนเปรียบเทียบกับการทดลองเพื่ออธิบายการ เกิดสารเชิงซ้อนการลอกแบบที่มีความจำเพาะจากโครงสร้างโพรงระดับนาโน

คำสำคัญ พอลิเมอร์ลอกแบบ, อินดินาเวียร์, ทฤษฎีเดนซิตี้ฟังก์ชัน, พลศาสตร์เชิงโมเลกุล,

โครงข่ายพันธะไฮโดรเจน

โมเลกุลลอกแบบเป็นกระบวนการที่พอลิเมอร์สร้างโพรงจำเพาะในการจดจำสารจำเพาะหนึ่งๆ ซึ่งใน การทำพอลิเมอร์ลอกแบบ จะมีการนำสารที่ต้องการวิเคราะห์มาใช้เป็นโมเลกุลแม่แบบในตัวทำละลายที่ เหมาะสมและเติมสารที่เป็นลิแกนด์ก็คือมอนอเมอร์ซึ่งจะทำอันตรกิริยาต่อโมเลกุลแม่แบบ ทั้งในรูปการสร้าง พันธะเคมีและแรงระหว่างโมเลกุลก่อให้เกิดเป็นสารเชิงซ้อนหลายโมเลกุล (multimolecular complex) หาก ชะเอาโมเลกุลแม่แบบออกจากเนื้อพอลิเมอร์ ก็จะได้โพรงยึดจับที่จำเพาะต่อสเตอริโอเคมีและหมู่ฟังก์ชันของ โมเลกุลแม่แบบ ทั้งนี้ จุดกำเนิดของเทคนิคดังกล่าวมาจากทฤษฎีอธิบายการทำงานของเอนไซม์และแอนติ บอดี้ ในช่วงต้น 1970 Walff และทีมวิจัยได้ตีพิมพ์งานที่แสดงถึงความสามารถในการใช้หมู่ฟังก์ชันที่สร้าง โพรงลอกแบบโดยอาศัยพันธะโคเวเลนซ์มีประสิทธิภาพในการจดจำโมเลกุล หลังจากนั้น Mosbach และทีมวิจัยได้แสดงให้เห็นถึงการสร้างโพรงลอกแบบโดยอาศัยแรงระหว่างโมเลกุล เป็นที่มาของวิธีการเตรียมพอลิ เมอร์ลอกแบบ (molecular imprinting polymer, MIP) ที่เป็นที่นิยมต่อมา ความเข้าใจในพื้นฐานการเกิด อันตรกิริยาโดยเฉพาะการเกิดพันธะไฮโดรเจนซึ่งเป็นแรงระหว่างโมเลกุลที่มีพลังงานสูงสุดจึงนับว่าเป็นส่วน สำคัญในการออกแบบพอลิเมอร์ลอกแบบ

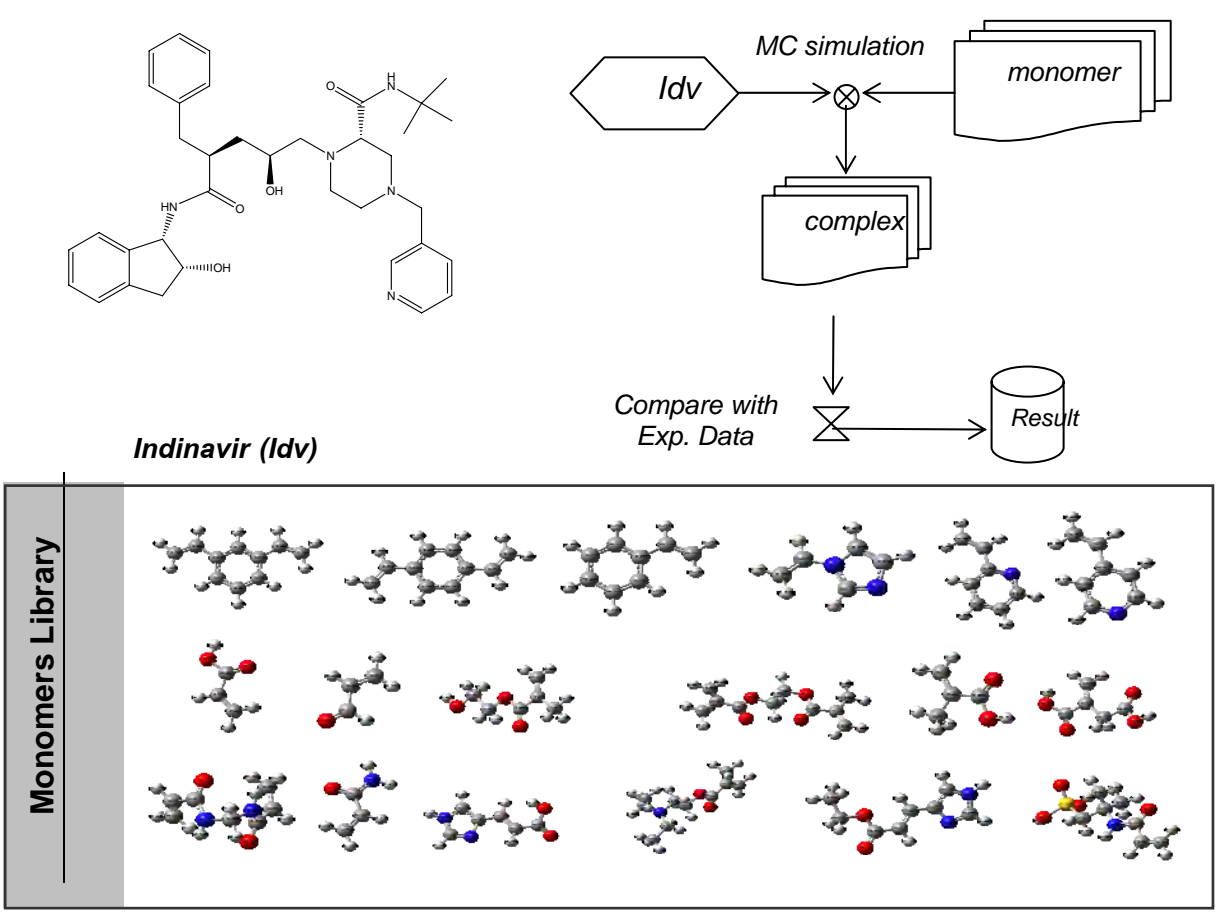
โมเลกุลแม่แบบที่มักวิจัยในการทำพอลิเมอร์ลอกแบบ ได้แก่ อนุพันธ์ของกรดอะมิโน น้ำตาล และสารที่มีฤทธิ์ทางยา ในงานวิจัยนี้จะศึกษาอินดินาเวียร์ (indinavir, idv) ซึ่งเป็นสารออกฤทธิ์กับ เอนไซม์เอชไอวี 1 – โปรติเอส (HIV-1 protease หรือ HIV-1Pr) เป็นเอนไซม์ที่มีบทบาทสำคัญในการขยาย จำนวนของไวรัสเอดส์ ในกระบวนการขยายจำนวนของไวรัสชนิดนี้ ไวรัสซึ่งมีสายพันธุกรรมหรือยีนส์เป็น อาร์-เอ็น-เอ (RNA) และถูกห่อหุ้มไว้อีกชั้นหนึ่งด้วยเปลือกนอก ซึ่งมีปุ่มยื่นออกมาภายนอกปุ่มโปรตีนเหล่านี้ ที่มีชื่อว่า gp120 จะไปยึดจับกับโปรตีนพิเศษบนเซลล์ในระบบภูมิคุ้มกันเรียกว่า CD4 เมื่อจับแล้ว RNA ของ ไวรัสเอดส์จะเข้าสู่เซลล์ จากนั้นเอนไซม์รีเวอร์สทรานสคริปเทส (HIV reverse transcriptase) จะเปลี่ยน RNA ของไวรัสไปเป็น DNA ซึ่งจะสามารถแทรกเข้าไปในสายพันธุกรรม ของเซลล์ร่างกายได้โดย DNA ของไวรัส จะเข้ามาเชื่อมกันกับของเซลล์ร่างกายโดยเอนไซม์ อินทีเกรส (HIV integrase) ทำให้เกิดขบวนการคัดลอก (transcription) ได้เป็น RNA ของไวรัส จากนั้นจะเกิดการขบวนการแปลรหัส (translation) จาก RNA เป็น โปรตีนได้สายโปรตีนขนาดยาว และสายโปรตีนขนาดยาวถูกตัดเพื่อให้ได้เป็นโปรตีนที่เป็นประโยชน์ต่อไวรัส โดยเอนไซม์โปรติเอส ทั้งนี้ ในปัจจุบันการพัฒนาการคำนวณและคอมพิวเตอร์ความเร็วสูง สามารถนำมาใช้ กับการคำนวณสำหรับระบบพอลิเมอร์ลอกแบบได้ ซึ่งจะเป็นเป้าหมายของงานวิจัยนี้โดยสร้างห้องสมุดใน คอมพิวเตอร์ (virtual library) ของหมู่ฟังก์ชันมอนอเมอร์ที่จะใช้ยึดจับกับแม่แบบ เพื่อจะใช้เป็นฐานข้อมูลใน การออกแบบ และทำการคัดกรองกับโมเลกุลแม่แบบเป้าหมายโดยการจำลองทางคอมพิวเตอร์ ซึ่งสามารถ เลือกหมู่ฟังก์ชันที่มีความจำเพาะสูงสุดสำหรับจะสร้าง MIP พอลิเมอร์แม่แบบที่จะสร้างนี้จะใช้ ยา Indinavir เป็นแม่แบบซึ่งเป็นยาในกลุ่ม Nonnucleoside Reverse Transcriptase Inhibitor (NNRTIS) ที่ใช้ เป็นหนึ่งในสูตรยาร่วม 3 ชนิดในการรักษาผู้ติดเชื้อ HIV โดยในการรักษาจะให้ยาอย่างเป็นระบบควบคู่กับ การตรวจสอบปริมาณยาในผู้ป่วยอย่างใกล้ชิด (therapeutic drug monitoring program) ซึ่งจะช่วยให้ผู้ป่วย ได้รับยาในปริมาณที่เหมาะสม นอกจากนี้ยังช่วยลดอาการข้างเคียง ชะลอการดื้อยา และปลอดภัยกับหญิงมี ครรภ์ที่ติดเชื้อ จากการศึกษาวิจัยพบว่าระดับเชื้อไวรัส HIV แปรผันโดยตรงกับปริมาณของ indinavir ใน

พลาสมาซึ่งถูก metabolize ได้ช้ากว่ายาต้านไวรัสชนิดอื่นๆ ดังนั้น indinavir จึงเป็นยาที่สำคัญสำหรับการ ตรวจวิเคราะห์ใน therapeutic drug monitoring program ซึ่งผลงานวิจัยนี้จะนำไปเปรียบเทียบกับแอนติบอดี สังเคราะห์ หรือพอลิเมอร์ลอกแบบในการตรวจวิเคราะห์ indinavir โดยวิธีทางอิมมูโนเอสเซย์ ซึ่งเป็นวิธีที่มี ความจำเพาะและความไวในการตรวจวิเคราะห์สูง วิธีการไม่ยุ่งยากไม่ต้องอาศัยผู้เชี่ยวชาญหรือเครื่องมือ ราคาแพง นอกจากนี้ยังสามารถพัฒนาไปสู่การตรวจวิเคราะห์แบบ automation analysis หรือ strip test ทำ ให้สะดวกรวดเร็ว และช่วยลดค่าใช้จ่ายในการรักษา การใช้คอมพิวเตอร์ในการคำนวณจะช่วยให้สามารถหาหมู่ฟังก์ชันมอนอเมอร์ที่เหมาะสมสำหรับลอกแบบ indinavir ซึ่งมีกว่า 20 ชนิด และสามารถหาอัตราส่วนที่ เหมาะสมระหว่าง indinavir และมอนอเมอร์ สำหรับเตรียมพอลิเมอร์ลอกแบบที่เสถียรและเหมาะสมที่สุดได้

วิธีการทดลอง

การเ<u>ตรียมโครงสร้างเริ่มต้นของ indinavir และ monomer library</u>

ในเบื้องต้นได้จำลองและหาโครงสร้างเสถียรสุดของ indinavir โดย B3LYP/6-31G* และ acrolein, acrylamide, acrylamido-2-methyl-1-propanesufonic acid, acrylic acid, acrylonitrile, allylamine, m-divinyl benzene, p-divinylbenzene, N,N'-diethylamino ethyl methacrylate, ethylene glycol dimethacrylate, 2-hydroxyethyl methacrylate, itaconic acid, methacrylic acid, N,N'-methylene bisacrylamide, urocanic acid ethyl ester, vinyl benzene, 1-vinyl imidazole, 2-vinyl imidazole, และ 4-vinyl imidazole โดย MP2 method สำหรับใช้ในการจำลองตามรูปที่ 1



รูปที่ 1 การเตรียมโครงสร้างเริ่มต้นของ indinavir และ monomer library

การประเมินการยึดจับของมอนอเมอร์ต่างๆ ด้วยวิธีมอนติ คาร์โล

ในส่วนนี้ หามอนอเมอร์ที่เหมาะสมสำหรับยึดจับกับ indinavir สร้างโครงสร้างโมเลกุลแม่แบบ indinavir ที่เหมาะสม ด้วย simulate annealing และคำนวณพลังงานต่ำสุดในแต่ละรอบด้วยสนามแรง COMPASS ความน่าจะเป็นในการสร้างโครงร่างใหม่ การหมุน การเคลื่อนที่ในแนวตรงที่เท่ากัน สร้าง โครงสร้างสารเชิงซ้อนระหว่าง indinavir และมอนอเมอร์ และ คำนวณพลังงาน คำนวณพลังงานการยึดจับ ระหว่าง indinavir และมอนอเมอร์ โดยพลังงานในการยึดจับประเมินได้จาก

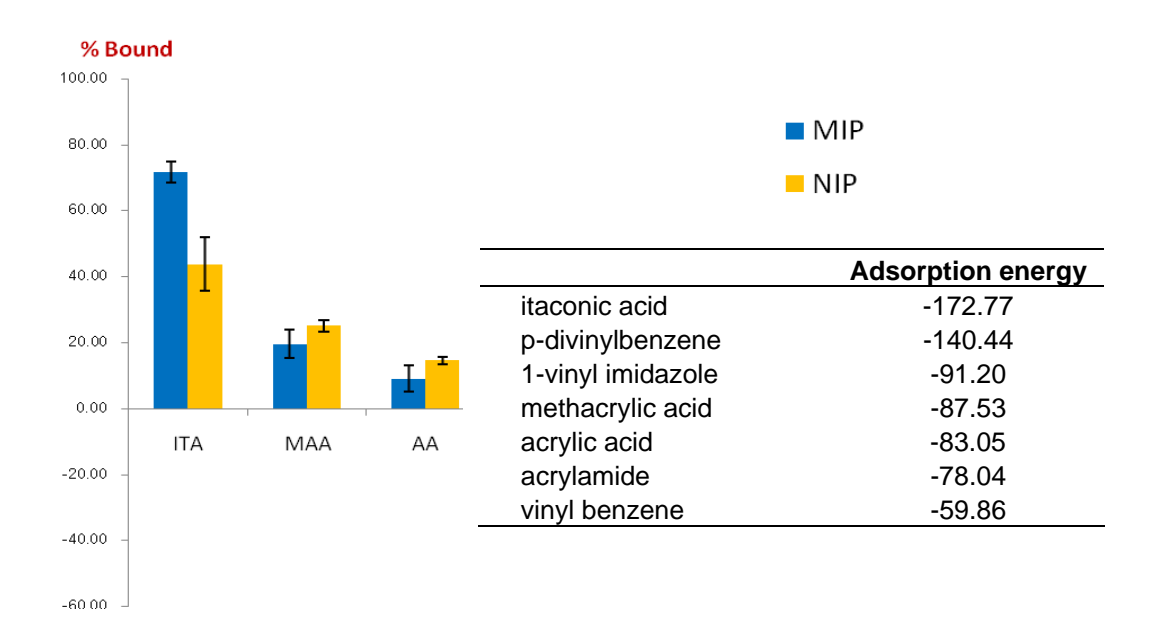
$$\Delta E = E_{indinavir - monomer complex} - E_{indinavir} - E_{monomer}$$

เพื่อนำผลคำนวนที่ได้มาทำนายอัตราส่วนระหว่าง indinavir และมอนอเมอร์ที่เหมาะสม ในการสังเคราะห์พอลิ เมอร์ลอกแบบที่เสถียรโดยการจำลองพลวัติระหว่าง indinavir และมอนอเมอร์ที่คาดว่าเหมาะสม ในสภาวะที่มี ตัวทำละลาย และทำการ simulate annealing จากผลการคัดกรองดังกล่าวผู้วิจัยได้นำมอนอเมอร์ที่เหมาะสม ไปคำนวณโดยวิธีมอนติ คาร์โลที่ใช้อัตราส่วนอินดินาเวียร์ต่อมอนอเมอร์ต่างๆ กันด้วยสัดส่วน 1:1 ถึง 1:9 จากนั้น นำผลที่ได้ไปคำนวณหาพลังงานยึดจับใน DMF โดยคำนวณด้วย COSMO ใน Dmol³ และ เปรียบเทียบโครงข่ายพันธะไฮโดรเจนที่เกิดขึ้น

ผลการทดลองและบทวิจารณ์

1. การเตรียมมอนอเมอร์และการหาสัดส่วนที่เหมาะสมด้วยวิธีมอนติ คาร์โล

พบว่าในส่วนการคำนวณในเบื้องต้นที่อัตราส่วน 1:5 ของ indinavir และ acrolein, acrylamide, acrylamido-2-methyl-1-propanesufonic acid, acrylic acid, acrylonitrile, allylamine, m-divinyl benzene, p-divinylbenzene, N,N'-diethylamino ethyl methacrylate, ethylene glycol dimethacrylate, 2-hydroxyethyl methacrylate, itaconic acid, methacrylic acid, N,N'-methylene bisacrylamide, urocanic acid ethyl ester, vinyl benzene, 1-vinyl imidazole, 2-vinyl imidazole, และ 4-vinyl imidazole ให้ผลที่ สอดคล้องกับผลการทดลองดังแสดงในรูปที่ 2 จากผลการคำนวณและทดลองแสดงถึงความสามารถในการ จับของ itaconic acid (ITA) และ methacrylic acid (MAA) ผู้วิจัยจึงเลือกสารสองชนิดนี้ในการหาปัจจัยที่มีผล ในการจับกับอินดินาเวียร์ในสัดส่วนต่างๆกัน โดยทำการทดลองการจับด้วยมอนติ คาร์โลและนำโครงสร้างที่ ได้มาคำนวณพลังงานต่ำสุดในสภาวะที่มีตัวทำละลายด้วยทฤษฎีเดนซิตี้ฟังก์ชันเพื่อหาพลังงานยึดจับและ วิเคราะห์อันตรกิริยาระหว่างโมเลกุล



ITA = Itaconic acid

MAA = Methacrylic acid

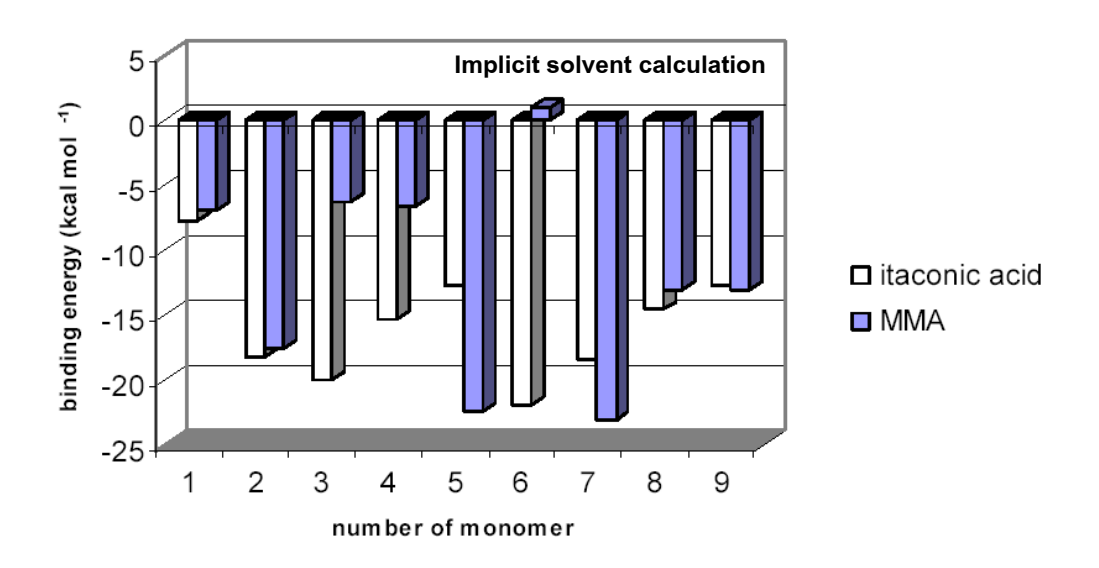
AA = Acrylic acid

รูปที่ 2 การประเมินการยึดจับของมอนอเมอร์ต่างๆ ด้วยวิธีมอนติ คาร์โลที่มีการเติมมอนอเมอร์ : idv ที่ อัตราส่วน 5:1 เทียบกับผลการทดลอง (ซ้ายมือ)

2. อันตรกิริยาระหว่างโมเลกุลและพลังงานยึดจับ

ในการจับของ itaconic acid (ITA) และ methacrylic acid (MAA) กับอินดินาเวียร์ในสัดส่วนต่างๆกัน ได้ผลแสดงดังรูปที่ 3 จากกราฟจะเห็นว่าใน implicit solvent ที่จำลองสภาวะการทดลองของการเตรียม พอลิเมอร์ลอกแบบใน DMF หากใช้ ITA เป็นลิแกนด์ในการเตรียมสารเชิงซ้อนก่อนการเกิดปฏิกิริยาการเติม ในการทำพอลิเมอไรเซชัน ควรใช้อัตราส่วนมอนอเมอร์ต่อสารแม่แบบที่ค่า 3:1, 6:1, 7:1 ขณะที่หากใช้ MAA จะควรใช้อัตราส่วนที่ 5:1 หรือ 7:1

	ratio		vacuum			binding energy			
monomer	ratio	total E adsorption E		dEad/dNi	cpx	idv	monomer	$\Delta \mathbf{E}$	(kcal/mol)
	1:1	-104,3200	-36,3400	-36,3400	-2469.7343	-1974,5883	-495.1335	-0.0124	-7.7893
	1:2	-206,7600	-70,8000	-35,0000	-2964,8880	-1974,5872	-990.2717	-0.0291	-18.2445
	1:3	-315,2800	-111,3500	-39,7600	-3460,0348	-1974,5875	-1485,4154	-0.0319	-20.0374
	1:4	-411,9600	-140,0600	-34,2500	-3955,1639	-1974,5870	-1980,5526	-0.0244	-15.2825
ITA	1:5	-510,7600	-170,8800	-37,0100	-4450,3018	-1974,5870	-2475,6945	-0.0203	-12.7428
	1:6	-605,0100	-197,1500	-33,9000	-4945,4552	-1974,5887	-2970,8314	-0.0351	-22.0160
	1:7	-707,6100	-231,7800	-30,8400	-5440,5957	-1974,5868	-3465,9795	-0.0294	-18.4224
	1:8	-751,3200	-207,5100	-22,7000	-5935,7235	-1974,5901	-3961,1101	-0.0233	-14.6194
	1:9	-877,1000	-265,3100	-31,5500	-6430.8808	-1974,5854	-4456,2751	-0.0203	-12.7693
	1:1	-63,4200	-21,0500	-21,0500	-2281,1054	-1974,5889	-306.5056	-0,0109	-6.8599
	1:2	-122,8800	-38,1400	-18,1800	-2587,6233	-1974.5879	-613.0073	-0.0281	-17.6214
	1:3	-180,7900	-53,6800	-21.8900	-2894.1290	-1974,5907	-919.5282	-0.0101	-6.3437
	1:4	-238,0100	-68,5300	-20,4200	-3200,6444	-1974,5898	-1226,0439	-0,0106	-6,6665
MAA	1:5	-300,3200	-88,4700	-16,6800	-3507.1542	-1974,5878	-1532,5306	-0.0357	-22.4153
	1:6	-344,5200	-90,3000	-17,7400	-3813,6619	-1974,5901	-1839,0734	0,0015	0,9642
	1:7	-411,4200	-114,8300	-14,5000	-4120,1821	-1974,5853	-2145,5599	-0.0368	-23.1174
	1:8	-470,4200	-131,4660	-21,2600	-4426,6989	-1974,5876	-2452,0905	-0.0208	-13.0575
	1:9	-513.3100	-131,9900	-12.8800	-4733.1818	-1974.5888	-2758.5721	-0.0209	-13.0912



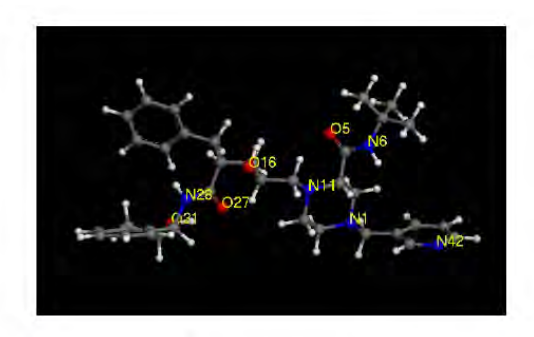
รูปที่ 3. ผลการจับระหว่างมอนอเมอร์กับอินดินาเวียร์ที่สัดส่วนต่างๆ ในสุญญากาศและใน DMF

3. โครงข่ายพันธะไฮโดรเจนในโครงสร้างยึดจับ

-ในตาราง 1 ได้แสดงโครงข่ายพันธะไฮโดรเจนที่ระบุ H-bond donor, H-bond acceptor และระยะที่ใช้

ตาราง 1. โครงข่ายพันธะไฮโดเจนที่เกิดในโครงสร้างเชิงซ้อนแบบหลายโมเลกุล

			Ide mon	omer in binding		La	v-binding monon		-		Monomer	monomon.	
1	ratio	idv	monomer	angle	distance	monomer	neighbor	angle	distance	monomer	neighbor	angle	distance
-				175.1090		monomer	neignoor	angie	distance	monomer	neignbor	angie	distance
	1:1	N6-H C-N42	C1=O5 O6-H	150.1630	2.2160 1.7670	}	1			-	-	1	
	1:2	C=05	O7-H	152.8050	1.7300								
		C-027	O9-H	164.6960	1.7280	i	i			i	i	i	i
	i	N6-H	C-08	156.8170	2.2290								
	i	C-N42	C9-H	170.9500	1.6380	ĺ	i	i i	i l	i	ĺ	ĺ	ĺ
l i	1:3	O16-H	C-O8	174.0180	1.8970	O7-H	C=O8 (2)	158.1190	1.8560	1]	j	
						C=O6	O7-H(3)	148.6820	1.8630				
		C-O16	O7-H	162.9990	1.6900								
		N6-H	C-08	167.0620	2.2230	Į.	!				ļ.	Į.	
		C-N42	O9-H	163,3080	1.6660	07.11	0.000	100.0510	1.777.				
	1:4	C-O16	O9-H	177.1980	1.7000	O7-H C=O6	C=O6 (2) O7-H (4)	160.0540 158.9800	1.7550 1.8010		-	ł	
		C-N42	07-Н	143.2540	1.8360	O9-H	C=O6 (4)	165.4470	1.9100				
		N28-H	C-09	165.3120	2.3450	C9-11	C-06(4)	165.4470	1.9100			ŀ	
	1:5	O16-H	C-08	171.5400	1.9070	C-07	O7-H(3)	141.9610	1.9040	C-07	O9-H (4)	169.1370	1.9090
Α.		C-O5	O9-H	167.7720	1.7290	O7-H	C=O8 (4)	160.3730	1.8070				
ITA		C-O16	O9-H	169.6440	1.6650	C-O6	O9-H(3)	169.7290	1.8100			ì	
_						O7-H	C=O8 (5)	172.1380	1.7700		<u> </u>	<u> </u>	
	1:6	C-05	O7-H	154.0480	1.7750								
		N6-H	C-O8	174.6940	2.0820	O9-H (2)	C=O6 (3)	157.7860	1.8800	C=O8 (3)	O7-H (4)	151.1740	1.9570
		C-N42	O7-H	168.6480	1.5340	C=O6 (2)	O9-H (4)	171.4770	1.6450	C=O8 (4)	O7-H (5)	156.0840	1.8450
	1:7	O16-H	C=06	154.7800	2.2850	C=O6	O7-H(4)	159.4030	1.7610	C=O6 (4)	O7-H (2)	162.2740	1.7300
						O9-H	C-O7 (3)	135.9510	2.2000	C=06(3)	O7-H (5)	154.6960	1.8190
		N6-H	C-08	175.0180	2.2080	!	!	!		C-O7(2)	O7-H (6)	152.8820	1.8950
		C-N42	O9-H O7-H	175.7160 153.9730	1.6020 1.7110								
	1:8	C-O5 C-N42	O7-H	168.8560	1.5390	C-O6	O7-H	165.2690	1.7020				
	1:8	C=05	O9-H	161.3220	1.7130	O7-H	C=O6 (4)	166.5800	1.7020	O7-H(4)	C=O6 (5)	157.9190	1.8510
	1.9	C-03	OS-H	101.5220	1.7130	07-11	C-06(4)	100.5800	1.7210	O9-H(4)	C=06(6)	162.3300	1.8340
		C-O27	O9-H	172.4890	1.6380	C-O6	O9-H(3)	165.6900	1.8200	G5-I1(4)	C-00(0)	102.3300	1.8540
						C-08	O7-H (7)	148.8270	2.0630	O9-H(7)	C=O8 (5)	154.8370	1.9200
			i i		i		07-11(7)	140.0270	23030	C=06 (7)	O7-H (5)	161.3180	1.7740
	i	O31-H	C-O8	159.1300	2.0120								
	1:1	O16-H	C1-O5	167.4400	2.0370								
		C=05	O6-H	164.6240	1.7690								
	1:2	C=O5	O6-H	175.1300	1.6990								
		N6-H	C1-05	163.0560	2.1540	!	!	!				!	
	1:3	C-N42	O6-H	177.3410 170.2120	1.6580	C1-O5	0.0 11.00	170.3450	1.6730				
	1:3	C-O16 O16-H	O6-H C-O6	145.2100	1.7250 2.0830	C1=05	O6-H(2) O6-H(3)	170.3450	1.8230			1	
	1:4	C-O16	O6-H	169.8080	1.7100	C1-05	O6-H (2)	178.5600	1.7580	1	1	1	-
	1.4	N28-H	C1-05	173.4130	2.0500	CI-00	(30-11(2)	178.2000	1.7580				
	1:5	O16-H	C1-O5	160,4000	1.9800								
		C=05	O6-H	166.8210	1.9530	i	i				<u> </u>	i	i
		C-O16	O6-H	162.8200	1.6990	C1-O5	O6-H(5)	166.8480	1.7620				
Y.		C=05	O6-H	172.5140	1.7840))	
MAA		C=O27	O6-H	162.0090	1.7470	Į.	Į	ļ j				Į.	
Σ	1:6	N6-H	C-06	166.4630	2.3520	O6-H	C1=O5 (2)	173.7590	1.6470		ļ	Į.	
						C1=O5	O6-H(2)	175.6410	1.6940				
	1:7	O16-H	C1-05	168.0320	2.0490	!	!				!	!	
		C=05	O6-H	165.4300	1.7750	-	ļ					-	
		C-N42 C-O31	O6-H O6-H	169.9520 166.3970	1.6720 1.7390	-						-	
		O31-H	C1=O5	153.2060	1.9730	O6-H	C1=O5 (5)	159.6660	1.8070				
	1:8	N6-H	C1-05	165.8930	2.2870	CO-F1	C1-05(5)	139,000	1.8070			i	
	1.0	C-N42	O6-H	175.3340	1.6560	i	i				i	i	
		N28-H	C-06	160.1470	2.6450								
	1:9	C-O16	O6-H	174.0160	1.7150								
		N28-H	C-06	139.6230	2.4770	i	i	i	i	i	i	i	i
Į I													







ในการสร้างพันธะไฮโดรเจน โครงสร้างเชิงซ้อนที่ประกอบด้วยพันธะไฮโดรเจนที่มีจำนวนมากและซับซ้อนจะ ช่วยให้โครงสร้างนั้นๆมีความเสถียร จากข้อมูลที่วิเคราะห์จากสารเชิงซ้อนที่เกิดในการจำลองนี้พบว่าส่วน ใหญ่อินดินาเวียร์จะเป็น H-bond acceptor ที่บริเวณ N42-C และ C=O5 ในขณะที่อินดินาเวียร์จะเป็น H-bond donor ที่บริเวณ N6-H และ O16-H ซึ่งจากลักษณะการสร้างอัตรกิริยาดังกล่าวบ่งชี้ถึงบทบาทของหมู่ เอไมด์ที่ติดกับ i-butyl group และหมู่คาร์บอนิลตรงกลางโมเลกุลของอินดินาเวียร์ในการสร้างโครงสร้างเชิงซ้อน ก่อนการเกิดปฏิกิริยาพอลิเมอไรเซชัน รูปแบบลักษณะการจับเช่นนี้สอดคล้องกับการยึดจับระหว่าง HIV-1Pr กับอินดินาเวียร์ที่พบในโครงสร้างที่วิเคราะห์ด้วยรังสีเอกซ์

หนังสืออ้างอิง

- 1. Nair, A. C.; Bonin, I.; Tossi, A.; Welsh, W. J.; Miertus, S. *Journal of Molecular Graphics and Modelling* **2002**, *21*, 171-179.
- 2. Vacca, J. P., Dorsey, B. D.; Schleif, W. A.; Levin, R. B.; McDaniel, S. L.; Darke, P. L.; Zugay, J.; Quintero, J. C.; Blahy, O. M.; Roth, E.; Sardana, V. V.; Schlabach, A. J.; Graham, P. I.; Condra, J. H.; Gotlib, L.; Holloway, M. K.; Lin, J.; Chen, I.-W.; Vastag, K.; Ostovich, D.; Anderson, P. S.; Emini, E. A.; and Huff. J. R. L-735, 524, *Proc. Natl. Acad. Sci. USA* **1994**, *91*,4096–4100.
- 3. Gulick, R. M.; Mellors, J. W.; Havlir, D.; Eron, J. J.; Gonzalez, C.; McMahon, D.; Richman, D. D.; Valentine, F. T.; Jonas, L.; Meibohm, A.; Emini, E. A.; Chodakewitz, J. A. N. Engl. J. Med. 1997, 337(11), 734-739.
- Vacca, J. P.; Dorsey, B. D.; Schleif, W. A.; Levin, R. B.; McDaniel, S. L.; Darke, P. L.; Zugay, J.; Quintero, J. C.; Blahy, O. M.; Roth, E.; Sardana, V. V.; Schlabach, A. J.; Graham, P. I.; Condra, J. H.; Gotlib, L.; Hollaway, M. K.; Lin, J., Chen, I-W; Vastag, K.; Ostovic, D.; Anderson, P. S.; Emini, E. A.; Huff, J. R. *Proc. Natl. Acad. Sci. USA* 1994, *91*, 4096–4100.
- 5. Pav JW, Rowland LS, Korpalski DJJ Pharm Biomed Anal 1999, 20, 91–98.
- Rezk NL, Tidwell RR, Kashuba ADM J Chromatogr B Analyt Technol Biomed Life Sci 2004, 805, 241–247.
- 7. Chi J, Jayewardene AL, Stone JA, Aweeka FT J Pharm Biomed Anal 2003, 31, 953-959.
- 8. Azoulay S, Nevers MC, Creminon C, Heripret L, Durant J, Dellamonica P et al Antimicrob Agents Chemother **2004**, 48, 104–109.

Output จากโครงการวิจัยที่ได้รับทุนจาก สกอ. และ สกว.

1. ผลงานวิจัยที่ตีพิมพ์ในวารสารวิชาการระดับนานาชาติ

- **Nimmanpipug, P.***, Kareuhanon, W., Pattarawarapan, M., Lee, V. S. Prepolymerization Adduct and Hydrogen Bond Pattern of Non-Covalent Molecularly Imprinting Polymer for Indinavir, *Molecular Simulation* **2010**, *in preparation*.
- Kareuhanon, W; Lee, V. S.; **Nimmanpipug**, **P**.; Tayapiwatana, C.; Pattarawarapan, M. Synthesis of Molecularly Imprinted Polymers for Nevirapine using Dummy Template Imprinting Approach Chromatographia **2009**, 70 (11-12), pp. 1531-1537. (impact factor 2008= 1.467).
- **Nimmanpipug, P.***, Lee, V. S.; Wolschann, P., Hannongbua, S. Litchi Chinensis-derived terpenoid as anti-HIV-1 protease agent: Structural design from molecular dynamics simulations, *Molecular Simulation*, **2009**, 35, 673-680. (impact factor = 1.325 source: 2008 Thomson Reuters, Journal Citation Reports)
- R. Jongkol, R. Choommongkol, B. Tarnchompoo, **P. Nimmanpipug** and P. Meepowpan*, Syntheses of methylenolactocin and nephrosterinic acid *via* diastereoselective acylation and chemoselective reduction-lactonization, *Tetrahedron* **2009**, 65.
- Sangprasert, W., Lee, V. S.; Boonyawan, D.; Tashiro, K.; **Nimmanpipug, P*.** Sulfur Hexafluoride Plasma Surface Modification of Gly-Ala and Ala-Gly as *Bombyx Mori* Silk Model Compounds: Mechanism Investigations, *J. of Mol. Struct.* **2010**, 963 (2-3), pp. 130-136. ((impact factor = 1.594 source: 2008 Thomson Reuters, Journal Citation Reports).
- Lee VS*, Tue-ngeun P, Nangola S, Kitidee K, Jitonnom J, **Nimmanpipug P**, Jiranusornkul S, Tayapiwatana C*. Pairwise decomposition of residue interaction energies of single chain Fv with HIV-1 p17 epitope variants. *Mol. Imm.* **2010**, 47 (5), pp. 982-990. (impact factor 2007 = 3.742)
- Khomhoi, P.; Sangprasert, W.; Lee, V. S.; **Nimmanpug**, P.* Theoretical Study of the Bombyx mori Silk Surface Functionalization: Quantum calculation of Glycine-Alanine unit reacting with fluorine and molecular dynamic simulation of wettability, *Chiang Mai Journal of Science*, **2010**, 37(1), 1-10.
- Ngaojampa, C.; Nimmanpipug, P.; Yu, L.; Anantalabhochai, S.; Lee, V. S.* Molecular Simulations of Interactions between Low-energy Nitrogen Ions and A-DNA in Vacuum, *J. of Mol. Graph. Model.* **2010**, *28*, 533-539. (impact factor 2008 = 2.347)
- Chaiwong, C., Tunma, S., Sangprasert, W., **Nimmanpipug, P.**, Boonyawan, D.* Graft polymerization of flame-retardant compound onto silk via plasma jet, *Surface and Coatings Technology* **2010**, *in press*.

2. การนำผลงานวิจัยไปใช้ประโยชน์

ผลงานวิจัยนี้จะนำไปเปรียบเทียบกับแอนติบอดีสังเคราะห์ หรือพอลิเมอร์ลอกแบบในการ ตรวจวิเคราะห์ indinavir โดยวิธีทางอิมมูโนเอสเซย์ ซึ่งเป็นวิธีที่มีความจำเพาะและความไวในการ ตรวจวิเคราะห์สูง วิธีการไม่ยุ่งยากไม่ต้องอาศัยผู้เชี่ยวชาญหรือเครื่องมือราคาแพง นอกจากนี้ยัง สามารถพัฒนาไปสู่การตรวจวิเคราะห์แบบ automation analysis หรือ strip test ทำให้สะดวก รวดเร็ว และช่วยลดค่าใช้จ่ายในการรักษา การใช้คอมพิวเตอร์ในการคำนวณจะช่วยให้สามารถหา หมู่ฟังก์ชันมอนอเมอร์ที่เหมาะสมสำหรับลอกแบบ indinavir ซึ่งมีกว่า 20 ชนิด และสามารถหา อัตราส่วนที่เหมาะสมระหว่าง indinavir และมอนอเมอร์ สำหรับเตรียมพอลิเมอร์ลอกแบบที่เสถียร และเหมาะสมที่สุดได้

3. ผลงานอื่น ๆ

3.1 ผลงานวิจัยที่เสนอในที่ประชุมระดับนานาชาติ

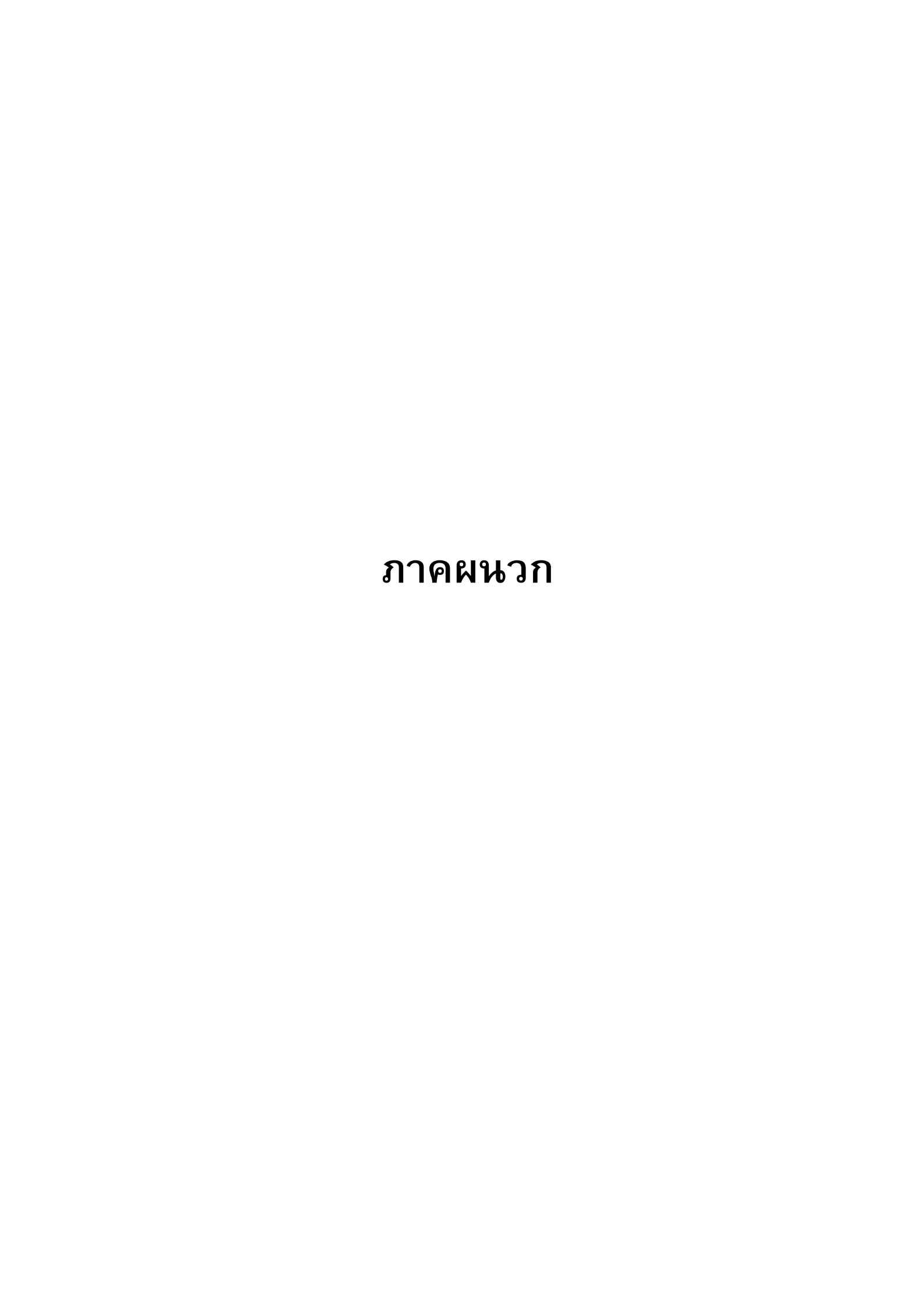
- **Nimmanpipug, P.**; Lee, V. S.; Monajjemi, M. Monte Carlo Simulation of Solvent Effects in Molecular Imprinted Polymers Rational Design, The third Asian Simulation and Modeling (AZIMMOD), January 22-23, 2009, Kasetsart University, Bangkok, Thailand.
- Sangprasert, W.; Boonyawan, D.; Lee, V.S.; **Nimmanpipug, P**.; "Air Plasma Modification on Poly(methyl methacrylate) Denture Base" 6th ISAMAP, 21-23 November, 2009, Bangkok, Thailand.
- C. Chaiwong, S. Tunma, W. Sangprasert, **P. Nimmanpipug** and D. Boonyawan, Graft Polymerization of Flame-Retardant Compound onto Silk via Plasma Jet, 10th International Workshop on Plasma-Based Ion Implantation & Deposition, September 7-11, 2009, Brazil.
- Krongdang, S.; Jantawannakul, P.; **Nimmanpipug, P.**; Lee, V. S.; "Homology modeling and molecular dynamics study of protease from American foul brood disease", Apimondia 2009, September 15-20, 2009, Montpellier, France.
- Lee, V.S.; Tue-ngeun, P.; Nangola, S.; Kitidee, K.; Jitonom, J., **Nimmanpipug, P.** Supat Jiranusornkul, S.; Tayapiwatana, C. "Structure and dynamics of anti-P17 single chain Fv" The 4th Annual Symposium of the Protein Society of Thailand, August 26-28, 2009, Chulabhorn Research Institute Conference center, Thailand.
- Yu, L. D.; **Nimmanpipug, P.**; Lee, V. S.; Anuntalabhochai, S. "Ion Beam Nanobiology" 3rd IEEE international nanoelectronics conference, Jan. 4-8, 2010, Hong Kong.

- Yu, L. D.; Norarat, R.; Sarapirom, S.; Semsang, N, Ngaojampa, C.; **Nimmanpipug, P**.; Lee, V. S.; Anuntalabhochai, S. "A Basic Investigation on Low-energy Ion Irradiation Effect on Lives Low-energy ion irradiation of naked DNA", IAEA topical meeting on accelerator technology and applications, May 4-8, 2009, Vienna.
- Ngaojampa, C.; **Nimmanpipug, P.**; Yu, L. D.; Anuntalabhochai, S.; Lee, V. S. "Molecular dynamics simulation of low-energy ion irradiation effect on DNA structure change", The 10th international workshop on plasma-based ion implantation and deposition, Sep. 7-11, 2009, Sao Paulo, Brazil.
- Lee, V. S.; **Nimmanpipug, P.**; Settakorn,, C.; Monajjemi, M. Salt effects on nucleic acids solution: Monte Carlo Simulation Study, The third Asian Simulaiton and Modeling (AZIMMOD), January 22-23, 2009, Kasetsart University, Bangkok, Thailand.
- Yana, J.; Lee V. S.; Songsiriritthigul, P.; Medhisuwakul, M.; Vannarat, S.; Vilaithong, T.; **Nimmanpipug, P.** "Molecular Dynamics Simulations of Ion Bombardment on Nafion Side Chain Cluster Model" The Pure and Applied Chemistry Conference 2009 Phitsanulok, Thailand, 14-16 Jan, 2009.
- Krongdang, S.; Jantawannakul, P.; **Nimmanpipug, P.**; Lee, V. S. Comparative Protease Structure Modeling of American Foulbrood in Honeybee, PURE AND APPLIED CHEMISTRY INTERNATIONAL CONFERENCE 2009 (PACCON 2009), January 14-16, 2009, Naresuan University, Phitsanulok, Thailand.
- Tue-ngeun, P.; Jiranusornkul, S.; Jitonnom, J.; Jaiinphon, K.; **Nimmanpipug, P.**; Kasinrerk, W.; Tayapiwatana, C.; Lee, V. S. Molecular Dynamics of single-chain antibody to HIV epitope at c-terminal of P17, PURE AND APPLIED CHEMISTRY INTERNATIONAL CONFERENCE 2009 (PACCON 2009), January 14-16, 2009, Naresuan University, Phitsanulok, Thailand.
- Jitonnom, J.; **Nimmanpipug, P.**; Songjang, K.; Shank, L.; Lee, V.S.; Mulholland, A.J. Binding of Potent Peptide Derived from Propeptide of Plutella xylostella Midgut Trypsin by Homology Modelling and Docking, January 6-8, 2009, Yorkshire Museum and Gardens, York, UK.
- P. Nimmanpipug, V. S. Lee, J. Yana, W. Sangprasert, and C. Ngaojampa "Molecular Modeling of Low Energy Ion Bombardment/Plasma Treatment in Polymer Design" 14th International Annual Symposium on Computational Science and Engineering (ANSCSE14), Mae Fah Luang University, Chiangrai, Thailand, March 23-26, 2010.

- V. S. Lee, **P. Nimmanpipug**, K. Kodchakorn, and C. Tayapiwatana "Molecular Dynamics Simulations of Antibody ScFv Fragments without Disulfide Bond" 14th International Annual Symposium on Computational Science and Engineering (ANSCSE14), Mae Fah Luang University, Chiangrai, Thailand, March 23-26, 2010.
- Yana, J.; Lee V. S.; Vannarat, S.; Dokmaisrijan, S.; Medhisuwakul, M.; Vilaithong, T.; **Nimmanpipug, P.** "MD simulation of Nafion surface modification by Ar⁺ bombardment" 14th International Annual Symposium on Computational Science and Engineering (ANSCSE14), Mae Fah Luang University, Chiangrai, Thailand, March 23-26, 2010.
- Sangprasert, W.; Yavirach, P.; Boonyawan D.; Lee V.S.; **Nimmapipug, P.**; "Molecular Calculation of Plasma Treatment Efficiency on PMMA and FRC as Denture Materials" 14th International Annual Symposium on Computational Science and Engineering (ANSCSE14), Mae Fah Luang University, Chiangrai, Thailand, March 23-26, 2010.
- Nokthai, P.; Shank, L.; **Nimmanpipug, P.**; Lee, V. S. "Molecular modeling of active site of peroxidase" Proceeding of the 10th Annual National Symposium on Computational Science Engineering (ANSCSE14), Mae Fah Luang University, Chiang Rai, Thailand, March 23-26, 2010.
- "QM/MM Study On The Catalytic Mechanism of Family 18 Chitinase" 14th
 International Annual Symposium on Computational Science and Engineering
 (ANSCSE14), Mae Fah Luang University, Chiangrai, Thailand, March 23-26, 2010.
- " A Conditional Random Fields-Based for CpG islands prediction in Rice" 14th International Annual Symposium on Computational Science and Engineering (ANSCSE14), Mae Fah Luang University, Chiangrai, Thailand, March 23-26, 2010.
- "3D Pharmacophore and Molecular Docking of AFB Metalloprotease and Peptide Analogs for Novel Antimicrobial Inhibitors" 14th International Annual Symposium on Computational Science and Engineering (ANSCSE14), Mae Fah Luang University, Chiangrai, Thailand, March 23-26, 2010.

3.2 ผลงานวิจัยที่เสนอในที่ประชุมระดับชาติ

- Computational Screening for Molecularly Imprinted Polymer Rational Design, การ ประชุมเพื่อ เสนอผลงานวิจัยของนักวิจัยรุ่นใหม่ และพบกับเมชีวิจัยอาวุโส สกว., 15-17 October 2009, Phetchaburi, Thailand (Poster presentation).
- Shoombuatong, W; Jitpakdi, P;Prasitwattanaseree, S; **Nimmanpipug, P** and Tayapiwatana,C; Chaijaruwanich, J; Disulfide Bond Formation Prediction Using Graphical Model;, PERCH-CIC CongressVI, May 3-6, 2009, Jomtien Palm Beach Resort Pattaya, Thailand (Oral presentation).
- Lee, V.S.; Tue-ngeun, P.; Nangola, S.; Kitidee, K.; Jitonom, J., Nimmanpipug, P. Supat Jiranusornkul, S.; Tayapiwatana, Chatchai. "Structure and dynamics of anti-P17 single chain Fv" The 4th Annual Symposium of the Protein Society of Thailand, August 26-28, 2009, Chulabhorn Research Institute Conference center, Thailand.



Prepolymerization Adduct and Hydrogen Bond Pattern of Non-Covalent Molecularly

Imprinting Polymer for Indinavir

Piyarat Nimmanpipug, Natthaporn Phutthawong, Mookda Pattarawarapan, Vannajan

Sanghiran Lee

Department of Chemistry and Center of Excellence for Innovation in Chemistry, Faculty of

Science, Chiang Mai University, Chiang Mai 50200, Thailand; E-Mail: piyaratn@gmail.com

Abstract

In this study, Monte Carlo simulation and density functional calculations for the

design of molecularly imprinted polymers (MIPs) are intestigated. Molecular template,

indinavir, using the rational choice of suitable monomer set used in MIP was designed.

Monte Carlo simulations were performed for four difference groups based on their

functional group: nitrogen containing hydrocarbon (amine), aromatic hydrocarbon,

oxygen containing hydrocarbon (acid and ester), and amino-like hydrocarbon. The

prepolymerization adducts of the template at different functional monomers were

discovered in this study. The binding energy and hydrogen bond networks were analyzed

and compared with experimental results to clarify the preferably imprinting complex

forming the selective polymer with nanopore structure.

Keywords:

Molecular Imprinting Polymer, Indinavir, DFT, MC simulation,

hydrogen bond network

1. Introduction

Indinavir (IDV; L-735,524, MK-0639, Crixivan manufactured by Merck) is a protease inhibitor used as a component of highly active antiretroviral therapy for being used alone or in combination for the treatment of adults with HIV infection since FDA approval in 1996 [1]. Indinavir was much more powerful than any prior antiretroviral drug; using it with dual with nucleoside analog reverse transcriptase inhibitors (NRTIs) for treating HIV-positive adults with advanced or progressive immunodeficiency [2]. Unfortunately, indinavir wears off quickly after dosing and therefore requires dosing very precisely every eight hours in order to threat HIV from forming drug resistant mutations including resistances to other protease inhibitors. Reduced inhibition was observed for 10–11 different mutants of active site residues that can directly alter interactions with indinavir [3]. The mutation of conserved residues M46 and V82 are the most common with indinavir treatment, followed by mutations of I54, L90, L24, G73, V32, I84, G48 and F53 at lower frequencies [4]. Therefore, in order to reduce a risk of treatment failure or drug resistance routine monitoring of IDV level in patient is necessary.

Several methods for quantitative analysis of IDV have been developed such as LC [5, 6], LC-MS-MS [7], and immunoassay [8]. For the analysis of biological samples, the methods generally require a sample pretreatment step to separate and / or preconcentrate the analyte prior to analysis. The synthesis of a new sorbent material that can selectively retain IDV would facilitate routine analysis of the drug level present in such complex matrices. Molecularly imprinted polymers (MIPs) have been interested in analytical science and technology. Such polymers have many potential applications ranging from solid phase extraction (SPE) materials, antibody-like sorbent assays, and selective recognition layers in

sensing devices from their chemical and mechanical stability together with high selectivity for specific template.

The most common use technique for the MIP preparation is via the non-covalent imprinting [9]. In this approach, functional monomer is allowed to self-assembly with the template molecule in the pre-polymerization mixture. Subsequence radical polymerization with a cross-linker helps stabilized the template-monomer complex. Extraction of the template leaves behind recognition sites of functional and shape complementarily to the template.

Currently, there are only two reports of MIPs for anti-HIV drugs [10] [11]. In 2002, O'Brien and co-workers [10] proposed an approach to the preparation of MIPs of IDV that have highly selective sites. Infrared spectroscopy (IR) was used to characterize the interaction between IDV and monomer, methacrylic acid (MAA), and the optimum functional monomer concentration for polymerization was obtained. In 2006, Chianella and co-workers [11] reported the synthesis of MIPs for abacavir, antiretroviral activity against HIV-1, using computational approach to select the best monomers. The MIP prepared from the best monomer gave the high binding capacity up to 157 mg of drug per gram of polymer.

As molecular recognition of biologically relevant molecules governs essential biological interactions, the creation of synthetic selective receptor-like macromolecule capable of recognizing molecular targets of interest with high affinity and selectivity have been one of long-term goals for chemical, biological and pharmaceutical research scientists. To obtain specific nano-pore structure, synthesis conditions in term of monomer structure and solvent are needed to be designed.

To understand MIP from chemical and physical basic, the molecular interactions involving in the templating process in self-assembly will be clarified. In this study, a combination of Monte Carlo (MC) simulation and quantum calculations for the design of

MIPs is studied. Molecular template using the rational choice of suitable monomer set used in MIP was designed using the methods. MC simulations were performed at various temperatures in different solvent effects and dielectrics. The prepolymerization adducts between the template at different functional monomers will be gotten for indinavir (IDV) template.

2. Calculation and Experimental Methods

2.1 Density Functional Calculation

Totally 20 different monomers: acrolein, acrylamide, acrylamido-2-methyl-1-propanesufonic acid, acrylic acid, acrylonitrile, allylamine, *m*-divinyl benzene, *p*-divinylbenzene, *N*,*N*'-diethylamino ethyl methacrylate, ethylene glycol dimethacrylate, 2-hydroxyethyl methacrylate, itaconic acid, methacrylic acid, *N*,*N*'-methylene bisacrylamide, urocanic acid ethyl ester, vinyl benzene, 1-vinyl imidazole, 2-vinyl imidazole, and 4-vinyl imidazole, was generated for investigate molecular recognition properties as shown in Figure 1. To get the reliable molecular geometry, the template structure was minimized using density functional theory B3LYP 6-31G* method of Gaussian 03 program. Configurational and conformational searches of monomer-IDV complexes were carried out with a Monte Carlo simulation technique with COMPASS forcefield. The docked bimolecular complexes were set by a random rotation around all three axes at its center of mass and translational movement in three-dimensional space. Each monomer was allowed to be flexible and rotate randomly toward IDV using Materials studio 4.2 suite of program.

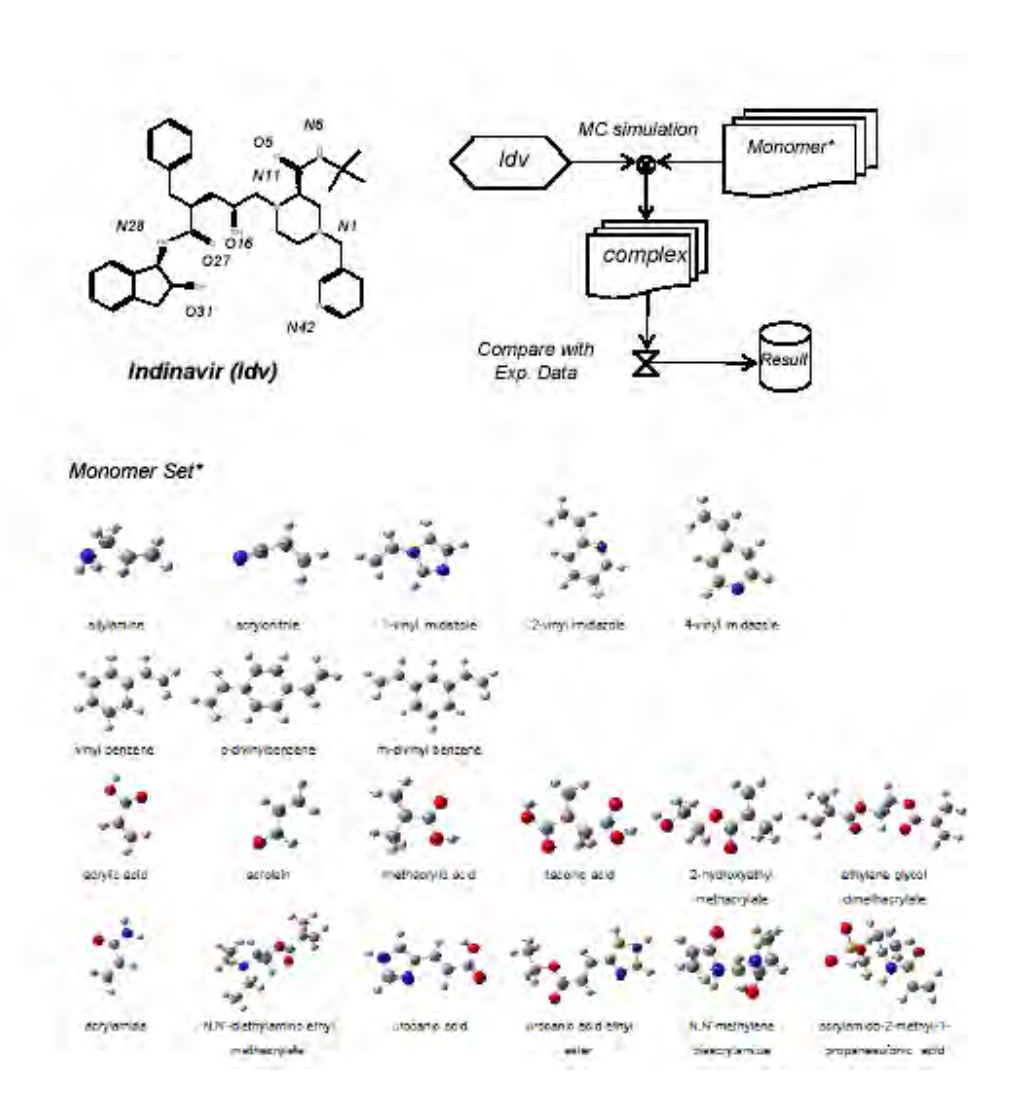


Figure 1 Molecular imprinting simulation procedure

2.2 Monte Carlo Simulation

The Metropolis Monte Carlo method is used in Materials studio 4.2 suite of program. The MC method samples the configurations in an ensemble by generating a set of configurations, m, n, ..., where the probability of transition from m to n is π_{mn} . In case that configuration m is sampled with a frequency ρ_m , by mean, $\rho_m \pi_{mn}$ of them are transformed to n. In the same way, configurations n are transformed to m with probability of $\rho_n \pi_{nm}$. The flux density of the flow, ρ , will be, then, preserved. The balance condition for equilibrium is as following:

$$\rho_m \pi_{mn} = \rho_n \pi_{nm}$$

In the MC method, the transforms configuration m to n is a two-stage process. Starting with sampling a configuration with probability α_{mn} . Then, transition probability, π_{mn} , can be calculated using the equation:

$$\pi_{mn}=\alpha_{mn}P_{mn}$$

transitions of a configuration m to a higher probability $(\rho_n > \rho_m)$ will be accepted, on the other hand, transitions to configurations with a lower favorable $(\rho_n < \rho_m)$ are less likely to be accepted.

2.3 Solvation effects

To investigate solvent effect on the prepolymerization adduct simulated from previous section, each complex was optimized using BLYP method of GGA in implicit COSMO solvent with dielectric constant of 38.3 mimicking the salvation of complexes by dimethylformamide. The calculations run until energy convergence reach 10⁻⁵ in Dmol3 module of MS studio 4.4 program packages.

2.3 Experimental Method

2.3.1 Reagents

IDV was obtained as a gift from the Government Pharmaceutical Organization (GPO) Thailand. Ethylene glycol dimethacrylate (EGDMA), itaconic acid (ITA), acrylic acid (AA), vinyl benzene (VB), vinylimidazole (1-Vi), and acrylamide (ACM) were purchased from Fluka, France. Methacrylic acid (MAA), divinyl benzene (DVB) were obtained from Merck, Darmstadt, Germany. Benzoyl peroxide (BPO) was obtained from Jassen Chemical, Beerse,

Belgium and was recrystallized from methanol before use. Other chemicals were all of analytical grade and they were used without purification.

2.3.2 Preparation of molecularly imprinted polymers

Appropriate amounts of IDV and functional monomer were dissolved in DMF and incubated for 10 min. The cross-linker, EGDMA, and benzoyl peroxide used as initiator were then added sequentially. The flask was sealed with rubber cap and was purged with nitrogen for 10 min. The polymerization was then carried out at 60 °C in oven for 24 h. The resulting bulk rigid polymers were ground into fine powder. The template was extracted with 20% acetic acid in methanol. The polymer particles were washed with acetonitrile to get rid of residual acetic acid. Finally, the particles were dried at 60°C in an oven. Non-imprinted polymers (NIPs) were prepared by same procedure but without addition of template.

2.3.3 Batch rebinding studies

The binding experiment was carried out by adding 5 mg of each polymer in polypropylene microtube containing 1 ml of 0.1 mg/ml IDV in different solvents; acetonitrile (MeCN) and 1,2-dichloroethane (DCE). The solution was incubated for 15 h at room temperature, and then the polymer particles was separated by centrifugation at 10000 rpm for 10 min. Supernatant (500 ml) was then withdrawn and was analyzed by UV spectrophotometer at λmax 260 nm. All analyses were performed in triplicate. The percentage bound (% bound) of IDV was calculated according to equation 1

$$\% Bound = Q/Q_{initial} \times 100$$
 (1)

where Q is the amount of IDV bound to the polymer and $Q_{initial}$ is the initial amount of IDV before adding the polymer.

3. Results and Discussions

3.1 Monomer library and prepolymerization adducts: The lowest binding energy per monomer of each compound was gotten from MC simulation. Among variety functional monomer: itaconic acid, *p*-divinylbenzene, 1-vinyl imidazole, and methacrylic acid show the lowest binding energy stabilized from H-bonding and *van der Waals* interactions. As *p*-divinylbenzene and 1-vinyl imidazole are mostly used as cross linker, only itaconic acid and methacrylic acid will be investigated in details. Atom number of indinavir, itaconic acid, and methacrylic acid were declared in Figure 2 for notification in simulation analysis in the next section.

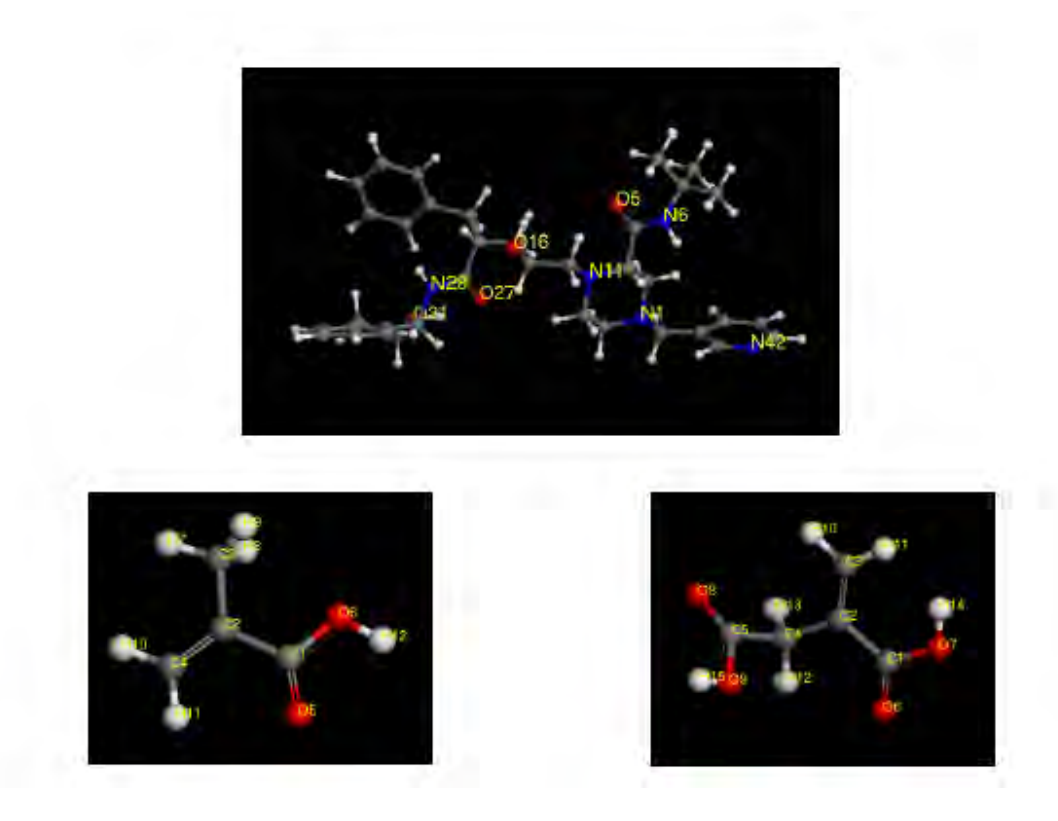


Figure 2 Optimized structures of indinavir (top), methacrylic acid (right down), itaconic acid (left down)

3.2 Choices of Monomer for MIP – Monte Carlo Simulation and Experimental Selections

The IDV binding ability of the MIPs prepared with different monomers at IDV:monomer ratio of 1:5 was evaluated in two different media; acetonitile (MeCN) and 1,2-dichloroethane (DCE). MeCN was selected as media in place of DMF which was used in the MIP synthesis because DMF have UV cutoff at the same absorption wavelength as IDV while polarity of MeCN is comparable to DMF. DCE was also selected as another binding media because of its low dielectric constant which should be able to facilitate the hydrogen bonding interaction between IDV to polymers.

Figure 3 shows the percentage binding of IDV to MIPs. In both MeCN and DCE media, the polymers P(ITA) containing ITA as the monomer gives the highest percentage bound of IDV, followed by P(MAA) synthesized from MAA monomer. In polar media solvent like MeCN, much higher amount of IDV was bound to P(ITA) than P(MAA). However, in DCE which is less polar than MeCN, binding of ITA to P(MAA) was significantly enhanced.

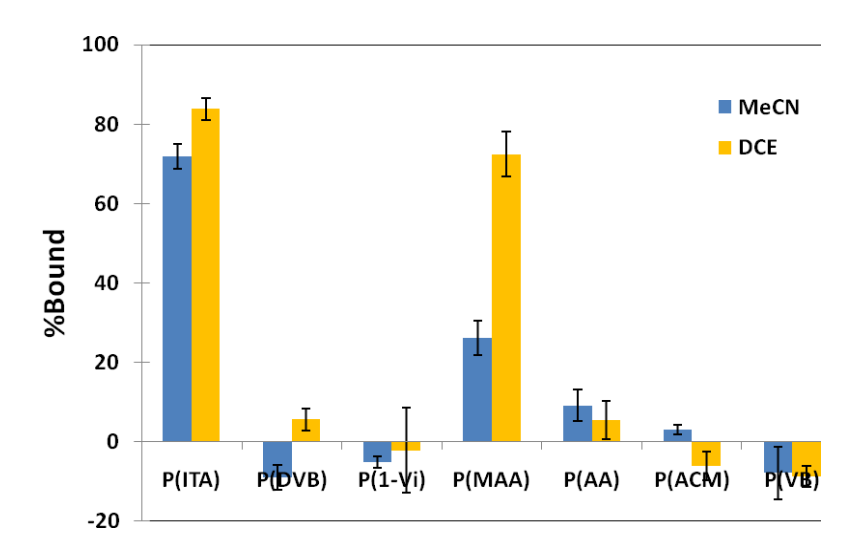


Figure 3. The percentage bound of IDV to MIPs in MeCN and DCE media.

To further investigate the effect of template: monomer ratio on binding efficiency of MIPs, MIPs were prepare with ITA and MAA as monomers by varying ITA:monomer ratios from 1:4 to 1:7. Result from template rebinding study in DCE was shown in Figure 4. The highest percentage of IDV bound to MIPs was observed at IDV:monomer ratio of 1:5 for both P(ITA) and P(MAA) polymers.

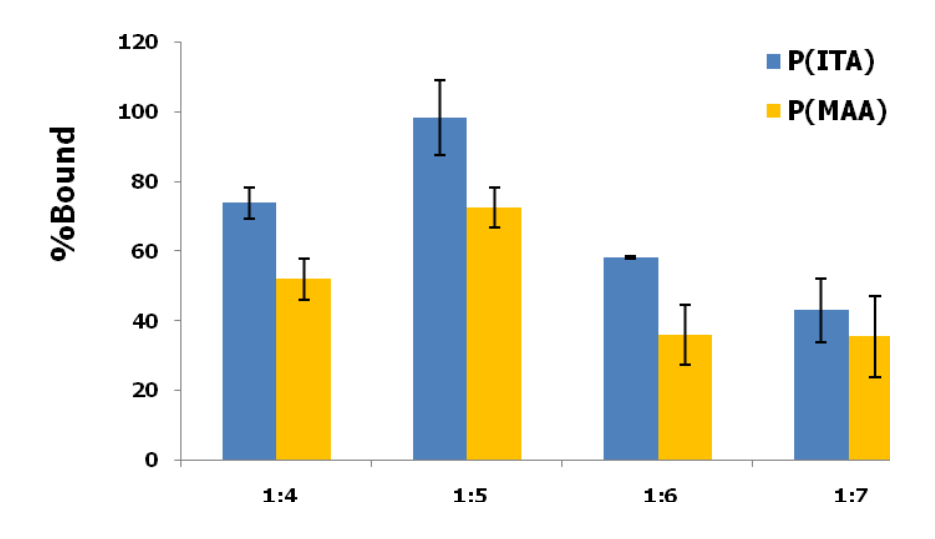


Figure 4. The percentage bound of IDV to MIPs with various ITA:monomer ratios in DCE.

3.3 Molecular Interactions in Template Recognition – Binding Energy

The only two probable candidates with lowest binding energy estimated from MC simulation, itaconic acid and methacrylic acid were investigated in this section to clarify the factors govern the stable complexes with IDV. The optimized ratio of monomer to its template, IDV, was obtained theoretically using density functional calculation in implicit solvent. The binding energy of itaconic acid in DMF is lowest with ratio of 3:1, 6:1, and 7:1 while methacrylic acid prefers the complex with idv with ratio of 5:1 and 7:1. The change of binding energy ranking from complex in vacuum under MC simulation to complex in solvent

environment was found as shown in Table1. The number of ITA forming stable complex with IDV alter from 1, 3, and 5 to 3, 6, and 7. For MAA, the number in the complex changes from 1, 3, 4, and 8 to 5 and 7.

Table 1 Binding energy calculation using density functional theory BLYP in Dmol³ module.

monomer	ratio		vacuum			binding energy			
monomer	rado	total E	adsorption E	dsorption E dEad/dNi		cpx idv		ΔE	(kcal/mol)
	1:1	-104.3200	-36.3400	-36.3400	-2469.7343	-1974.5883	-495.1335	-0.0124	-7.7893
	1:2	-206.7600	-70.8000	-35.0000	-2964.8880	-1974.5872	-990.2717	-0.0291	-18.2445
	1:3	-315.2800	-111.3500	-39.7600	-3460.0348	-1974.5875	-1485.4154	-0.0319	-20.0374
	1:4	-411.9600	-140.0600	-34.2500	-3955.1639	-1974.5870	-1980.5526	-0.0244	-15.2825
ITA	1:5	-510.7600	-170.8800	-37.0100	-4450.3018	-1974.5870	-2475.6945	-0.0203	-12.7428
	1:6	-605.0100	-197.1500	-33.9000	-4945.4552	-1974.5887	-2970.8314	-0.0351	-22.0160
	1:7	-707.6100	-231.7800	-30.8400	-5440.5957	-1974.5868	-3465.9795	-0.0294	-18.4224
	1:8	-751.3200	-207.5100	-22.7000	-5935.7235	-1974.5901	-3961.1101	-0.0233	-14.6194
	1:9	-877.1000	-265.3100	-31.5500	-6430.8808	-1974.5854	-4456.2751	-0.0203	-12.7693
	1:1	-63.4200	-21.0500	-21.0500	-2281.1054	-1974.5889	-306.5056	-0.0109	-6.8599
	1:2	-122.8800	-38.1400	-18.1800	-2587.6233	-1974.5879	-613.0073	-0.0281	-17.6214
	1:3	-180.7900	-53.6800	-21.8900	-2894.1290	-1974.5907	-919.5282	-0.0101	-6.3437
	1:4	-238.0100	-68.5300	-20.4200	-3200.6444	-1974.5898	-1226.0439	-0.0106	-6.6665
MAA	1:5	-300.3200	-88.4700	-16.6800	-3507.1542	-1974.5878	-1532.5306	-0.0357	-22.4153
	1:6	-344.5200	-90.3000	-17.7400	-3813.6619	-1974.5901	-1839.0734	0.0015	0.9642
	1:7	-411.4200	-114.8300	-14.5000	-4120.1821	-1974.5853	-2145.5599	-0.0368	-23.1174
	1:8	-470.4200	-131.4660	-21.2600	-4426.6989	-1974.5876	-2452.0905	-0.0208	-13.0575
	1:9	-513.3100	-131.9900	-12.8800	-4733.1818	-1974.5888	-2758.5721	-0.0209	-13.0912

3.4 Hydrogen Bond Network in MIPs

Table 2 shows the hydrogen bond network including H-bond donor, acceptor and distance between IDV and monomer. The high number of H-bond and complex network architecture indicates a strong interaction. The most interactive part as H-bond acceptor forming H-bond with monomer is N42-C and C=O5, respectively while H-bond donor parts are dominated by N6-H and O16-H. These results indicate the role of amide group next to i-butyl group and carbonyl group at the center of IDV molecule governing prepolymerization adduct resulting in tight binding interaction. This binding pattern was also found in the binding pocket of HIV-1 protease X-ray crystallographic structures (PDB ID: 2BPX ,1SDT, 1SDU, 1SDV and well recognized as P1 and P2. Structural comparison of the inhibitor complexes reveals

certain common features with the pattern of complementary hydrogen bonds between their backbone atoms.

Table 2 H-bond analysis in binding of each monomer and idv, idv-binding monomer and monomer, and the extended H-bond network: monomer and monomer.

			Ide mee	omer in binding		T-1	v-binding monor		-				
i i	ratio	idv	monomer	angle	distance		neighbor	angle	distance		Monomer neighbor	angle	distance
\vdash						monomer	neighbor	angle	distance	попошег	neighbor.	angle	distance
	1:1	N648	C1=O5	175.1090	2.2160	!	!	!	!!		!	!	
!		C-N42	D6-H	150.1630	1.7979	!	!	!	!!		!	!	
	1:2	C=05	D7-H	192,5090	1.7300								
		C=027	D9-H	164.6960	1.7290				-				
		N648	C-06	156.9170	2.2290	!	!		!!		!	!	
	1:3	C-N42 O16-H	C9-H C=O8	170.9500 174.0190	L6390 L8970	0748	C=CB (2)	158.1190	1.9560		!	!	
	1:3	OH-H	C-La	174,0180	1.8979	D=06	O7-H (3)	149.6820	1,5630		: I	ł	}
		0.016	0746	162,9990	1.6990	L-Us	CO-46 (A)	148.6620	13630	1	: I	1	1
		N648	C=D5	167.8628	2.2230	ŀ	1			1	¦	ł	}
l i	i	C-N42	0946	163,3060	1.6990	i	i	i			i I	i	i
l 1	1:4	0.016	D9-H	177.1990	1.7999	0748	C=06 (2)	160.0540	1.7930		i I	i	
	1.4	0.4046	1.55-44	0.77.4890	1	C=06	07-H (4)	155.5500	1.5010		i		
l i	i	C-N42	D74E	143.2540	1.5360	09-61	C=06 (4)	165,4470	1.9100				
l i	i	N29-H	C-09	165.3120	2.3450)				i I	i	i
l i	1:5	O16-H	C=06	171.5400	1.9970	0-07	07-8 (3)	141.9610	1,5040	C-07	0948 (4)	169.1370	1.9090
- ₹		C=05	D9-H	167,7720	1.7290	0748	C=C8 (4)	160.3730	1.8070				
TA	i	C-D16	D9-H	169.6449	1.6650	C=06	O9-H (3)	169,7290	1.8100				
_	i	L-010				0748	C=CB (5)	172,1390	1.7700	i	i	i	i
	1:6	C=05	D74E	154.0480	1.7750								
l i		N648	C=06	174,6940	2.0920	0948 (2)	C=06 (3)	157,7960	1.5800	C=06 (3)	0748 (4)	151,1740	1.9570
l i	i	C-N42	D74E	165.6450	1.5340	C=06 (2)	O9-H (4)	171.4779	1.6450	C=D5 (4)	0748 (5)	156.0840	1.9450
	L:T	016-8	C=06	154.7800	2.2550	C=06	0.7-11 (4)	159,4030	1.7610	C=D6 (4)	0748 (2)	162:2740	1.7300
l i			i	i	i	0948	C-OT (3)	135.9510	2.2000	C=D6 (3)	0748 (5)	154.6960	1.8190
l i	i l	N648	C=06	175.0190	2.3090	i	1	1		C-OT (2)	0748 (6)	152.8820	1.9950
l i	i	0.842	D9-H	175.7160	1.6920	i	i	i	i				
Ιi		C=05	0746	153.9730	1.7110								
Ιi	1:5	C-N42	D74E	165.5560	L5390	C=06	07-8	165.2090	1.7929	İ	i l	ĺ	İ
li	1:9:	C=05	D9-H	161.3220	L.T130	0748	C=06 (4)	166.5899	1.7210	DT-44 (4)	C=D6 (5)	15T.9190	1.9510
		1	1	1	ı	I		1	1	D9-H (4)	C=D6 (6)	162.3300	1.5340
Ιí		C=027	0940	172,4890	1.6390	C=06	09-1(3)	165,6900	1.8280			ì	1
l i	i	i	j	j	j	C+OB	02-H (7)	149.9279	2.0630	D9-H (7)	C=06 (5)	154.8370	1.9200
IJ		1	1	1	1	l	I	1	1	C=06 (7)	0748 (5)	161.3190	1.7740
1 1		03140	C=06	159.1340	2.0020	l							
!	1:1	016-8	C1=05	167.4400	2.0370								
		C=05	D6-H	164.6240	1.7890	l		,	, ,			,	
!	1:2	C=05	D6-H	175.1340	1.6990				$\overline{}$				
!		19648	C1=05	163.0560	2.1540	ļ	ļ	ļ	! !		!	ļ	
!		C-N42	0640	177.3410	1.6590	ļ	ļ	ļ	! !		!	ļ	
!	1:3-	C-D16	D6-H	179.2129	L.7250	C1=D6	O6-H(2)	170.3450	1.6730				
!		016-11	C-06	145.2100	2.0530	C1=06	O6-H (3)	165.9540	1.8230		!	!	
!	1:4	C-D16	D6-H	169.5050	1.7100	C1=08	O6-H(2)	178.5699	1.7580		!	Į .	
		N25-H	C1=05	173.4130	2.0500				\vdash		\vdash		
. !	1:5	O16-H	C1=O5	169.4000	1.9900	!	!				!	l .	
!		0=05	064	166.5230	1.9530	01-04	06.11.00	100 0400			!	l	
		C-016	064	162.5200	1.0990	C1=06	O6-H (5)	166.8490	1.7620			—	
MAA		C=05	D6-H	172.5140	1.7540				\vdash			-	
è		C=027	D6-H	162.0090	1.5420						!!	ł	
~	1:6	N648	C-06	166.4630	2.3920	C1=D5	C1=05 (2)	173.7590 175.6410	1,6470				
	L:T	O16-H	C1=05	165.0320	2.0490	CI-D8	O6-H (2)	175,5400	1,0940				
	1:3	CHOS		165,4300		1	1						1
		C=05	D6-H	165,4369	1.7750 1.6720				\vdash			—	
									-				
		C-0314E	D6-H C1=D5	166.3979	L.1390 L.9730	06-8	C1=D5 (5)	129,6690	1.5979		:		
	1:5	0914E N64E	C1=05	153,2060	2.2970	O8-61	C1=D5/S)	159,6650	1,5070		-		
	1:30	D0046 C-3642	0646	175.3340	2.2970 1.6560	i	i				; I	i	
		N29-H	C-06	175.3340	2.6450	i	i				;		
	1:9	N28-H C-O16	D6-H	174.0160	2.6450 L.7150	ŀ	1						
	1.9	N28-H	C-06	139.6230	2,4770	i	i				i I	i	
1 4		D-042	06-16	165,8470	1.7940	i	i				i I	1	1
		D992	LEH	193.8479	1.7949								

4. Conclusions

The highest percentage of IDV bound to MIPs was observed at IDV:monomer ratio of 1:5 for both P(ITA) and P(MAA) polymers The prepolymerization adducts of the template at different functional monomers were discovered in this study. The binding energy and hydrogen bond networks were analyzed and compared with experimental results to clarify the preferably imprinting complex forming the selective polymer with nanopore structure.

5. References

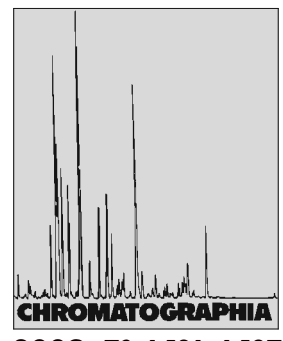
- 1. Nair, A. C.; Bonin, I.; Tossi, A.; Welsh, W. J.; Miertus, S. *Journal of Molecular Graphics and Modelling* **2002**, *21*, 171-179.
- Vacca, J. P., Dorsey, B. D.; Schleif, W. A.; Levin, R. B.; McDaniel, S. L.; Darke, P. L.;
 Zugay, J.; Quintero, J. C.; Blahy, O. M.; Roth, E.; Sardana, V. V.; Schlabach, A. J.; Graham,
 P. I.; Condra, J. H.; Gotlib, L.; Holloway, M. K.; Lin, J.; Chen, I.-W.; Vastag, K.; Ostovich,
 D.; Anderson, P. S.; Emini, E. A.; and Huff. J. R. L-735, 524, *Proc. Natl. Acad. Sci. USA* 1994, 91,4096–4100.
- 3. Gulick, R. M.; Mellors, J. W.; Havlir, D.; Eron, J. J.; Gonzalez, C.; McMahon, D.; Richman, D. D.; Valentine, F. T.; Jonas, L.; Meibohm, A.; Emini, E. A.; Chodakewitz, J. A. N. Engl. J. Med. 1997, 337(11), 734-739.
- 4. Vacca, J. P.; Dorsey, B. D.; Schleif, W. A.; Levin, R. B.; McDaniel, S. L.; Darke, P. L.; Zugay, J.; Quintero, J. C.; Blahy, O. M.; Roth, E.; Sardana, V. V.; Schlabach, A. J.; Graham, P. I.; Condra, J. H.; Gotlib, L.; Hollaway, M. K.; Lin, J., Chen, I-W; Vastag, K.; Ostovic, D.; Anderson, P. S.; Emini, E. A.; Huff, J. R. *Proc. Natl. Acad. Sci. USA* **1994**, *91*, 4096–4100. 5. Pav JW, Rowland LS, Korpalski DJ (1999) J Pharm Biomed Anal 20:91–98.
- 6. Rezk NL, Tidwell RR, Kashuba ADM (2004) J Chromatogr B Analyt Technol Biomed Life Sci 805:241–247. doi:10.1016/j.jchromb.2004.03.002

doi:10.1016/S0731-7085(98)00312-4

- 7. Chi J, Jayewardene AL, Stone JA, Aweeka FT (2003) J Pharm Biomed Anal 31:953–959. doi:10.1016/S0731-7085(02)00708-2
- 8. Azoulay S, Nevers MC, Creminon C, Heripret L, Durant J, Dellamonica P et al (2004) Antimicrob Agents Chemother 48:104–109. doi:10.1128/AAC.48.1.104-109.2004
- 9. Richard J. Ansell and Klaus Mosbach, Analyst, July 1998, Vol. 123 (1611–1616)

- 10. O'Brien T.P., Grinberg N., Bricker G., Wyvratt J. and Snow N.H., *Enant.*, 2002, **7**, 139-148.
- 11. Chiannella I., Karim K., Piletska E.V., Preston C. and Piletsky S.A., Anal. Chem. Acta, **2006**, 559, 73-78.

Synthesis of Molecularly Imprinted Polymers for Nevirapine by Dummy Template Imprinting Approach



2009, 70, 1531-1537

Weeranuch Kareuhanon¹, Vannajan Sanghiran Lee¹, Piyarat Nimmanpipug¹, Chatchai Tayapiwatana², Mookda Pattarawarapan^{1,⊠}

Received: 2 June 2009 / Revised: 14 August 2009 / Accepted: 30 September 2009 Online publication: 8 November 2009

Abstract

Nevirapine (NVP) and its structurally related analogs including nicotinamide (NAM), benzamide (BZM) and benzophenone (BZP) were used as templates in the synthesis of molecularly imprinted polymers for NVP. Molecular modeling was used to estimate binding energy of the complex formation between methacrylic acid (MAA) monomer and the selected templates, while equilibrium binding studies were applied to evaluate the polymer binding efficiency. The data indicated that NAM is the best candidate to prepare MIPs for retaining NVP due to a relatively similar binding energy between the NVP–MAA and NAM–MAA complex. The NAM-imprinted polymer showed a high binding affinity and selectivity toward NVP. When the polymer was applied as a sorbent in solid-phase extraction of NVP from human plasma, high recovery and reproducibility were obtained.

Keywords

Column liquid chromatography Molecular imprinting and modeling Dummy template Nevirapine and nicotinamide

Introduction

Nevirapine (NVP) is a non-nucleoside reverse transcriptase inhibitor (NNRTI) which is widely used for the treatment of human immunodeficiency virus type-1 (HIV-1) infection [1]. It binds directly to reverse transcriptase and inhibits the viral DNA polymerase activities. Studies have shown that the plasma levels of NNRTI seem to be connected with virologic efficacy and NVP viral drug

resistance can confer cross resistant to the other NNRTIs in the drug class [2, 3]. In order to reduce a risk of treatment failure or drug resistance, routine monitoring of NVP level in patients is therefore necessary.

Several methods for quantitative analysis of NVP have been developed such as LC [4, 5], LC–MS–MS [6], and immunoassay [7]. For the analysis of biological samples, the methods generally require a sample pretreatment step to separate and/or preconcentrate the analyte prior to analysis. The synthesis of a new sorbent material that can selectively retain NVP would facilitate routine analysis of the drug level present in such complex matrices.

Molecularly imprinted polymers (MIPs) are highly selective materials which can be tailor-made by polymerization of selected monomer and cross-linker in the presence of target analyte, acting as the template for assembly of its own recognition sites [8, 9]. After polymerization and subsequent template removal, rigid polymeric materials with recognition sites specific for the template molecule are generated.

In previous studies, MIPs were applied successfully in the solid-phase extraction (SPE) of various analytes [10].

¹ Department of Chemistry and Center of Excellence for Innovation in Chemistry, Faculty of Science, Chiang Mai University, Chiang Mai 50200, Thailand; E-Mail: mookda@chiangmai.ac.th

² Division of Clinical Immunology, Faculty of Associated Medical Sciences, Chiang Mai University, Chiang Mai 50200, Thailand

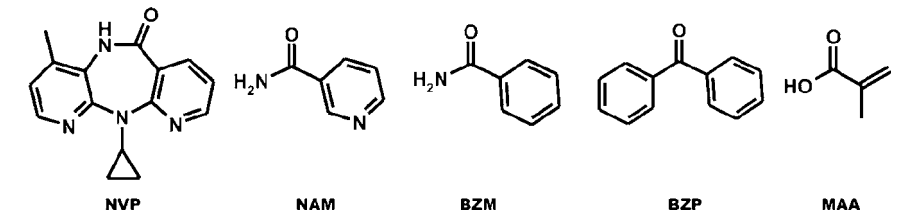


Fig. 1. Structures of the templates and the MAA monomer

However, the leakage of trace amounts of the imprinted molecules from the MIPs can hinder the accuracy and precision of the assay [11]. To overcome such problems, a structurally related analog of the target analyte or so called "dummy template" has been applied to produce MIPs [12–15]. Using this strategy, leakage of the dummy template would appear as a separate peak and would not interfere with the trace analysis.

In this work, water-compatible MIPs are desired for effective recognition of NVP in aqueous environments. NVP and its structurally related analogs including nicotinamide (NAM), benzamide (BZM), and benzophenone (BZP) were imprinted to investigate binding performances of the MIPs. Molecular modeling was used to predict the binding energy of template-monomer interactions to provide an insight in the NVP recognition of the imprinted polymers. Equilibrium binding studies were applied to probe the MIPs binding affinity and selectivity toward NVP. A suitable imprinted polymer was then selected to be used as a sorbent in solid-phase extraction of NVP.

Experimental

Materials and Instruments

NVP was kindly provided by the Government Pharmaceutical Organization (GPO), Bangkok, Thailand. NAM, BZM, and BZP, methacrylic acid (MAA), and trimethylpropane trimethacrylate (TRIM) were purchased from Aldrich (Milwaukee, WI, USA). Benzoyl peroxide was obtained from Janssen Chemical (Beerse, Belgium) and was recrystalized from methanol prior to use. Plasma samples were obtained from the

Research Institute for Health and Sciences, Chiang Mai University (Chiang Mai, Thailand). All other chemicals were purchased from other commercial suppliers and used without further purification.

UV absorbance measurements and spectra were recorded on a Lambda 25 UV–Vis spectrophotometer (Perkin Elmer, Waltham, MA, USA) with 1-cm quartz cells.

Molecular Modeling

Geometrical optimizations for the search of possible interactions of functional monomer, MAA, with the four templates (Fig. 1), NVP, NAM, BZM, and BZP, were carried out using semiempirical (PM3) [16], ab initio (HF/6-31G*) [17], and density functional methods (B3LYP/6-31G*) [18]. Further single point energy calculations were then performed on the optimized structure to estimate the binding energy between the template and monomer (ΔE) from

$$\Delta E_{\text{template}} = (E_{\text{complex}} - E_{\text{template}} - E_{\text{monomer}})$$

The optimized complex structures using density functional theory (DFT) with B3LYP/6-31G* were analyzed in detail. All the quantum calculations were performed using Gaussian 03 software [19].

Syntheses of MIPs

A set of polymers was synthesized using MAA as a functional monomer and TRIM as a crosslinker. Four templates including NVP, NAM BZM and BZP were used to synthesize P(NVP), P(NAM), P(BZM), and P(BZP), respectively. The template (0.25 mmol) and

MAA (1 mmol) were first dissolved in 15 mL THF-MeOH-H₂O (5:4:1, v/v) in a 50 mL round bottom flask and incubated for 10 min. TRIM (1 mmol) and benzoyl peroxide (0.125 mmol) were then added sequentially and the flask was sealed with a rubber cap. After the flask was purged with nitrogen for 10 min, the polymerization was carried out at 60 °C in an oven for 24 h. Template removal was done by extracting the obtained polymers with methanol/acetic acid (9/1, v/v) using Soxhlet extractor, followed by washing with methanol and acetonitrile to remove any residual acetic acid. The particles were dried at 50 °C in an oven and under vacuum conditions. Non-imprinted polymer (NIP) was prepared using the same procedure but without the addition of template.

Equilibrium Binding Study of MIPs

The 5 mg of powder polymer was added into 1 mL of 0.2 mM solution of each substrate in 0.01 M phosphate buffer pH 7 containing 0.05% Tween 20. The samples were incubated on a rocking table at 25 °C overnight. After the polymer was isolated from the mixture by centrifugation, the clear supernatant was analyzed by UV-Vis spectrophotometer at λ 281, 262, 272 and 258 nm for NVP, NAM, BZM and BZP. respectively. The initial amount of analyte before adding the polymer $(Q_{initial})$ and the amount of analyte bound to the polymer (Q) were determined from calibration curve for each corresponding analyte.

The selectivity of the MIPs toward NVP was investigated by equilibrium rebinding studies using the polymer concentration of 5 mg mL⁻¹. The equilibrium binding study was performed as previously described for template rebinding studies excepted that 0.2 mM NVP in 0.01 M phosphate buffer pH 7 containing 0.05% Tween 20 was used as a test solution. The amount of the NVP before and after adding polymers was determined using UV spectrophotometer at λ_{max} 281 nm. These experiments were done in triplicate for each polymer. The

Table 1. Calculated binding energies of the complex formation

Complex structure	Distance	Distance (Å)		Binding ener	Binding energy (ΔE) (kcal ⁻¹ mol)				
	R1	R2	R3	PM3	HF/6-31G*	B3LYP/6-31G*			
NVP_MAA_MAA_MAA NAM_MAA_MAA BZM_MAA BZP_MAA	1.69 1.70 1.68 1.79	1.00 1.00 1.00 1.01	0.97 0.97 0.97 0.97	-12.64 -10.38 -7.80 -3.89	-34.72 -25.40 -15.82 -9.03	-47.30 -34.18 -21.18 -15.09			

R1 the shortest intermolecular distance of H–O between template and MAA, R2 bond length of O–H of carboxyl of MAA in complex, R3 bond length of O–H of carboxyl of free MAA

quantity of the analyte was determined by reference to a calibration curve.

Polymer Characterization

Scanning electron microscopy (SEM) images were recorded on a scanning electron microscope (JEOL, 6335F, Tokyo, Japan). SEM specimens were prepared by diluting the particle dispersions with acetone and placing one drop each on a stub. The drops were allowed to dry at room temperature and then sputter coated with gold prior to imaging. Surface area analysis was performed by N₂ adsorption on Autosorb-1-MP (Quantachrome Corporation, Boynton Beach, FL, USA). A 100 mg quantity of dry polymers were used and degassed at 120 °C under nitrogen flow for approximately 4 h prior to measurement. The nitrogen adsorption/desorption data were recorded at the liquid nitrogen temperature (77 K). The specific surface area was calculated using the BET equation.

Solid-Phase Extraction Procedure

Commercial SPE cartridges (5 mm in diameter) were packed dry with 50 mg of polymer and the upper frit was placed on top. Using a vacuum manifold, the SPE cartridges were conditioned with 1 mL of MeOH, followed by 2×1 mL of 0.01 M phosphate buffer pH 7 containing 0.05% Tween 20. Samples (1 mL) were then transferred onto the SPE cartridge. The loaded columns were washed with 5×1 mL of phosphate buffer pH 7, followed by eluting with 5×1 mL of acetonitrile. All fractions of eluate were

combined, evaporated under vacuum, and reconstituted in 500 μ L of acetonitrile before analysis by LC.

LC Conditions

LC analysis was performed using an Agilent Technologies (Santa Clara, CA, USA) LC system employing a model 1100 quaternary gradient pump and variablewavelength detector. Separations were carried out on $4.0 \times 250 \text{ mm}$, 5 µm Hewlett-Packard (Bremen, Germany) C₁₈-column. The gradient mobile phase consisted of 15 mM of phosphate buffer pH 7.2 as solvent A and pure acetonitrile as solvent B. The flow rate used was 1.0 mL min⁻¹ with gradient system 10-90% solvent B in 10 min. The injection volume was 20 µL throughout the study and the chromatogram was detected by a single wavelength of 281 nm.

Preparation of NVP-Spiked Plasma Samples

An appropriate amount of NVP was added into 500 μL of blank human plasma. Cold acetonitrile (1 mL) was then added to precipitate protein in the samples [20]. The mixtures were vortex mixed for 2 min, followed by centrifugation at 8,586g for 5 min. Aliquots of 500 μL of clear supernatants were diluted with 500 μL of 0.01 M phosphate buffer pH 7 containing 0.05% Tween 20 before applied onto the SPE cartridge.

Method Validation

The linearity of the method was evaluated by analyzing extracts of spiked

plasma standards at NVP concentrations of 0.5, 1.0, 5.0, 10.0, 25.0 and 100 $μg mL^{-1}$ (n = 3) and a linear regression coefficient (R^2) was calculated. The percentage recovery (%recovery) of analyte was determined by comparing the peak response of extracted standards to that of un-extracted standard prepared at the same theoretical concentration. The intra-day precision and accuracy of the method were determined by analyzing extracts of spiked plasma standards at NVP concentrations of 1 and 10 mg L^{-1} (n = 5). Relative standard deviation (%RSD) and relative accuracy (%RA) were then calculated.

Results and Discussion

Binding Energy of the Monomer–Template Interactions

Strength and quantity of the interactions between template and functional groups in the MIPs are the two main factors that govern the recognition efficiency of the imprinted polymers. To select suitable dummy template for MIP preparation, molecular modeling has been used to predict the binding energy between the monomer and the possible templates [21]. In this study, binding energies between the selected templates and the functional monomer methacrylic acid (MAA) (Fig. 1) were calculated and the structures of template-monomer complexes were simulated to investigate the recognition mechanism.

Comparison of the binding energy of the complex formation between the four templates and MAA in vacuum are shown in Table 1 where $\Delta E(\text{NVP}_{-}\text{MAA MAA MAA}) < \Delta E(\text{NAM MAA})$

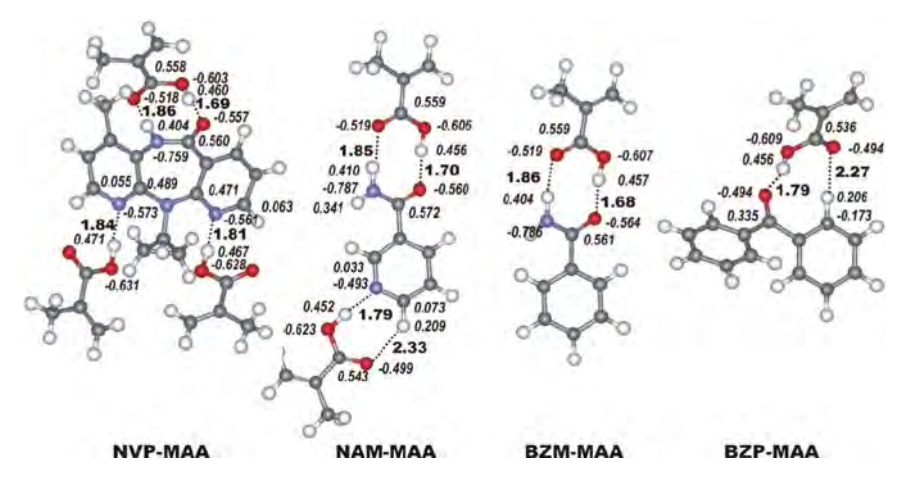


Fig. 2. The optimized structures of monomer-template complexes formed between. (a) NVP-MAA, (b) NAM-MAA, (c) BZM-MAA, and (d) BZP-MAA

MAA) $<\Delta E(BZM_MAA) < \Delta E(BZP_MAA)$. The lower binding energy indicates the higher strengths of interaction that leads to higher binding affinity in the complex formation. The results obtained indicate that the interaction between NVP and MAA is stronger than NAM-MAA, BZM-MAA and BZP-MAA, respectively.

The optimized complex structures using density functional theory (DFT) with B3LYP/6-31G* of the monomertemplate complexes are illustrated in Fig. 2. Partial charges are shown in italic, and hydrogen bonds are presented in bold (indicated by dashed lines). In the online version of this publication hydrogen, carbon, nitrogen, and oxygen are shown in white, gray, blue and red, respectively. Calculation of partial charges on each of the atoms of NVP, NAM, BZM, BZP shows several sites (on nitrogens of the six/seven-membered rings and the amide group, and carbonyl oxygen) are likely to have electrostatic and/or hydrogen bonding interactions with the functional monomer (MAA). The elongations of bond length R2 in the complexes shown in Table 1 indicate the possibility of ion-pair formation in which acidic protons of MAA may leave the oxygen atom and approach the oxygen atom of the templates.

Synthesis of MIPs

To investigate a template effect in molecular imprinting, NVP, NAM,

BZM and BZP were used as the templates in the synthesis of imprinted polymers, P(NVP), P(NAM), P(BZM) and P(BZP), respectively. MAA was used as a functional monomer since it has shown to provide a strong interaction with basic templates [22]. TRIM was used as a cross-linker since it can produce MIPs with high selectivity and load capacity [23]. It has also been shown that MIPs prepared in high polar media such as methanol-water system exhibit higher recognition ability in aqueous media than those prepared in low polar organic solvents [24, 25]. In this study, THF-methanol-water system was thus used as a porogenic solvent in the synthesis of the imprinted polymers. Non imprinted polymer (NIP) used as a control polymer was prepared under the same conditions but without addition of template. All polymers were obtained as white powder with percentage yield ranging from 85 to 95%.

Binding Efficiency and NVP Selectivity of Imprinted Polymers

Binding performances of the obtained MIPs in phosphate buffer pH 7 were determined by template rebinding studies under equilibrium [26, 27]. Tween 20 was added into the test solutions as a surfactant to reduce nonspecific hydrophobic binding. [28]. The concentrations of the polymers used in these studies were pre-adjusted to the optimum values

in order to obtain maximum binding specificity.

For each polymer, the percentage bound (%Bound) of its corresponding template and the imprinting factor (α) were calculated according to Eqs. (1) and (2), respectively.

% Bound =
$$\frac{Q}{Q_{\text{initial}}} \times 100$$
 (1)

where Q is the amount of analyte bound to the polymer and Q_{initial} is the initial amount of analyte before adding the polymer.

$$\alpha = \frac{\% Bound_{MIP}}{\% Bound_{NIP}}$$
 (2)

where $\%Bound_{MIP}$ and $\%Bound_{NIP}$ represent the percentage of bound analyte by MIPs and NIP, respectively.

The NVP cross-selectivity of the prepared MIPs were also evaluated by determining of the selectivity factors, ε , calculated according to Eq. (3).

$$\varepsilon = \frac{\% Bound_{NVP}}{\% Bound_{template}}$$
 (3)

where %Bound_{NVP} represents the percentage of bound NVP by MIP and %Bound_{template} represents the percentage of bound the corresponding template by MIP.

According to Table 2, the %Bound of the corresponding template to P(BZP) is the highest, followed by that of P(NVP), P(BZM) and P(NAM). However, the α values of P(NVP) and P(NAM) are higher than those of P(BZM) and P(BZP). The high α values mean that binding of the analyte on the MIPs results from specific binding interactions. Thus, the binding of BZP to P(BZP) is presumably due to nonspecific hydrophobic adsorption. The unusual high %Bound value for P(BZP) may be caused by template bleeding. When considering NVP cross-selectivity of the MIPs, P(NAM) showed the highest binding selectivity toward NVP. This observation is as predicted since NVP contains two basic nitrogens on the pyridyl rings with an amide bond which arrange in the same direction as those in NAM. The three possible binding sites of NVP would allow it to bind stronger than NAM as was already observed in computational molecular modeling. It is

noted that when the equilibrium binding study was performed in organic solvents, such as THF, acetonitrile, and methanol, little or no measurable binding was observed for both the MIP and NIP. This result suggests that binding interactions between the polymers and their corresponding templates do not rely on hydrogen bonding which is the dominate interaction in nonpolar media. In accordance to the above finding, it seems that the more hydrophobic the template, the better the adsorption on the polymers (in order of hydrophobicity: NAM < BZM < NVP < BZP). This data implies that in aqueous media, recognition mechanism of the polymers relies mainly on hydrophobic and ion-pair interactions. Similar observation has also been reported in literatures [26, 29].

Characterization of NAM-Imprinted Polymer

P(NAM) was selected for further studies in order to elucidate the nature of the imprinting effect. Morphology and surface area of P(NAM) and the corresponding NIP were investigated using scanning electron microscope (SEM) and the Brunauer-Emett-Teller (BET) analysis, respectively [30]. Figure 3 is the SEM micrographs of P(NAM) and the NIP. The images show slight differences in the morphology of the MIP and NIP. While P(NAM) composed of agglomerates of globules and more hollow microparticles of different sizes, the control polymer showed rather smaller platelet-like particles. The surface areas calculated for P(NAM) and the NIP were 366.15 and 219.21 m² g⁻¹, respectively. A higher surface area presence in the imprinted polymer indicates that more binding sites were created during the imprinting process. This data is consistent with the previous reported results that the MIPs tend to have higher surface area than that of corresponding NIPs [31].

Binding Characteristics of P(NAM)

An adsorption isotherm experiment was performed for accessing the binding

Table 2. Binding characteristics of MIPs in 0.01 M phosphate buffer pH 7

MIP	$\%Bound_{template}$	α	%Bound _{NVP}	3
P(NVP)	97.5 ± 1.4	2.54	$\begin{array}{c} 97.5 \pm 1.4 \\ 98.0 \pm 0.69 \\ 81.2 \pm 2.1 \\ 106 \pm 0.92 \end{array}$	1.00
P(NAM)	38.0 ± 4.9	2.03		2.58
P(BZM)	51.7 ± 6.3	1.60		1.57
P(BZP)	116 ± 2.2	1.01		0.92

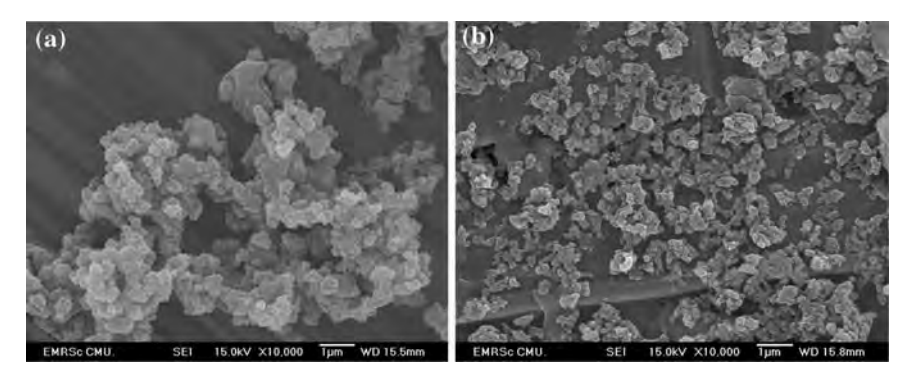


Fig. 3. SEM images of (a) P(NAM) and (b) NIP with 10,000× magnification

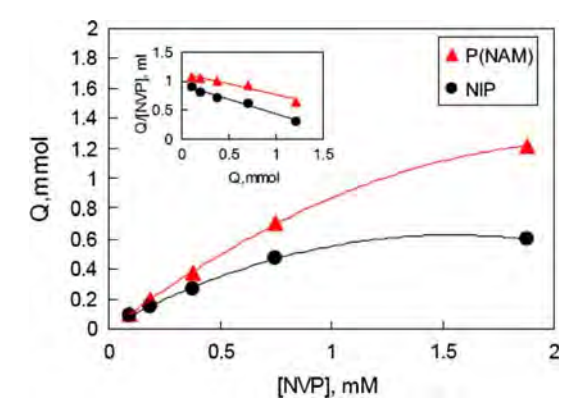


Fig. 4. Binding isotherm and Scatchard plots of P(NAM) and NIP; Q, amount of NVP bound to 5 mg of the polymers; $V=1.0~\mathrm{mL}$; Adsorption time: 16 h

affinity of P(NAM) in comparison with the NIP. As shown in Fig. 4, the imprinted polymer has higher affinity for NVP than the non-imprinted control, and nonlinear profiles were obtained. To estimate the binding parameters of P(NAM) and the NIP, the binding data was plotted according to the Scatchard equation [32]. The upwardly straight lines were obtained. The apparent maximum number of binding sites (Q_{max}) and the dissociation constant (K_d) of P(NAM) can be calculated to be 62.11 μ mol g⁻¹ and 58.37 mmol L⁻¹, respectively, and their corresponding values of the NIP were 37.51 μ mol g⁻¹ and $43.44 \text{ mmol L}^{-1}$. Higher binding capacity and affinity in P(NAM) was possibly due to the imprinting effect of the binding sites.

SPE of NVP by P(NAM) and the Control Polymer (NIP)

To determine the selectivity of P(NAM) for NVP, the percentage recoveries of NVP after extraction with SPE columns packed independently with P(NAM) and NIP were evaluated. The recoveries after ten consecutive elutions with 1 mL of ACN are shown in Fig. 5. For the NIP, nearly all NVP was eluted from the column in the first elution and only 79%

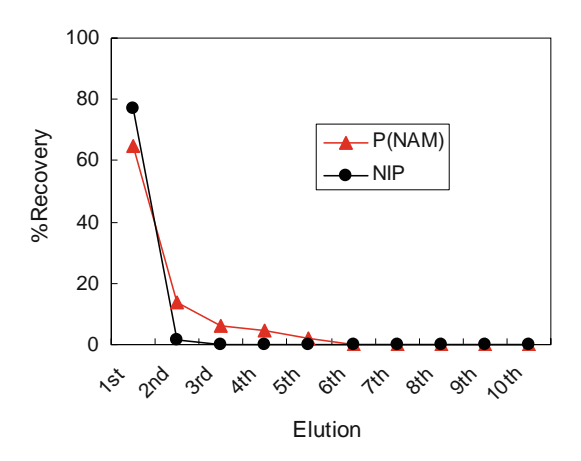
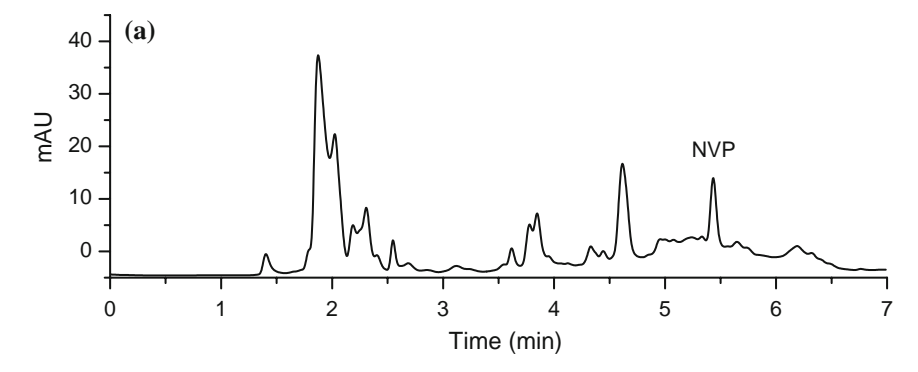


Fig. 5. Percentage recoveries of NVP obtained after SPE with P(NAM) and NIP

Table 3. %Recovery of NVP and NAM from spiked plasma samples after SPE

NVP:NAM	%Recovery of NVP	%Recovery of NAM
1:0 1:1 1:6 1:12	98.6 ± 3.7 97.3 ± 8.9 98.5 ± 1.9 89.7 ± 1.3	71.6 ± 1.7 75.3 ± 2.2 67.0 ± 1.2



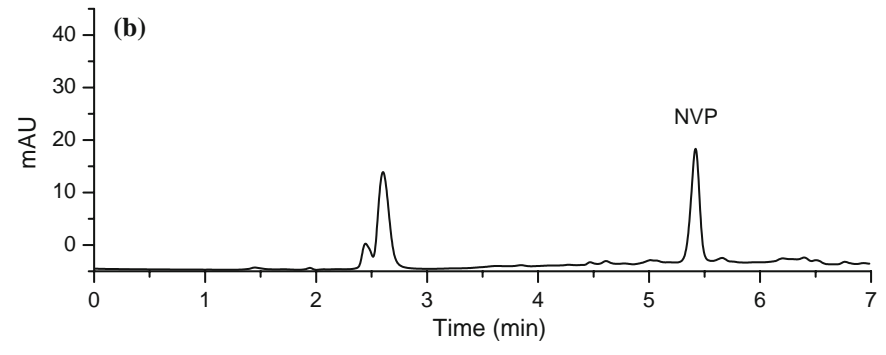


Fig. 6. LC chromatograms of NVP-spiked plasma sample at 5 mg L $^{-1}$ obtained (a) before extraction, and (b) after extraction on P(NAM). LC chromatogram monitored at λ 281 nm using gradient system of 10–90% B, 10 min (mobile phase; A = 15 mM phosphate buffer pH 7.2, B = acetonitrile)

total recovery of NVP was obtained. On the other hand, elution of NVP from the P(NAM) column requires at least five times elution to completely remove NVP. Higher total recovery of NVP (91.87%) was also observed in comparison to that of the NIP column. The difference in the retention of NVP on the

MIP and NIP indicates that there are selective binding cavities on the MIP that can bind NVP stronger than the control polymer.

Effect of NAM on the Recovery of NVP

To investigate the effect of NAM on the recovery of NVP, standard samples containing NVP and NAM in the molar ratios of 1:0, 1:1, 1:6 and 1:12 were applied to the P(NAM) extraction column.

The results from this experiment are shown in Table 3. The presence of NAM in up to six fold excess levels relative to NVP has almost no effect on the recoveries of NVP. Nevertheless, when the amount of NAM was increased to twelve fold (2.4 mM), the recovery of NVP was slightly decreased. These results suggest that competitive binding between NAM and NVP can take place, provided that very large excess of NAM is present in the NVP samples. Since the levels of NAM found in biological samples were generally lower than 0.2 mM, it is unlikely that NAM will interfere with the extraction recoveries of NVP when P(NAM) was used as the solid sorbent in SPE.

MISPE of NVP from Spiked Plasma Samples

The aim of this study was to demonstrate the applicability of the P(NAM) in the extraction of NVP from real plasma sample. The polymer was thus used as a sorbent in SPE column. Spiked plasma samples at 5 mg L⁻¹ of NVP was then loaded, washed, and eluted, followed by analysis with LC. Figure 6 shows an LC chromatogram of NVP spiked plasma samples obtained before and after extraction with P(NAM). The chromatographic results indicate that after extraction, NVP can be obtained in high purity and the nearby interferences were completely removed.

To validate the MISPE method for NVP analysis, linearity, precision and accuracy were determined using NVP spiked plasma standards. The linearity of the standard calibration curve for NVP was evaluated over the NVP concentration range of 0.5-100 mg L⁻¹ and a linear regression coefficient (R^2) observed was 0.995. The NVP recoveries were found to be $90.6 \pm 3.3\%$ and $97.6 \pm 1.4\%$ at the NVP concentrations of 1 and 10 mg L⁻¹, respectively. The intra-day precision was evaluated by five repeated injections of each spiked plasma samples (1 and 10 mg L^{-1}) and calculated to be 2.5 and 3.9% RSD. Relative accuracy was calculated as 100.2 and 100.5%. The results show that the performance of this MISPE method is well within the limits required for assays to be validated.

Conclusions

Molecularly imprinted polymers that can bind NVP selectively were prepared using the dummy template imprinting approach. Molecular modeling predicted that NAM could provide the relatively strong binding interaction with MAA in comparison to that of NVP. NAM-imprinted polymer also shows high binding affinity and selectivity toward NVP which allows effective sample clean-up when the polymer was applied as a sorbent in solid-phase extraction of NVP. These results indicated that the polymer could be applied in facilitating routine analysis of NVP in patient plasma.

Acknowledgments

The authors gratefully acknowledge the Government Pharmaceutical Organization (GPO), Thailand for providing NVP for this study, the Center of Excellence for Innovation in Chemistry (PERCH-CIC), the Thailand Research Fund (TRF) and Commission on Higher

Education, Ministry of Education for financial support to this research.

References

- Van Leth F, Phanuphak P, Ruxrungtham K, Baraldi E, Miller S, Gazzard B et al (2004) Lancet 363:1253–1263. doi:10.1016/ S0140-6736(04)15997-7
- Najera I, Richman DD, Olivares I, Rojas JM, Peinado MA, Perucho M et al (1994) AIDS Res Hum Retroviruses 10:1479– 1488. doi:10.1089/aid.1994.10.1479
- 3. Richman DD (1994) AIDS Res Hum Retroviruses 10:901–905. doi:10.1089/aid. 1994.10.901
- Pav JW, Rowland LS, Korpalski DJ (1999) J Pharm Biomed Anal 20:91–98. doi:10.1016/S0731-7085(98)00312-4
- Rezk NL, Tidwell RR, Kashuba ADM (2004) J Chromatogr B Analyt Technol Biomed Life Sci 805:241–247. doi: 10.1016/j.jchromb.2004.03.002
- Chi J, Jayewardene AL, Stone JA, Aweeka FT (2003) J Pharm Biomed Anal 31:953–959. doi:10.1016/S0731-7085(02) 00708-2
- Azoulay S, Nevers MC, Creminon C, Heripret L, Durant J, Dellamonica P et al (2004) Antimicrob Agents Chemother 48:104–109. doi:10.1128/AAC.48.1.104-109.2004
- Nicholls IA (1998) J Mol Recognit 11:79–
 doi:10.1002/(SICI)1099-1352(199812)
 11:1/6 < 79:AID-JMR394 > 3.0.CO;2-B
- Mayes AG, Whitcombe MJ (2005) Adv Drug Delivery Rev 57:1742–1778. doi: 10.1016/j.addr.2005.07.011
- Tamayo FG, Turiel E, Martin-Esteban A (2007) J Chromatogr A 1152:32–40. doi: 10.1016/j.chroma.2007.02.109
- 11. Pichon V (2007) J Chromatogr A 1152:41–53. doi:10.1016/j.chroma.2007. 02.109
- Andersson LI, Paprica A, Arvidsson T (1997) Chromatographia 46:57–62. doi: 10.1007/BF02490930
- 13. Venn RF, Goody RJ (1999) Chromatographia 50:407–414. doi:10.1007/BF02 490734
- Martin P, Wilson ID, Jones GR (2000) J Chromatogr A 889:143–147. doi:10.1016/ S0021-9673(00)00570-7

- Matsui J, Fujiwara K, Takeuchi T (2000) Anal Chem 72:1810–1813. doi:10.1021/ ac9911950
- Stewart JJP, Csaszar P, Pulay P (1982) J Comput Chem 3:227–228. doi:10.1002/ jcc.540030214
- 17. Hartree DR (1928) Proc Camb Philol Soc 24:426–437. doi:10.1017/S0305004100015954
- Andzelm J, Sosa C, Eades RA (1993) J Phys Chem 97:4664–4669. doi:10.1021/ j100120a018
- Frisch MJ, Trucks GW, Schlegel HB, Gill PMW, Johnson BG, Robb MA et al (1995) Gaussian 94, Revision B.3ÈE.2. Gaussian, Inc., Pittsburgh
- Song JZ, Chen HF, Tian SJ, Sun ZP (1998) J Chromatogr B Biomed Sci Appl 708:277–283. doi:10.1016/S0378-4347(97) 00635-X
- 21. Salvador JP, Estevez MC, Marco MP, Sanchez-Baeza F (2007) Anal Lett 40:1294–1306. doi:10.1080/00032710701 326668
- 22. Cormack Peter AG, Elorza Amaia Z (2004) J Chromatogr B Analyt Technol Biomed Life Sci 804:173–182. doi:10.1016/j.jchromb.2004.02.013
- Kempe M (1996) Anal Chem 68:1948– 1953. doi:10.1021/ac9512160
- 24. Haupt K, Dzgoev A, Mosbach K (1998) Anal Chem 70:628–631. doi:10.1021/
- Sun HW, Qiao FX (2008) J Chromatogr A 1212:1–9. doi:10.1016/j.chroma.2008. 09.107
- Moring SE, Wong OS, Stobaugh JF (2002) J Pharm Biomed Anal 27:719–728. doi:10.1016/S0731-7085(01)00495-2
- Hsieha RY, Tsaib HA, Syu MJ (2006) Biomaterials 27:2083–2089. doi:10.1016/ j.biomaterials.2005.09.024
- Andersson LI, Abdel-Rehim M, Nicklasson L, Schweitz L, Nilsson S (2002) Chromatographia 55:S65–S69. doi: 10.1007/BF02493355
- 29. Cai W, Gupta RB (2004) Sep Purif Technol 35:215–221. doi:10.1016/S1383-5866(03)00143-6
- Gregg SJ, Sing KSW (1982) In: Adsorption, Surface Area and Porosity, 2nd edn. Academic Press, London
- 31. Bruggemann O (2001) Biomol Eng 18:1–7. doi:10.1016/S1389-0344(01)00076-4
- Matsui J, Miyoshi Y, Doblhoff-Dier O, Takeuchi T (1995) Anal Chem 67:4404– 4408. doi:10.1021/ac00119a032

This article was downloaded by: [Chiang Mai University Library]

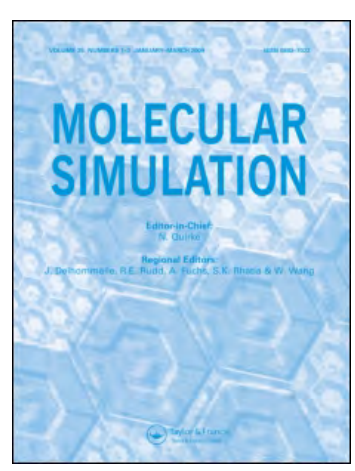
On: 24 May 2010

Access details: *Access Details:* [subscription number 780894007]

Publisher Taylor & Francis

Informa Ltd Registered in England and Wales Registered Number: 1072954 Registered office: Mortimer House, 37-

41 Mortimer Street, London W1T 3JH, UK



Molecular Simulation

Publication details, including instructions for authors and subscription information: http://www.informaworld.com/smpp/title~content=t713644482

Litchi chinensis-derived terpenoid as anti-HIV-1 protease agent: structural design from molecular dynamics simulations

Piyarat Nimmanpipug ^a; Vannajan S. Lee ^a; Peter Wolschann ^b; Supot Hannongbua ^c ^a Department of Chemistry, Faculty of Science, Center for Innovation in Chemistry, Chiang Mai University, Chiang Mai 50200, Thailand ^b Institute of Theoretical Chemistry, University of Vienna, Vienna 1090, Austria ^c Department of Chemistry, Faculty of Science, Chulalongkorn University, Bangkok 10300, Thailand

To cite this Article Nimmanpipug, Piyarat , Lee, Vannajan S. , Wolschann, Peter and Hannongbua, Supot (2009) 'Litchi chinensis-derived terpenoid as anti-HIV-1 protease agent: structural design from molecular dynamics simulations', Molecular Simulation, 35: 8, 673 - 680

To link to this Article: DOI: 10.1080/08927020802714841 URL: http://dx.doi.org/10.1080/08927020802714841

PLEASE SCROLL DOWN FOR ARTICLE

Full terms and conditions of use: http://www.informaworld.com/terms-and-conditions-of-access.pdf

This article may be used for research, teaching and private study purposes. Any substantial or systematic reproduction, re-distribution, re-selling, loan or sub-licensing, systematic supply or distribution in any form to anyone is expressly forbidden.

The publisher does not give any warranty express or implied or make any representation that the contents will be complete or accurate or up to date. The accuracy of any instructions, formulae and drug doses should be independently verified with primary sources. The publisher shall not be liable for any loss, actions, claims, proceedings, demand or costs or damages whatsoever or howsoever caused arising directly or indirectly in connection with or arising out of the use of this material.



Litchi chinensis-derived terpenoid as anti-HIV-1 protease agent: structural design from molecular dynamics simulations

Piyarat Nimmanpipug^a*, Vannajan S. Lee^a, Peter Wolschann^b and Supot Hannongbua^c

^aDepartment of Chemistry, Faculty of Science, Center for Innovation in Chemistry, Chiang Mai University, Chiang Mai 50200, Thailand; ^bInstitute of Theoretical Chemistry, University of Vienna, Vienna 1090, Austria; ^cDepartment of Chemistry, Faculty of Science, Chulalongkorn University, Bangkok 10300, Thailand

(Received 3 August 2008; final version received 27 December 2008)

The molecular structures of the binding between human immunodeficiency virus-1 protease (HIV-1PR) and various inhibitors including existing extensive natural products extracts have been investigated for anti-HIV drug development. In this study, the binding of HIV-1PR and a terpenoid from *Litchi chinensis* extracts (3-oxotrirucalla-7,24-dien-21-oic acid) was investigated in order to clarify the inhibition effectiveness of this compound. Molecular dynamics (MD) simulations of HIV-1PR complex with 3-oxotrirucalla-7,24-dien-21-oic acid were performed including water molecules. The MD simulation results indicated the formation of hydrogen bonds between the oxygen atoms of the inhibitor and the catalytic aspartates, which are commonly found in inhibitors—protease complexes. On the other hand, no hydrogen bonding of this particular inhibitor to the flap region was found. In addition, the radial distribution function of water oxygens around the catalytic carboxylate nitrogens of Asp29 and Asp30 suggests that at least one or two water molecules are in the active site region whereas direct interaction of the inhibitor was found for catalytic carboxylate oxygen of Asp25. The results of this simulation, in comparison with the structures of other HIV-PR inhibitor complexes, could lead to a better understanding of the activity of 3-oxotrirucalla-7,24-dien-21-oic acid.

Keywords: 3-oxotirucalla-7,24-dien-21-oic acid; HIV-1 protease; MD simulation; natural product

1. Introduction

Human immunodeficiency virus-1 protease (HIV-1PR) is an important enzyme due to its role in the replication of HIV-1 by processing two precursor polyproteins, Pr55gag and Pr160gag-pol, into structural proteins and replication enzymes. Inactivation of this enzyme results in the formation of immature, non-infectious viral particles. Therefore, this enzyme is an attractive target in intensively focused anti-AIDS drug design research [1]. HIV-1 PR is an aspartic protease, and a homodimer with C2. Each monomer consists of 99 amino acid residues that possess a loop structure containing the active site triad Asp25(25') – Thr26(26')-Gly27(27'). A cavity for the insertion of the substrate is formed by these loop structures containing the active site triads and the flap regions which are presumably related to the entry and affinity of the substrate to the enzyme [1-7].

Terpenoids are widespread natural products with a high diversity of biological and pharmacological activities. 3-Oxotrirucalla-7,24-dien-21-oic acid, a triterpene in the extracts of *Litchi chinensis* seeds isolated by Tu et al. [8], was found to have activity against HIV-1PR. The inhibitory activity of this triterpene was reported to be $IC_{50} = 20 \text{ mg/l}$ (42.9 μ M) by Ma et al. [9]. In general, this potency against

HIV-1PR is in the middle of the range for triterpenes, which have a range from 230 to 4 μ M [10,11]. Even though the extracts from such a natural product still have a relatively high IC₅₀ value, chemical modification of the anti-HIV protease triterpenes were shown to improve the potency of the natural product two- to five-fold [12]. In order to use 3-oxotrirucalla-7,24-dien-21-oic acid as a lead compound for possible drug candidates, computeraided modelling is a very useful tool in the chemical design of modifications based on the understanding of the interaction of the lead with the respective enzyme.

To date, the detailed inhibition mechanism of triterpenes to HIV-1PR is still not completely understood. Combination of molecular docking and molecular dynamics (MD) simulation of this HIV-1PR triterpenoid complex will allow the designation of new anti-HIV agents from the abundant triterpenes in natural products. In this paper, the orientation and the binding conformation of 3-oxotrirucalla-7,24-dien-21-oic acid including water molecules in the HIV-1PR cavity site were examined using MD simulation results. These results also provide insight into the structural origins of this moderate IC₅₀ value in comparison with six food and drug administration (FDA) approved anti-HIV-1PR drugs.

2. Methods

2.1 Preparation of the starting structure of HIV-1PR

The initial HIV-1PR structure was obtained from the HIV-1PR complex with saquinavir at 2.3 Å resolution (1HXB entry in Protein Data Bank (PDB) database). The structural water and the inhibitor of the selected crystal data were then removed for the preparation of the HIV-1PR. Hydrogen atoms were added to this structure using LEaP libraries of AMBER and a minimisation run was performed in order to remove any potentially bad contacts using force field parameter99 within the program package AMBER, version 7 [13,14]. A cut-off distance at 12 Å for van der Waals forces was used in the minimisations (simulations).

2.2 Preparation of the initial structure of the inhibitor

The starting molecular conformation of 3-oxotirucalla-7,24-dien-21-oic acid was built based on the chemical structure reported from NMR and solid-state X-ray crystallographic data [9]. The geometry, as shown in Figure 1, was optimised using AM1 implemented in the program package Spartan'04.

2.3 Preparation of HIV-1PR-inhibitor complex by molecular docking and molecular mechanics methods

The structure of the HIV-1PR-inhibitor was obtained by docking 3-oxotirucalla-7,24-dien-21-oic acid to HIV-1PR, respectively. HIV-1PR was kept rigid and Gasteiger—Marsili charges [15] were used. Grid maps were calculated using the module AutoGrid in AutoDock 3.0 program [16–18] for protease structure. The centre of the grid was assigned at the centre of the cavity, between the two catalytic aspartates. The number of grid points in each direction of Cartesian coordinates was 60 with a spacing of 0.375 Å. This parameter set covered the active site completely letting the ligand move by exploring the enzyme active site without any constraints regarding the box size. The inhibitor was positioned in the active site of HIV-1PR in many different ways using a Lamarckian genetic algorithm. The solvation effect was also included in this docking study.

2.4 Molecular dynamic simulations

The energy minimised conformation of HIV-1PR-inhibitor generated from the previous calculations was used as the starting structure for further analysis. The molecular mechanics potential energy (EP) minimisations and MD simulations were carried out with the program package AMBER, version 7 [13,14]. Calculations were performed using the parameter99 force field reference for HIV-1PR and 3-oxotirucalla-7,24-dien-21-oic acid. The atom types for 3-oxotirucalla-7,24-dien-21-oic acid were assigned

by mapping their chemical properties (element, hybridisation and bonding schemes) to the AMBER atom type library and the Gasteiger charges were used.

The enzyme-inhibitor complex was solvated with a TIP3P water model (9298 water molecules) with cell dimensions of $61.06 \times 66.56 \times 75.88 \,\text{Å}^3$ and treated in the simulation under periodic boundary conditions. All of the MD simulations reported here were done under an isobaric-isothermal ensemble (NPT) using constant pressure of 1 atm and constant temperature of 298 K. The volume was chosen to maintain a density of 1 g/cm³. A cut-off distance (12 Å) was applied for the non-bonded pair interaction. Three sodium and eight chloride ions were added to neutralise and buffer the system. The EP minimisations holding the HIV-1PR and 3-oxotirucalla-7,24-dien-21-oic acid fixed were performed on the systems using the steepest descent method. After a short minimisation simulation at 298 K with the solvent water molecules and anions for the enzyme and ligand fixed, the temperature of the whole system was gradually increased by heating it to 298 K for the first 60 ps, and then it was kept at 298 K from 61 to 1800 ps. The temperature was kept constant according to the Berendsen algorithm [19]. The trajectories at the temperature (298 K for 1800 ps) were kept and analysed in detail.

3. Results and discussion

3.1 Structural flexibility of 3-oxotirucalla-7,24-dien-21-oic acid in active site of HIV-1PR

The optimised structure of 3-oxotirucalla-7,24-dien-21-oic acid is shown in Figure 1(a). This molecular structure agrees well with that reported from NMR and solid-state X-ray crystallographic data [9]. The preliminary complex structure was deduced from the molecular docking. The 10-run docking calculations were used in a prior prediction of binding affinities and to simulate crystal geometry as a candidate of the ligand/protein complex and re-docking in order to improve the clustering results. The candidate structure from molecular docking (Figure 1(b)) shows that the molecular torsion angles of flexible part labelled as tor1-8 mentioned in Figure 1 and Table 1 totally changed, resulting in the flipping of carboxylic group of the flexible part. To include the flexibility of the enzyme structure, an MD simulation was performed starting from this docking structure. The conformation of the inhibitor changed into the new equilibrium shown in Figure 1(c). As shown in Table 1, the averaged conformation from MD simulation after reaching equilibrium is almost the same as that found in the X-ray structure except tor5 and tor6. In addition, according to Figure 2, the distribution of tor6 is relatively broad $(SD = 38.71^{\circ})$ indicating the highest flexibility of this part. The transitions of tor5 and tor6 are considered to be in relationship with the binding affinity and will be further discussed.

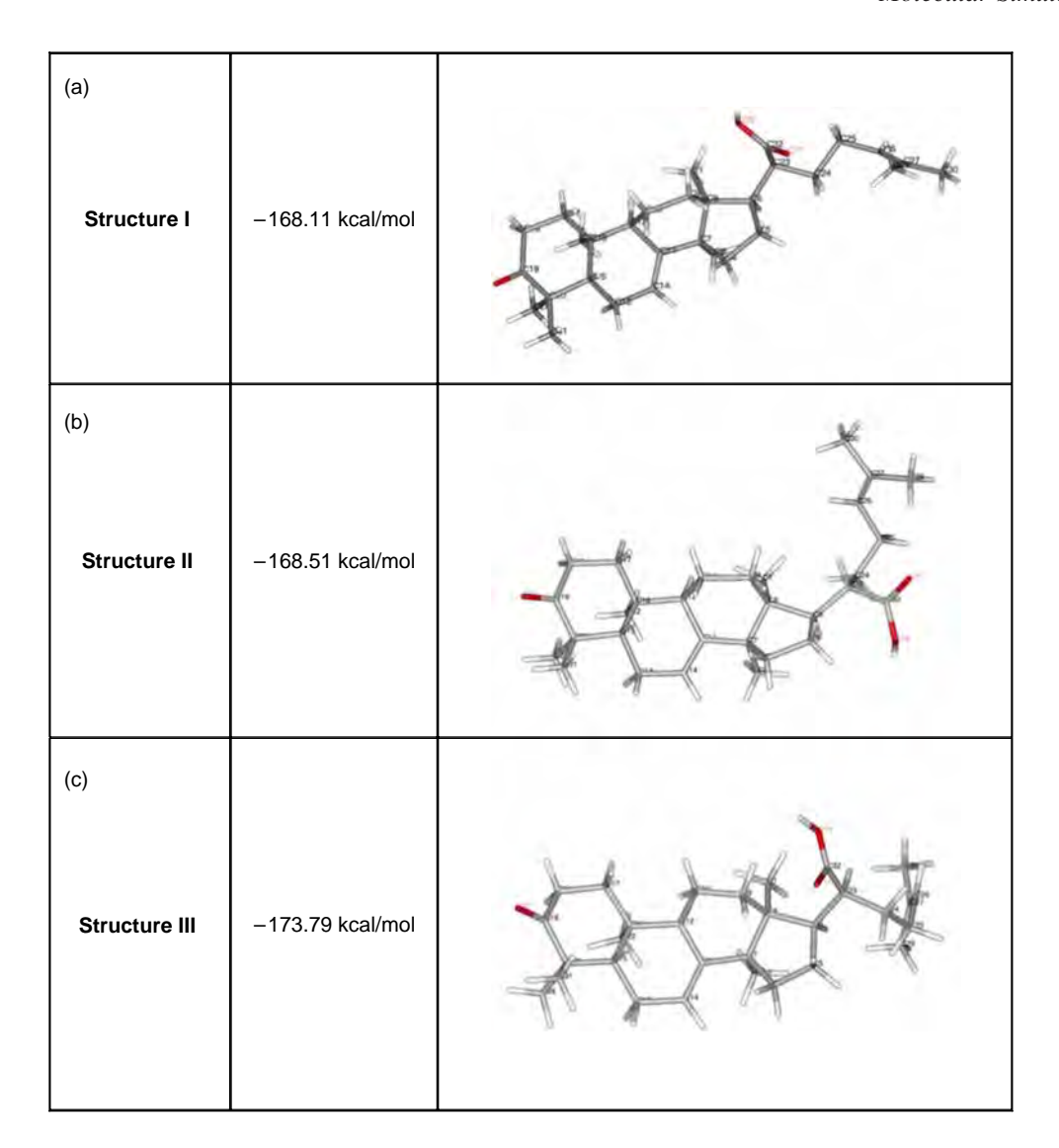


Figure 1. Chemical structure of 3-oxotirucalla-7,24-dien-21-oic acid and molecular geometries after (a) optimisation, (b) molecular docking and (c) explicit MD simulation.

Table 1. Average torsion angles in 3-oxotirucalla-7,24-dien-21-oic acid after optimisation, molecular docking and explicit MD simulation.

Torsion	Abbreviation	Opt	Dock	MD
C8-C6-C23-C32	tor1	58.6	159.3	64.0
C6-C23-C32-O77	tor2	94.7	-144.7	60.0
C6-C23-C32-O78	tor3	-86.7	33.8	-119.0
C8-C6-C23-C24	tor4	179.5	-79.7	-171.0
C23-C24-C25-C26	tor5	164.3	-70.3	62.0
C24-C25-C26-C27	tor6	82.3	126.3	-126.0
C25-C26-C27-C30	tor7	179.8	179.8	180.0
C25-C26-C27-C29	tor8	0.2	0.2	0.0

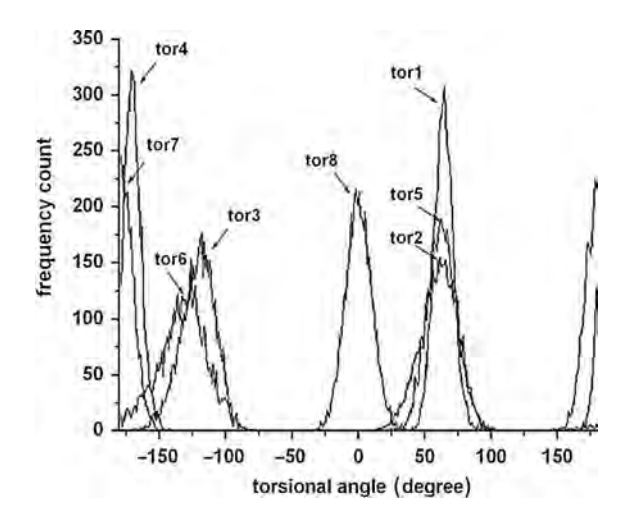


Figure 2. Eight bond torsions distributions of 3-oxotirucalla-7,24-dien-21-oic acid after 1200 ps of explicit MD simulation.

3.2 Binding structure of HIV-1PR-terpenoid complex

The minimised structure (Figure 3(a)) from molecular docking shows the direction of OH group in inhibitor points to the catalytic site of enzyme (N:Asp29 and N:Asp29') as a crude complex structure. In the MD simulation, the total energy, EP and kinetic energy over simulations from 0 to 1800 ps were investigated. After the equilibrium stage, 3-oxotirucalla-7,24-dien-21-oic acid was found to bind to the enzyme at catalytic site Asp25 and Asp29 (Figure 3(b)). As shown in Table 2, the energy minimised structure obtained from MD simulations directs CO and OH group of the inhibitor to the catalytic site of enzyme, O:Asp25 and N:Asp29, respectively, with more than 89% hydrogen bond formation. The transition of the binding structure during molecular dynamic simulation can be observed from the interatomic distance plot against simulation time in Figure 4, the transition of the enzyme residue binding position from N:Asp29' to O:Asp25 after 300 ps. According to Figure 4, N:Asp29' is too far from the inhibitor, so this residue cannot form a strong hydrogen bond interaction with the triterpene inhibitor. On the other hand, O:Asp25' shows two possible equilibrium stages that indicate a 15% possibility of a hydrogen bond to O78 of 3-oxotirucalla-7,24-dien-21-oic acid (Table 2).

3.3 Roles of water molecule in active site

The catalytic mechanism of the protease is most likely a combination of favourable binding of the inhibitor with the enzyme and the role of the water molecules in the enzyme pocket. With the optimal configuration of the enzyme—inhibitor complex, a water molecule was needed

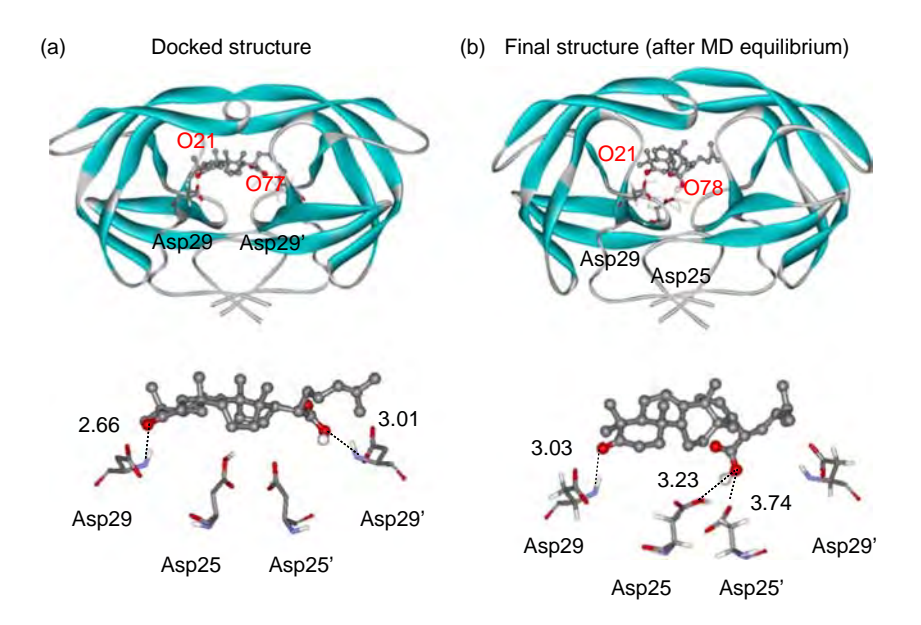


Figure 3. The structure of HIV-1PR-inhibitor (a) docking method and (b) the final structure after explicit MD simulation. The binding residues were shown in sticks.

Table 2. Possible hydrogen bonds between 3-oxotirucalla-7,24dien-21-oic acid and HIV-1PR after reach equilibrium in explicit MD simulation.

	H-bond formation (%)	Average distance (Å)
Case 1: HIV-1PR as donor and	Inh as acceptor	
ASH25:OD2HD2-Inh:O78	1.98	3.07
ASP29:NH-Ihn:O21	94.71	2.97
ASP30:NH-Inh:O21	1.73	3.21
ALA28':NH-Inh:O78	3.27	3.05
Case 2: Inh as donor and HIV-1	PR as acceptor	
Inh:O78H79-ASH25:OD1	0.04	3.17
Inh:O78H79-ASH25:OD2	89.18	2.95
Inh:O78H79-ASP25/:OD1	12.98	2.93
Inh:O78H79-ASP25':OD2	2.00	2.95

to facilitate proton transfer in the catalytic process. In this study, radial distribution functions to the oxygen atom of water molecule were evaluated centred at the hydrogen bond forming atoms (amide oxygens and nitrogen) of the all possible amino residues in Table 2. There is no water involved in the binding of Asp25, Asp25' and Ala28' meanwhile the solvation shells including coordination numbers of water bound Asp29 and Asp30 are given in Figure 5. In the first shell (about 2.7 Å), there are two water molecules close to Asp29. A water molecule moving in and out of the second shell (about 5 Å) of Asp29 and Asp30 was also observed here.

3.4 Comparison of HIV-1PR-terpenoid and HIV-1PR-commercial drugs complexes

The X-ray crystallographic structures of HIV-1PR complexed with six commercial anti-HIV-1PR drugs; amprenavir (1HPV), lopinavir (1MUI), ritronavir (1HXW), indinavir (1HSG), nelfinavir (1OHR) and saquinavir (1HXB) were used here. The orientations of six drugs in the active site were compared with 3-oxotirucalla-7,24-dien-21-oic acid as shown in Figure 6. The essential subsites of anti-HIV-1PR drugs and 3-oxotrirucalla-7,24-dien-21-oic acid were superimposed and shown in the right figure of Figure 7. In comparing with HIV-six commercial drugs complexes, the anti-HIV activity of 3-oxotrirucalla-7,24-dien-21-oic acid would be resulted from the presence of P2 and P2'. The distribution of the energy decomposition analysis for the interacting residue pairs of HIV-1PR with 3-oxotrirucalla-7,24-dien-21-oic acid were also illustrated in Figure 7. It has a peak close to zero range from -2.0 to 0.5 kcal/mol. There is some unfavourable interaction, indicated by the positive energy in the P1 subsite region, which interacts with the flap region at Gly48-Ile50

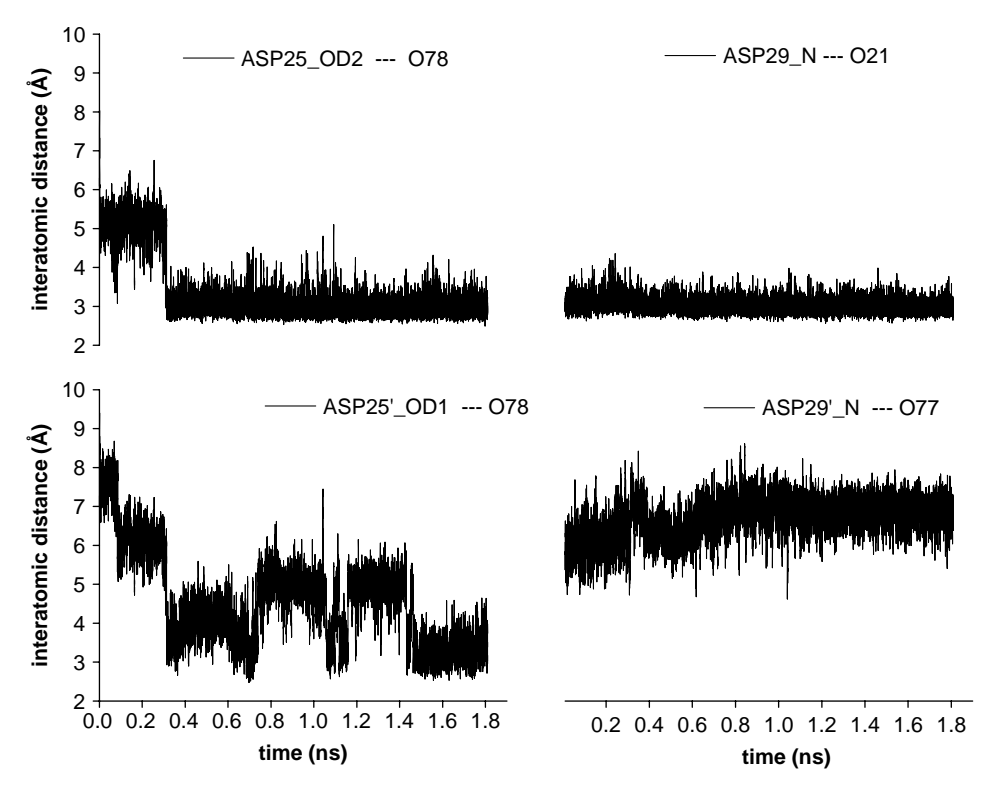


Figure 4. Changes of the distances from the O atom of the inhibitor to the H-bond binding group of the Asp25, Asp25', Asp29 and Asp29' at the catalytic site.

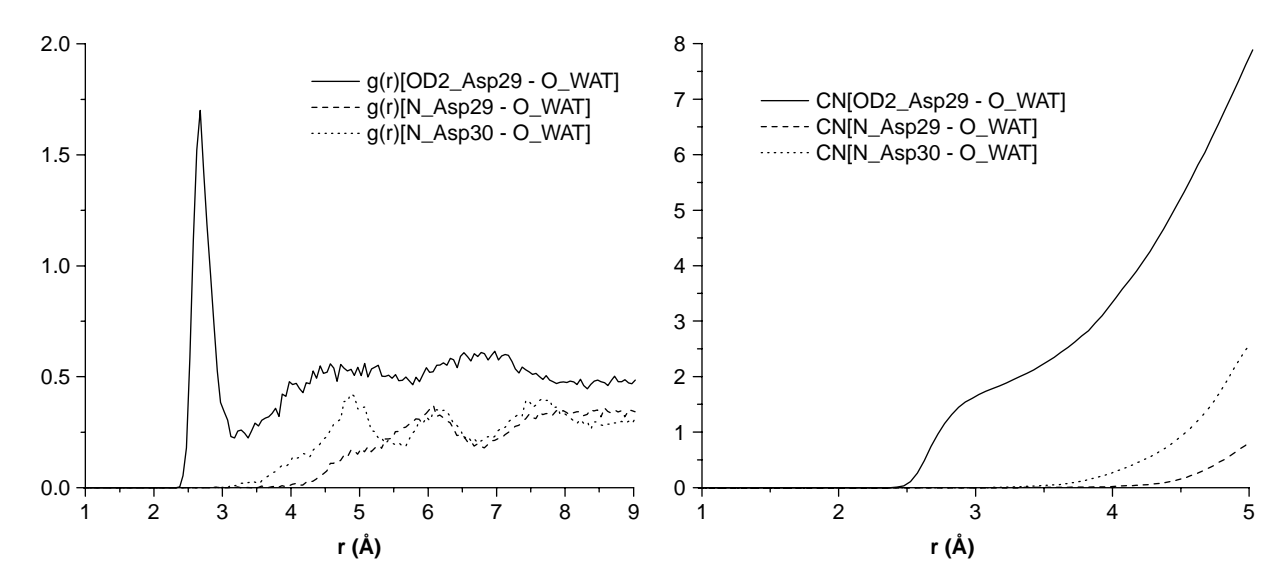


Figure 5. Radial distribution function of water oxygens around the Asp29 and Asp30.

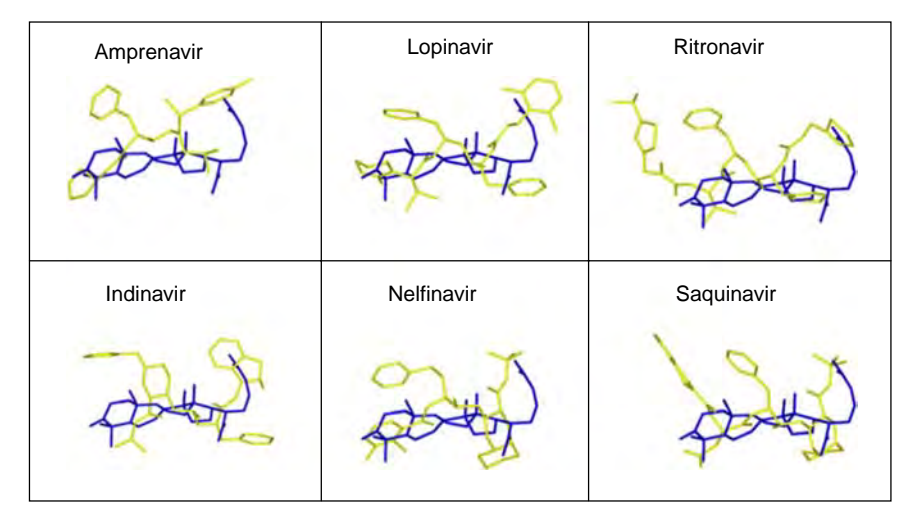


Figure 6. Superimposition of all atoms between 3-oxotirucalla-7,24-dien-21-oic acid and six commercial drugs in enzyme-inhibitor complexes.

of HIV-1PR. The preferable negative free energy of the HIV-1PR flap region interacting with saquinavir P1 was reported by Wittayanarakul et al. [20]. This evidence indicates that the activity of triterpene will be improved by the addition of P1 subsite.

4. Conclusions

In this study, the binding of HIV-1 protease and *L. chinensis* extracts (3-oxotrirucalla-7,24-dien-21-oic acid) was investigated. MD simulations of HIV-1 protease complex with 3-oxotrirucalla-7,24-dien-21-oic acid in water were performed. The initial structure of the

enzyme-inhibitor complex was constructed based on docking the 3-oxotrirucalla-7,24-dien-21-oic acid structure, optimised by semi-empirical calculation, AM1, with the X-ray crystallographic HIV-1 protease structure (PDB code: 1HXB). The MD calculation results predict the hydrogen bond being formed between the oxygen atoms of the inhibitor and catalytic aspartates, which is common to protease-inhibitor complexes. However, there is no hydrogen bonding of the inhibitor to the flap region. Structural parameters were investigated in order to compare the complex structures in all three systems throughout the MD trajectory. In addition, radial distribution function of water oxygens around the catalytic

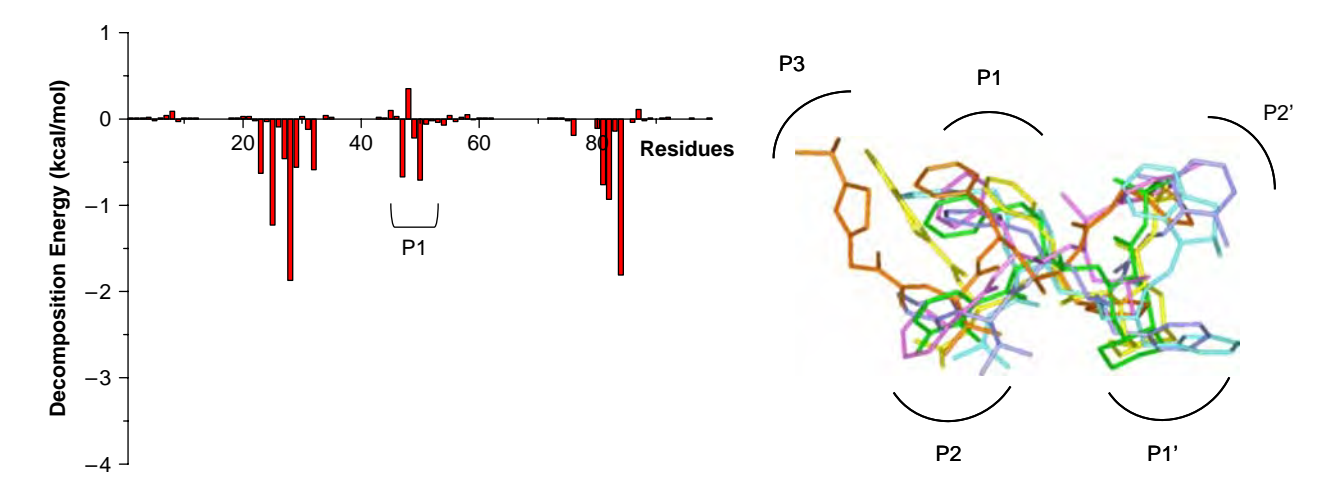


Figure 7. Subsites P1, P1', P2, P2' and P3 shown in the superimposition of six commercial drugs.

carboxylate nitrogens of Asp29 and Asp30 suggested that at least one or two water molecules will be in the active site region whereas a direct bound of the inhibitor to the catalytic carboxylate oxygen of ASP25 was found. Our simulation results compared with HIV-six commercial drugs complexes indicate the anti-HIV activity of 3-oxotrirucalla-7,24-dien-21-oic acid will be improved by addition of P1 subsite.

Acknowledgements

We would like to express our grateful acknowledgement to the Computational Simulation and Modeling Laboratory, Chiang Mai University and Computational Nanoscience Consortium Nanotechnology Thailand for the access to the computer. We would also like to acknowledge the Commission on Higher Education, Thailand Research Fund, and the Center of Innovation in Chemistry, Commission on Higher Education, Ministry of Education, Thailand for financial support.

References

- [1] O. Aruksakunwong, S. Promsri, K. Wittayanarakul, P. Nimmanpipug, V.S. Lee, A. Wijitkosoom, P. Sompornpisut, and S. Hannongbua, Current development on HIV-1 protease inhibitors, Curr. Comput. Aided Drug Des. 3 (2007), pp. 201-213.
- [2] R. Lapatto, T. Blundell, A. Hemmings, J. Overington, A. Wilderspin, S. Wood, J.R. Merson, P.J. Whittle, D.E. Danley, K.F. Geoghegan, et al., X-ray analysis of HIV-1 proteinase at 2.7 Å resolution confirms structural homology among retroviral enzymes, Nature 342 (1989), pp. 299-302.
- [3] M.A. Navia, P.M.D. Fitzgerald, B.M. McKeever, C.-T. Leu, J.C. Heimbach, W.K. Herber, I.S. Sigal, P.L. Darke, and J.P. Springer, Three-dimensional structure of aspartyl protease from human immunodeficiency virus HIV-1, Nature 337 (1989), pp. 615-620.
- [4] N. Okimoto, T. Tsukui, K. Kitayama, M. Hata, T. Hoshino, and M. Tsuda, Molecular dynamics study of HIV-1 protease-substrate complex: roles of the water molecules at the loop structures of the active site, J. Am. Chem. Soc. 122 (2000), pp. 5613-5622.

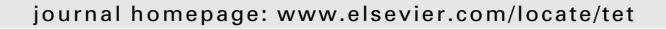
- [5] O. Aruksankunwong, S. Hannongbua, and P. Wolschann, Hydrogen bonding in molecular recognition by HIV-1 protease, J. Mol. Struct. 790 (2006), pp. 174-182.
- [6] O. Aruksakunwong, K. Wittayanarakul, P. Sompornpisut, V. Sanghiran, V. Parasuk, and S. Hannongbua, Structural and dynamical properties of different protonated states of mutant HIV-1 protease complexed with the saquinavir inhibitor studied by molecular dynamics simulations, J. Mol. Graph. Model. 25 (2006), pp. 324-332.
- [7] S. Promsri, P. Chuichay, V. Sanghiran, V. Parasuk, and S. Hannongbua, Molecular and electronic properties of HIV-1 protease inhibitor C60 derivatives as studied by the ONIOM method, J. Mol. Struct.: THEOCHEM 715 (2005), pp. 47-53.
- [8] P. Tu, Q. Luo, and J. Zheng, Studies of chemical constituents in seed of Litchi chinensis, Zhongcaoyao 33 (2002), pp. 300-303
- [9] C.-M. Ma, N. Nakamura, M. Hattori, H. Kakuda, J.-C. Qiao, and H.-L. Yu, Inhibitory effects on HIV-1 protease of constituents from the wood of Xanthoceras sorbifolia, J. Nat. Prod. 63 (2000), pp. 238-242.
- [10] L. Huang and C.H. Chen, Molecular targets of anti-HIV-1 triterpenes, Curr. Drug Targets Infect. Disord. 2 (2002), pp. 33-36.
- [11] L. Huang and C.H. Chen, The molecular targets of anti-HIV-1 triterpenes, an update, Med. Chem. Rev. Online 2 (2005), pp. 423-427.
- [12] I.C. Sun, Y. Kashiwada, S.L. Morris-Natschke, and K.H. Lee, Plant-derived terpenoids and analogues as anti-HIV Agents, Curr. Topics Med. Chem. 3 (2003), pp. 155-169.
- [13] D.A. Case, D.A. Pearlman, J.W. Caldwell, T.E. Cheatham III, J. Wang, W.S. Ross, C.L. Simmerling, T.A. Darden, K.M. Merz, R.V. Stanton, et al., AMBER 7, University of California, San Francisco, CA, 2002.
- [14] D.A. Pearlman, D.A. Case, J.W. Caldwell, W.S. Ross, T.E. Cheatham III, S. DeBolt, D. Ferguson, G. Seibel, and P. Kollman, AMBER, a package of computer programs for applying molecular mechanics, normal mode analysis, molecular dynamics and free energy calculations to simulate the structural and energetic properties of molecules, Comput. Phys. Commun. 91 (1995), pp. 1-41.
- [15] J. Gasteiger and M. Marsili, Iterative partial equalization of orbital electronegativity-a rapid access to atomic charges, Tetrahedron 36 (1980), pp. 3219-3228.
- [16] D.S. Goodsell and A.J. Olson, Automated docking of substrates to proteins by simulated annealing, Proteins Struct. Funct. Genet. 8 (1990), pp. 195-202.

- [17] G.M. Morris, D.S. Goodsell, R. Huey, and A.J. Olson, *Distributed automated docking of flexible ligands to proteins: parallel applications of AutoDock 2.4*, J. Comput. Aided Mol. Des. 10 (1996), pp. 293–304.
- [18] G.M. Morris, D.S. Goodsell, R.S. Halliday, R. Huey, W.E. Hart, R.K. Belew, and A.J. Olson, *Automated docking using a Lamarckian genetic algorithm and an empirical binding free energy function*, J. Comput. Chem. 19 (1998), pp. 1639–1662.
- [19] H.J.C. Berendsen, J.P.M. Postma, W.F. Van Gunsteren, A. Dinola, and J.R. Haak, *Molecular dynamics with coupling to an external* bath, J. Chem. Phys. 81 (1984), pp. 3684–3690.
- [20] K. Wittayanarakul, O. Aruksakunwong, P. Sompornpisut, V. Sanghiran-Lee, V. Parasuk, S. Pinitglang, and S. Hannongbua, Structure, dynamics and solvation of HIV-1 protease/saquinavir complex in aqueous solution and their contributions to drug resistance: molecular dynamic simulations, J. Chem. Inf. Model. 45 (2005), pp. 300–308.



Contents lists available at ScienceDirect

Tetrahedron





Syntheses of methylenolactocin and nephrosterinic acid via diastereoselective acylation and chemoselective reduction–lactonization

Rattana Jongkol^a, Ruangrat Choommongkol^a, Bongkoch Tarnchompoo^b, Piyarat Nimmanpipug^a, Puttinan Meepowpan^{a,*}

ARTICLE INFO

Article history:
Received 5 January 2009
Received in revised form 22 May 2009
Accepted 4 June 2009
Available online 10 June 2009

Keywords: α -Methylene- γ -butyrolactones Acylation Reduction Lactonization

ABSTRACT

The syntheses of methylenolactocin, nephrosterinic acid and their derivatives can be achieved by using the efficient diastereoselective acylation of dimethyl itaconate–anthracene adduct followed by tandem chemoselective reduction–lactonization.

© 2009 Elsevier Ltd. All rights reserved.

1. Introduction

The paraconic acids are a group of highly substituted γ -butyro-lactones isolated from different species of moss, lichens, fungi and cultures of *Penicillium* sp. 1,2 Among them, methylenolactocin, 3,4 nephrosterinic acid, 5,6 and protolichesterinic acid, 7,8 are noted for their biological activities, being antibacterial agents, 9a-1 antifungal, 9b antitumor, 9h anti-inflammatory 9m and displaying inhibitory activity on 12(S)-HETE production in human platelets 9n while some of these compounds also display growth-regulating effects. 90 Due to their important potential pharmacological applications, 10 several formal and total syntheses of members of this class of metabolite have attracted widespread attention.

Previous work has reported the total syntheses of methylenolactocin, nephrosterinic acid and protolichesterinic acid in both racemic and enantiomerically pure forms employing the versatile starting material, dimethyl itaconate–anthracene adduct (1)¹¹ via tandem aldol–lactonization reactions, isomerization of the C-4' configuration followed by flash vacuum pyrolysis and hydrolysis of the ester group (Scheme 1).^{4n,r}

This present work aims at controlling the stereochemistries at C-4′ and C-5′ using diastereoselective acylation and tandem chemoselective reduction–lactonization as key steps. The process is outlined in Scheme 2.

2. Results and discussion

In a typical diastereoselective acylation using alkanoyl chloride; n-heptanoyl chloride (10b) was added to the lithium ester enolate 9 at -78 °C for 15 min and the mixture stirred at 0 °C for 1 h. The crude product was subjected to column chromatography (silica gel, using EtOAc/hexane=0.5:9.5 as eluent) to yield 7b in 63% yield and the minor product, 8b, in 4% yield after crystallization from ethyl acetate/hexane. The relative stereochemistries at the α -position of the β -ketodiester adducts 7b and 8b were determined by NOE experiments (Fig. 1). In the case of compound 7b, the proton H_c (δ appeared at 3.03 ppm) showed greater interaction with H_b than H_y ; thus the orientation of H_c is on the upper face as shown. Conversely, the orientation of proton H_c (δ appeared at 3.43 ppm) of compound 8b is on the opposite face. However, the NOE results could not unequivocally confirm the orientations of the COOMe and n-C7 H_{15} CO groups.

These NOE results were compared with geometry optimizations of compounds **7b** and **8b** carried out using Gaussian 03 Programs 12,13 at the B3LYP/6-31G level of Density Functional Theory (DFT). The optimized structures are shown in Figure 2. From these calculations, compound **8b** is thermodynamically more stable than compound **7b** with a lower energy of 3.96 kcal/mol. The **7b** model showed that the distance from H_c to H_a , H_b , and H_y are 2.41, 3.10, and 3.89 Å respectively. In comparison, H_c is displaced from H_a , H_b , and H_y at distance of 3.70, 4.10, and 2.51 Å respectively in the minimized structure of **8b**. Results from the computational calculation are in agreement with the NOE results.

^a Department of Chemistry and Center for Innovation in Chemistry, Faculty of Science, Chiang Mai University, 239 Huay Kaew Road, Chiang Mai 50200, Thailand

b National Center for Genetic Engineering and Biotechnology (BIOTEC), 113 Thailand Science Park, Phahonyothin Road, Klong 1, Klong Luang, Pathumthani 12120, Thailand

^{*} Corresponding author. Tel.: +66 53 943 341 5x317; fax: +66 53 892 277. E-mail address: puttinan@chiangmai.ac.th (P. Meepowpan).

6; R = n-C₅H₁₁ (Methylenolactocin); n-C₁₁H₂₃ (Nephrosterinic acid) and n-C₁₃H₂₇ (Protolichesterinic acid)

Scheme 1. Total syntheses of methylenolactocin, nephrosterinic acid and protolichesterinic acid. Reagents and conditions: (i) a. 1.2 equiv LDA, THF, -78 °C to 0 °C, 2 h, b. 1.2 equiv RCHO, 0 °C to rt, 3 h, c. aq NH₄Cl, 30% HCl; (ii) 0.5 equiv NaOMe, THF/MeOH (2:1), rt, 6 days; (iii) FVP; (iv) 2-butanone, 6 N HCl, reflux, 2 h.

Scheme 2. Synthetic pathway of *trans-***6** via acylation and tandem reduction–lactonization reactions.

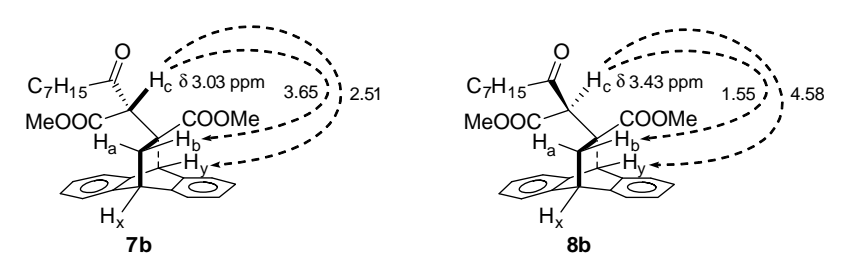


Figure 1. NOE results of $\beta\text{--ketodiester}$ adducts 7b and 8b.

The stereochemical outcome of the acylation reaction can be explained by the chair-like transition states: $\bf A$ and $\bf B$ (Scheme 3). The transition structure $\bf A$ would lead to the major product $\bf 7b$. In contrast, the transition structure $\bf B$ would lead to the formation of the minor product $\bf 8b$. The latter is less favorable due to the large steric repulsion between the Cl atom and the anthracene ring. 4n

Under similar reaction conditions, the lithium ester enolate **9** was allowed to react with various alkanoyl chlorides (**10a–e**), e.g., $R=n-C_5H_{11}$; $n-C_9H_{19}$; $n-C_{11}H_{23}$ and C_6H_5 , to yield **7a–e** as the major products and **8a–e** as the minor products, respectively as detailed in Table 1.

It is possible that the β -ketodiester adducts **8** might be the result of isomerization of **7** under acylation conditions. To prove this hypothesis, three extra reaction conditions were carried out and results are as follows: treatment of the lithium ester enolate **9** with benzoyl chloride (**10e**) at -78 °C for 15 min and quickly quenching with saturated NaHCO₃ gave only recovered **1** in 98% yield. Secondly, the reaction mixture of the lithium ester enolate **9** and **10e** at -78 °C was left stirring at 0 °C for 15 min to also yield the recovered **1**. Lastly, addition of **10e** to the lithium ester enolate **9** at 0 °C for 15 min provided the β -ketodiester adducts **7e** and **8e**

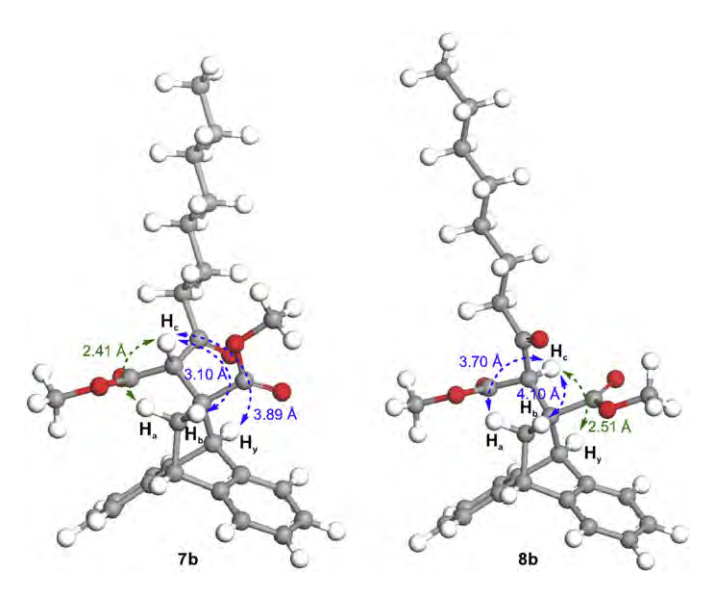
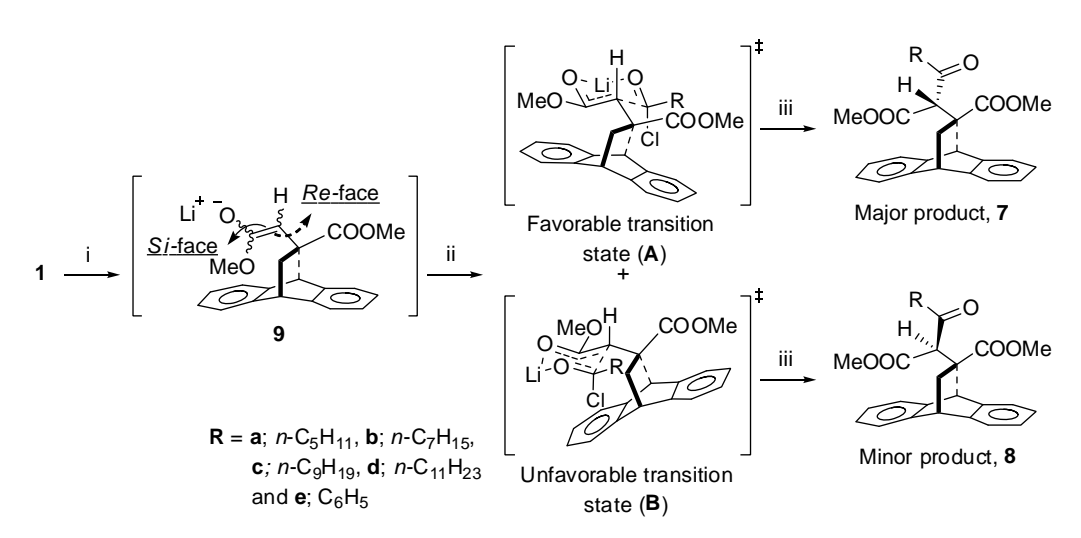


Figure 2. Structures of 7b and 8b from Gaussian 03 Programs at the B3LYP/6-31G level of DFT

Having efficiently prepared the β -ketodiester adducts **7**, attention was turned to their chemoselective reduction to obtain spirolactones **5**. Initially, we began by optimizing reaction conditions of the diastereoslective reduction of the model compound, the β -ketodiester adduct **7e**, using various amounts of NaBH₄ (1, 3, 5 and 10 equiv) in THF/MeOH (1:3) (Table 2). Results showed that the use of 5 equiv of NaBH₄ (Entry 3) gave high yields of spiro-lactones **3e** and **5e**, respectively (17 and 61% yields).

The structure of compounds cis-3e and trans-5e were determined from their 1H NMR, ^{13}C NMR, IR and mass spectroscopic data. 4n In the 1H NMR spectrum of cis-3e, the protons H_c and H_d appeared at 2.54 and 5.51 ppm with a coupling constant J of 5.6 Hz while the same protons in trans-5e appeared at 3.05 and 6.05 ppm with a coupling constant J of 10.2 Hz. By observations from NOE experiments of compound cis-3e and trans-5e, the relative stereochemistries of these compounds were finally confirmed (Fig. 3). Irradiation of the proton H_d of cis-3e gave only a NOE effect on the proton H_c ; thus the orientation of proton H_d is on the upper face and syn- with proton H_c . Furthermore, irradiation of proton H_d of trans-5e caused only NOE effect on the proton H_y , while irradiation of the proton H_c gave only NOE effects on the proton H_b ; thus the orientation of proton H_d is at the lower face and anti- to proton H_c .



Scheme 3. A plausible reaction mechanism of diastereoselective acylation of the adduct **1** with acid chloride. Reagents and conditions: (i) 1.2 equiv LDA, THF, -78 °C to 0 °C, 2 h; (ii) 1.2 equiv RCOCl (**10**), -78 °C to 0 °C, 1 h; (iii) saturated NaHCO₃.

in 75 and 18% yields respectively. The above results clearly indicated that no isomerization took place under acylation conditions. It should be added that upon treatment of the β -ketodiester adduct 7e with LDA (1.2 equiv) under acylation conditions employed the isomerized products 8e was obtained in 12% yield (87% unchanged material).

Table 1 Diastereoselective acylation reactions of adduct 1 with various alkanoyl chlorides (10a-e)

Entry	RCOCl (10)	Yield ^{a,b} (%)		Diastereomeric ratio ^b of 7/8
		7	8	
1	10a : n-C ₅ H ₁₁ COCl	58	4	94:6
2	10b : n-C ₇ H ₁₅ COCl	63	4	94:6
3	10c : n-C ₉ H ₁₉ COCl	53	6	90:10
4	10d: n-C ₁₁ H ₂₃ COCl	49	11	82:18
5	10e : C ₆ H ₅ COCl	73	19	79:21

^a Compounds 7a-e and 8a-e were fully characterized by 1 H NMR, 13 C NMR, IR and HRMS (ESI).

These results strongly confirm the orientation of the α -proton of β -ketodiester adduct **7e** is upper face and can be considered to be representative of **7a–d**. In addition, the β -ketodiester adducts **8e** was also obtained (colourless oil, 19%). NaBH₄ reduction of **8e** furnished the spiro-lactone *cis*-**2e** (white solid, mp 204.9–206.0 °C (CH₂Cl₂/hexane), 44% yield) as the only product isolated. The stereochemistry of *cis*-**2e** was fully confirmed by NOE experiments (Fig. 4).

In order to increase the diastereoselectivity of the reduction product (hence the final product), we decided to perform the NaBH $_4$ reduction in wet-THF system as previously reported by several groups. ^{15,16} Results are presented in Table 3 which demonstrates that the highest diastereoselectivity of **7e** were achieved by using NaBH $_4$ (5 equiv) in THF/H $_2$ O (8:1) at 0 °C for 4 h (Entry 5).

These conditions were therefore employed for the reduction reactions of compounds **7a–d** and the results are shown in Table 4.

We have indepently demonstrated that the trans-products obtained were not the results of base induced isomerization of the carbon-bearing the ester functionality (C-4'). Thus treatment of *cis*-3e, obtained earlier, with NaBH₄ or NaOMe in MeOH or MeOH/THF provided only the recovered starting material.

 $^{^{\}rm b}$ Yields and diastereomeric ratios of acylation products (**7a-e** and **8a-e**) were determined by $^{\rm 1}$ H NMR analysis.

 Table 2

 Reduction of β-ketodiester adduct 7e with various amounts of NaBH4 in THF/MeOH

Entry	Equiv of NaBH ₄	Conditions	Yield ^a (%)		Diastereomeric ratio	% Conversion
			cis- 3e	trans- 5e	of trans- 5e /cis- 3e	
1	1	THF/MeOH (1:3)	22	58	73:27	54
2	3	THF/MeOH (1:3)	22	60	73:27	100
3	5	THF/MeOH (1:3)	17	61	78:22	100
4	10	THF/MeOH (1:3)	18	35	66:34	100

a Yields of isolated compounds.

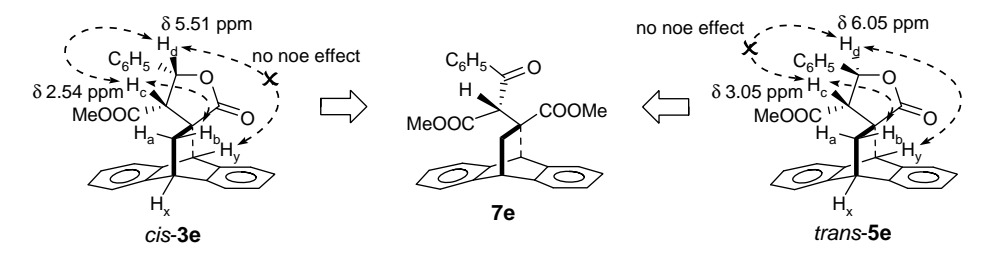


Figure 3. NOE results of spiro-lactones (cis-3e and trans-5e).

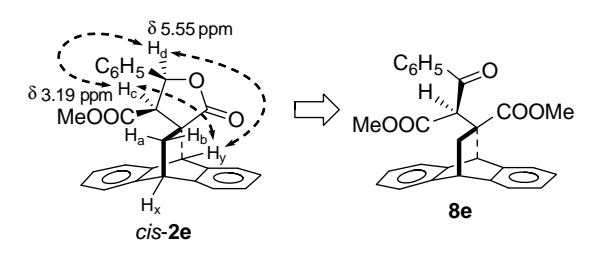


Figure 4. NOE results of spiro-lactone (cis-2e).

A plausible reaction mechanism is depicted in Scheme 4 which involves the Felkin–Anh model (\mathbf{C}). The reduction of β -ketodiester $\mathbf{7}$ with NaBH₄ in a wet-THF system proceeds via the Felkin–Anh face to give the alkoxide $\mathbf{11}$ which, upon workup,

furnished the final *trans*-**5**. trans-Products (**5a**-**e**) can be transformed to natural products, e.g., methylenolactocin ($R=n-C_5H_{11}$) and nephrosterinic acid ($R=n-C_{11}H_{23}$), and unnatural products ($R=n-C_7H_{15}$, $n-C_9H_{19}$ and C_6H_5) by flash vacuum pyrolysis and hydrolysis, respectively.⁴ⁿ

3. Conclusion

Synthetic methodology for methylenolactocin, nephrosterinic acid and their derivatives using diastereoselective acylation and tandem chemoselective reduction–lactonization as key steps has been developed. The approach is short, practical, efficient with high stereoselectivity and can be applied to both alkyl and aryl groups. The methodology is very useful for enantiomeric synthesis of compounds in this class.

Table 3 Reduction of β -ketodiester adducts 7e with various amounts of NaBH $_4$ in wet-THF systems

Entry	Equiv of NaBH ₄	Conditions	Yield ^a (%)		Diastereomeric ratio	% Conversion
			cis- 3e	trans- 5e	of trans- 5e /cis- 3e	
1	5.0	THF/H ₂ O (2:1)	15	80	84:16	100
2	5.0	THF/H ₂ O (4:1)	7	72	91:9	100
3	1.5	THF/H ₂ O (8:1)	1	53	98:2	77
4	3.0	THF/H ₂ O (8:1)	4	65	94:6	98
5	5.0	THF/H ₂ O (8:1)	2	70	97:3	100
6	7.0	THF/H ₂ O (8:1)	3	77	96:4	99
7	5.0	THF/H ₂ O (16:1)	5	92	95:5	67

^a Yields of isolated compounds.

Table 4 Reduction of β -ketodiester adducts (7a–e) with 5 equiv of NaBH₄ in THF/H₂O (8:1)

Entry	R	Yield ^a (%)		Diastereomeric ratio	% Conversion
		cis- 3e	trans- 5e	of trans- 5e /cis- 3e	
1	7a : n-C ₅ H ₁₁	6	70	92:8	84
2	7b : <i>n</i> -C ₇ H ₁₅	19	78	80:20	81
3	7c : <i>n</i> -C ₉ H ₁₉	4	90	96:4	76
4	7d : n-C ₁₁ H ₂₃	8	89	92:8	81
5	7e : C ₆ H ₅	2	70	97:3	100

^a Yields of isolated compounds.

R = a; n- C_5H_{11} , **b**; n- C_7H_{15} , **c**; n- C_9H_{19} , **d**; n- $C_{11}H_{23}$ and **e**; C_6H_5

Scheme 4. Tandem chemoselective reduction–lactonization reactions with NaBH₄ via the attachment of hydride (H⁻) and β -ketodiester adducts (7a–e).

4. Experimental section

4.1. General methods

All reactions were carried out under nitrogen or argon. Unless otherwise noted, materials were obtained from commercial suppliers and used without further purification. Melting points were determined by using a Gallenkamp Electrothermal apparatus and were uncorrected. The ¹H and ¹³C NMR spectra were recorded on Bruker DRX 400 MHz spectrometers and chemical shifts were given in ppm downfield from tetramethylsilane (TMS). All NMR spectra were measured in CDCl₃ and chemical shifts were reported as δ -values in parts per million (ppm) relative to residue CHCl₃ as internal reference (1 H: δ 7.26, 13 C: δ 77.00) and coupling constants (I values) were reported in hertz (Hz). Peak multiplicities are indicated as follows: s (singlet), d (doublet), t (triplet), dt (doublet of triplets), ddd (doublet of doublet of doublets) and m (multiplet). Infrared spectra were taken with a FT-IR model TENSER 27 (Bruker) spectrometer and absorption frequencies were reported in reciprocal centimeters (cm⁻¹). Mass spectra (electrospray ionization mode, ESI-MS) were measured on a micromass Q-TOF-2™ (Waters) spectrometer. Flash column chromatography was performed employing Merck silica gel 60 and Merck silica gel 60H. Preparative thin layer chromatography (PLC) plates were carried out using Merck silica gel 60 PF₂₅₄. Analytical thin layer chromatography was performed with Merck silica gel 60 F₂₅₄ aluminum plates. Solvents were dried over CaH2 and distilled before used. Tetrahydrofuran (THF) was freshly distilled from sodium and benzophenone ketyl under nitrogen. Diisopropylamine was distilled over CaH2 and stored under nitrogen. n-Butyllithium was purchased from Fluka and Across as solution in hexane and titrated periodically according to the 2,5-dimethoxybenzyl alcohol method. Acid chlorides were freshly distilled under reduce pressure.

4.2. Chemistry

4.2.1. General procedure for the synthesis of 11-carbomethoxy-11-(1'-alkanoyl or 1'-benzoyl-1'-carbomethoxymethyl)-9,10-dihydro-9,10-ethanoanthracenes (**7a-e** and **8a-e**)

To a 100 mL round-bottomed flask equipped with a magnetic stirrer bar, fitted with a three-way stopcock and nitrogen inlet. n-Butyllithium (1.30 mL, 1.80 mmol, 1.4 M in hexane) was added to a stirring solution of diisopropylamine (0.30 mL, 2.16 mmol) in THF (5 mL) at $-78 \,^{\circ}\text{C}$, then stirred at $0 \,^{\circ}\text{C}$ for 1 h. To the LDA solution, dimethyl itaconate-anthracene adduct (1) (504.6 mg, 1.50 mmol) in THF (10 mL) was added at -78 °C and stirred at 0 °C for 2 h. At -78 °C, alkanovl or benzovl chloride (10) (1.80 mmol) was added to the reaction mixture and left stirring at 0 °C for 1 h. The resulting mixture was quenched with an aqueous saturated solution of NaHCO₃ and extracted with CH₂Cl₂ (3×15 mL). The combined organic layer were dried (MgSO₄), filtered and concentrated in vacuo. Purification of the residue by flash column chromatography (EtOAc/ hexane=1:9 as eluent) followed by preparative thin layer chromatography (EtOAc/hexane=1:9 as developing solvent) gave the β -ketodiester adducts **7** and **8**.

4.2.1.1. 11-Carbomethoxy-11-(1'-hexanoyl-1'-carbomethoxymethyl)-9,10-dihydro-9,10-ethanoanthracenes (**7a** and **8a**). Compound **7a** (58%): white solid; mp 198–199 °C (CH₂Cl₂/hexane); R_f (10% EtOAc/hexane) 0.25; $\nu_{\rm max}$ (KBr) 2956, 2868, 1745, 1468, 1241 cm⁻¹; $\delta_{\rm H}$ (400 MHz, CDCl₃) 0.83 (3H, t, J=7.2 Hz, Me), 0.98, 2.86, 4.26 (3H, ABX system, J=13.2, 3.1, 2.3 Hz, CH_2 , ArCH), 1.04–1.50 (6H, m, CH_2),

2.05 (1H, dt, J=17.8, 7.2 Hz, CHCO), 2.42 (1H, dt, J=17.8, 7.6 Hz, CHCO), 3.03 (1H, s, COCHCOOMe), 3.35 (3H, s, COOMe), 3.84 (3H, s, COOMe), 5.01 (1H, s, ArCH), 7.02–7.66 (8H, m, ArH); δ_C (100.6 MHz, $CDCl_3$) 13.8, 22.3, 22.8, 30.9, 37.8, 43.9, 44.1, 50.2, 52.1, 52.4, 53.7, 64.2, 122.9, 123.5, 124.4, 125.8, 126.6, 126.7, 139.5, 143.2, 143.9, 168.5, 173.9, 204.5; HRMS (ESI) m/z: (M+Na)⁺, found 457.1990. $C_{27}H_{30}O_5$ Na requires 457.1991.

Compound **8a** (4%): colourless oil; R_f (10% EtOAc/hexane) 0.27; ν_{max} (liquid film) 2952, 2864, 1756, 1719, 1460, 1242 cm⁻¹; δ_{H} (400 MHz, CDCl₃) 0.88 (3H, t, J=6.9 Hz, Me), 1.69, 2.83, 4.28 (3H, ABX system, J=13.2, 3.2, 2.3 Hz, CH₂, ArCH), 1.12–1.70 (6H, m, CH₂), 2.23 (1H, ddd, J=17.6, 8.3, 6.2 Hz, CHCO), 2.48 (1H, ddd, J=17.6, 8.4, 6.6 Hz, CHCO), 3.34 (3H, s, COOMe), 3.39 (1H, s, COCHCOOMe), 3.48 (3H, s, COOMe), 4.70 (1H, s, ArCH), 6.99–7.53 (8H, m, ArH); δ_{C} (100.6 MHz, CDCl₃) 13.9, 22.5, 23.1, 31.1, 35.1, 41.4, 44.0, 51.0, 52.1, 52.2, 54.6, 65.3, 123.0, 123.6, 124.2, 125.4, 125.7, 126.5, 126.6, 127.0, 139.0, 140.0, 143.5, 144.5, 169.7, 174.1, 203.5; HRMS (ESI) m/z: (M+Na)⁺, found 457.1991. $C_{27}H_{30}O_5$ Na requires 457.1991.

4.2.1.2. 11-Carbomethoxy-11-(1'-octanoyl-1'-carbomethoxymethyl)-9,10-dihydro-9,10-ethanoanthracenes (**7b** and **8b**). Compound **7b** (63%): white solid; mp 200–202 °C (CH₂Cl₂/hexane); R_f (10% EtOAc/hexane) 0.23; ν_{max} (KBr) 2940, 2850, 1720, 1741, 1712, 1450, 1250 cm⁻¹; δ_{H} (400 MHz, CDCl₃) 0.89 (3H, t, J=7.1 Hz, Me), 0.98, 2.86, 4.26 (3H, ABX system, J=13.2, 3.1, 2.3 Hz, CH₂, ArCH), 1.06–1.48 (10H, m, CH₂), 2.05 (1H, dt, J=17.7, 7.2 Hz, CHCO), 2.42 (1H, dt, J=17.7, 7.6 Hz, CHCO), 3.03 (1H, s, COCHCOOMe), 3.36 (3H, s, COOMe), 3.85 (3H, s, COOMe), 5.01 (1H, s, ArCH), 7.01–7.64 (8H, m, ArH); δ_{C} (100.6 MHz, CDCl₃) 14.0, 22.6, 23.2, 28.7, 28.9, 31.6, 37.8, 43.9, 44.2, 50.2, 52.1, 52.4, 53.8, 64.2, 122.9, 123.5, 124.4, 125.8, 126.6, 126.7, 139.5, 143.2, 143.9, 168.5, 173.9, 204.5; HRMS (ESI) m/z: (M+Na)⁺, found 485.2305. C₂₉H₃₄O₅Na requires 485.2304.

Compound **8b** (4%): colourless oil; R_f (10% EtOAc/hexane) 0.34; $\nu_{\rm max}$ (liquid film) 2929, 2849, 1748, 1719, 1460, 1247 cm⁻¹; $\delta_{\rm H}$ (400 MHz, CDCl₃) 0.88 (3H, t, J=7.1 Hz, Me), 1.05–1.65 (10H, m, CH_2), 1.69, 2.83, 4.28 (3H, ABX system, J=13.2, 3.1, 2.2 Hz, CH_2 , ArCH), 2.23 (1H, ddd, J=17.6, 8.4, 6.2 Hz, CHCO), 2.47 (1H, ddd, J=17.6, 8.6, 6.3 Hz, CHCO), 3.34 (3H, s, COOMe), 3.42 (1H, s, COCHCOOMe), 3.48 (3H, s, COOMe), 4.70 (1H, s, COCHCOOMe), 3.48 (3H, s, COOMe), 3.40, 51.0, 52.2, 54.6, 65.3, 123.0, 123.6, 124.2, 125.4, 125.7, 126.5, 126.6, 127.0, 139.0, 140.1, 143.5, 144.5, 169.7, 174.1, 203.5; (ESI) m/z: $(M+Na)^+$, found 485.2304. $C_{29}H_{34}O_{5}Na$ requires 485.2304.

4.2.1.3. 11-Carbomethoxy-11-(1'-decanoyl-1'-carbomethoxymethyl)-9,10-dihydro-9,10-ethanoanthracenes (**7c** and **8c**). Compound **7c** (53%): colourless oil; R_f (10% EtOAc/hexane) 0.30; ν_{max} (liquid film) 2930, 2870, 1748, 1720, 1450, 1240 cm $^{-1}$; δ_{H} (400 MHz, CDCl $_{3}$) 0.89 (3H, t, J=7.1 Hz, Me), 0.99, 2.86, 4.26 (3H, ABX system, J=13.2, 3.1, 2.3 Hz, CH $_{2}$, ArCH), 1.06–1.48 (14H, m, CH $_{2}$), 2.04 (1H, dt, J=17.6, 7.2 Hz, CHCO), 2.42 (1H, dt, J=17.6, 7.6 Hz, CHCO), 3.03 (1H, s, COCHCOOMe), 3.36 (3H, s, COOMe), 3.84 (3H, s, COOMe), 5.01 (1H, s, ArCH), 7.00–7.66 (8H, m, ArH); δ_{C} (100.6 MHz, CDCl $_{3}$) 14.1, 22.6, 23.2, 28.7, 29.2, 29.3, 31.8, 37.8, 43.9, 44.2, 50.1, 52.1, 52.4, 53.7, 64.2, 122.9, 123.5, 124.4, 125.8, 126.6, 126.7, 139.5, 143.2, 143.9, 168.5, 173.9, 204.5; HRMS (ESI) m/z: (M+Na) $^+$, found 513.2617. C $_{31}$ H $_{38}$ O $_{5}$ Na requires 513.2617.

Compound **8c** (6%): colourless oil; R_f (10% EtOAc/hexane) 0.36; ν_{max} (liquid film) 2926, 2855, 1740, 1720, 1460, 1244 cm⁻¹; δ_{H} (400 MHz, CDCl₃) 0.87 (3H, t, J=7.1 Hz, Me), 1.05–1.75 (14H, m, CH_2), 1.79, 2.83, 4.28 (3H, ABX system, J=13.2, 3.2, 2.3 Hz, CH_2 , ArCH), 2.23 (1H, ddd, J=17.6, 8.4, 6.1 Hz, CHCO), 2.47 (1H, ddd, J=17.6, 8.6, 6.3 Hz, CHCO), 3.34 (3H, s, COOMe), 3.42 (1H, s, COCHCOOMe), 3.48 (3H, s, COOMe), 4.70 (1H, s, CHCO), 7.00–7.52 (8H, m, CHCO), 3.41, 22.7, 23.4, 29.0, 29.3, 29.4, 29.7, 31.9, 35.1, 41.5, 44.0, 51.0, 52.1, 52.2, 54.6, 65.3, 123.0, 123.6, 124.2, 125.4, 125.7,

126.5, 126.6, 127.0, 139.0, 140.0, 143.5, 144.5, 169.7, 174.1, 203.5; HRMS (ESI) m/z: $(M+Na)^+$, found 513.2617. $C_{31}H_{38}O_5Na$ requires 513.2617.

4.2.1.4. 11-Carbomethoxy-11-(1'-dodecanoyl-1'-carbomethoxymethyl)-9,10-dihydro-9,10-ethanoanthracenes (**7d** and **8d**). Compound **7d** (49%): colourless oil; R_f (10% EtOAc/hexane) 0.33; ν_{max} (liquid film) 2931, 2858, 1748, 1720, 1458, 1236 cm $^{-1}$; δ_{H} (400 MHz, CDCl $_{3}$) 0.88 (t, J=7.1 Hz, Me), 0.98, 2.86, 4.26 (3H, ABX system, J=13.2, 3.1, 2.3 Hz, CH $_{2}$, ArCH $_{3}$, 1.07–1.48 (18H, m, CH $_{2}$), 2.04 (1H, dt, J=17.7, 7.2 Hz, CHCO), 2.42 (1H, dt, J=17.7, 7.6 Hz, CHCO), 3.03 (1H, s, COCHCOOMe), 3.36 (3H, s, COOMe), 3.88 (3H, s, COOMe), 5.01 (1H, s, ArCH), 7.00–7.66 (8H, m, ArH); δ_{C} (100.6 MHz, CDCl $_{3}$) 14.1, 22.7, 23.2, 28.8, 29.3, 29.4, 29.6, 31.9, 37.8, 43.9, 44.2, 50.2, 52.1, 52.4, 53.8, 64.2, 122.9, 123.5, 124.4, 125.8, 126.6, 126.7, 139.5, 143.2, 143.9, 168.5, 174.0, 204.5; HRMS (ESI) m/z: (M+H) $^+$, found 519.3115. $C_{33}H_{43}O_{5}$ requires 519.3110.

Compound **8d** (11%): colourless oil; R_f (10% EtOAc/hexane) 0.39; $\nu_{\rm max}$ (liquid film) 2925, 2853, 1756, 1720, 1460, 1246 cm $^{-1}$; $\delta_{\rm H}$ (400 MHz, CDCl $_3$) 0.87 (3H, t, J=7.0 Hz, Me), 1.10–1.42 (18H, m, CH_2), 1.68, 2.82, 4.28 (3H, ABX system, J=13.2, 3.2, 2.3 Hz, CH_2 , Ar CH_2), 2.22 (1H, ddd, J=17.6, 8.5, 6.0 Hz, CHCO), 2.46 (1H, ddd, J=17.6, 8.6, 6.3 Hz, CHCO), 3.33 (3H, s, COOMe), 3.42 (1H, s, COCHCOOMe), 3.47 (3H, s, COOMe), 4.69 (1H, s, COCHCOOMe), 3.47 (100.6 MHz, COCHCOOMe), 14.1, 22.7, 23.4, 28.9, 29.3, 29.5, 29.6, 31.9, 35.1, 41.5, 44.0, 51.0, 52.1, 52.2, 54.6, 65.2, 123.0, 123.6, 124.2, 125.4, 125.6, 126.5, 126.6, 127.0, 138.9, 140.0, 143.5, 144.5, 169.7, 174.1, 203.5; HRMS (ESI) m/z: (M+Na) $^+$, found 541.2930. $C_{33}H_{42}O_5Na$ requires 541.2930.

4.2.1.5. 11-Carbomethoxy-11-(1'-benzoyl-1'-carbomethoxymethyl)-9,10-dihydro-9,10-ethanoanthracenes (**7e** and **8e**). Compound **7e** (73%): white solid; mp 188–190 °C (CH₂Cl₂/hexane); R_f (10% EtOAc/hexane) 0.10; $\nu_{\rm max}$ (KBr) 2947, 1740, 1606, 1438, 1234 cm⁻¹; $\delta_{\rm H}$ (400 MHz, CDCl₃) 1.05, 2.96, 4.25 (3H, ABX system, J=13.3, 3.1, 2.3 Hz, CH₂, ArCH), 3.42 (3H, s, COOMe), 3.74 (3H, s, COOMe), 3.91 (1H, s, COCHCOOMe), 5.12 (1H, s, ArCH), 7.03–7.76 (13H, m, ArH); $\delta_{\rm C}$ (100.6 MHz, CDCl₃) 37.9, 43.9, 50.3, 52.2, 52.5, 54.3, 59.8, 123.0, 123.6, 124.4, 125.8, 126.6, 126.9, 128.0, 128.7, 133.5, 136.6, 139.5, 143.3, 143.9, 168.5, 174.1, 194.0; HRMS (ESI) m/z: (M+Na)⁺, found 463.1521. C₂₈H₂₄O₅Na requires 463.1521.

Compound **8e** (19%): colourless oil; R_f (10% EtOAc/hexane) 0.13; $\nu_{\rm max}$ (liquid film) 2950, 1737, 1691, 1597, 1448, 1232 cm $^{-1}$; $\delta_{\rm H}$ (400 MHz, CDCl $_3$) 2.51, 2.94, 4.36 (3H, ABX system, J=13.7, 2.9, 2.8 Hz, CH_2 , ArCH), 3.17 (3H, s, COOMe), 3.31 (3H, s, COOMe), 4.60 (1H, s, COCHCOOMe), 4.87 (1H, s, ArCH), 6.94–7.87 (13H, m, ArH); $\delta_{\rm C}$ (100.6 MHz, CDCl $_3$) 33.3, 44.2, 52.2, 53.9, 61.4, 123.4, 123.5, 124.5, 124.9, 125.5, 126.3, 126.6, 126.7, 128.3, 128.6, 133.4, 136.2, 138.7, 140.7, 143.9, 144.9, 167.8, 174.5, 194.1; HRMS (ESI) m/z: (M+Na) $^+$, found 463.1522. $C_{28}H_{24}O_5$ Na requires 463.1521.

4.2.2. General procedure for the synthesis of tetrahydro-4'-carbomethoxy-5'-(alkyl or phenyl)-2'-furanone-3'-spiro-11-9,10-dihydro-9,10-ethanoanthracenes (cis-3a-e and trans-5a-e) by using NaBH₄ in wet-THF system

To a cooled (0 °C) solution of β -ketodiester adduct (7) (0.23 mmol) in THF (4 mL) and H₂O (0.5 mL) was added NaBH₄ (1.20 mmol, 5.0 equiv). The reaction mixture was stirred at 0 °C for 4 h and then quenched by dropwise addition of acetone (1 mL). After that the resulting solution was extracted with CH₂Cl₂ (3×15 mL) and the combined organic portions were dried (MgSO₄), filtered and concentrated in vacuo. Purification of the residue by flash column chromatography (EtOAc/hexane=1:9 as eluent) followed by preparative thin layer chromatography (EtOAc/hexane=1:9 as developing solvent) obtained *cis*-3 as the minor product and *trans*-5 as the major product.

4.2.2.1. Tetrahydro-4'-carbomethoxy-5'-pentyl-2'-furanone-3'-spiro-11-9, 10-dihydro-9,10-ethanoanthracenes (cis-**3a** and trans-**5a**). Compound cis-**3a** (6%): white solid; mp 211.1–212.2 °C (CH₂Cl₂/hexane) [lit.⁴ⁿ mp 210–212 °C (CH₂Cl₂/hexane)]; R_f (10% EtOAc/hexane) 0.17; $\nu_{\rm max}$ (KBr) 2946, 2865, 1785, 1734, 1464, 1204, 1163 cm⁻¹; $\delta_{\rm H}$ (400 MHz, CDCl₃) 0.85 (3H, t, J=6.8 Hz, Me), 1.17–1.64 (8H, m, CH_2), 1.99, 2.09, 4.39 (3H, ABX system, J=12.4, 3.2, 2.2 Hz, CH_2 , ArCH), 2.24 (1H, d, J=5.2 Hz, CH_2) CHCOOMe), 3.83 (3H, s, COOMe), 4.31 (1H, dt, J=8.3, 5.2 Hz, CH_2), 4.64 (1H, s, ArCH), 7.00–7.51 (8H, m, ArH); $\delta_{\rm C}$ (100.6 MHz, CDCl₃) 13.8, 22.3, 25.4, 30.9, 31.4, 40.7, 43.7, 46.8, 50.6, 51.6, 58.2, 76.4, 122.3, 123.9, 124.3, 125.9, 126.1, 126. 7, 127.4, 139.5, 140.8, 142.1, 143.3, 170.3, 176.9; HRMS (ESI) m/z: $(M+H)^+$, found 405.2064. $C_{26}H_{29}O_4$ requires 405.2066.

Compound *trans*-**5a** (70%): white solid; mp 117.5–118.9 °C (CH₂Cl₂/hexane) [lit.⁴ⁿ mp 118–119 °C (hexane)]; R_f (10% EtOAc/hexane) 0.30; v_{max} (KBr) 2946, 2870, 1780, 1449, 1212, 1164 cm⁻¹; δ_{H} (400 MHz, CDCl₃) 0.89 (3H, t, J=6.8 Hz, Me), 1.24–1.73 (8H, m, CH₂), 2.09, 2.48, 4.36 (3H, ABX system, J=12.5, 3.1, 2.4 Hz, CH₂, ArCH), 2.75 (1H, d, J=10.4 Hz, CHCOOMe), 3.00 (3H, s, COOMe), 4.50 (1H, s, ArCH), 5.02 (1H, ddd, J=10.4, 8.3, 3.0 Hz, CHO), 7.04–7.31 (8H, m, ArH); δ_{C} (100.6 MHz, CDCl₃) 13.9, 22.4, 25.3, 31.4, 34.2, 37.1, 43.8, 46.7, 51.1, 51.7, 56.1, 77.5, 123.1, 123.4, 124.6, 125.1, 125.8, 126.5, 126.6, 127.5, 137.9, 140.0, 143.3, 145.4, 168.6, 176.3; HRMS (ESI) m/z: (M+Na)⁺, found 427.1891. C₂₆H₂₈O₄Na requires 427.1885.

4.2.2.2. Tetrahydro-4'-carbomethoxy-5'-heptyl-2'-furanone-3'-spiro-11-9,10-dihydro-9,10-ethanoanthracenes (cis-**3b** and trans-**5b**). Compound cis-**3b** (19%): white solid; mp 131.0–132.2 °C (CH₂Cl₂/hexane); R_f (10% EtOAc/hexane) 0.15; $\nu_{\rm max}$ (KBr) 2930, 2857, 1782, 1730, 1460, 1210, 1172 cm⁻¹; $\delta_{\rm H}$ (400 MHz, CDCl₃) 0.85 (3H, t, J=6.7 Hz, Me), 1.16–1.64 (12H, m, CH₂), 1.98, 2.08, 4.39 (3H, ABX system, J=12.4, 3.2, 2.2 Hz, CH₂, ArCH), 2.23 (1H, d, J=5.1 Hz, CHCOOMe), 3.82 (3H, s, COOMe), 4.31 (1H, dt, J=8.3, 5.1 Hz, CHO), 4.64 (1H, s, ArCH), 7.00–7.52 (8H, m, ArH); $\delta_{\rm C}$ (100.6 MHz, CDCl₃) 14.0, 22.5, 25.7, 28.9, 29.2, 31.0, 31.6, 40.7, 43.7, 46.8, 50.6, 51.6, 58.2, 76.4, 122.3, 123.9, 124.3, 125.9, 126.1, 126.7, 127.4, 139.5, 140.8, 142.1, 143.3, 170.3, 176.9; HRMS (ESI) m/z: (M+Na)+, found 455.2198. $C_{28}H_{32}O_4$ Na requires 455.2198.

Compound trans-**5b** (78%): white solid; mp 112.4–113.4 °C (CH₂Cl₂/hexane); R_f (10% EtOAc/hexane) 0.18; ν_{max} (KBr) 2941, 2850, 1775, 1734, 1459, 1208, 1169 cm⁻¹; $\delta_{\rm H}$ (400 MHz, CDCl₃) 0.89 (3H, t, J=7.1 Hz, Me), 1.21–1.73 (12H, m, CH_2), 2.10, 2.49, 4.37 (3H, ABX system, J=12.5, 3.0, 2.4 Hz, CH_2 , ArCH), 2.76 (1H, d, J=10.4 Hz, CHCOOMe), 3.01 (3H, s, COOMe), 4.51 (1H, s, ArCH), 5.03 (1H, ddd, J=10.4, 8.3, 3.0 Hz, CHO), 7.05–7.33 (8H, m, ArH); $\delta_{\rm C}$ (100.6 MHz, CDCl₃) 14.0, 22.6, 25.7, 29.0, 29.2, 31.7, 34.2, 37.2, 43.8, 46.7, 51.1, 51.6, 56.1, 77.5, 123.1, 123.4, 124.7, 125.1, 125.9, 126.5, 126.6, 127.5, 137.9, 140.0, 143.3, 145.4, 168.6, 176.3; HRMS (ESI) m/z: $(M+H)^+$, found 433.2379. $C_{28}H_{33}O_4$ requires 433.2379.

4.2.2.3. Tetrahydro-4'-carbomethoxy-5'-nonyl-2'-furanone-3'-spiro-11-9,10-dihydro-9,10-ethanoanthracenes (cis-**3c** and trans-**5c**). Compound cis-**3c** (4%): white solid; mp 120–121.1 °C (CH₂Cl₂/hexane); R_f (10% EtOAc/hexane) 0.19; $\nu_{\rm max}$ (KBr) 2929, 2857, 1782, 1734, 1460, 1204, 1173 cm⁻¹; $\delta_{\rm H}$ (400 MHz, CDCl₃) 0.87 (3H, t, J=6.7 Hz, Me), 1.15–1.68 (16H, m, CH_2), 1.99, 2.09, 4.40 (3H, ABX system, J=12.4, 3.1, 2.1 Hz, CH_2 , ArCH), 2.24 (1H, d, J=5.1 Hz, CHCOOMe), 3.83 (3H, s, COOMe), 4.31 (H, dt, J=8.2, 5.1 Hz, CHO), 4.65 (1H, s, ArCH), 7.01–7.53 (8H, m, ArH); $\delta_{\rm C}$ (100.6 MHz, CDCl₃) 14.1, 22.6, 25.7, 28.9, 29.2, 29.3, 29.4, 31.0, 31.6, 40.7, 43.7, 46.8, 50.7, 51.6, 58.2, 76.4, 122.3, 123.9, 124.3, 125.9, 126.1, 126.7, 127.4, 139.5, 140.8, 142.1, 143.3, 170.3, 176.9; HRMS (ESI) m/z: $(M+Na)^+$, found 483.2508. $C_{30}H_{36}O_4Na$ requires 483.2511.

Compound *trans-***5c** (90%): white solid; mp 115.5–115.6 °C (CH₂Cl₂/hexane); R_f (10% EtOAc/hexane) 0.23; $\nu_{\rm max}$ (KBr) 2941, 2850, 1780, 1734, 1454, 1204, 1159 cm⁻¹; $\delta_{\rm H}$ (400 MHz, CDCl₃) 0.88 (3H, t, J=7.1 Hz, Me), 1.22–1.71 (16H, m, CH_2), 2.09, 2.48, 4.36 (3H,

ABX system, J=12.5, 3.0, 2.4 Hz, CH₂, ArCH), 2.75 (1H, d, J=10.4 Hz, CHCOOMe), 3.00 (3H, s, COOMe), 4.49 (1H, s, ArCH), 5.01 (1H, ddd, J=10.4, 8.3, 3.0 Hz, CHO), 7.04–7.31 (8H, m, ArH); δ _C (100.6 MHz, CDCl₃) 14.1, 22.6, 25.7, 29.2, 29.3, 29.4, 31.8, 34.2, 37.2, 43.8, 46.7, 51.1, 51.7, 56.1, 77.5, 123.1, 123.4, 124.6, 125.1, 125.9, 126.5, 126.6, 127.5, 137.9, 140.0, 143.3, 145.4, 168.6, 176.3; HRMS (ESI) m/z: (M+Na)⁺, found 483.2511. C₃₀H₃₆O₄Na requires 483.2511.

4.2.2.4. Tetrahydro-4'-carbomethoxy-5'-undecyl-2'-furanone-3'-spiro-11-9,10-dihydro-9,10-ethanoanthracenes (cis-**3d** and trans-**5d**). Compound cis-**3d** (8%): white solid; mp 160–161 °C (CH₂Cl₂/hexane) [lit.⁴ⁿ mp 159–160 °C (CH₂Cl₂/hexane)]; R_f (10% EtOAc/hexane) 0.22; $\nu_{\rm max}$ (KBr) 2926, 2854, 1770, 1729, 1454, 1223, 1164 cm⁻¹; $\delta_{\rm H}$ (400 MHz, CDCl₃) 0.87 (3H, t, J=7.0 Hz, Me), 1.17–1.64 (20H, m, CH₂), 1.99, 2.09, 4.39 (3H, ABX system, J=12.4, 3.2, 2.2 Hz, CH₂, ArCH), 2.23 (1H, d, J=5.1 Hz, CHCOOMe), 3.82 (3H, s, COOMe), 4.30 (1H, dt, J=8.3, 5.1 Hz, CHO), 4.64 (1H, s, ArCH), 7.00–7.51 (8H, m, ArH); $\delta_{\rm C}$ (100.6 MHz, CDCl₃) 14.1, 22.6, 25.7, 29.2, 29.3, 29.4, 29.6, 31.0, 31.9, 40.7, 43.7, 46.8, 50.7, 51.7, 58.2, 76.6, 122.3, 123.9, 124.3, 125.9, 126.2, 126.7, 127.4, 139.5, 140.8, 142.1, 143.3, 170.3, 176.9; HRMS (ESI) m/z: (M+H)⁺, found 489.3008. C₃₂H₄₁O₄ requires 489.3005.

Compound *trans*-**5d**(89%): white solid; mp 78.9-79.1 °C (CH₂Cl₂/hexane) [lit. ⁴ⁿ mp 78-79 °C (hexane)]; R_f (10% EtOAc/hexane) 0.31; ν_{max} (KBr) 2926, 2870, 1785, 1734, 1469, 1212, 1164 cm⁻¹; δ_{H} (400 MHz, CDCl₃) 0.88 (3H, t, J=7.1 Hz, Me), 1.21–1.71 (20H, m, CH₂), 2.09, 2.48, 4.36 (3H, ABX system, J=12.5, 3.0, 2.4 Hz, CH₂, ArCH), 2.75 (1H, d, J=10.4 Hz, CHCOOMe), 2.99 (3H s, COOMe), 4.50 (1H, s, ArCH), 5.01 (1H, ddd, J=10.4, 8.4, 3.0 Hz, CHO), 7.05–7.30 (8H, m, ArH, ArH); δ_{C} (100.6 MHz, CDCl₃) 14.1, 22.7, 25.7, 29.3, 29.4, 29.5, 29.6, 31.9, 34.3, 37.2, 43.9, 46.7, 51.2, 51.8, 56.2, 77.6, 123.1, 123.4, 124.7, 125.1, 125.9, 126.5, 126.6, 127.6, 137.9, 140.0, 143.3, 145.5, 168.7, 176.4; HRMS (ESI): (M+H)+, found 489.3006. C₃₂H₄₁O₄ requires 489.3005.

4.2.2.5. Tetrahydro-4'-carbomethoxy-5'-phenyl-2'-furanone-3'-spiro-11-9,10-dihydro-9,10-ethanoanthracenes (cis-**3e** and trans-**5e**). Compound cis-**3e** (2%): white solid; mp 220–221 °C (CH₂Cl₂/hexane); R_f (10% EtOAc/hexane) 0.09; ν_{max} (KBr) 2951, 1795, 1734, 1454, 1208, 1143 cm⁻¹; δ_{H} (400 MHz, CDCl₃) 2.20, 2.26, 4.49 (3H, ABX system, J=12.4, 3.1, 2.3 Hz, CH₂, ArCH), 2.54 (1H, d, J=5.6 Hz, CHCOOMe), 3.28 (3H, s, COOMe), 4.77 (1H, s, ArCH), 5.51 (1H, d, J=5.6 Hz, CHO), 6.97–7.56 (13H, m, ArH); δ_{C} (100.6 MHz, CDCl₃) 40.8, 43.8, 46.9, 50.9, 51.4, 61.0, 76.9, 124.0, 124.4, 125.4, 126.0, 126.3, 126.8, 127.5, 128.2, 128.5, 139.3, 140.7, 142.0, 169.3, 176.7; HRMS (ESI): (M+H)⁺, found 411.1594. C₂₇H₂₃O₄ requires 411.1596.

Compound *trans*-**5e** (70%): white solid; mp 228.9–229.9 °C (CH₂Cl₂/hexane); R_f (10% EtOAc/hexane) 0.12; $\nu_{\rm max}$ (KBr) 2951, 2870, 1774, 1734, 1459, 1205, 1161 cm⁻¹; $\delta_{\rm H}$ (400 MHz, CDCl₃) 2.11, 2.55, 4.38 (3H, ABX system, J=12.5, 3.0, 2.4 Hz, CH₂, ArCH), 2.96 (3H, s, COOMe), 3.05 (1H, d, J=10.2 Hz, CHCOOMe), 4.66 (1H, s, ArCH), 6.05 (1H, d, J=10.2 Hz, CHO), 7.05–7.44 (13H, m, ArH); $\delta_{\rm C}$ (100.6 MHz, CDCl₃) 37.4, 43.8, 46.7, 51.5, 51.8, 59.0, 78.4, 123.2, 123.4, 124.8, 125.2, 126.0, 126.3, 126.6, 126.7, 127.6, 128.6, 128.9, 137.2, 137.8, 139.9, 143.3, 168.1, 176.0; HRMS (ESI): (M+H)⁺, found 411.1595. C₂₇H₂₃O₄ requires 411.1596.

4.3. Computational procedure

The calculations were carried out in a Pentium IV-based PC computer. Density functional calculations were performed with the Gaussian 03 program¹² (Revision C.02, Gaussian, Inc., Wallingford CT) at the B3LYP/6-31G level. The three-dimensional molecular graphics of the energetically optimized **7b** and **8b** were produced from the GaussView program, version 3.09.¹³

Acknowledgements

Financial supports from The Thailand Research Fund (TRF), the Center for Innovation in Chemistry (PERCH-CIC), Commission on Higher Education, Ministry of Education and National Center for Genetic Engineering and Biotechnology (BIOTEC) are gratefully acknowledged. In addition, we thank Department of Chemistry, Faculty of Science, Chiang Mai University for facilities supporting this research. We are indebted to Mrs. Surisa Kongthong of BIOTEC for NOE data.

References and notes

- 1. Mori, K.: Yamane, K. Tetrahedron 1982, 38, 2919-2921.
- 2. (a) Hoffmann, H. M. R.; Rabe, J. *Angew. Chem., Int. Ed. Engl.* **1985**, *24*, 94–110 and references cited therein; (b) Petragnani, N.; Ferraz, H. M. C.; Silva, G. V. J. *Synthesis* **1986**, 157–183; (c) Sibi, M. P.; Deshpande, P. K.; La Loggia, A. J. *Synlett* **1996**, 343–345 and references cited therein.
- (a) Park, B. K.; Nakagawa, M.; Hirota, A.; Nakayama, M. Agric. Biol. Chem. 1987, 51, 3443–3444; (b) Park, B. K.; Nakagawa, M.; Hirota, A.; Nakayama, M. J. Antibiot. 1988, 41, 751–758; (c) Nakayama, M.; Nakagawa, S.; Boku, T.; Hirota, A.; Shima, S.; Nakanishi, O.; Yamada, Y. Jpn. Kokai Tokkyo Koho 1989, JP 01016776 A, 20/01/1989; Chem. Abstr. 1990, 112, 34404f.
- 4. For total and formal syntheses of methylenolactocin: (a) Carlson, R. M.; Oyler, A. R. J. Org. Chem. 1976, 41, 4065-4069; (b) Honda, T.; Kimura, N. J. Chem. Soc., Chem. Commun. 1994, 77-78; (c) Takahata, H.; Uchida, Y.; Momose, T. J. Org. Chem. 1995, 60, 5628-5633; (d) Vaupel, A.; Knochel, P. Tetrahedron Lett. 1995, 36, 231-232; (e) Mawson, S. D.; Weavers, R. T. Tetrahedron 1995, 51, 11257-11270; (f) Zhu, G.; Lu, X. Tetrahedron: Asymmetry 1995, 6, 885-892; (g) Zhu, G.; Lu, X. J. Org. Chem. 1995, 60, 1087-1089; (h) Drioli, S.; Felluga, F.; Forzato, C.; Nitti, P.; Pitacco, G. Chem. Commun. 1996, 1289-1290; (i) Saicic, R. N.; Zard, S. Z. Chem. Commun. 1996, 1631-1632; (j) Sarkar, S.; Ghosh, S. Tetrahedron Lett. 1996, 37, 4809-4810; (k) Ghatak, A.; Sarkar, S.; Ghosh, S. Tetrahedron 1997, 53, 17335-17342; (1) Chandrasekharam, M.; Liu, R. S. J. Org. Chem. 1998, 63, 9122-9124; (m) Mandal, P. K.; Maiti, G.; Roy, S. C. J. Org. Chem. 1998, 63, 2829-2834; (n) Lertvorachon, J.; Meepowpan, P.; Thebtaranonth, Y. Tetrahedron 1998, 54, 14341-14358; (o) Masaki, Y.; Arasaki, H.; Itoh, A. Tetrahedron Lett. 1999, 40, 4829-4832; (p) Forbes, J. E.; Saicic, R. N.; Zard, S. Z. Tetrahedron 1999, 55, 3791-3802; (q) Loh, T. P.; Lye, P. L. Tetrahedron Lett. 2001, 42, 3511-3514; (r) Kongsaeree, P.; Meepowpan, P.; Thebtaranonth, Y. Tetrahedron: Asymmetry 2001, 12, 1913-1922; (s) Ariza, X.; Garcia, J.; Lopez, M.; Montserrat, L. Synlett 2001, 120-122; (t) Felluga, F.; Fermeglia, M.; Ferrone, M.; Pitacco, G.; Pricl, S.; Valentin, E. Helv. Chim. Acta 2002, 85, 4046-4054; (u) Chhor, R. B.; Nosse, B.; Sorgel, S.; Bohm, C.; Seitz, M.; Reiser, O. Chem.—Eur. J. 2003, 9, 260-270; (v) Ariza, X.; Fernandez, N.; Garcia, J.; Lopez, M.; Montserrat, L.; Ortiz, J. Synthesis 2004, 128-134; (w) Hon, Y.-S.; Hsieh, C.-H.; Liu, Y.-W. Tetrahedron 2005, 61, 2713-2723; (x) Braukmueller, S.; Brueckner, R. Eur. J. Org. Chem. 2006, 2110-2118; (y) Blanc, D.; Madec, J.; Popowyck, F.; Ayad, T.; Phansavath, P.; Ratovelomanana-Vidal, V.; Genet, J.-P. Adv. Syn. Catal. 2007, 349, 943-950; (z) Hajra, S.; Karmakar, A.; Giri, A. K.; Hazra, S. Tetrahedron Lett. 2008, 49, 3625-3627.
- 5. Asahina, Y.; Yanagita, M.; Sakurai, Y. Chem. Ber. 1937, 70B, 227-235.
- 6. For total syntheses of nephrosterinic acid, see: Refs. 4a, d, n and r.
- 7. (a) Zopf, W. Liebigs Ann. Chem. **1902**, 324, 39–78; (b) Asahina, Y.; Asano, M. J. Pharm. Sci. Jpn. **1927**, 539, 1–17; (c) Asahina, Y.; Yanagita, M. Chem. Ber. **1936**, 69B, 120–125.
- For total and formal syntheses of protolichesterinic acid: (a) Van Tamelen,
 E. E.; Bach, S. R. J. Am. Chem. Soc. 1958, 80, 3079–3086; (b) Loffler, A.; Pratt,
 R. D.; Pucknat, J.; Gelbard, G.; Dreiding, A. S. Chimica 1969, 23, 413–416; (c)
 Martin, J.; Watts, P. C.; Johnson, F. J. Org. Chem. 1974, 39, 1676–1681; (d)
 Damon, R. E.; Schlessinger, R. H. Tetrahedron Lett. 1976, 17, 1561–1564; (e)

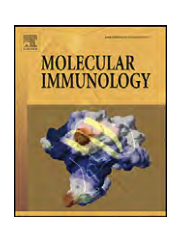
- Chen, M. J.; Liu, R. S. *Tetrahedron Lett.* **1998**, 39, 9465–9468; (f) Murta, M. M.; de Azevedo, M. B. M.; Greene, A. E. *J. Org. Chem.* **1993**, 58, 7537–7541; (g) Martin, T.; Rodriguez, C. M.; Martin, V. S. *J. Org. Chem.* **1996**, 61, 6450–6453; (h) See Refs. 4a, k, m, n and o.
- (a) Bérdy, J. Handbook of Antibiotic Compounds; CRC: Boca Raton, FL, 1982; Vol. IX and references cited therein; (b) Cavallito, C. J.; Fruehuauf, McK. D.; Bailey, J. N. J. Am. Chem. Soc. 1948, 70, 3724-3726; (c) Shibata, S.; Miura, Y.; Sugimura, H.; Toyoizumi, Y. Yakugaku Zasshi 1948, 68, 300-303; Chem. Abstr. 1951, 45, 6691i; (d) Fujikawa, F.; Hitosa, Y.; Yamaoka, M.; Fujiwara, Y.; Nakazawa, S.; Omatsu, T.; Toyoda, T. Yakugaku Zasshi 1953, 73, 135–138; Chem. Abstr. 1954, 48, 230a; (e) Borkawski, B.; Wozniak, W.; Gertig, H.; Werakso, B. Diss. Pharm. **1964**, *16*, 189–194; *Chem. Abstr.* **1965**, *62*, 1995b; (f) Sticker, O. *Pharm. Acta Helv.* **1965**, 40, 483–495; *Chem. Abstr.* **1965**, 63, 8778d; (g) Sticker, O. *Pharm. Acta Helv.* 1965. 40. 385-394: Chem. Abstr. 1965. 63. 12026c: (h) Hirayama. T.: Fujikawa. F.: Kasahara, T.: Otsuka, M.: Nishida, N.: Mizuno, D. Yakugaku Zasshi 1980, 100, 755-759; Chem. Abstr. **1980**, 93, 179563f; (i) Ingolfsdottir, K.; Hjalmarsdottir, M.; Sigurdsson, A.; Gudjonsdottir, G. A.; Brynjolfsdottir, A.; Steingrimsson, O. Antimicrob. Agents Chemother. **1997**, 41, 215–217; (j) Ingolfsdottir, K.; Chung, G. A. C.; Skulason, V. G.; Gissurarson, S. R.; Vilhelmsdottir, M. Eur. J. Pharm. Sci. **1998**, 6, 141–144; (k) Turk, A. O.; Yilmaz, M.; Kivanc, M.; Turk, H. Z. Naturforsch. C **2003**, 58, 850–854; (I) Hughes, M. A.; McFadden, J. M.; Townsend, C. A. Bioorg. Med. Chem. Lett. **2005**, 15, 3857–3859; (m) Freysdottir, J.; Omarsdottir, S.; Ingolfsdottir, K.; Vikingsson, A.; Olafsdottir, E. S. Int. Immunopharmacol. 2008, 8, 423-430; (n) Bucar, F.; Schneider, I.; Ogmundsdottir, H.; Ingolfsdottir, K. Phytomedicine 2004, 11, 602-606; (o) Huneck, S.; Schreiber, K. Phytochemistry 1972, 11, 2429-2434
- 10. Barros, M. T.; Maycock, C. D.; Ventura, M. R. Org. Lett. 2003, 5, 4097-4099.
- For synthesis and applications of dimethyl itaconate-anthracene adduct (1): (a) Golfiler, M.; Prange, T. Bull. Soc. Chim. Fr. 1974, 1159-1160; (b) Kodpinid, M.; Siwapinyoyos, T.; Thebtaranonth, Y. J. Am. Chem. Soc. 1984, 106, 4862-4865; (c) Mahidol, C.; Thebtaranonth, C.; Thebtaranonth, Y.; Yenjai, C. Tetrahedron Lett. 1984, 30, 3857-3860; (d) Thebtaranonth, Y. Pure Appl. Chem. 1997, 69, 609-614.
- Frisch, M. J.; Trucks, G. W.; Schlegel, H. B.; Scuseria, G. E.; Robb, M. A.; Cheeseman, J. R.; Montgomery, J. A., Jr.; Vreven, T.; Kudin, K. N.; Burant, J. C.; Millam, J. M.; Iyengar, S. S.; Tomasi, J.; Barone, V.; Mennucci, B.; Cossi, M.; Scalmani, G.; Rega, N.; Petersson, G. A.; Nakatsuji, H.; Hada, M.; Ehara, M.; Toyota, K.; Fukuda, R.; Hasegawa, J.; Ishida, M.; Nakajima, T.; Honda, Y.; Kitao, O.; Nakai, H.; Klene, M.; Li, X.; Knox, J. E.; Hratchian, H. P.; Cross, J. B.; Bakken, V.; Adamo, C.; Jaramillo, J.; Gomperts, R.; Stratmann, R. E.; Yazyev, O.; Austin, A. J.; Cammi, R.; Pomelli, C.; Ochterski, J. W.; Ayala, P. Y.; Morokuma, K.; Voth, G. A.; Salvador, P.; Dannenberg, J. J.; Zakrzewski, V. G.; Dapprich, S.; Daniels, A. D.; Strain, M. C.; Farkas, O.; Malick, D. K.; Rabuck, A. D.; Raghavachari, K.; Foresman, J. B.; Ortiz, J. V.; Cui, Q.; Baboul, A. G.; Clifford, S.; Cioslowski, J.; Stefanov, B. B.; Liu, G.; Liashenko, A.; Piskorz, P.; Komaromi, I.; Martin, R. L.; Fox, D. J.; Keith, T.; Al-Laham, M. A.; Peng, C. Y.; Nanayakkara, A.; Challacombe, M.; Gill, P. M. W.; Johnson, B.; Chen, W.; Wong, M. W.; Gonzalez, C.; Pople, J. A. Gaussian O3, Revision C.02, Gaussian: Wallingford, CT, 2004.
- Dennington, R., II; Keith, T.; Millam, J.; Eppinnett, K.; Hovell, W. L.; Gilliland, R. GaussianView, Version 3.09, Semichem: Shawnee Mission, KS, 2003.
- (a) Firouzabadi, H.; Zeynizadeh, F. Bull. Chem. Soc. Jpn. 1997, 70, 155–167 and the references cited therein; (b) Hudlicky, M. Reduction in Organic Chemistry; Ellis Horwood: Chichester, UK, 1984.
- 15. Zeynizadeh, B.; Behyar, T. Bull. Chem. Soc. Jpn. 2005, 78, 307-315.
- For the use of NaBH₄ in THF/H₂O system in reduction, see: (a) Matteoli, U.; Beghetto, V.; Schiavon, C.; Scrivanti, A.; Menchi, G. Tetrahedron: Asymmetry 1997, 8, 1403–1409; (b) Tamami, B.; Mahdavi, H. Tetrahedron 2003, 59, 821– 826; (c) Issa, F.; Fischer, J.; Turner, P.; Coster, M. J. J. Org. Chem. 2006, 71, 4703– 4705; (d) See Ref. 15.

FISEVIER

Contents lists available at ScienceDirect

Molecular Immunology

journal homepage: www.elsevier.com/locate/molimm



Pairwise decomposition of residue interaction energies of single chain Fv with HIV-1 p17 epitope variants

Vannajan Sanghiran Lee^{a,*}, Panthip Tue-ngeun^a, Sawitree Nangola^b, Kuntida Kitidee^b, Jitrayut Jitonnom^a, Piyarat Nimmanpipug^a, Supat Jiranusornkul^c, Chatchai Tayapiwatana^{b,d,**}

- a Computational Simulation and Modeling Laboratory (CSML), Department of Chemistry and Center for Innovation in Chemistry, Chiang Mai University, Chiang Mai, 50200, Thailand
- b Division of Clinical Immunology, Department of Medical Technology, Faculty of Associated Medical Sciences, Chiang Mai University, Chiang Mai, 50200, Thailand
- ^c Department of Pharmaceutical Sciences, Faculty of Pharmacy, Chiang Mai University, Chiang Mai, 50200, Thailand
- d Biomedical Technology Research Unit, National Center for Genetic Engineering and Biotechnology, National Science and Technology Development Agency at the Faculty of Associated Medical Sciences, Chiang Mai University, Chiang Mai, 50200, Thailand

ARTICLE INFO

Article history: Received 27 October 2009 Received in revised form 7 November 2009 Accepted 13 November 2009 Available online 21 December 2009

Keywords: HIV-1 p17 Epitope Single chain Fv Pairwise decomposition

ABSTRACT

Computational assisted modeling was carried out to investigate the importance of specific residues in the binding site of scFv. In this study, scFv against HIV-1 epitope at the C-terminal on p17 (scFv anti-p17) was used as a candidate molecule for evaluating the method. The wild-type p17 and its nine natural mutants were docked with scFv anti-p17. Potential mean force (PMF) scores predicted the most favorable binding interaction, and the correlation agreed well with the corresponding activity data from the peptide based ELISA. In the interaction with solvent molecules, the 3D structures of scFv anti-p17 and selected peptide epitopes were further investigated by molecular dynamics (MDs) simulation with the AMBER 9 program. Post-processing of the snapshot at equilibrium was performed to evaluate the binding free energy and pairwise decomposition or residue-based energy calculation of complexes in solution using the Molecular Mechanics Poisson–Boltzmann Surface Area (MM-PBSA) protocol. Our results demonstrated that the specific residues located in the complementary determining regions (CDRs) of scFv anti-p17, MET100, LYS101, ASN169, HIS228, and LEU229, play a crucial role in the effective binding interaction with the absolute relative decomposed energy more than 2.00 kcal/mol in comparison to the original substrate.

1. Introduction

The Gag p55 polyprotein of human immunodeficiency virus type 1 (HIV-1) plays a critical role in HIV-1 assembly and maturation. In the assembly step, the Gag polyprotein is directly targeted to the cell membrane to produce Gag dimerization or multimerization. Afterward, the viral-encoded protease cleaves the Gag precursor into the functional proteins: the matrix (MA or p17), capsid (CA or p24), nucleocapsid (NC) and p6 domains to form the infectious virus. The matrix protein (p17) is involved in many steps of

the HIV life cycle, especially the assembly and maturation steps (Ganser-Pornillos et al., 2008; Bukrinskaya, 2004). Tewari and coworkers investigated an intrabody strategy using the single chain antibody fragment (scFv) derived from hybridoma-secreting antip17 antibody inside HIV-1 infected cells, which interfered with the viral replication process. This antibody specifically binds to the C-terminal epitope (DTGHSSQVSQNY) of the p17 domain (Tewari et al., 1998). The scFv platform can be expressed in both prokaryotic and eukaryotic systems and is able to be engineered in order to improve its functional affinity and stability (Quintero-Hernandez et al., 2007; Pavoni et al., 2006; Park et al., 2006). The potential applications of scFv have been explored in many areas of research, including diagnostics and gene therapy (Inui et al., 2009; Shen et al., 2008; Wang et al., 2008; Depetris et al., 2008; Stocks, 2005).

Computational approaches and protein structural analysis can provide relevant information about the functional roles of the scFv residues (Arcangeli et al., 2008). Fast protocols using force field based scoring functions and knowledge-based approaches for predicting binding affinities of protein-ligand complexes have been established. Some popular scoring functions for estimating binding affinities of protein-ligand complexes are DOCK (Ewing et al., 2001), AutoDock (Morris et al., 1998), PMF (Muegge and Martin,

^{*} Corresponding author. Current address: Computational Simulation and Modelling Laboratory (CSML), Department of Chemistry and Center for Innovation in Chemistry, Faculty of Science, Chiang Mai University, Chiang Mai, 50200, Thailand. Tel.: +66891100216.

^{**} Corresponding author. Current address: Division of Clinical Immunology, Department of Medical Technology, Faculty of Associated Medical Sciences, Chiang Mai University, Chiang Mai, 50200, Thailand. Tel. +66818845141.

E-mail addresses: vannajan@gmail.com (V.S. Lee), ptuengeun@gmail.com (P. Tue-ngeun), sawitree2727@hotmail.com (S. Nangola), kitidee_010@hotmail.com (K. Kitidee), jitrayut.018@gmail.com (J. Jitonnom), piyaratn@gmail.com (P. Nimmanpipug), supatjira@hotmail.com (S. Jiranusornkul), asimi002@hotmail.com (C. Tayapiwatana).

1999), GOLD (Jones et al., 1997), LUDI (Bohm, 1998), FlexX (Rarey et al., 1996), and Ligscore (Krammer et al., 2005). Since most of the reactions of biological interest occur in water, the evaluation of the solvent effect represents an important aspect of the analytical and numerical molecular modeling approaches. Such computational approaches that consider the solvent as a part of a simulation system can be divided into several major groups: (i) continuum electrostatic methods, (ii) explicit solvent models with microscopic detail, and (iii) hybrids of the first two methods (Kollman, 1993: Smith and Pettitt, 1994; van Gunsteren et al., 1994; Tomasi and Persico, 1994; Leach, 1996; Gao, 1996; Levy and Gallicchio, 1998). An additional term is sometimes added to the force field to account for specific hydrogen bonding interactions. The more sophisticated methods have three-body nonadditive terms added. These methods include molecular dynamics (MD) (Pearlman et al., 1995; Brooks et al., 1983), Monte Carlo (MC) methods (Jorgensen, 1996), or a combination of these for sampling, and represent an advantage in terms of precision. These approaches can yield a reliable approximation method that allows one to (i) use a single trajectory of a complex between a receptor and a ligand; (ii) extract energies for the complex and all binding components by mapping their coordinates from the single trajectory; (iii) scan the sites of interest for the 'hot spots' in the receptor-ligand interface; and (iv) evaluate what the changes to the binding free energy would be upon modifications/mutations of the residues at the binding interface.

With the major advances in computer processing and clustering techniques, we are now able to perform molecular simulations of a large biomolecular system on a reasonable time scale. In this study, scFv anti-p17 was simulated based on molecular modeling of its homologue structure. The antibody-antigen complex models were generated using the flexible docking program incorporating binding activity data obtained from the peptide ELISA. The scFv anti-p17 structure with its epitopes at the C-terminal on the p17 fragment of HIV-1 and its natural mutant epitopes were analyzed in detail. In addition, the dynamic simulation method was applied to analyze the antibody-antigen interacting surface and to quantify the energetic nature of the complexes resulting from protein-ligand binding in water by applying the Molecular Mechanics-Poisson-Boltzmann Surface Area (MM-PBSA) proto-

col. The latter analysis can provide interesting information, such as electrostatic and van der Waals energies, solvation energies and entropic contributions at the binding interface. Our goal is to improve our understanding of the molecular basis of antigen recognition by scFv anti-p17.

2. Experimental

2.1. Computer assisted modeling

2.1.1. Homology modeling

The primary sequence of the scFv anti-p17 protein has previously been obtained by Tewari et al. (1998). The sequence of the light (VL) and heavy (VH) chain variable domains of scFv anti-p17 were compared with the primary sequences of all immunoglobulins deposited in the Protein Data Bank using the BLAST program (Altschul et al., 1997). The Complementary Determinant Region (CDR) definition of scFv anti-p17 variable domains was investigated using the Kabat method (Kabat et al., 1983).

The best match for the VH of scFv anti-p17 was the VH of idiotype-anti-idiotype Fab complex (pdb id:1iai), sharing 82% of sequence identity with the template, whereas the most homologous VL of scFv anti-p17 was the VL of the Fab fragment of a neutralizing antibody directed against an epitope of gp41 from HIV-1 (pdb id:1nld), sharing 96% of sequence identity with the template. These structures were used as templates for homology modeling of the 3D structure of scFv anti-p17 using the MODELLER program. The orientations of the VH and VL chains were generated by superposition using a crystal structure of the anti-DNA binding antibody (pdb id:2gki) as a scaffold template.

To minimize the steric clashes, the structure of scFv anti-p17 was subjected to energy minimization with 500 steps of steepest descent followed by 500 steps of conjugate gradient until the convergence criterion of 0.05 kcal/mol/Å was obtained, using the AMBER03 force field (Case et al., 2006). Structural validation of the scFv anti-p17 was checked using PROCHECK; more than 92% of the residues were in the most favored regions of the Ramachandran plot, and overall G-factors were inside the expected regions for structures with 2.0 Å resolutions. It is generally acknowledged that antigen binding occurs in a variety of ways, and thus leads to

Table 1PMF scores and residues on CDR loops of scFv at 4.5 Å from each of four peptide epitopes. The common amino acids are in boldface type.

Peptide names	Peptide sequences	PMF score	Amino Acid in 4.5 Å from peptide epitope	
	(kcal/	(kcal/mol)	Nonpolar hydrophobic	Polar hydrophilic
p17.1	¹²¹ DTGHSSQVSQNY ¹³²	-902.11	GLY33 (H1), TRP50 (H2) , MET100 (H3) , GLY226 (L3) , LEU229 (L3)	SER99 (H3), SER103 (H3), ASP163 (L1), ASP190 (L2), THR227 (L3)
p17.2	¹²¹ DTGHS <u>N</u> QVSQNY ¹³²	-899.18	TRP50 (H2) , MET100 (H3) , GLY161 (L1), LEU185 (L2), GLY226 (L3) , LEU229 (L3)	THR59 (H2), SER99 (H3), LYS101 (H3), SER103 (H3), SER162 (L1), ASP163 (L1), THR227 (L3), HIS228 (L3)
p17.3	¹²¹ DTGHSSQISQNY ¹³²	-882.65	TRP50 (H2), MET100 (H3), PHE167 (L1), GLY226 (L3), LEU229 (L3)	SER99 (H3), LYS101 (H3), ASP163 (L1), TYR184, ASP190 (L2), SER191, THR227 (L3), GLN231 (L3)
p17.4	¹²¹ DTGH <u>N</u> SQVSQNY ¹³²	-898.71	GLY33 (H1), MET100 (H3) , GLY226 (L3) , LEU229 (L3)	ASP31 (H1), TYR32 (H1), ASN52 (H2), SER99 (H3), LYS101 (H3), HIS228 (L3), GLN231 (L3)
p17.5	¹²¹ NTGHSSQVSQNY ¹³²	-843.51	TRP50 (H2), MET100 (H3), PHE167 (L1), LEU185 (L2), LEU229 (L3)	ASN35 (H1), SER99 (H3), LYS101 (H3), ASN169 (L1), TYR184, ASP190 (L2), SER191, THR227 (L3), HIS228 (L3)
p17.6	¹²¹ DTG <u>N</u> SSQVSQNY ¹³²	-846.12	GLY33 (H1), TRP50 (H2) , MET100 (H3) , LEU229 (L3)	SER99 (H3), LYS101 (H3) , LYS165 (L1), TYR184, SER191
p17.7	¹²¹ DTGHSSQ <u>A</u> SQNY ¹³²	-829.94	TRP50 (H2), MET100 (H3), PHE167 (L1), GLY226 (L3)	THR59 (H2), LYS101 (H3), LYS165 (L1), LYS188 (L2), THR227 (L3) , HIS228 (L3)
p17.8	¹²¹ DTGHS <u>K</u> QVSQNY ¹³²	-926.79	TRP50 (H2), MET100 (H3), PHE167 (L1), GLY226 (L3), LEU229 (L3)	THR59 (H2), SER99 (H3), LYS101 (H3), SER103 (H3), SER162 (L1), ASP163 (L1), THR227 (L3)
p17.9	¹²¹ DTG <u>NN</u> SQVSQNY ¹³²	-841.02	TRP50 (H2), MET100 (H3), PHE167 (L1), LEU185, LEU229 (L3)	THR59 (H2), SER99 (H3), LYS101 (H3), LYS165, ASN169 (L1), TYR184, ASP190 (L2), SER191, HIS228 (L3)

The underlined letters are the mutated residue in each sequence compared to the wild type.

a differing arrangement of antibody conformations. In scFv antip17, there are actually six unique hypervariable units. Each of the chains contains three of the six loops that form the binding groove. The hypervariable portions of the loops on the heavy chain are designated H1(31–35), H2(50–66) and H3(99–104) while those on the light chain are L1(154–169), L2(185–190), and L3(224–232) (Tewari et al., 1998). These regions are also known as complementary determining regions (CDRs), which have a higher binding affinity to the antigen.

2.1.2. Molecular docking

Nine peptides, an original HIV-1 epitope at the C-terminal (121DTGHSSQVSQNY132) on p17 and eight natural mutants (Table 1), were built partly based on a crystal structure from the Protein Databank (pdb id:1kj4). The initial structures of the nine modeled peptides were energy minimized (1000 steps of Adopted Basis Newton Raphson (ABNR)) using CHARMm force field with a RMS gradient of 0.01 kcal/(Å mol) in Discovery Studio 1.7. Structures of scFv anti-p17 (a homology model) complexed with the peptides were constructed using the docking procedure in the BioMedCaChe 2.0 (Fujitsu, Inc.) program, in which the CDR loops (L1-L3 and H1–H3) were defined as the potential binding sites. Both the peptides and the binding sites were set to be flexible during the docking simulation. Each of the docking complexes were energetically evaluated based on the potential of mean force (PMF) that describes the potential energies involving bond stretching, angle bending, torsional, and non-bonded interactions such as Amber van der Waals and hydrogen bond interactions of molecules (Muegge and Martin, 1999). The PMF scores of each peptide were evaluated by a genetic algorithm with a population size of 50, crossover rate of 0.80. elitism of 5, mutation rate of 0.2, and the maximum cycle generation was set to be 40,000. The size of the grid box was $30 \times 30 \times 30$ Å. Finally, the complex structures were analyzed and the interaction energy between the peptides and antibody was calculated.

2.1.3. Molecular dynamics (MD) simulations and binding free energy calculation

MD simulations were carried out at the molecular mechanics level using the AMBER03 force field as implemented in the AMBER9 suite of programs (Case et al., 2005). Structures of antibody-peptide were solvated in a cubic box of TIP3P water extending at least 10 Å in each direction from the solute, and the cut-off distance was kept to 12 Å to compute the nonbonded interactions. All simulations were performed under periodic boundary conditions (Weber et al., 2000), and long-range electrostatics were treated by using the particle-mesh-Ewald method (Darden et al., 1993; Essmann et al., 1995). The time step was set to 1 fs and the trajectory was recorded every 0.1 ps.

Prior to MD simulations, the systems were relaxed by a series of steepest descent (SD) and conjugated gradient (CG) minimizations. The 2-ns MD simulations were performed based on each of the minimized systems by gradually heating over 60 ps from 0 to 310 K with the protein atoms fixed using a force constant of $5 \, \text{kcal/mol/Å}^2$. Then, a 200 ps pressure-constant period (NPT) was applied to obtain an equilibrated density of the constrained protein atoms. The following step was a 40 ps-volume-constant period (NVT) at a force constant of 2.5 kcal/mol/Ų followed by 100 ps dynamics at a force constant of $1.25 \, \text{kcal/mol/Å}^2$. Finally, a $1.6 \, \text{ns}$ unrestrained MD simulation (no force applied on any protein atoms) was performed for each fully flexible system in the NVT ensemble at a constant temperature of $310 \, \text{K}$. A total of $500 \, \text{snapshots}$ were collected at 1 psintervals from the last $500 \, \text{ps}$ of MD for binding free energy analysis.

Based on the selected MD snapshots, the binding free energy for each antibody-peptide system could be estimated using MM-PBSA (Molecular Mechanics Poisson-Boltzmann Surface Area) (Kollman et al., 2000) and MM-GBSA (Molecular Mechanics Generalized

Born Solvent Area) (Chong et al., 1999). The binding free energies ($\Delta G_{\text{binding}}$) were determined from the free energies of the complex, protein and peptide according to the equation:

$$\Delta G_{\text{binding}} = \Delta G_{\text{water}}(\text{complex}) - [\Delta G_{\text{water}}(\text{protein}) + \Delta G_{\text{water}}(\text{peptide})]$$

The binding free energies for each species in turn were estimated from the absolute molecular mechanical energies ($E_{\rm MM}$), the solvation free energies ($G_{\rm PB/GB} + G_{\rm nonpolar}$) and the vibration, rotation and translation entropies. Each of these terms was calculated as follows:

$$\Delta G_{\text{water}} = E_{\text{MM}} + \Delta G_{\text{solvation}} - T\Delta S$$
;

 $G_{\text{solvation}} = G_{\text{solvation-electrostatic}} + G_{\text{nonpolar}};$

 $E_{\text{MM}} = E_{\text{internal}} + E_{\text{electrostatic}} + E_{\text{vdW}};$

$$E_{\text{internal}} = E_{\text{bond}} + E_{\text{angle}} - E_{\text{torsion}}$$

where the internal energy $E_{\rm internal}$ has three contributions: $E_{\rm bond}$, $E_{\rm angle}$, and $E_{\rm torsion}$, which represent the strain energy in bonds, angles and torsion angles caused by their deviation from the equilibrium values; $E_{\rm electrostatic}$ and $E_{\rm vdW}$ are the electrostatic and van der Waals interaction energies, respectively; $-T\Delta S$ is the change of conformational entropy upon peptide binding, which is not considered here because of its high computational demand and relatively low accuracy of prediction (Hou et al., 2002). All energies are averaged along the MD trajectories.

 $E_{\rm MM}$ was determined with the *sander* module of the AMBER suite with an infinite cut-off for all interactions. For the MM-PBSA calculations, $\Delta G_{\rm PB}$ was calculated with a built-in module, the *pbsa* program in AMBER9 which solves the Poisson–Boltzmann equation. The grid size for the PB calculations was 0.5 Å. In the MM-GBSA calculations, $\Delta G_{\rm GB}$ was calculated using the GB model with the parameters developed by Tsui and Case (2000). The values of the interior and exterior dielectric constants were set to 1 and 80, respectively. $\Delta G_{\rm np}$ was estimated based on the solvent accessible surface area (SASA) as $\Delta G_{\rm np} = 0.0072 \times {\rm SASA}$, using the *molsurf* program (Kabat et al., 1983) and (Case et al., 2006). The scFv anti-p17/peptide interaction energy profiles were generated by decomposing the total binding free energies into residue-residue interaction pairs by the MM-GBSA decomposition process in the *mm_pbsa* program of AMBER9 (Gohlke et al., 2003; Hou et al., 2008).

2.2. Affinity determination

2.2.1. Vector construction

A vector for expressing scFv that specifically binds to the Cterminal epitope (121 DTGHSSQVSQNY132) of the p17 fragment of HIV (scFv anti-p17) was constructed. Briefly, to generate the gene encoding scFv anti-p17 as described previously (Tewari et al., 1998), total RNA was extracted from hybridoma cells, MH-VM33C9/ATCC HB8975, using an RNeasy Mini kit (Qiagen, Hilden, Germany) and the first-strand cDNA was synthesized using a Transcriptor High Fidelity cDNA synthesis kit (Roch, Mannheim, Germany). The resulting cDNA was further amplified for the VH and VL fragments using specific primers, and the two fragments were linked together using Fw VHP17 and Rev VLP17 primers by overlapping PCR, which resulted in the completed fragment encoding scFv anti-p17. The fragment was treated with Sfil restriction enzyme and cloned into Sfil-treated pComb3X phagemid vector (a gift from Dr. C.F. Barbas, Scripps Research Institute, USA) resulting in the pComb3X-scFvp17 vector. The sequence of scFv anti-p17 was analyzed by standard sequencing methods (1st Base, Singapore).

The pComb3X-scFvp17 vector was subsequently transformed into the non-suppressor *Escherichia coli* strain HB2151.

The primers used for the amplification reactions were as follows: (1) Fw VHP17 (5'-ATATGCTAGCGGCCCAGGCGCCCAGATC-CAGTTGGTGCAGT-3'), (2) Rev VHP17 (5'-CGACCCTCCACCGCG-GACCCGCCACCTCCAGACCCTCCGCCACCTGCA GAGACAGTGACC-AGAGTCCC-3') for V_H fragment generation, (3) Fw VLP17 (5'-GGGTCCGGCGGTGGAGGGTCGGATGTTGTGATGACCCGACTCCA-3') and 4) Rev VLP17 (5'-TATAAGCTTTCATTAAGCGTAGTCCGGAACGT-CGTACGGGTACTGGCCGCCCCT GCCTTTGATTTCCAGCTTGGTACCTCC-3') for V_L fragment generation.

2.2.2. Preparation of soluble scFv anti-p17

The soluble scFv anti-p17 was produced by expressing pComb3X-scFvp17 vector in the non-suppressor E. coli strain HB2151. The bacterial cells harboring the vector were grown in 10 ml of Terrific broth (1.2% (w/v)) tryptone, 2.4% (w/v) yeast extract, 0.4% [w/v] glycerol, 17 mM KH₂PO₄, 72 mM K₂HPO₄) containing ampicillin (100 μg/ml) at 37 °C for 18 h with shaking. One hundred microliters of precultured bacteria were inoculated in 100 ml of the same medium containing 1% (w/v) glucose and ampicillin (100 μg/ml), with shaking continued at 37 °C until an optical density (OD) of 1.5 at 600 nm was reached. To induce the protein expression, IPTG was added to the culture at a final concentration of 1 mM. After induction, the bacteria were grown at 25 °C for 20 h. The culture supernatant containing extracellular soluble scFv anti-p17 was collected by centrifugation at $5000 \times g$ for 30 min at 4 °C. Protein was precipitated with saturated (NH₄)₂SO₄ in an ice bath and concentrated with Amicon Ultra centrifugal filter units (Millipore, Cork, Ireland). Finally, the concentrated protein was reconstituted with 1.5 ml of 0.15 M PBS, pH 7.2. The concentrated protein was separated in 12% SDS-PAGE under reducing conditions, and transferred to a nitrocellulose membrane (GE Healthcare, Buckinghamshire, UK). The blotted membrane was blocked with 5% skimmed-milk in PBS for 1 h at room temperature (RT) with shaking and then treated with anti-HA antibody (Sigma-Aldrich, St. Louis, MO). After incubation, the membrane was washed 5 times with washing buffer (0.05% Tween-20 in PBS) and peroxidase-conjugated goat antimouse immunoglobulin antibodies were added to the membranes. The peroxidase reaction was visualized using a SuperSignal West Pico Substrate (Pierce, Rockford, USA).

2.2.3. Evaluation of the binding activity of scFv anti-p17 by ELISA

To evaluate the binding activity of scFv anti-p17 with mutant peptides, four peptides were synthesized (GenScript, Piscataway, New Jersey, USA) and tested with the scFv protein using a standard ELISA procedure. Peptide p17.1 represented the wild-type epitope while another peptide represented the mutant peptides. The amino acid sequences of all synthetic peptides are shown in Table 1. Briefly, $100 \mu l$ of $50 \mu g/ml$ of each peptide in coating buffer (0.1 M NaHCO₃, pH 8.6) were added to microtiter plates (NUNC, Roskilde, Denmark) and incubated overnight at 4°C. The coated wells were then blocked with 200 µl of blocking buffer (2% BSA in TBS) for 1 h at RT. The wells were washed five times with washing buffer (0.05% Tween-20 in TBS). 100 µl of 200 µg/ml of scFv anti-p17 protein in blocking buffer were added to each well and incubated for 1 h at RT. After incubation, the excess antibody was eliminated by washing. Subsequently, the wells were incubated for 1 h at RT with 100 µl of HRP-conjugated goat anti-mouse IgS antibody (KPL, Maryland, USA) diluted 1/3000 in blocking solution. Wells were then washed again prior to adding 100 µl of 3,3′,5,5′tetramethyl-benzidine (TMB) substrate. The optical densities (OD) at 450 nm were measured by an ELISA plate reader (TECAN, Austria) after adding 100 µl of 1 N HCl.

To assess the binding affinity between scFv anti-p17 and mutant peptides, a peptide competitive ELISA was performed. The same

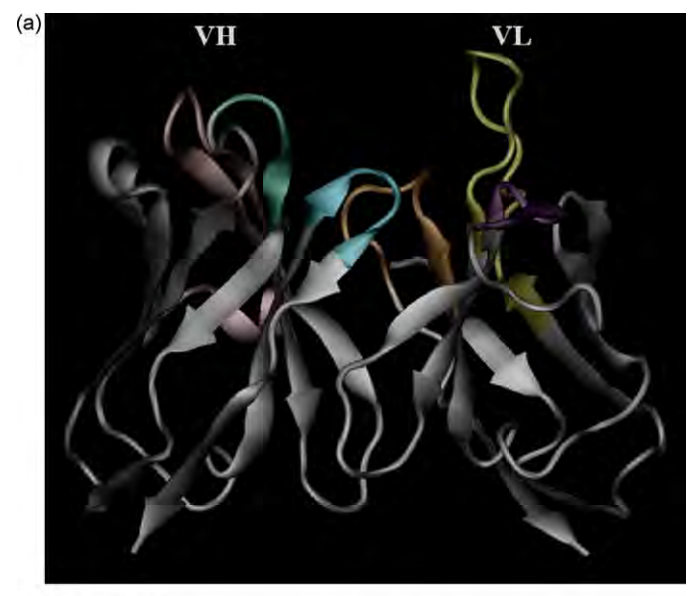
procedure was followed as described for the peptide ELISA; the scFv protein was mixed with $100 \, \text{ng/ml}$ of each mutant peptide and incubated for 1 h at RT. $100 \, \mu$ l of the mixture were applied into individual peptide p17.1 pre-coated wells and incubated for 1 h at RT. After washing the wells, the bound scFv anti-p17 was monitored by adding $100 \, \mu$ l of HRP-conjugated goat anti-mouse IgS antibody. Wells were then washed again and $100 \, \mu$ l of TMB substrate were subsequently added for 45 min. The enzymatic reaction was stopped by adding $100 \, \mu$ l of 1N HCl. The OD at 450 nm was measured by an ELISA plate reader. The OD values were converted to percentage inhibition values (PI) by using the following formula:

 $PI = 100 - \left(\left(\frac{B}{B_0} \right) \times 100 \right) B$ and B_0 are the OD values of scFv with peptide inhibitor and without peptide inhibitor respectively.

3. Discussion

3.1. Homology modeling of scFv and complex model

We selected VH and VL fragments of anti-p17 antibody from hybridoma cells MH-VM33C9/ATCC HB8975 for analysis. We had also prepared recombinant scFv anti-p17 by cloning the gene encoding VH and VL into a prokaryotic expression vector. For the homology modeling, the scFv antibody with the peptide epi-



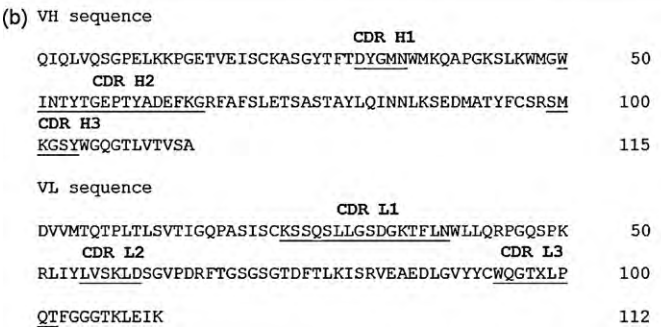


Fig. 1. Molecular models of scFv anti-p17. (a) 3D structural model for scFv anti-p17. VH and VL domains are colored *white.* The hypervariable binding loops are colored *green* (H1), *pink* (H2), *cyan* (H3), *yellow* (L1), *purple* (L2), and *orange* (L3). (b) Amino acid sequences of the hypervariable binding VH (1-114) and VL (131-241) domains of scFv anti-p17 and an artificial linker shown in bold (GGGGS)₃; the loops in the heavy chain (CDRH1: 31-35, CDRH2: 50-66, and CDRH3: 99-104), and the loops in the light chain (CDRL1: 154-169, CDRL2: 185-190, and CDRL3: 224-232) of the scFv antibody. (For interpretation of the references to color in this figure legend, the reader is referred to the web version of the article.).

Table 2Relationship between the binding activities from competitive ELISA and those from MM-PBSA methodology at 310 K.

Method	Contribution	Peptide Names				CD147
		p17.1	p17.3	p17.7	p17.8	
MM	Δ(L(-227.32	-174.34	-169.29	-91.34	
	ΔVDW	-72.28	-55.46	-48.01	-68.95	
	ΔGAS	-299.60	-229.81	-217.30	-160.29	
PBSA	$\Delta ext{PB}_{ ext{SUL}}$	-11.02	-9.73	-8.54	-10.56	
	ΔPB_{CAL}	280.63	230.71	217.07	144.47	
	ΔPB_{SOL}	269.61	220.99	208.53	133.91	
	ΔPB_{ELE}	53.31	56.37	47.78	53.13	
	ΔPB_{TOT}	-29.98	-8.82	-8.77	-26.38	
GBSA	ΔGB_SUL	-11.02	-9.73	-8.54	-10.56	
	ΔGB_CAL	273.07	220.02	207.41	136.89	
	ΔGB_SOL	262.05	210.29	198.87	126.33	
	ΔGB_{ELE}	45.75	45.68	38.12	45.55	
	ΔGB_TOT	-37.55	-19.52	-18.43	-33.97	
	Experimental value ^a	75.94	55.25	44.60	79.46	7.94

ELE, electrostatic interactions; VDW, van der Waals interactions between the fragments; GAS, addition ELE + VDW + INT being the binding enthalpic contributions in vacuo; PB_{SUR} , nonpolar contribution to solvation; PB_{CAL} , polar contribution of solvation; PB_{SUR} + PB_{CAL} ; PB_{ELE} , PB_{EAL} + ELE addition; PB_{TOT} , total binding free energy calculated by the MM-PBSA method.

tope was assembled and modeled based on a homology modeling approach. The three dimensional structure and the amino acid sequence of scFv anti-p17 are shown in Fig. 1. The models of scFv, nine peptide epitopes, and the scFv-peptide complexes were generated separately. The sequences of mutated peptides that were obtained from the GenBank database comprised the following positions: the single mutation of S126N, V128I, S125N D121N, H124N, V128A, S126K, and the double mutation of H124N and S125N. The sequences of all peptide epitopes that were initially positioned outside the binding region were docked against scFv in the same manner. The PMF scores (Table 1) of the complex structures were calculated with the BioMedCaChe 2.0 (Fujitsu, Inc.) program, where flexible peptide epitopes were docked into flexible side chain proteins. The peptide epitopes and the side chains of the amino acids of the CDR domains were kept flexible during the docking simulation. The PMF scores were in the range of -829.939 to -926.793 kcal/mol. The peptides bound in two orientations, where the N-terminal (p17.1, p17.2, p17.4-p17.6, and p17.8) and the C-terminal (p17.3, p17.7, and p17.9) of peptide sequences were directed toward the binding pocket. All interactions of the optimum docking structures reflected the negative binding energies in all models, indicating favorable binding in all complexes. Less favorable binding of peptide 17.3 and p17.9 to scFv was due to their inverted binding of the N-terminal to the outside of the binding pocket. The C-terminal sequences of p17.3 and p17.9 had better fits in the binding pocket. A similar binding pattern as for the substrate with the N-terminal sequence towards the inside of the pocket was also observed, but had higher binding energy scores. Interestingly, we found that mutation of a particular epitope at S125K of peptide p17.8 caused the maximum enhancement of the binding energy. The interacting amino acids of scFv within 4.5 Å from an individual docked peptide are listed in Table 1. The common binding residues of scFv are composed of the combination of hydrophilic and hydrophobic amino acids: Trp50 (H2), Thr59 (H2), Ser99 (H3), Met100 (H3), Lys101 (H3), Ser103 (H3), Asp163 (L1), Phe167 (L1) Asp190 (L2), Gly226 (L3), Thr227 (L3), His228 (L3), and Leu229 (L3), as indicated in boldface type.

3.2. Comparison of calculated binding free energy with experimental data

The DNA encoding scFv fragment of anti-p17 was successfully generated and cloned into a pComb3X phagemid vector,

resulting in the pComb3X-scFvp17 vector. This vector was subsequently transformed in non-suppressor *E. coli* (HB2151) for soluble expression of scFv anti-p17. The bacterial cells harboring pComb3X-scFvp17 vector were cultured and induced with 1 mM IPTG. The soluble protein in the culture supernatant was precipitated by ammonium precipitation and concentrated with an Amicon Ultra centrifuge filter. The scFv anti-p17 was expressed in its soluble form by induction, secreted into culture supernatant and revealed by western immunoblotting. A band with a molecular weight of approximately 30 kDa, corresponding to the molecular size of scFv, was detected in the concentrated protein (data not shown).

In order to investigate protein binding efficiency, peptide ELISA was employed to demonstrate the binding activity of scFv anti-p17 to its target peptide (p17.1), and the chosen mutant peptides (p17.3, p17.7 and p17.8) (Fig. 2). Positive signals were observed in all peptide coated wells, indicating that this recombinant scFv could bind to all mutant peptides. Peptide p17.8 gave the highest signal followed by p17.1, p17.3 and p17.7, respectively. All soluble mutant peptides were able to inhibit the binding between the scFv and immobilized p17.1 peptide (Table 2), as revealed by the percentage inhibition value (Pl), but the CD147 peptide had no significant inhibitory effect. Peptides p17.1 and p17.8 exhibited the highest

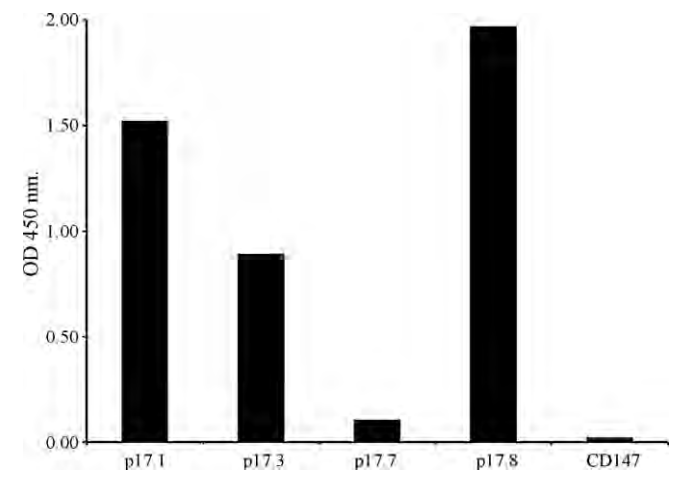


Fig. 2. The binding activity of soluble scFv anti-p17 from peptide ELISA.

a Competitive ELISA: PI (%)

inhibitory effects compared to the other two peptides, p17.3 and p17.7, at the same concentration.

Comparison of experimental activities with the results derived from MM-PBSA and MM-GBSA calculations suggested that the experimental value for MM-PBSA had a nearby correlation $(r^2 = 0.88)$ with the calculated binding free energy of MM-GBSA $(r^2 = 0.90)$, as shown in Table 2. Initially, favorable configurations for forming a scFv anti-p17-antigen complex system were built by molecular docking. The binding structures of the ligand to its receptor were analyzed based on the energy of the ligand or receptor. From the PMF scores, we selected four peptide epitopes consisting of one wild-type peptide (p17.1) and three mutated peptides (p17.3, p17.7, and p17.8) for further investigation by MDs and peptide ELISA. Peptide p17.7 had the lowest score and p17.8 had the highest score, whereas p17.3 had very similar score to that of the wild-type peptide. To understand the binding interaction in water, the binding free energies of those complexes were simulated by molecular dynamics simulations (MDs), and the Molecular Mechanics Poisson-Boltzmann Surface Area methodology was applied to calculate the binding free energy of all residues of the complexes. Table 2 lists the terms that contributed the calculation of binding free energy for the selected complex. The value of PB_{TOT} was used to compare the simulation with the experimental results. The more negative the value, the more favorable the binding. The binding energies identified by the MM-PBSA protocol were ranked as follows: peptide p17.1 < p17.8 < p17.3 < p17.7 with the values of -29.98, -26.38, -8.82, -8.77, and kcal/mol, respectively. The results were consistent with PMF scores from molecular docking data, which divided the mutants into two groups of high and low activities. The binding free energy indicated highly favorable binding of scFv with peptides p17.1 and p17.8, about 18 kcal/mol more negative than p17.3. Consequently, we identified the p17.3, p17.4, p17.5, p17.6, p17.7 and p17.9 as the low affinity binding peptides, whereas the p17.1, p17.2, and p17.8 were identified as the high affinity binding peptides with our scFv.

The major contributions to the binding free energy arise from the electrostatic energy, as calculated by the molecular mechanic (MM) force field (ELE); from the electrostatic contribution to the solvation free energy, as calculated by PB (PB_{CAL}); and van der Waals contribution from MM (VDW). For the four binding peptides, both van der Waals and electrostatic energies were quite varied among the low and high activities groups, indicating that both terms are factors determining the binding activity. Peptide p17.8 had a somewhat lower electrostatic contribution ($-91.34\,\mathrm{kcal/mol}$). Among the other sequences, however, the combination with VDW and the sum of nonpolar and polar contributions to solvation (PB_{SOL}) resulted in a total negative binding free energy. This supported a favorable scFv–peptide complex in pure water. The result does not equal the real binding free energy since we did not estimate the entropy contribution to binding in this study.

3.3. Decomposition of energy on the amino acid residues in CRD loops and specific contact upon binding

The interpretation of macroscopic data in terms of microscopic interactions of scFv with a peptide binding sequence can be done by decomposing the calculated binding free energies as a sum of components that correspond to the contributions of different energy terms or different parts of the system. Therefore, important residues of anti-HIV p17 scFv will show strong interactions in association with its antigen. To gain further insight into the key residue interactions, the overall agreement between the calculated and experimental values for the ligands obtained by the MM-PBSA approach allows us to be optimistic of the results when estimating protein-ligand interactions. Table 3 and Fig. 3 illustrate the results of this analysis, plotting the relative decomposed energies versus common amino acids on the CDR loops of scFv anti-p17 and each of four peptide epitopes. All amino acids in the scFv sequences were found to exhibit positive or negative influences on binding to the substrate molecules. Several residues of the wild-type

Table 3Common interacting residues found among the natural peptide sequences in the docking study.

Residue	Loop	Decomposed er	ergy (kcal/mol)		
		p17.1	p17.3	p17.7	p17.8
ASP31	H1	0.26	0.35 (0.09)	0.28 (0.02)	0.24 (-0.02)
TYR32	H1	0.04	-0.05(-0.09)	0.03 (-0.01)	0.01(-0.03)
GLY33	H1	0.01	-0.08(-0.09)	-0.02(-0.03)	-0.11(-0.12)
ASN35	H1	0.14	-0.14(-0.28)	-0.09(-0.23)	-0.34(-0.48)
TRP50	H2	-1.73	-3.76 (-2.03)	-2.05 (-0.32)	-4.90 (-3.17)
ASN52	H2	0.03	-0.25(-0.28)	-0.05(-0.08)	-0.84(-0.87)
THR59	H2	0.04	-0.56(-0.60)	-0.57(-0.61)	-0.61(-0.65)
SER99	Н3	-0.18	-0.17 (0.01)	0.09 (0.27)	-0.62(-0.44)
MET100	Н3	-3.80	-1.02 (2.78)	-3.27 (0.53)	-3.59(0.21)
LYS101	Н3	-2.91	-0.56 (2.35)	-1.10(1.81)	4.24 (7.15)
SER103	Н3	-0.11	0.06 (0.17)	0.03 (0.14)	-1.31(-1.2)
GLY161	L1	0.01	-0.01 (-0.02)	-0.07 (-0.08)	-0.02(-0.03)
SER162	L1	0.11	0.03(-0.08)	-0.07 (-0.18)	0.20 (0.09)
ASP163	L1	0.40	0.28(-0.12)	0.39 (-0.01)	-0.27(-0.67)
LYS165	L1	-0.50	-0.16 (0.34)	-0.26(0.24)	0.46 (0.96)
PHE167	L1	-2.26	-3.14(-0.88)	-1.59(0.67)	-4.87 (-2.61)
ASN169	L1	-2.66	0.00 (2.66)	0.09 (2.75)	-0.22(2.44)
TYR184	-	-2.41	-2.06 (0.35)	-1.44(0.97)	-1.79(0.62)
LEU185	L2	-0.07	-1.24(-1.17)	-1.13(-1.06)	-2.06(-1.99)
LYS188	L2	-0.14	-0.07 (0.07)	-0.30(-0.16)	0.02 (0.16)
ASP190	L2	0.26	-0.37(-0.63)	0.20(-0.06)	-0.10(-0.36)
SER191	_	-0.03	0.00 (0.03)	0.00 (0.03)	0.01 (0.04)
GLY226	L3	-0.18	-0.57(-0.39)	-0.07 (0.11)	-1.29(-1.11)
THR227	L3	-0.30	-0.32(-0.02)	-1.85(-1.55)	-2.90(-2.6)
HIS228	L3	-3.93	0.14 (4.07)	-0.42 (3.51)	-1.12 (2.81)
LEU229	L3	-4.53	-0.70 (3.83)	-1.15 (3.38)	-2.07 (2.46)
GLN231	L3	-0.52	-2.75 (-2.23)	-1.20(-0.68)	0.14 (0.66)

Relative energy to p17.1 is in parenthesis. The amino acids which have significant contribution with the absolute relative energy larger than 2 Kcal/mol are indicated in bold letters.

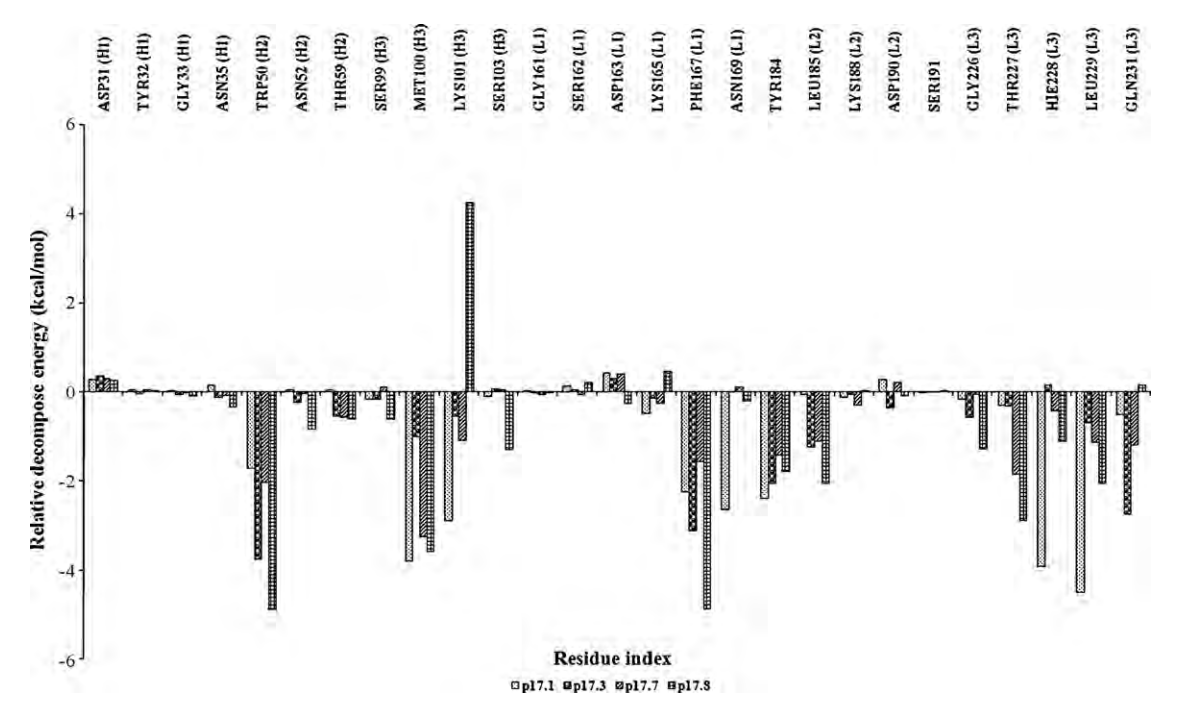


Fig. 3. List of the decomposed energies of the common amino acids in CDR loops of scFv.

p17.1 (Trp50, Met100, Lys101, Phe167, Asn169, Thr227, His228, Leu229 and Gln231) were verified to have significant effective contributions with the absolute relative energy larger than 2 kcal/mol for the stabilization energy as highlighted in Table 3. There was strong interdependence of the effects of the individual residues in the epitope sequences. Among three mutated peptides, poor binding and/or weak interaction, with relative energy above 2 kcal/mol in comparison with wild-type p17.1, was obtained from Met100, Lys101, Asn169, His228, and Leu229 of scFv. Better binding was indicated by the lower decomposed energy with the absolute relative energy below 2 kcal/mol. The difference between high and low affinity binding depends on the interaction of each sequence with the amino acids in the CDR region of scFV. The Trp50 of scFv exhibited more binding interaction with both p17.3 (V128I) and

p17.8 (S125K) than the wild-type peptide. Sequence p17.1 shows the strongest binding among all sequences, with Met100, Lys101, Asn169, His228, and Leu229, whereas sequence p17.8 exhibited the strongest binding with different amino acids such as Try50, Phe167 and Thr227. This is compared to only one strong binding interaction among other sequences with Gln231 as observed in sequence 17.3 and no strong binding interaction with 17.7 resulted in a low binding affinity. These interactions make a significant contribution to the overall binding. As mentioned in the previous section, the decomposed energies of some residues in scFv have positive values with peptide epitopes. A particularly strong case, with decomposed energy of 4.24 kcal/mol, was observed for p17.8 binding with Lys101. However, the sum of all those energy terms resulted in favorable binding. Overall we found that Met100(H3), Lys101(H3),

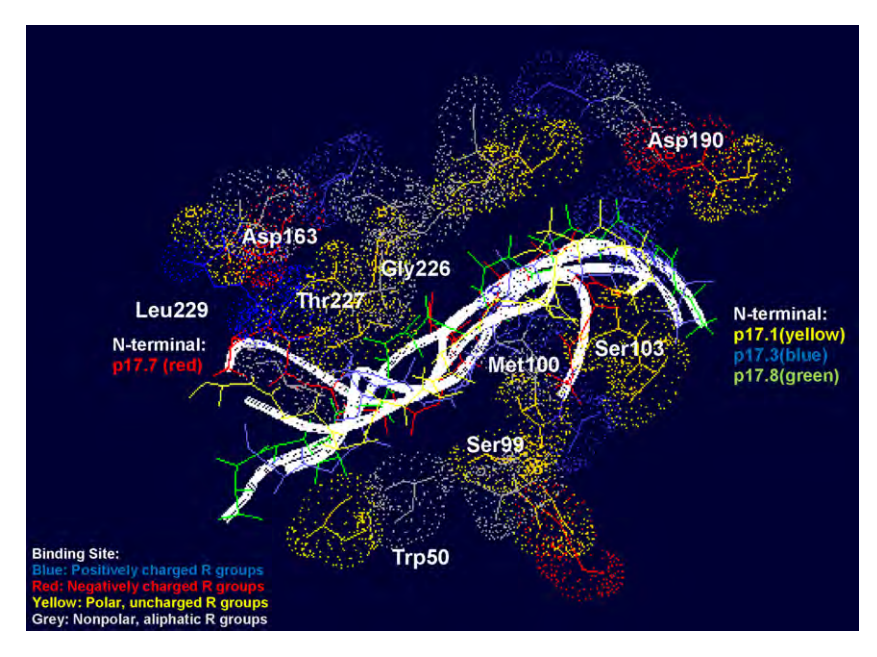


Fig. 4. The residues interaction of the final MD complex structures between scFv anti-p17 and four peptide epitopes.

Asn169(L1), His228(L3), and Leu229(L3) exhibited strong interactions with peptide p.17.1. From the MD structure in the last 500 ps, we also observed strong hydrogen bonding interactions with more than 95% occupancy for R181 in L2 with D121 and Q127 of the substrate sequence.

Further analysis of the final MD complex structures is shown in Fig. 4. As expected, p17.3 bound in different patterns among other sequences since its C-terminal has binding sites oriented toward the inside of the pocket instead of the N-terminal. Our study using pairwise decomposition of residue interaction energies has allowed us to gain insight into the interactions between anti-p17 single chain Fv with its peptide epitopes for HIV-1.

4. Conclusions

Computer models were combined with laboratory experiments for the efficient determination and the identification of the most important residues for scFv in binding with natural peptide substrates, ScFv anti-p17 was built from its X-ray structure homologue, and the complexes of scFv anti-p17 with its natural epitope were generated using a flexible docking method. The efficacy of combining the scFv antibody with peptide epitopes according to the potential mean force scoring correlated well with peptide ELISA results. Molecular dynamics simulations were performed on selected peptides to evaluate their interaction in water. Overall structural changes of binding peptides in response to enzyme binding in water were investigated by the root mean square displacement. Poorly binding peptides exhibit a larger root mean square displacement than do tightly binding peptides. MM-PBSA and pairwise decomposition energies were calculated from postanalysis of molecular dynamics structures. The calculated binding free energies concurred well with experimentally determined high binding affinity (decomposed energy >2 kcal/mol) and low binding affinity of investigated peptides to anti-p17 scFv. Several amino acids, MET100, LYS101, ASN169, HIS228, and LEU229, in the complementary determining regions (CDRs) were defined for their major contribution to the binding efficiency of natural HIV epitope at the C-terminal on p17. This technique could be applied to elucidate the most important amino acids involved in the binding of scFv with its target molecules. Moreover, the identified amino acids can be modified for improving the binding activity.

Acknowledgements

The authors would like to express grateful acknowledgement the financial support from the Thailand Research Fund (TRF), the Research Chair Grant of National Sciences and Technology Development Agency (Thailand), the Center for Innovation in Chemistry (PERCH-CIC), Commission on Higher Education, Ministry of Education of Thailand, and the Computational Nanoscience Consortium (CNC), the National Nanotechnology Center (NANOTEC) and National Science and Technology Development Agency (NSTDA), Thailand for the access to Discovery Studio Version 1.7 program package. The authors would also like to thank Dr. Dale Taneyhill for proofreading the manuscript.

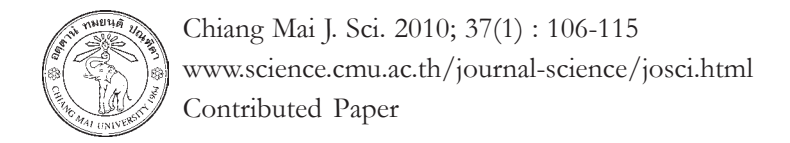
Contributors: SN, KK, CT contributed with experimental design, performance of all experiments, and writing of the manuscript. VSL and PT participated in all calculations and JJ assisted with the antibody modeling building. VSL, PN, SJ, and CT contributed with supervising and writing of the manuscript. All authors read and approved the final manuscript.

References

Altschul, S.F., Madden, T.L., Schäffer, A.A., Zhang, J., Zhang, Z., Miller, W., Lipman, D.J., 1997. Gapped BLAST and PSI-BLAST: a new generation of protein database search programs. Nucleic Acids Res. 25, 3389–3402.

- Arcangeli, C., Cantale, C., Galeffi, P., Rosato, V., 2008. Structure and dynamics of the anti-AMCV scFv(F8): effects of selected mutations on the antigen combining site. J. Struct. Biol. 164, 119–133.
- Bohm, H.J., 1998. Prediction of binding constants of protein-ligands: a fast method for the prioritization of hits obtained from de novo design or 3D database search programs. J. Comput. Aided Mol. Des. 12, 309–323.
- Brooks, B.R., Bruccoleri, R.E., Olafson, B.D., States, D.J., Swaminathan, S., Karplus, M., 1983. CHARMM: A program for macromolecular energy, minimization, and dynamics calculations. J. Comput. Chem. 4, 187–217.
- Bukrinskaya, A.G., 2004. HIV-1 assembly and maturation. Arch. Virol. 149, 1067–1082.
- Case, D.A., Cheatham III, T.E., Darden, T., Gohlke, H., Luo, R., Merz, J.K.M., Onufriev, A., Simmerling, C., Wang, B., Woods, R.J., 2005. The Amber biomolecular simulation programs. J. Comput. Chem. 26, 1668–1688.
- Case, D.A., Darden, T.A., Cheatham III, T.E., Simmerling, C.L., Wang, J., Duke, R.E., Luo, R., Merz, K.M., Pearlman, D.A., Crowley, M., 2006. AMBER 9. University of California, San Francisco, CA.
- Chong, L.T., Duan, Y., Wang, L., Massova, I., Kollman, P.A., 1999. Molecular dynamics and free-energy calculations applied to affinity maturation in antibody 48G7. Proc. Natl. Acad. Sci. U.S.A. 96. 14330–14335.
- Darden, T., York, D., Pedersen, L., 1993. Particle mesh Ewald: an N log(N) method for Ewald sums in large systems. J. Chem. Phys. 98, 10089–10092.
- Depetris, M., Casalis, P., Kratje, R., Etcheverrigaray, M., Oggero, M., 2008. A scFv antibody fragment as a therapeutic candidate to neutralize a broad diversity of human IFN-alpha subtypes. J. Immunol. Methods 334, 104–113.
- Essmann, U., Perera, L., Berkowitz, M.L., Darden, T., Lee, H., Pedersen, L., 1995. A smooth particle mesh ewald potential. J. Chem. Phys. 103, 8577–8592.
- Ewing, T.J.A., Makino, S., Skillman, A.G., Kuntz, I.D., 2001. DOCK 4.0: Search strategies for automated molecular docking of flexible molecule database. J. Comput. Aided Mol. Des. 15, 411–428.
- Ganser-Pornillos, B.K., Yeager, M., Sundquist, W.I., 2008. The structural biology of HIV assembly. Curr. Opin. Struct. Biol. 18, 203–217.
- Gao, J., 1996. Hybrid quantum mechanical/molecular mechanical simulations: an alternative avenue to solvent effects in organic chemistry. Acc. Chem. Res. 29, 298–305
- Gohlke, H., Kiel, C., Case, D., 2003. Insights into protein-protein binding by binding free energy calculation and free energy decomposition for the Ras-Raf and Ras-RalGDS complexes. J. Mol. Biol. 330, 891–913.
- Hou, T., Guo, S., Xu, X., 2002. Predictions of binding of a diverse set of ligands to gelatinase-A by a combination of molecular dynamics and continuum solvent models. J. Phys. Chem. B 106, 5527–5535.
- Hou, T., Zhang, W., Case, D.A., Wang, W., 2008. Characterization of domain-peptide interaction interface: a case study on the amphiphysin-1 SH3 domain. J. Mol. Biol. 376, 1201-1214.
- Inui, H., Takehara, A., Doi, F., Nishi, K., Takai, M., Miyake, S., Ohkawa, H., 2009. A scFv antibody-based immunoaffinity chromatography column for clean-up of bisphenol A-contaminated water samples. J. Agric. Food. Chem. 57, 353–358.
- Jones, G., Willett, P., Glen, R.C., Leach, A.R., Taylor, R., 1997. Development and validation of a genetic algorithm for flexible docking. J. Mol. Biol. 267, 727–748.
- Jorgensen, W.L., 1996. BOSS 3. 6. Yale University, New Haven, CT.
- Kabat, E.A., Wu, T.T., Bilofsky, H., Reid-Milner, M., Perry, H., 1983. Sequences of Proteins of Immunological Interest. NIH Publications No. 369–847, Bethesda, MD
- Kollman, P.A., 1993. Free energy calculations: applications to chemical and biochemical phenomena. Chem. Rev. 93, 2395–2417.
- Kollman, P.A., Massova, I., Reyes, C., Kuhn, B., Huo, S., Chong, L., Lee, M., Lee, T., Duan, Y., Wang, W., Donini, O., Cieplak, P., Srinivasan, J., Case, D.A., Cheatham 3rd., T.E., 2000. Calculating structures and free energies of complex molecules: combining molecular mechanics and continuum models. Acc. Chem. Res. 33, 889–897.
- Krammer, A., Kirchhoff, P.D., Jiang, X., Venkatachalam, C.M., Waldman, M., 2005. LigScore: a novel scoring function for predicting binding affinities. J. Mol. Graph. Model. 23, 395–407.
- Leach, A.R., 1996. Molecular Modelling: Principles and Applications. Addison Wesley Longman Ltd., Singapore.
- Levy, R.M., Gallicchio, E., 1998. Computer simulations with explicit solvent: recent progress in the thermodynamic decomposition of free energies and in modeling electrostatic effects. Annu. Rev. Phys. Chem. 49, 531–567.
- Morris, G.M., Goodsell, D.S., Halliday, R., Huey, R., Hart, W.E., Belew, R.K., Olson, A.J., 1998. Automated docking using a Lamarckian genetic algorithm and an empirical binding free energy function. J. Comput. Chem. 19, 1639–1662.
- Muegge, I., Martin, Y.C., 1999. A general and fast scoring function for protein-ligand interactions: a simplified potential approach. J. Med. Chem. 42, 791–804.
- Park, S.G., Jung, Y.J., Lee, Y.Y., Yang, C.M., Kim, I.J., Chung, J.H., Kim, I.S., Lee, Y.J., Park, S.J., Lee, J.N., Seo, S.K., Park, Y.H., Choi, I.H., 2006. Improvement of neutralizing activity of human scFv antibodies against hepatitis B virus binding using CDR3 V(H) mutant library. Viral. Immunol. 19, 115–123.
- Pavoni, E., Flego, M., Dupuis, M.L., Barca, S., Petronzelli, F., Anastasi, A.M., D'Alessio, V., Pelliccia, A., Vaccaro, P., Monteriu, G., Ascione, A., De Santis, R., Felici, F., Cianfriglia, M., Minenkova, O., 2006. Selection, affinity maturation, and characterization of a human scFv antibody against CEA protein. BMC Cancer 6, 41.
- Pearlman, D.A., Case, D.A., Caldwell, J.W., Ross, W.R., Cheatham, T.E., Ferguson, D.M., Seibel, G.L., Singh, U.C., Weiner, P., Kollman, P.A., 1995. AMBER4.1 (UCSF). University of California, San Francisco, CA.
- Quintero-Hernandez, V., Juarez-Gonzalez, V.R., Ortiz-Leon, M., Sanchez, R., Possani, L.D., Becerril, B., 2007. The change of the scFv into the Fab format improves the

- stability and in vivo toxin neutralization capacity of recombinant antibodies. Mol. Immunol. $44,\,1307-1315.$
- Rarey, M., Kramer, B., Lengauer, T., Klebe, G., 1996. A fast flexible docking method using an incremental construction algorithm. J. Mol. Biol. 261, 470–489.
- Shen, Z., Yan, H., Zhang, Y., Mernaugh, R.L., Zeng, X., 2008. Engineering peptide linkers for scFv immunosensors. Anal. Chem. 80, 1910–1917.
- Smith, P.E., Pettitt, B.M., 1994. Modeling solvent in biomolecular systems. J. Phys. Chem. 98, 9700–9711.
- Stocks, M., 2005. Intrabodies as drug discovery tools and therapeutics. Curr. Opin. Chem. Biol. 9, 359–365.
- Tewari, D., Goldstein, S.L., Notkins, A.L., Zhou, P., 1998. cDNA encoding a single-chain antibody to HIV p17 with cytoplasmic or nuclear retention signals inhibits HIV-1 replication. J. Immunol. 161, 2642–2647.
- Tomasi, J., Persico, M., 1994. Molecular interactions in solution: an overview of methods based on continuous distributions of the solvent. Chem. Rev. 94, 2027–2094.
- Tsui, V., Case, D.A., 2000. Molecular dynamics simulations of nucleic acids with a generalized Born solvation model. J. Am. Chem. Soc. 122, 2489–2498.
- van Gunsteren, W.F., Luque, F.J., Timms, D., Torda, A.E., 1994. Molecular mechanics in biology: from structure to function, taking account of solvation. Annu. Rev. Biophys. Biomol. Struct. 23, 847.
- Wang, G.P., Qi, Z.H., Chen, F.P., 2008. Treatment of acute myeloid leukemia by directly targeting both leukemia stem cells and oncogenic molecule with specific scFv-immunolipoplexes as a deliverer. Med. Hypotheses 70, 122–127.
- Weber, W., Hünenberger, P., McCammon, J., 2000. Molecular dynamics simulations of a polyalanine octapeptide under Ewald boundary conditions: influence of artificial periodicity on peptide conformation. J. Phys. Chem. B 104, 3668–4575.



Theoretical Study of the *Bombyx mori* Silk Surface Functionalization: Quantum Mechanical Calculation of the Glycine-Alanine Unit Reacting with Fluorine and Molecular Dynamic Simulation of Wettability

Padungsee Khomhoi, Waleepan Sangprasert, Vannajan S. Lee, and Piyarat Nimmanpipug^{*}

Department of Chemistry and Center for Innovation in Chemistry, Faculty of Science, Chiang Mai University, Chiang Mai 50200, Thailand.

Received: 4 June 2009 Accepted: 22 July 2009

ABSTRACT

SF₆ plasma has been used to improve the hydrophobic properties of Thai Silk. In this study, possible reactions were investigated via a glycine-alanine (GA) model; the main component that dominates intermolecular interactions reflecting the physical properties of silk. Quantum mechanical (QM) calculations using density functional theory (DFT) and molecular dynamic (MD) simulations were utilized to investigate possible mechanisms for the interaction between GA, fluorine radicals (F*) and fluorine anions (F*). The hydrogen abstraction reactions of radicals are the lowest activation energy pathways and should be the most preferable pathway in the plasma treatment process. From the MD simulation, the interaction energies of water with the silk surface and irradiated surface were -4.65 and -2.63 kcal/(mole of water), respectively.

Keywords: Bombyx mori silk; plasma treatment; DFT; MD simulations.

1. INTRODUCTION

Plasma treatment is an environmental friendly technique for modifying the surface of a fiber in order to improve wettability, shrink resistance, interfacial adhesion, hydrophilicity and dyeing properties [1-5]. Low pressure plasma treatments have been proposed for modifying hydrophobic properties in order to adapt the latter to specific applications [6,7]. Treatment with sulphur hexafluoride plasma is one of the most successful approaches to chemical modification and hydrophobization of silk surfaces [8-10].

Experimentally, the hydrophobic-hydrophilic character and the wettability of a surface have been characterized macroscopically by the contact angle at the interfaces. The structure of the interface is analyzed in terms of density functions, radial distribution functions, and the orientation of the water molecules, potential drop, and hydrogen bonding characteristics. The amount of wetting depends on the energies (or surface tensions) of the interfaces involved such that the total energy is minimized [11-15].

^{*}Author for correspondence; e-mail address: npiyarat@chiangmai.ac.th

Silk fiber is a natural animal fiber. The size of the fibroin fiber is approximately 15-25 µm with a density between 1.33-1.35 g/cm³, and is mostly composed of glycine (44 %) and alanine (30 %). Thai silk, like Chinese silk, is obtained from Bombyx mori (B. mori) but differs somewhat in appearance [16,17]. Marsh et al. proposed a pseudo unit silk structure comprising an antiparallel β -pleated sheet structure of silk fibroin. In previous studies, B. mori silk modified by treatment with low temperature SF₆ plasma was found to have increased hydrophobic properties at the silk surface [8,9]. This result indicated that changes in functional groups of B. mori silk fibers may be detected from the creation of CF groups on the silk surface, which act to improve the hydrophobic properties of the silk [10,18].

In order to clarify the nature of the chemical modification of B. mori silk surfaces in the SF₆ plasma treatment process, a molecular model of B. mori silk and the fluorine atom after plasma treatment was investigated at a fundamental level. Quantum mechanical (QM) calculations were used in order to understand the mechanism of fluorine atoms in SF, plasma reacting with the silk surface. Density functional theory (DFT), which takes into account both exchange and correlation effects at relatively small computational costs, has been used to determine the changes in functional groups of B. mori silk fibers. In this study, QM calculations were used to find the transition structure and activation energy of silk reacting with SF, plasmas. In addition, silk surfaces were generated based on crystallographic data for MD simulations. In the latter case, the fluorinated surfaces were generated based on QM results. The hydrophobic natures of the surfaces were investigated by MD simulation of surface contact with water molecules.

2. THEORETICAL METHOD

QM calculation using the DFT method and MD simulations were used to investigate possible mechanisms, e.g. fluorine substitution and hydrogen abstraction, for the interaction between Glycine-Alanine (GA) and fluorine radicals (F*) and fluorine anions (F*).

2.1 The Reaction between Fluorine and Silk Surface

2.1.1 Quantum Mechanical (QM) Method

GA modelling according to the molecular conformation extracted from X-ray crystallographic data [19] was used to represent untreated B. mori silk surfaces (Figure 1). The geometries of all stationary points were fully optimized using BHandHLYP density functional theory with 6-31G(d) basis set using the Gaussian 03 Program Package (Revision C.02, Gaussian, Inc., Wallingford CT) [20, 21]. At the same level, frequency analysis was done for the nature of the stationary points and each transition state with one imaginary frequency. Four reaction mechanisms for both fluorine radicals (F) and fluorine anions (F) were proposed (Figure 2).

2.2 Molecular Dynamics Simulations of the Water-amorphous Silk Surface

Classical molecular dynamics simulations were performed to investigate the interaction of water with the surfaces of the un-irradiated and irradiated silk crystal structures. The initial amorphous model of un-irradiated silk was generated using an amorphous cell construction module, using the amber force field system. The system contained 10 molecules, each with 15 repeated sequences of glycine-alanine generated using Material Studio 4.2 software [22]. For the irradiated structure, hydrogens of the methyl group of the alanine unit were replaced with fluorine atoms. The amorphous model of the irradiated structure

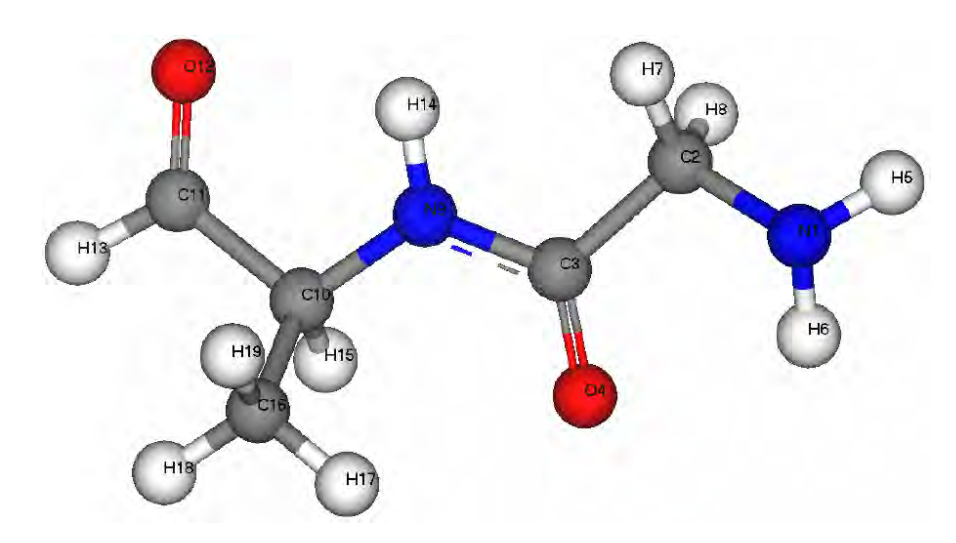


Figure 1. Structure of glycine-alanine (GA) model of *Bombyx mori* Silk studied by computational method.

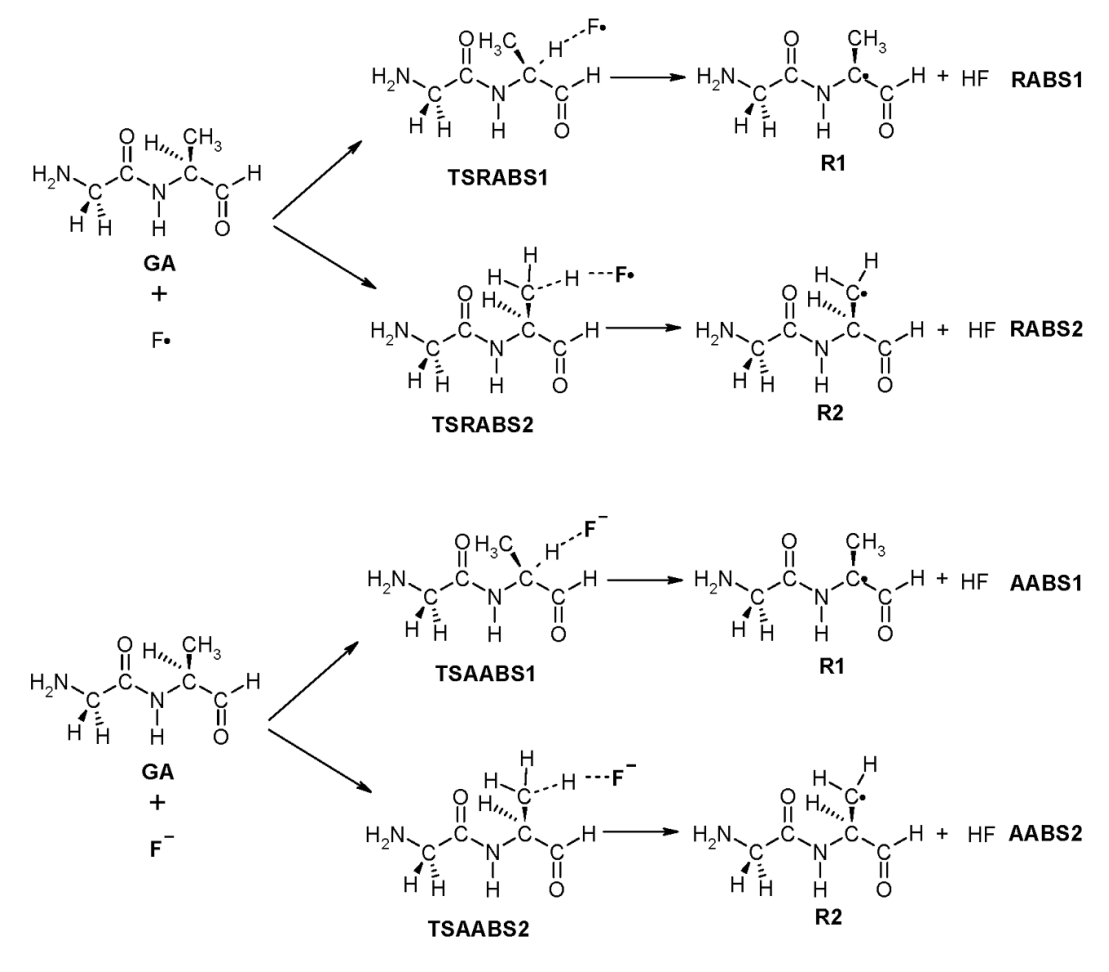


Figure 2. H-abstraction of fluorine radical and fluorine anion from SF₆ plasma reacting with the silk surface.

was then generated using the same procedure as described above. Energy minimization and molecular dynamics simulations at a fixed particle number N, constant ambient pressure P = 1 atm, and at temperatures 298 K were performed using the AMBER 9 simulation package [23] with the parm99 forcefield for 400 ps with a 1.0 fs timestep. Simulations are done employing the Berendsen scheme [24] and the particle-mesh Ewald method [25] was used for the periodic treatment of coulombic interactions. Both amorphous structures with the dimension about $19 \times 19 \times 70 \text{ Å}^3$ and approximate density of 1.23 g/cm³ were optimized. For modeling the water amorphous silk surface, the vacuum space was

half-filled with 401 water molecules and then placed in the simulation cell above the silk surface. The water-amorphous silk surface was minimized until 0.01 rms atom cut-off convergence was achieved. The minimized solvated model of the silk surface is shown in Figure 3. Afterward, NVT molecular dynamics was performed for 1.6 ns at 298 K with a 1.0 fs time step. Both structures were contained in a periodic box size of $55 \times 38 \times 71 \, \text{Å}^3$. The thickness of the water-amorphous silk model was about 18 Å with a 10 Å thickness of water from the silk surface in a 10 Å vacuum thickness. The trajectories were analyzed in detail.

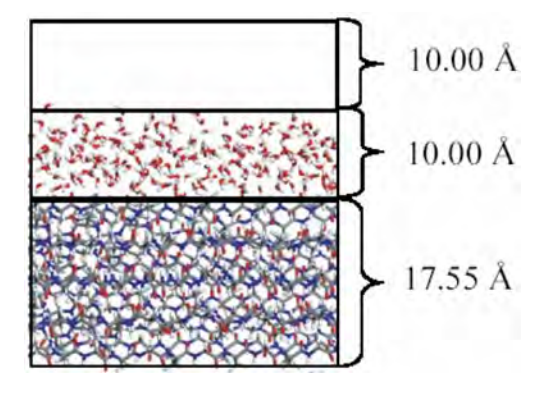


Figure 3. The minimized structure of water/silk and water/irradiated silk surface.

2.2 Interactions between Silk Surface and Fluorinated Silk Surface with Water

Molecular dynamic simulations were used to study the interaction of water with

the surfaces of the un-irradiated and irradiated silk crystal structure. For the irradiated structure, we used the structure with the lowest energy of fluorine interacting with silk from the quantum calculation and replaced one hydrogen with a fluorine atom in the

methyl group of the alanine unit in the silk crystal structure. Four hundred and one water molecules were introduced onto the irradiated and un-irradiated silk surfaces. The surface-water cell was minimized until a 0.01 rms atom cut-off convergence criterion was achieved. The minimized solvated model of the silk surface is shown in Figure 3. Afterward, NVT molecular dynamics was performed for 1.6 ns at 298 K with a 1.0 fs time step. Both

structures were contained in a periodic box of size $55 \times 38 \times 71 \text{ Å}^3$. The thickness of the silk model was 17.5 Å and was covered with water up to 10 Å from the silk surface in a vacuum of 10 Å.

3. RESULTS AND DISCUSSION

3.1 The Reaction between Energetic Fluorine and The Silk Surface 3.1.1 QM Method

The elementary reactions, the transition state structures and the activation energies were proposed and calculated for the reactions between the GA model and the fluorine radical/fluorine anion in the sulphur hexafluoride plasma. Energy profiles and the structures of species corresponding to the minima and transition states (TS) along the reaction coordinate.

Under the experimental conditions with low-pressure plasma, fluorine atoms are efficiently attached to the silk surface by SF₆

plasma treatment, most probably via a hydrogen abstraction [18]. Abstraction of a hydrogen atom on the silk surface can be accomplished by means of several ions and radicals formed within the plasma, as confirmed by the presence of radical species on silk surface after treatment. Then, the chemical bond between carbon radicals on the surface and fluorine radicals can be formed, as confirmed by the presence of CF-CF and CH2-CHF groups in the highresolution XPS spectra [10]. Several possible hydrogen abstraction mechanisms of Glycine-Alanine (GA) with fluorine radicals (F) and fluorine anions (F⁻) were proposed and calculated for the reactions between the GA model and the fluorine radical/fluorine anions in the sulphur hexafluoride plasma.

The transition states and the activation energies of the reactions are depicted in Figure 4 and Table 1. The energy of F[•] + GA and F⁻ + GA was set to be zero as a reference.

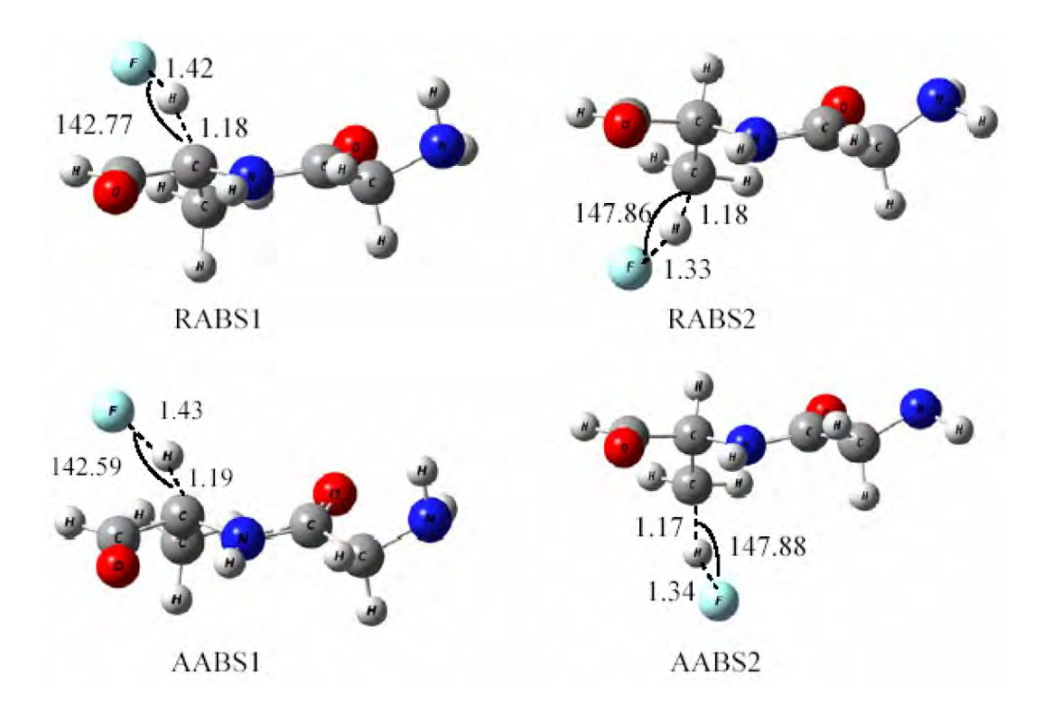


Figure 4. The transition state structures of surface interaction of fluorine radical and fluorine anion.

3.1.1 Hydrogen Abstraction Reaction for Fluorine Radicals

In the mechanism of the hydrogen abstraction from GA molecules by fluorine radicals, the transition state structures for the fluorine radical abstracts of the hydrogen atoms of GA molecules are shown in Figure 4. The length of the breaking C-H bond of TS_RABS1 is 1.18 Å while the C-H bond of the GA molecule is 1.091 Å long. The forming H-F bond is 1.42 Å long; this bond is 0.922 Å in HF itself. The F–H–C bond angle is 142.77 degrees. From TS_RABS2 structure, the length of the C-H bond that is being broken is 1.18 Å, while the other two C-H bonds are 1.085 Å long. The H-F distance is 1.33 Å long in the transition state. The F-H-C bond angle is 147.86 degrees.

3.1.2 Hydrogen Abstraction Reaction for Fluorine Anion

Regarding the mechanism of the hydrogen abstraction from the GA molecule by fluorine anions, the transition state structures for the fluorine radical abstracts of the hydrogen of the GA molecule are shown in Figure 4. The breaking C-H bond of TS_AABS1 is 1.19 Å long, while the C-H bond of the GA molecule is 1.091 Å long. The forming H-F bond is 1.43 Å, long; this bond is 0.922 Å in HF itself. The F-H-C bond angle is 142.59 degrees. From the structure of TS_AABS2, the length of the C-H bond that is being broken is 1.17 Å, while the other two C-H bonds are 1.085 Å long. The forming H–F bond is 1.34 Å long; this bond is 0.922 Å in HF itself. The F-H-C bond angle is 147.88 degrees.

3.1.3 Comparison of Energy Profile between Radical and Anionic Fluorine

The activation energy of the hydrogen abstraction reaction is shown in Table1. The first step in this mechanism features the F anion

approaching the hydrogen atom of GA, forming a weakly-bound complex CR_RABS1 and CR_RABS2. Then CR_RABS1 and CR_RABS2 are transformed to radical products and HF via surmounting an energy barrier with values of 2.62 and 0.31 kcal/mol, for transition states TS_ RABS1 and TS_ RABS2, respectively.

The activation energy of anionic hydrogen abstraction (AABS), is shown in Table 1. The first step in this mechanism features the F anion approaching the hydrogen atom of GA, forming strongly-bound complexes CR_ AABS1 and CR_AABS2. Then CR_AABS1 and CR_AABS2 transform to CP_AABS1 and CP_AABS2 via surmounting an energy barrier with values of 3.02 and 22.73 kcal/mol for transition states TS_ AABS1 and TS_ AABS2, respectively. This result corresponds to HOMO-LUMO and electrostatic properties [18]. The F ion prefers the alanine unit, where a molecular orbital is unoccupied (3). In summary, the energies of the CR and TS complexes of the ionic system are lower than those of the radical system. The energy barriers of radical reactions were found to be lower than those of the ionic reactions. Moreover, the products of the radical reactions are more stable than the products of the ionic reactions.

The total energy of H-abstraction in the ionic reaction is less stable than for the H radical in the radical reaction. Comparing these two reactions, The H-abstraction mechanism is preferable in this case, as shown in Table1 and Figure 5.

3.2 Interaction of Silk Surface and Irradiated Silk Surface with Water

The low-temperature fluorine plasma treatment produces a different wettability of the silk surface (Figure 5). The quantum calculation has suggested that there is a modification of the Ala unit by introduction

Table 1. Relative energies at BHandHLYP/6-31G(d) basis set of the Reactant (R/A), Complex Reactant (CR), Zero Point Vibration Energy (ZPVE), Transition State (TSs) and Activation Energy (ΔE_a) (in kcal/mol).

Pathway	R/A	CR	ZPVE	TSs	ZVPE	$\Delta extbf{E}_{ extbf{a}}$
RABS1	0	-348851.3588	103.6596	-348846.4924	101.4160	2.6229
RABS2	0	-348851.3588	103.0498	-348848.5571	100.5533	0.3051
AABS1	0	-348923.6211	103.9805	-348918.8440	102.2192	3.0159
AABS2	0	-348923.6212	103.9760	-348899.0155	102.0993	22.7291

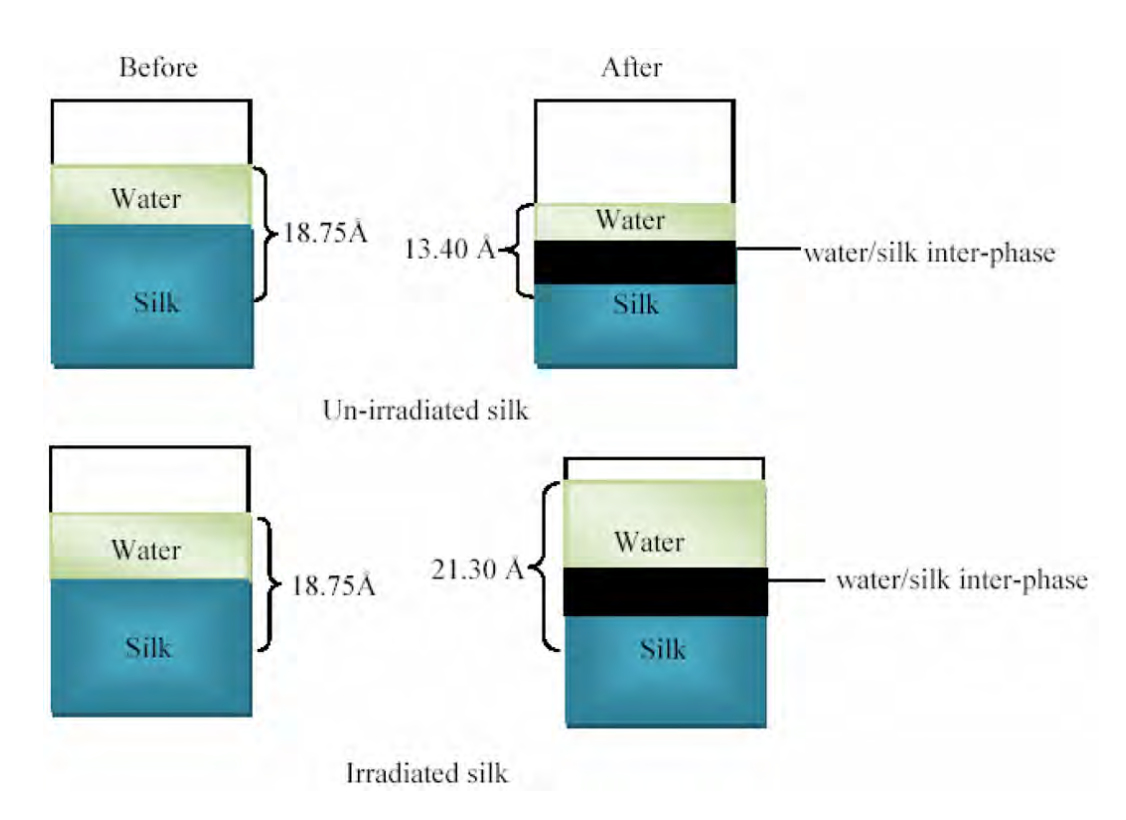


Figure 5. Molecular dynamics (MD) simulation of the water/un-irradiated (top) and water/irradiated (bottom) surface Interface. Comparison of the initial (left) and the final (right) MD structure and the distances from the outer water boundary to the center of mass of silk in angstrom unit were depicted.

of the fluorine atom at the methyl group. The carbon-fluorine bonds, which are also found in Teflon or poly(tetrafluoroethene), exhibit great hydrophobic properties in repelling of water. The molecular dynamics study provides useful information for

understanding the interfacial interaction mechanism at the atomic scale. The analysis of the molecular dynamic structures reveals a different distribution of water between the un-irradiated and irradiated silk surfaces. The final MD structures of the water-silk surface for two models is presented in Figure 5. From the simulation, the water can penetrate the un-irradiated surface better than the irradiated surface with the distance of 6 Å for the watersilk interface. More water molecules were distributed to cover most of vacuum area for the irradiated surface. In terms of the interaction energy between water and the silk surface, the total energies, potential energies, and kinetic energies of the systems were calculated. Both systems were found to be stabilized after about 1,000 ps of NVT dynamics. Snapshots were taken from the last dynamical trajectory at 1600 ps, and their structures were minimized in order to calculate the interaction energy between water and the silk model using the following equation:

$$\Delta E_{\text{wat silk}} = E_{\text{wat, silk}} - E_{\text{wat}} - E_{\text{silk}}$$
 (1)

Where ΔE_{wat_silk} , E_{wat} , E_{silk} and E_{wat_silk} are the energies in kcal per mole for the interaction energy of the water - silk surface, the energy of water, the energy of the silk surface, and the energy of the combined water and silk surface, respectively. All terms in equation (1) are calculated by the MM calculation. In order to calculate E_{wat} and E_{model} , the molecular

configurations were taken separately from that of E_{wat, model}. The energies for all systems are summarized in Table 2. Adsorption of water on the silk surface can be indicated from the negative values of $\Delta E_{\text{wat_silk}}$. The interaction energy between the water and different silk surfaces indicates that the interaction between the water-unirradiated surface is stronger than that of the water-irradiated surface. This contribution is strongly due to the electrostatic interaction. The interaction energy between the water-silk surfaces per mol of water at the interface was calculated. This theoretical result strongly agreed with the experimentally observed values for the surface energy of the untreated and treated silk, which were about 2 -5 kcal/mol [10]. The final structure of water molecules near the silk and irradiated silk crystalline model are presented in Figure 5. The water repellent properties of the model were determined in terms of distances measured from the center of the model (silk) to the regime of water. The distribution of water indicated that the irradiated silk model repels water at a radius of 21.3 Å, compared to the silk model with a corresponding radius of 13.4 Å.

Table 2. Interaction of silk surface and irradiated silk surface with water, energies in kcal/(mole cells).

Term in Eq. (1)	Energy				
101111 III Eq. (1)	Water-silk	Water-irradiated			
E wat, silk	-4467.50	-5290.68			
E wat	-2948.18	-3274.85			
E silk	345.06	-961.50			
Type of interaction					
E water-silk	-1864.37	-1054.34			
van der Waals	-76.03	-59.12			
Electrostatic	-1774.17	-981.04			
$\Delta E_{\text{wat_silk}}$, kcal/(mol water)	-4.65	-2.63			

4. CONCLUSIONS

The results from MD simulations and quantum calculations support the possibility of H abstraction from carbon atoms. In the quantum calculation, the activation energy for H-abstraction for F anionic reactions was 3.01-22.73 kcal/mol whereas for F radicals is the same energy was 0.31-2.62 kcal/mol. Therefore, the hydrogen abstraction reactions from F radicals may be the lowest activation energy pathway and should be the most probable pathway in the plasma treatment process. In addition, interactions between the silk surface and fluorinated silk surface with water were investigated via MD simulation. The interaction energies for water with the silk surface and irradiated surface were -4.65 and -2.63 kcal/(mole of water), respectively. This shows that water is attracted to the silk surface more than to the fluorinated surface.

ACKNOWLEDGEMENTS

We would like to acknowledge financial support of the Commission on Higher Education, Thailand Research Fund (TRF), and Center for Innovation in Chemistry (PERCHCIC). We would like to acknowledge facility provided by Computational Simulation and Modeling Laboratory (CSML), Department of Chemistry, Faculty of Science, Chiang Mai University, Thailand. The software resource is the courtesy of Computational Nanoscience Consortium (CNC) Nanotechnology (NANOTEC), Thailand for the access to Material Studio Version 4.2 program package.

REFERENCES

- Molina R., Jovancic P., Jocic D., Bertran E. and Erra P., Surface characterization of keratin fibres treated by water vapour plasma, Surf. Interface Anal., 2003; 35: 128-135.
- [2] Jin J.C. and Dai J.J., A study of wool

- dyeing with nitrogen plasma treated dyestuff, J. Text. Res., 2002; 23(2): 9-10.
- [3] Moon S.I. and Jang J., Factors affecting the interfacial adhesion of ultrahighmodulus polyethylene fibre-vinylester composites using gas plasma treatment, *J. Mater. Sci.*, 1998; **33**: 3419-3425.
- [4] Riccardi C., Barni R., Selli E., Mazzone G., Massafra M.R., Marcandalli B. and Poletti G., Surface modification of poly(ethylene terphthalate) fibers induced by radio frequency air plasma treatment, *Appl. Surf. Sci.*, 2003; **211**: 386-397.
- [5] Kin M.S. and Kang T.J., Dimensional and surface properties of plasma and silicone treated wool fabric, *Text. Res. J.*, 2002; **72(2)**: 113-120.
- [6] Kim Y., Lee Y., Han S. and Kim K., Improvement of hydrophobic properties of polymer surfaces by plasma source ion implantation, *Surf. Coat. Technol.*, 2006; 200: 4763-4769.
- [7] Wen C., Chuang M. and Hsiue G., Plasma fluorination of polymers in glow discharge plasma with a continuous process, *Thin Solid Films*, 2006; **503**: 103-109.
- [8] Chaivan P., Pasaja N., Boonyawan D., Suanpoot P. and Vilaithong T., Low-temperature plasma treatment for hydrophobicity improvement of silk, *Surf. Coat. Technol.*, 2005; **193**: 356-360.
- [9] Selli E., Riccardi C., Massafra M.R. and Marcandalli B., Surface Modifications of Silk by cold SF₆ Plasma Treatment, *Macromol. Chem. Phys.*, 2001; 202: 1672-1678.
- [10] Suanpoot P., Kueseng K., Ortmann S., Kaufmann R., Umongno C., Nimmanpipug P., Boonyawan D. and Vilaithong T., Surface analysis of hydrophobicity of Thai silk treated by SF6 plasma, *Surf. Coat. Technol.*, 2008; **202**: 5543-5549.
- [11] Wei Q., Liu Y., Hou D. and Huang F., Dynamic wetting behavior of plasma

- treated PET fibers, J. Mater. Process. Technol., 2007; **194**: 89-92.
- [12] Leroux F., Campagne C., Perwuelz A. and Gengembre L., Fluorocarbon nanocoating of polyester fabrics by atmospheric air plasma with aerosol, *Appl. Surf. Sci.*, 2008; **254**: 3902-3908.
- [13] Kulinich S.A. and Farzaneh M., On wetting behavior of fluorocarbon coatings with various chemical and roughness characteristics, *Vacuum*, 2005; **79**: 255-264.
- [14] Packham D.E., Surface energy, surface topography and adhesion, *Int. J. Adhes. Adhes.*, 2003; **23**: 437-448.
- [15] Palasantzas G. and De Hosson J. Th. M., Wetting on rough surfaces, *Acta Mater.*, 2001; **49**: 3533-3538.
- [16] Dhavalikar R.S., Amino acid composition of Indian silk fibroins and sericins. II. Sericins., *Indian J. Sci. Ind. Res.*, 1962; **21(C)**: 261-263.
- [17] Gulrajani, M.L., Degumming of silk, Rev. Prog. Colour. Relat. Top., 1992; 22: 79-89.
- [18] Nimmanpipug P., Sanghiran L.V., Janhom S., Chaivan P., Boonyawan D. and Tashiro K., Molecular Functionalization of Cold-Plasma-Treated Bombyx mori Silk, *Macromol. Symp.*, 2008; **264**: 107-112.
- [19] Takahashi Y., Gehoh M. and Yuzuriha K., Structure re□ nement and diffuse streak scattering of silk (Bombyx mori), *Int. J. Biol. Macromol.*, 1999; **24**: 127-138.
- [20] Frisch M.J., Trucks G.W., Schlegel H.B., Scuseria G.E., Robb M.A., Cheeseman J.R., Montgomery J.A. Jr., Vreven T., Kudin K.N., Burant J.C., Millam J.M., Iyengar S.S., Tomasi J., Barone V., Mennucci B., Cossi M., Scalmani G., Rega N., Petersson G.A., Nakatsuji H., Hada M., Ehara M., Toyota K., Fukuda R., Hasegawa J., Ishida M., Nakajima T., Honda Y., Kitao O., Nakai H., Klene M., Li X., Knox J.E., Hratchian H.P., Cross J.B., Bakken V., Adamo C., Jaramillo J.,

- Gomperts R., Stratmann R.E., Yazyev O., Austin A.J., Cammi R., Pomelli C., Ochterski J.W., Ayala P.Y., Morokuma K., Voth G.A., Salvador P., Dannenberg J.J., Zakrzewski V.G., Dapprich S., Daniels A.D., Strain M.C., Farkas O., Malick D.K., Rabuck A.D., Raghavachari K., Foresman J.B., Ortiz J.V., Cui Q., Baboul A.G., Clifford S., Cioslowski J., Stefanov B.B., Liu G., Liashenko A., Piskorz P., Komaromi I., Martin R.L., Fox D.J., Keith T., Al-Laham M.A., Peng C.Y., Nanayakkara A., Challacombe M., Gill P.M.W., Johnson B., Chen W., Wong M.W., Gonzalez C. and Pople J.A., Gaussian 03, Revision C.02, Gaussian, Inc., Wallingford, CT, 2004.
- [21] Dennington II R., Keith T., Millam J., Eppinnett K., Hovell W.L. and Gilliland R., GaussView, Version 3.0, Semichem, Inc., Shawnee Mission, KS, 2003.
- [22] Accelrys Software Inc. Materials Studio, Release 4.2, San Diego, Accelrys Software Inc., 2007.
- [23] Case D.A., Darden T.A., Cheatham III, T.E., Simmerling C.L., Wang J., Duke R.E., Luo R., Merz K.M., Pearlman D.A., Crowley M., Walker R.C., Zhang W., Wang B., Hayik S., Roitberg A., Seabra G., Wong K.F., Paesani F., Wu X., Brozell S., Tsui V., Gohlke H., Yang L., Tan C., Mongan J., Hornak V., Cui G., Beroza P., Mathews D.H., Schafmeister C., Ross W.S. and Kollman P.A., AMBER9, University of California, San Francisco, 2006.
- [24] Berendsen H.J.C., Postma J.P.M., van Gunsteren W.F., di Nola A. and Haak J.R., Dynamic simulation as an essential tool in molecular modeling, *J. Chem. Phys.*, 1984; **81**:3684-3690.
- [25] Darden T., York D. and Pedersen L., Particle mesh Ewald an Nlog(n) method for Ewald sums in large systems, *J. Chem. Phys.*, 1993; **98**:10089-10092.

ELSEVIER

Contents lists available at ScienceDirect

Journal of Molecular Graphics and Modelling

journal homepage: www.elsevier.com/locate/JMGM



Molecular simulations of ultra-low-energy nitrogen ion bombardment of A-DNA in vacuum

Chanisorn Ngaojampa ^a, Piyarat Nimmanpipug ^a, Liangdeng Yu ^{b,c}, Somboon Anuntalabhochai ^d, Vannajan Sanghiran Lee ^{a,*}

- ^a Computational Simulation and Modeling Laboratory (CSML), Department of Chemistry and Center for Innovation in Chemistry, Faculty of Science, Chiang Mai University, Chiang Mai 50200, Thailand
- b Plasma and Beam Physics Research Facility (PBP), Department of Physics and Materials Science, Faculty of Science, Chiang Mai University, Chiang Mai 50200, Thailand
- ^c Thailand Center of Excellence in Physics, Commission on Higher Education, 328 Si Ayutthaya Road, Bangkok 10400, Thailand

ARTICLE INFO

Article history: Received 21 May 2009 Received in revised form 26 November 2009 Accepted 30 November 2009 Available online 4 December 2009

Keywords: Molecular dynamics Monte Carlo Ion bombardment A-DNA

ABSTRACT

For investigating mechanisms involved in low-energy ion beam induced mutation, besides experiments using low-energy and low-fluence ions to bombard naked DNA, molecular simulations were carried out as an effort towards the insight in molecular interactions between ions and DNA. In the current study, Monte Carlo (MC) and molecular dynamics (MD) simulations were applied. The results of MC simulations provide some clues about the interaction energies and sites of preference of N-ion bombardment on an A-DNA short duplex strand. MD simulations of a single N-ion moving towards the same DNA strand with different linear velocities corresponding to bombardment energies of 0.1, 1, 10 and 100 eV revealed information about changes in bond lengths and visibly distorted structures of bombarded nucleotides. The simulations demonstrated that ion-bombardment-induced DNA change in structure was not a random but preferential effect.

© 2009 Elsevier Inc. All rights reserved.

1. Introduction

Recently, low-energy ion beam biotechnology, emerging as a novel and highly interdisciplinary subject, has rapidly been developed [1]. The technology uses low-energy (an order of 10 keV) heavy ion beam, instead of protons, to bombard biological organisms to induce biological effects. The effects can eventually be applied for mutation breeding and gene transfer with high efficiencies. With impressive successes in ion beam biotechnology applications, investigations on relevant mechanisms have followed up. Basically two interaction effects are involved, namely direct and indirect effects [2]. The direct effect comes from the ions direct interacting DNA to cause displacements of the atoms in DNA and therefore bond breakage. The indirect effect is due to ionbombardment-induced secondary effects such as emissions of secondary electrons and X-ray, generation of heat and production of radicals, which can also cause DNA structural changes. There is a puzzle in the issue of the direct effect. In the experiments on ion beam induction of mutation, normally plant seeds with embryos are ion-bombarded. Here, energetic ions must travel through the materials that cover DNA in the cell nucleus before they can directly interact with DNA. Theoretical calculation estimates that the most of the ion energy is lost before the ion can impact with DNA for 30-keV nitrogen ions to pass through organic materials of a-few-hundred nanometers. Questions raised then include whether and how the ultra-low-energy ions are still able to cause DNA damage to induce mutation. Along with experimental efforts, in which keV ions bombarded naked DNA in vacuum and DNA strand breaks and mutation induction were discovered [3–9], molecular simulation is of necessity in studying the interaction between ions even at ultra low energy and DNA at the molecular level to reveal the nature of the interaction. There have been a plenty of studies on ion interaction with solids [10,11] and high-energy radiobiology [12]. However, there are yet lacks of studies on low-energy ion interaction with biological organisms and particularly DNA.

It has been found from experiments that treatments of ion beam on biological matter do not give complete random results, but rather biased ones [13]. For example, in an experiment, the plasmid M_{13} mp18 with the *lacZ* gene was bombarded by N-ion and transferred into host bacteria JM103 *E. coli*. The results revealed that the dominant type of mutation was from a replacement (95%) while the rest was from the base deletion [14], but no insertion or replication of bases was detected. In addition, it was found that cytosine was the most sensitive residue taking more than 50% of the mutations. Another study using C-ion radiation [15] showed different non-random results with one base-deletions taking 38.5%

^d Molecular Biology Laboratory, Department of Biology, Faculty of Science, Chiang Mai University, Chiang Mai 50200, Thailand

^{*} Corresponding author. Tel.: +66 5394 3341; fax: +66 5389 2277. E-mail address: vannajan@gmail.com (V.S. Lee).

of mutations. A comparative study reported a different outcome between N-ion and $^{60}\text{Co-}\gamma$ ray treated *E. coli* containing *rpoB* genes [16]. It was found that CG-to-TA, AT-to-GC and AT-to-TA took majority in the substitution mutations (92.13% or 82/89) in $^{60}\text{Co-}\gamma$ radiation, while N-ion bombardment gave CG-to-TA and AT-to-TA as the major substitutions. Moreover, GC-to-CG and AT-to-GC were found induced by N-ion bombardment only but not by the γ -ray, whereas AT-to-CG was not found after N-ion implantation, but was only found in $^{60}\text{Co-}\gamma$ radiation.

From the above studies, it is clear that there are many distinct molecular mechanisms for radiation-induced mutation which can effect the possible mutations generated from a given mutation method. Ideally to be able to predict and controls of the amount and type of mutation generated by a given method further insight into the mechanisms controlling the processing of mutated DNA is required. Currently, very little knowledge about the molecular mechanisms or pathways of DNA damage during ion beam implantation or other types of radiations has been found [2,15]. To complement the small amount of experimental evidence, some researchers have attempted to use computational methods to investigate the irradiation of DNA. Such studies include simulating accurate structures of mini-circle and super-coiled DNA molecules [19-22], DNA movements [23,24], tracking simulations of radiation particles in DNA molecules [3,25-27] and quantum molecular calculations of DNA damaged by radiation [28,29]. However, no such work has been done with ion beams induced mutation.

In this study, molecular modeling methods were selected to investigate the molecular interactions and elementary processes of DNA during irradiation by ion beam. To complement the experiment work done with N⁺ ion beam irradiation, we chose this form of ion beam particles to examine computationally. The study was divided into two main parts: (i) a Monte Carlo (MC) simulation of N^+ on a DNA strand and (ii) a molecular dynamics (MD) simulation of the effect of N⁺ implantation on a DNA strand. The MC simulations aimed to specify the preferred sites of N⁺ implantation around an arbitrary short strand of DNA using commercial software packages. The MD simulation aimed to investigate possible changes in the structure of the same DNA molecules after the bombardment. In both parts of the experiment, the DNA was in the A-form to best resemble real world experimental conditions, in which naked solid state DNA samples were bombarded by ion beam under vacuum [9]. Predominantly, this study focused on low-energy ion irradiation, because highenergy (above 10² keV) ion irradiation can cause very strong interactions with the DNA structure resulting in extensive damage to the DNA. By focusing our investigation on low-energy ion irradiation, the interaction of ions on DNA molecular sites allows identifying details of the effect of ion interactions to DNA structural changes.

2. Methods

2.1. DNA preparation

A 30-base-pair-long DNA duplex with sequence 5'-AAGAATG-GAA TCAAAGTTAA CTTCAAAATT-3' was constructed in A-form which was the form commonly observed in the dehydrated samples of DNA under vacuum condition with a pressure of 10^{-4} Pa for ion-bombardment experiments on the glass surface as well as in crystallographic experiments. The selected residues numbered between 760 and 789 bps of the green fluorescent protein plasmid (pGFP) from GenBank, sequenced by Chalfie et al. [30]. This portion of DNA contained the sequence that translates into the flourophore of the functioning protein (green fluorescent protein, GFP). The DNA duplex was built in Discovery Studio 1.7.1

software [31]. The CHARMm27 force field [32] was applied on this molecule. To obtain the DNA structure in the equilibrium state in vacuum, DNA was neutralized with Na-ion. The energy minimization, heating, equilibration and production MD simulation were performed using the Standard Dynamic Cascade protocol. The steps of energy minimization were divided into two parts: 1000 steps of the steepest descent minimization, and 4000 steps of the adopted bases Newton–Raphson minimization. Afterwards, heating was performed for 60 ps from 0.0 to 323.0 K according to the experimental temperature. Then, the equilibration was performed for 2900 ps at 323.0 K. And finally, the production was performed for 40 ps at the same constant temperature. All processes were done in NPT ensemble with the total simulation time of 3 ns. The final DNA structure from the MD simulation was used as the substrate for the adsorption of N⁺.

2.2. Monte Carlo simulations of N⁺ around a DNA strand

In Materials Studio 4.3 [33], the minimized DNA structure was imported, and the N $^{+}$ ion was constructed. The COMPASS force field [34,35] was assigned to both DNA and ion. Then, the adsorption calculations using the Adsorption Locator module were performed for ion fluences of 18 and 27 ions on one DNA molecule (corresponding to 6×10^{13} and 9×10^{13} ions/cm 2 as in the ion-bombardment experiment [9], respectively). In the calculation, the simulated annealing algorithm was performed for 5 cycles, with 15,000 MC simulation steps for each cycle as in Supplementary Fig. S1. The initial temperature was 1000 K before cooling down gradually to 323.0 K during the simulations. The simulation searched for the 10 best configurations of adsorption along with their interaction energy.

The starting configuration was adjusted to the current temperature for many iterating steps. Applying the Metropolis Monte Carlo method decided whether to accept or reject the change of N^+ position. The probability to transform from configuration m to n defined as P_{mn} is:

$$P_{mn} = \min\left[1, \exp\left\{\frac{E_n - E_m}{k_B T}\right\}\right] \tag{1}$$

where k is the Boltzmann constant and T is the simulation temperature [36]. The total energy of configuration m (E_m) is calculated by the following sum:

$$E_m = E_m^{AA} + E_m^{AS} \tag{2}$$

where E_m^{AA} is the intermolecular energy between the adsorbate molecules (N⁺) and E_m^{AS} is the interaction energy between the adsorbate molecules and the substrate (DNA) [37].

After the simulations, the results were shown as the equilibrium structure of DNA substrate, radial distribution function (RDF) plots (g(r)), distances of maximum RDF (r_{max}) and RDF integrals in the interval of 0.0–4.0 Å $(I_{4\dot{A}})$. The RDFs were measured from the N⁺ to each of the rest of atom types in the DNA. The atom types were arbitrary defined in the discussion (shown in Fig. 1). The results point out that N⁺ ions have specific sites of adsorption preference.

2.3. Molecular dynamics simulations of N^+ ion bombardment of DNA

In Materials Studio, the final structure of the DNA strand adsorbing 27 ions (corresponding to fluence of 9×10^{13} ions/cm²) with the best interaction energy (the lowest or most negative energy) was used as the initial structure for the simulations of N⁺ bombardments. All the nitrogen ion residues were deleted except for the one in the middle of the DNA strand as shown in Fig. 2a. The ion was moved 10 Å further from the strand by editing its Cartesian coordinate in the program database (PDB) file. The classical MD

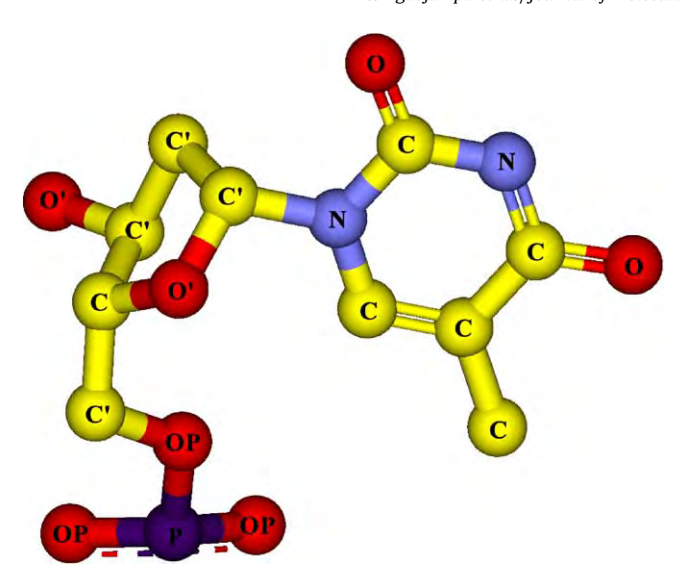


Fig. 1. Atom type definition of the nucleotide. For clear illustration of the MDs constructed DNA, the neutralization is not shown.

simulations of NPT (*N*: number of atoms, *P*: pressure, and *T*: temperature) ensembles at 323 K and 0 atm were performed for bombardments with energy of 0.1, 1, 10, and 100 eV in AMBER 9 [38]. The forcefields for DNA had partial charges explicitly parameterized for solution conditions, and thus might require modification for a vacuum condition. From the previous study by Rueda et al. [38,39], the charges of nucleobases in vacuo were scaled by a factor of 0.8 and the calculations showed that the changes in forcefield parameters had little effect in the conformational transition of the DNA duplex. The time step was 1 fs. The non-bonded cutoff was 9.0 Å. The residues 1–8, 22–38 and 52–60 at the end chains were held fixed. The velocity vectors applied in AMBER were calculated from the ion energy (*E*) and mass (*m*) using the equation:

$$v = \left(\frac{E}{2m}\right)^{1/2} \tag{3}$$

where v is the magnitude of the velocity (scalar quantity) and the unit vector for velocity direction was specified as well. The directions of the velocities were assumed to be in the direction from the ion to an arbitrary target atom in DNA calculated using the known coordinate of N^+ and the target atom.

3. Results and discussion

3.1. Ion and DNA interaction

From the energy report calculated by Adsorption Locator shown in Table 1, it was found that the best configuration of the DNA molecule adsorbing 27 N $^{+}$ ions had the interaction energy of -26.19 kcal/mol, which was 4.38 kcal/mol lower than the interaction energy of the one adsorbing 18 N $^{+}$ ions. The negative values of both fluences indicated that the adsorptions of N $^{+}$ on DNA molecules were thermodynamically favorable. The lower (more negative) interaction energy of the DNA molecule adsorbing 27 N $^{+}$ points out

Table 1The interaction energies of the best configuration for each ion fluence.

Ion beam fluence (×10 ¹³ ions/cm ²)	Equivalent number of N ⁺	Interaction energy (kcal/mol)
6	18	-21.810
9	27	-26.192

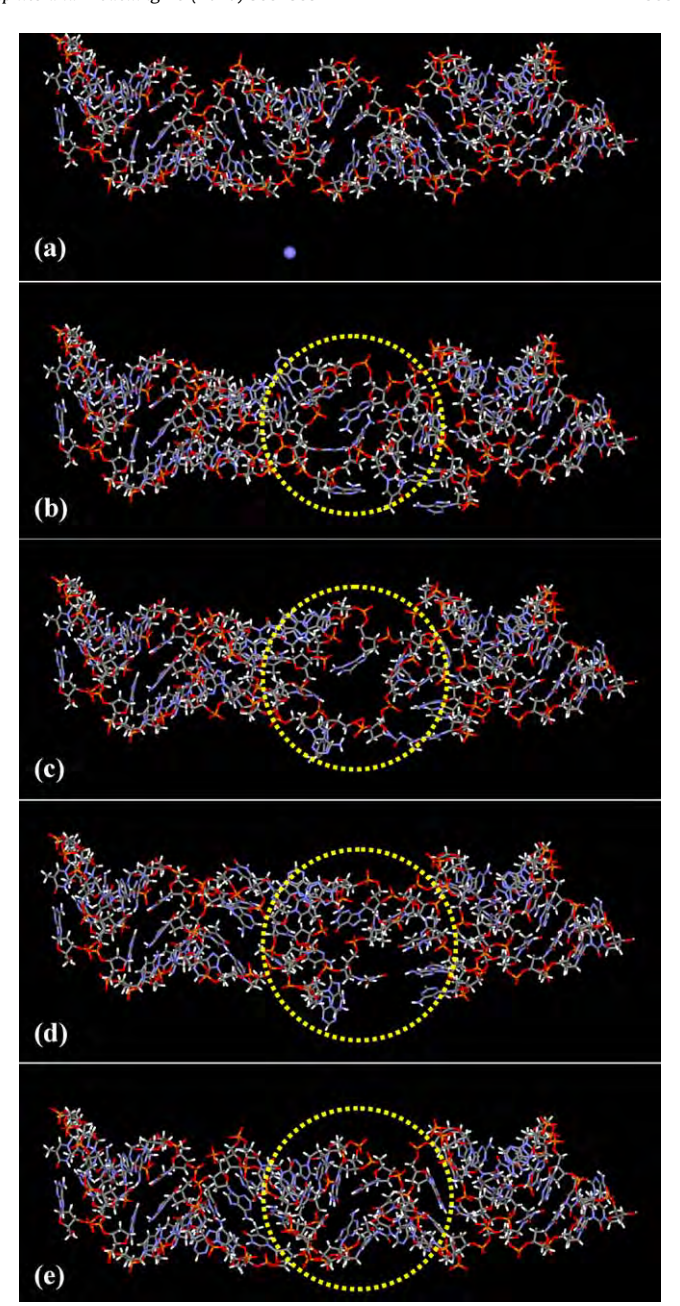


Fig. 2. The initial structure of DNA and the structures after bombardment with varied N-ion energy from selected simulation snapshots. (a) Initial structure; the particle at the low part represents the incident ion. (b) 0.1 eV at 4 ps. (c) 1 eV at 4 ps. (d) 10 eV at 4 ps. (e) 100 eV at 1 ps. The dash-circled areas are the main ion-bombardment-induced change parts.

that the 18 N $^{+}$ does not fill the DNA molecule's adsorption capacity since it releases even more energy when adsorbing an extra 9 ions. Moreover, it could be said that the adsorption capacity for the molecule was at least equal to 27 ions, or experimentally, 9×10^{13} ions/cm 2 . According to the experiment result reported earlier [9], when the ion fluence increases, the amount of DNA in the supercoiled form decreases and the amount in the linear form increases for N-ion bombardment. This indicates that nitrogen ions even with lower energy are effective in producing double strand breaks and thus more than capable of inducing gene mutation.

3.2. Radial distribution functions

Specific sites adsorption preference of N⁺ ions interacting with DNA from simulation was detailed. Table 2 summarizes the values

Table 2 Summary of the distance of maximum radial distribution functions, r_{max} , and the integral of radial distribution functions from 0.0 to 4.0 Å, $I_{4\dot{A}}$, of each atom type.

Fluence (×10 ¹³ ions/cm ²)	Atom type	r _{max} (Å)	$I_{4 ilde{A}}$
6	N	4.15	1.77
	0	6.25	1.46
	0′	5.15	1.48
	OP	3.25	3.20
	C	3.95	1.65
	C'	4.05	0.96
9	N	3.55	1.89
	0	3.25	4.15
	0′	3.75	3.73
	OP	3.35	3.30
	C	3.85	1.34
	C'	3.95	1.90

of r_{max} and $I_{4\hat{A}}$ for the best configuration at each fluence level. This table shows that, for fluence values equal to 6×10^{13} ions/cm², OP (O in phosphate) has the highest RDF integral value of 3.20, approximately twice as large as other cases. This pointed a fact that N⁺ preferred to be adsorbed at OP sites in phosphate groups of DNA. A straightforward explanation can be made from the basic chemical knowledge that oxygen atoms in phosphates have negative charge, which can bind strongly with positively charged species by electrostatic interaction. The distances of maximum radial distribution functions, r_{max} , also give similar results. OPs are suggested to have the strongest interaction with N⁺, as they have the least r_{max} while other atom types give far greater r_{max} values.

Different results were observed for the fluence of 9×10^{13} ions/ cm². Here, the three highest RDF integral values were all from oxygen atoms: O (O in bases), O' (O in sugars) and OP. The integral values for the three atom types were 4.15, 3.73 and 3.28, respectively. This might be because a larger number of ions increase the chance of interacting with other oxygen sites. Hence, oxygen is still the atom of preference for N⁺ irradiation. Other atom types give considerably smaller integral values. For this fluence, the values of r_{max} do not show as large differences as found with the previous fluence value. This might also be because of the more ions and thus the more chances to interact with other atoms. Still, oxygen atoms gave smaller value of r_{max} (3.25, 3.75 and 3.35 for O, O' and OP respectively) compared with those of other atom types (3.55, 3.85 and 3.95 for N, C and C', respectively). The results also agreed with the fact that oxygen atoms have large electronegativity, a measure of the ability of an atom to attract electrons it is sharing with another, and usually strongly polarize the formed bonds. Therefore, bonds with oxygen atoms are negative dipoles with partially negative charge on the oxygen side and thus they can still attract positively charged species. The RDF plots with the r_{max} reported in Table 2 indicate that N⁺ ions are likely to interact with OP, C, C', N, O' and O, respectively. The radial distribution function of N⁺ around OP in phosphates with a) the fluence of 6×10^{13} ions/ cm² and b) the fluence of 9×10^{13} ions/cm² was provided in Supplementary Fig. S2.

3.3. Molecular dynamic simulations

Our study used molecular dynamics to monitor the change in bond lengths within the DNA as the biomolecule was subjected to ion bombardment, and observed enormous changes in the bond length as described below. Large bond length changes might lead to bond breakage. However, the breakage of covalent bonds cannot be accounted from the simulation due to the limitation of classical MD. A quantum mechanics approach would be a solution for such simulation; however, it requires very small DNA duplexes in the simulation and also some approximations as well. Another

limitation of our approach as already mentioned in the method section resides in the forcefield for DNA, in which its partial charges parameterized for solution conditions may not be suitable in vacuo. Nevertheless, molecular dynamics techniques allow detailed time and space resolution for carefully selected systems which could provide details of the structural change in DNA after ion bombardment. The root mean square deviations (RMSD) were collected for every time step of the simulations to study the overall movement of the DNA structures during the simulation. The initial structure of DNA and the structures after bombardment with varied N-ion energy of 0.1, 1, 10, and 100 eV from selected simulation were snapshotted as shown in Fig. 2. At the simulation time of 4 ps, it is clearly seen large structural changes (Fig. 2b-d) in DNA for 0.1, 1, and 10 eV N-ion bombardment. For the highest ion energy of 100 eV, the ion seems to pass through DNA too quickly to snapshot for the change in the DNA structure and the structure even at 1 ps as illustrated in Fig. 2e does not show change compared with the initial structure shown in Fig. 2a. From the RMSD plots in Fig. 3, all bombardments exhibited rapid changes in RMSD during the simulations whereas the RMSDs for the unbombarded system at 298 and 323 K were smaller. At 100 eV ion bombardments, the RMSD peaked after 1.5 ps. Since large RMSD values represent a large movement and flexibility of the DNA structure, it is suggested that the flexibility might result in the simultaneous breakages of chemical bonds in DNA. The upcoming sections will present the changes in each type of bond lengths after the rapid changes in the RMSD.

The ranges and medians of the bond lengths of eight bond types were studied. The studied types included oxygen-phosphorus single bonds (O-P), oxygen-phosphorus aromatic bonds (O-P (ar)), carbon-carbon single bonds (C-C), carbon-nitrogen single bond (C-N), carbon-oxygen single bonds (C-O), carbon-carbon aromatic bonds (C-C (ar)), carbon-nitrogen aromatic bonds (C-N (ar)) and carbon-oxygen double bonds (C=O). The maximum, minimum and modal bond lengths in each bombardment were measured and reported in Tables 3–5. Relative deviations from the equilibrium lengths were noted in the parentheses on the right of the measured bond lengths. The results for the 100 eV bombardments were not presented because the simulation lasted for too short a time to notice bond length changes.

From the tables, the maximum bond lengths of all types were far higher than the equilibrium lengths for all bombardments. The bombardment producing the largest maximum bond lengths was the one with the 1 eV ion beam, followed by ones with 0.1 eV and 10 eV ion beams respectively. This indicates that the energy of 1 eV can cause the most stretching to all the bonds. In the same manner, the bombardment resulting in the largest minimum bond lengths

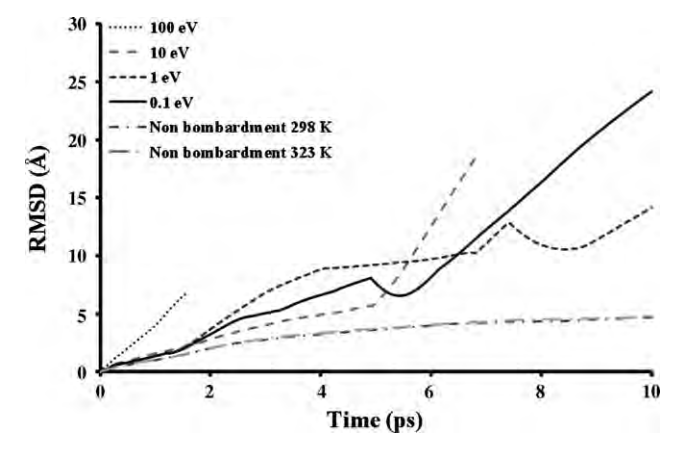


Fig. 3. RMSD plots for the MD simulations of ion bombardments at different ion energies in comparison with the unbombarded systems at 298 and 323 K.

Table 3Bond length maxima, minima and modes after 10 ps of 0.1 eV bombardment simulations.

Bond	Average	Bond length after 0.1 eV bombardment (Å)					
type	equilibrium length (Å)	Maximum		Minimum		Mode	
O-P	1.582	1.817	(+15%)	1.411	(-11%)	1.618	(+3%)
O-P (ar)	1.486	1.606	(+8%)	1.306	(-12%)	1.498	(+1%)
C-C	1.518	1.800	(+19%)	1.398	(-8%)	1.560	(+3%)
C-N	1.490	1.664	(+12%)	1.405	(-6%)	1.489	(-0%)
C-O	1.433	1.566	(+9%)	1.302	(-9%)	1.445	(+1%)
C-C (ar)	1.387	1.557	(+12%)	1.329	(-4%)	1.426	(+3%)
C-N (ar)	1.351	1.604	(+19%)	1.088	(-19%)	1.388	(+3%)
C=O	1.230	1.528	(+24%)	1.133	(-8%)	1.220	(-1%)

Table 4Bond length maxima, minima and modes after 10 ps of 1 eV bombardment simulations.

Bond	Average	Bond le	Bond length after 1 eV bombardment (Å)					
type	equilibrium length (Å)	Maximum		Minimum		Mode		
O-P	1.582	2.838	2.838 (+80%)		(-13%)	1.702	(+8%)	
O-P (ar)	1.486	2.236	(+50%)	0.971	(-35%)	1.498	(+1%)	
C-C	1.518	2.409	(+58%)	0.939	(-38%)	1.570	(+3%)	
C-N	1.490	2.153	(+44%)	1.398	(-6%)	1.543	(+4%)	
C-O	1.433	2.373	(+66%)	0.829	(-42%)	1.432	(-0%)	
C-C (ar)	1.387	2.116	(+53%)	1.116	(-20%)	1.408	(+2%)	
C-N (ar)	1.351	2.097	(+55%)	0.745	(-45%)	1.381	(+2%)	
C=O	1.230	1.787	(+45%)	0.958	(-22%)	1.221	(-0%)	

Table 5Bond length maxima, minima and modes after 6 ps of 10 eV bombardment simulations.

Bond	Average	Bond le	Bond length after 10 eV bombardment (Å)					
type	equilibrium length (Å)	Maximum		Minimum		Mode		
O-P	1.582	1.909	(+21%)	1.471	(-7%)	1.698	(+7%)	
O-P (ar)	1.486	1.798	(+21%)	1.271	(-14%)	1.481	(-0%)	
C-C	1.518	1.702	(+12%)	1.304	(-14%)	1.544	(+2%)	
C-N	1.490	1.618	(+9%)	1.396	(-6%)	1.515	(+2%)	
C-O	1.433	1.713	(+20%)	1.223	(-15%)	1.459	(+2%)	
C-C (ar)	1.387	1.648	(+19%)	1.310	(-6%)	1.399	(+1%)	
C-N (ar)	1.351	1.548	(+15%)	1.145	(-15%)	1.336	(-1%)	
C=0	1.230	1.319	(+7%)	1.054	(-14%)	1.218	(-1%)	

is still the one with 1 eV ion beam, followed by ones with 10 and 0.1 eV ion beam respectively. It is suggested that this energy gives the strongest shrinkage in overall bonds lengths. However, the bond lengths for 10 eV bombardments were measured at 6 ps since the simulation halted after that. So, the bond lengths due to this bombardment could be further elongated, and, by a rough approximation, the bond lengths could be close to ones bombarded if the simulation had lasted as long as 10 ps.

It was found that the bond type most sensitive to the ion bombardments was the O-P bonds. The maximum and modal lengths of this bond type had the largest deviation amongst all bond types, especially in 1 eV bombardment, where the bonds could elongate to as long as 2.838 Å (80% stretched from the equilibrium length). This corresponds to very large changes in overall RMSDs since the O-P bonds are a part of the DNA backbones. The DNA double helix could have an extreme stretching to twice of its normal length before its base pairs break, demonstrated by both theoretical modeling and nanomanipulation experiments [40]. As the DNA double helix is a multiply bonded structure, a nearly 100% stretching of the bond such as the one obtained above might cause breakage which can affect the overall structures and movements of DNA.

For further analysis of the bond lengths, the relative number of the elongated bonds for each type was recorded in order to study the changes of the bond lengths with changes of time. The percentages of the elongated bonds in DNA during the simulation of each bombardment were reported as line curves in Fig. 4. The percentage is calculated by dividing the counts of the elongated bonds (the bonds with more than 5% elongation) by the total counts of the bonds of the specific type. For example, if the total count of the O–P in the structure is 116, and the count of elongated O–P is 20, then the percent of the elongated bonds for the O–P in this structure is calculated as 20/116 = 17.2%.

From the figures, it was found that most of the bonds in the DNA tended to be elongated as time went by. This could be seen in the rising curves throughout the simulations. Some of the curves (especially for 0.1 eV bombardments) declined during some periods because the criterion of 5% elongation might still be too small for bond breakages. Furthermore, the three bond types with the largest percentage of the elongated bonds were O–P, C–C and C–C (*ar*) (navy, scarlet and orange graphs, respectively). And, the two types with the least percent of the elongated bonds were O–P (*ar*) and C=O (magenta and blue graphs respectively). So, major breakages would most probably occur in O–P, C–C and C–C (*ar*) as

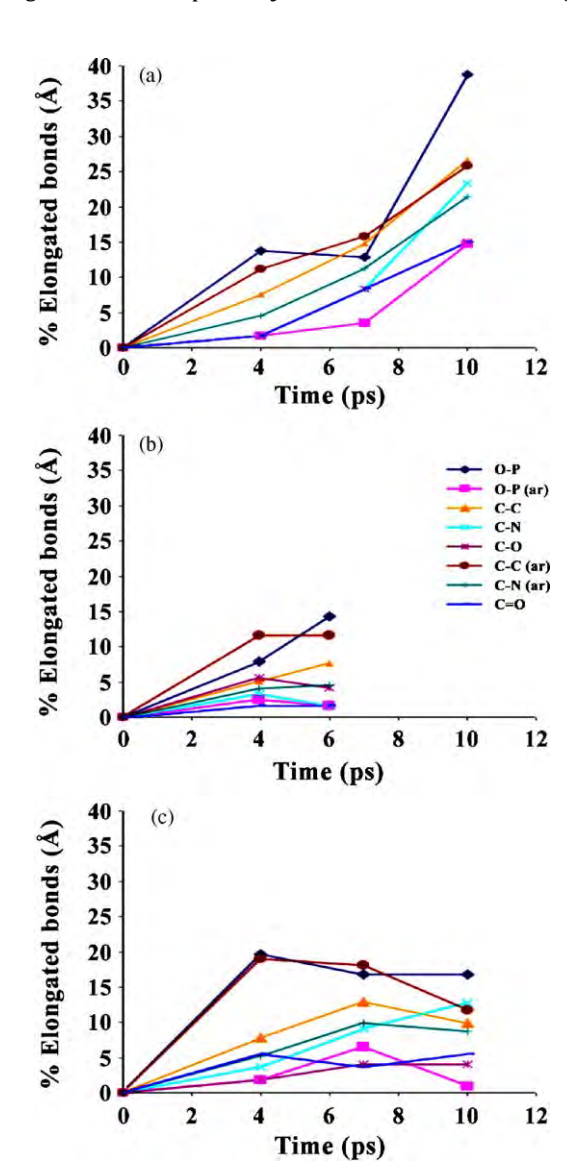


Fig. 4. Percentages of the elongated bonds in DNA during the simulation of (a) 10 eV, (b) 1 eV, and (c) 0.1 eV bombardments.

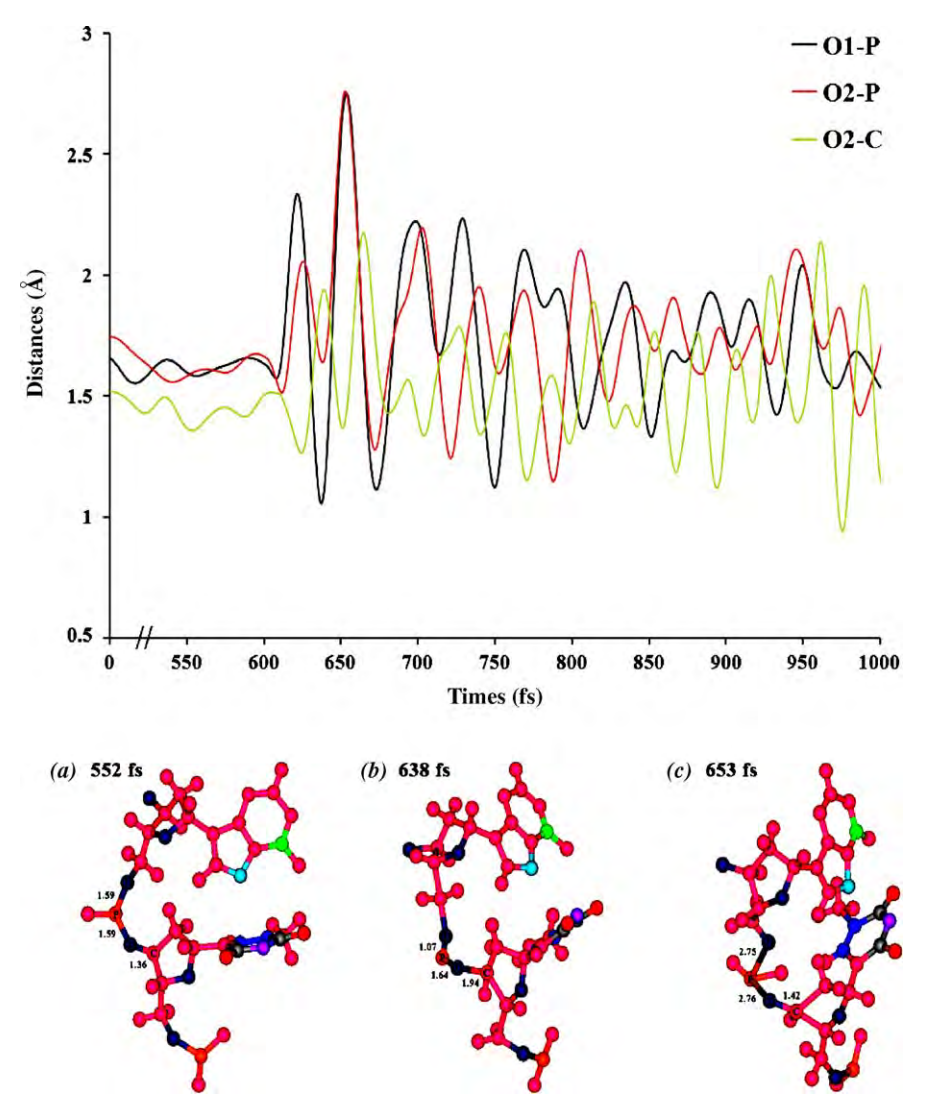


Fig. 5. Demonstration of the elongate distances of O1-P, O2-P, and O2-C as a function of time during 1 eV N-ion bombardment of DNA. At the lower part are the pictures of the structure (O1-P, O2-P and O2-C) selected at time of 552, 638, and 653 fs, respectively.

the DNA was bombarded, thus causing DNA damage. The elongate distances between O1-P, O2-P, and O2-C were observed during the first 1-ps trajectory of 1-eV N-ion bombardment of DNA as demonstrated in Fig. 5. The large displacement was started at 638 fs when the N-ion impacted on the DNA. The selected structure at 552, 638, and 653 fs showed the dynamics of the three breakable bonds at O1-P, O2-P and O2-C. From the usual thermal fluctuations, O-P and O-C fluctuation of the unbombarded system showed low RMSD below 0.5 at 298 and 323 K (the data is not shown). The counter ions were not included in the figure since they were distributed in other locations. The observation agrees well with the RMSD results shown in Fig. 3, which corresponded to rapid changes in the structures after ion bombardment in comparison with the lower RMSD observed in the unbombarded system at 298 and 323 K. The graphs of the bond lengths also showed sudden changes at a corresponding time (7-10 ps). This can be explained that if breakages occurred in the DNA molecule, the molecular structure would have more freedom to move. On the other hand, for the 10 eV bombardments, Fig. 3 shows a correspondence of the graphs with the RMSD only for O-P. In contrast, the 0.1 bombardment did not show such a correspondence.

When comparing the energies of ion bombardments with the mean bond enthalpies (normally a few hundreds to no more than a thousand kcal/mol) [30], we found that most of the mean bond

enthalpies were in the range of the energies of bombardments (0.1–10 eV corresponding to the energy range of 10–932 kJ/mol). The relevance of the ranges indicated the sensibility of the simulations.

4. Conclusion

Ultra-low-energy ion bombardment of DNA in vacuum condition was simulated with the example of 0.1–100 eV nitrogen ions to study effects of the ion-DNA interaction on DNA damage. Monte Carlo simulations of adsorption of N⁺ on DNA revealed some information of interactions of N $^{+}$ with DNA. The fluence of 9 \times 10 13 ions/cm² due to its lower interaction energy with DNA resulted in stronger adsorption of N⁺ on DNA molecule than the fluence of 6×10^{13} ions/cm². From the RDF analysis, N⁺ ions are likely to interact with OP, C, C', N, O', and O site in DNA. MD simulations of the N⁺ bombardment on DNA molecules exhibited some interesting behavior of the DNA after collisions with N⁺. Firstly, the RMSDs of the DNA bombarded by N+ showed rapid increases after collisions. This might be due to the stretching and then probable breakage of bonds in the structures leaving the molecules more flexible. Further investigation of the stretching bonds was also studied using bond length analysis. The analysis of the bond length maxima, minima and modes showed that all types of bonds had stretching and shrinkage after the bombardment. Additionally, the modes also gave the same tendency. The bombardment energy of 1 eV resulted in the most extreme maxima and minima, as well as the largest values of the modes of the bond lengths. The analysis also pointed out that the O–P bonds were the most sensitive to the collision. Lastly, the bond length changes with time for each bombardment were also studied. The O–P, C–C and C–C (ar) were the most vulnerable bonds in the DNA strands to ion bombardment. The bond enthalpies of these bond types corresponded well with the applied energy.

Acknowledgements

This research was supported by the Institute of Promotion of Science and Technology Teaching (IPST), the Thailand Research Fund (TRF), the Center for Innovation in Chemistry (PERCH-CIC), and the Thailand Center of Excellence in Physics (ThEP). The software resource is the courtesy of National Nanotechnology Center (NANOTEC), Thailand.

Appendix A. Supplementary data

Supplementary data associated with this article can be found, in the online version, at doi:10.1016/j.jmgm.2009.11.009.

References

- L.D. Yu, T. Vilaithong, I. Brown, Introduction to Ion Beam Biotechnology. English edition, originally authored by Yu Zengliang in Chinese, Springer Science & Business Media, New York, 2006.
- [2] Z. Wei, H. Xei, G. Han, Nucl. Instrum. Methods B95 (1994) 371.
- [3] Y. Zhao, Z. Tan, G.Y. Qiu, Y.H. Du, Nucl. Instrum. Methods B211 (2003) 211.
- [4] C.A. Hunniford, D.J. Timson, R.J.H. Davies, R.W. McCullough, Phys. Med. Biol. 52 (2007) 3729.
- [5] Y. Chen, B. Jiang, X. Ding, X. Liu, C. Chen, X. Guo, G. Yin, Radiat. Environ. Biophys. 37 (1998) 101.
- [6] S. Lacomb, Sech C. Le, V.A. Esaulov, Phys. Med. Biol. 49 (2004) N65.
- [7] Z.W. Deng, I. Bald, E. Illenberger, M.A. Huels, Phys. Rev. Lett. 95 (2005) 153201.
- [8] F.A. Chacon, Ion induced radiation damage on the molecular level, Ph.D. Thesis, University of Groningen, 2007.
- [9] R. Norarat, N. Semsang, S. Anuntalabhochai, L.D. Yu, Very low-energy and low-fluence ion beam bombardment of naked plasmid DNA, Nucl. Instrum. Methods B 267 (2009) 1650–1653.
- [10] H. Ryssel, I. Ruge, Ion Implantation, Wiley Chichester, 1996.
- [11] M. Nastasi, J.W. Mayer, J. Hirvonen, Ion-Solid Interactions: Fundamentals and Applications, Cambridge University Press, 1996.
- [12] E. Hall, Radiobiology for Radiobiologists, Lippincott Williams & Wilkins, 1993.
- [13] Z. Yu, Study on the interaction of low-energy ions with organisms, Surf. Coat. Technol. 201 (2007) 8006–8013.

- [14] J. Yang, L. Wu, L. Li, et al., Sequence analysis of lacZ? mutations induced by ion beam irradiation in double-stranded M₁₃mp₁₈ DNA, Sci. China C. Life. Sci. 40 (1997) 107–112.
- [15] Q. Wang, G. Zhang, Y.H. Du, Y. Zhao, G.Y. Qiu, Low-energy (30 keV) carbon ion induced mutation spectrum in the lacZ gene of M13mp18 double-stranded DNA, Mutat. Res. Fundam. Mol. Mech. Mutagen. 528 (2003) 55–60.
- [16] C.X. Xie, A. Xu, L.J. Wu, et al., Comparison of base substitutions in response to nitrogen ion implantation and ⁶⁰CO-γ ray irradiation in *Escherichia coli*, Genet. Mol. Biol. 27 (2004) 284–290.
- [19] E.A. Kummerle, E. Pomplun, A computer-generated supercoiled model of the pUC19 plasmid, Eur. Biophys. J. 34 (2005) 13–18.
- [20] C. Bouchiat, M. Mezard, Elastic rod model of a supercoiled DNA molecule, Eur. Phys. J. E. 2 (2000) 377–402.
- [21] F. Lankas, R. Lavery, J.H. Maddocks, Kinking occurs during molecular dynamics simulations of small DNA minicircles, Structure 14 (2006) 1527–1534.
- [22] W.K. Olson, V.B. Zhurkin, Modeling DNA deformations, Curr. Opin. Struct. Biol. 10 (2000) 286–297.
- [23] L.J. Maher, Mechanisms of DNA bending, Curr. Opin. Struct. Biol. 2 (1998) 688–694.
- [24] H. Nikjoo, C.E. Bolton, R. Watanabe, et al., Modelling of DNA damage induced by energetic electrons (100 eV to 100 keV), Radiat. Prot. Dosimetry 99 (2002) 77–80.
- [25] H. Nikjoo, D. Emfietzoglou, R. Watanabe, S. Uehara, Can Monte Carlo track structure codes reveal reaction mechanism in DNA damage and improve radiation therapy? Radiat. Phys. Chem. 77 (2008) 1270–1279.
- [26] R. Watanabe, H. Nikjoo, Modelling the effect of incorporated halogenated pyrimidine on radiation-induced DNA strand breaks, Int. J. Radiat. Biol. 78 (2002) 953–966.
- [27] H. Nikjoo, P. O'Neill, W.E. Wilson, D.T. Goodhead, Computational approach for determining the spectrum of DNA damage induced by ionizing radiation, Radiat. Res. 156 (2001) 577–583.
- [28] X. Li, M.D. Sevilla, L. Sanche, Density functional theory studies of electron interaction with DNA: can zero eV electrons induce strand breaks? J. Am. Chem. Soc. 125 (2003) 13668–13669.
- [29] J.M. Falcone, D. Becker, M.D. Sevilla, S.G. Swarts, Products of the reactions of the dry and aqueous electron with hydrated DNA: hydrogen and 5,6-dihydropyrimidines, Radiat. Phys. Chem. 72 (2005) 257–264.
- [30] M. Chalfie, Y. Tu, G. Euskirchen, W.W. Ward, D.C. Prasher, Green fluorescent protein as a marker for gene expression, Science 263 (1994) 802–805.
- [31] Discovery studio 1.7.1, Accelrys Software Inc., San Diego, CA, 2006.
- [32] N. Foloppe, A.D. MacKerell Jr., All-atom empirical force field for nucleic acids: I. Parameter optimization based on small molecule and condensed phase macromolecular target data. J. Comput. Chem. 21 (2000) 86-104.
- [33] Materials Studio Modeling 4.3, Accelrys Software Inc., San Diego, CA, 2008.
- [34] H. Sun, Compass: an ab initio force-field optimized for condensed-phase applications; overview with details on alkane and benzene compounds, J. Phys. Chem. B 102 (1998) 7338–7364.
- [35] D. Rigby, H. Sun, B.E. Eichinger, Computer simulations of poly-(ethylene oxide): force field, PVT diagram and cyclization behavior, Polym. Int. 44 (1997) 311–330.
- [36] N. Metropolis, A.W. Rosenbluth, M.N. Rosenbluth, A.H. Teller, E. Teller, Equation of state calculations by fast computing machines, J. Chem. Phys. 21 (1953) 1087– 1092.
- [37] D.A. Case, T.A. Darden, T.E. Cheatham Iii, et al., AMBER 9 (2004).
- [38] M. Rueda, S.G. Kalko, F.J. Luque, M. Orozco, The structure and dynamics of DNA in the gas phase, J. Am. Chem. Soc. 125 (2003) 8007–8014.
- [39] M. Rueda, F.J. Luque, M. Orozco, Nature of minor-groove binders DNA complexes in the gas phase, J. Am. Chem. Soc. 127 (2005) 11690–11698.
- [40] A. Lebrun, R. Lavery, Modelling extreme stretching of DNA, Nucl. Acids Res. 24 (12) (1996) 2260–2267.

ARTICLE IN PRESS

SCT-15562; No of Pages 5

Surface & Coatings Technology xxx (2010) xxx-xxx



Contents lists available at ScienceDirect

Surface & Coatings Technology

journal homepage: www.elsevier.com/locate/surfcoat



Graft polymerization of flame-retardant compound onto silk via plasma jet

C. Chaiwong a,b, S. Tunma a,b, W. Sangprasert C, P. Nimmanpipug C, D. Boonyawan a,b,*

- ^a Plasma and Beam Physics Research Facility, Physics and Materials Science Department, Science Faculty, Chiang Mai University 50200, Thailand
- ^b ThEP Center, CHE, 328 Si Ayutthaya Rd., Bangkok 10400, Thailand
- ^c Chemistry Department, Science Faculty, Chiang Mai University 50200, Thailand

ARTICLE INFO

Available online xxxx

Keywords: Silk Flame retardancy Plasma jet Graft polymerization MD simulations

ABSTRACT

We investigated the application of an atmospheric pressure plasma jet to impart flame retardancy to silk fabrics. Argon plasma jet was used to graft non-durable phosphorus-based flame retardant agent (Pyrovatim® PBS) onto silk. The treated fabric showed a higher level of flame retardancy as evaluated by using 45° flammability test. To evaluate the durability, the treated silk was submitted to washing process. It was found that Ar plasma conferred durable flame retardancy to the treated silk fabric since the flame retardant character retained after the washing process. Scanning electron microscopy revealed that the yarn of the Ar treated silk was uniformly covered with the PBS particles whereas PBS deposited locally on the untreated silk. Energy dispersive X-ray spectroscopy showed the presence of phosphorus up to 11 wt.% in the Ar treated silk. Fourier transform infrared spectroscopy exhibited the bondings between phosphorus and the silk molecular chains. The molecular dynamics simulations affirmed the incorporation of phosphorus in the structure of silk.

© 2010 Elsevier B.V. All rights reserved.

1. Introduction

Over the past decades, there has been an increasing concern over the fire hazard of materials. As a consequence, the fields of textile used are subject to material flammability regulations. Improving the flame retardant property of textiles become necessary to minimize the fire hazard under many circumstances [1] . Silk is one of the most commonly used textiles for interior decoration, such as upholsteries, curtains, and beddings, for its luxurious appearance. It is therefore of primary significance to improve the flame retardant property of silk fabrics in which the safety regulations are concerned. Flame retardant fabrics are typically prepared by treating the fabrics chemically with flame retardant agents. Phosphorous-based compounds are the most extensively used [2-5]. For natural fiber textiles, a number of studies focus on flame retardant property of cotton fabrics [3,4,6-8] and silk fabrics [9-11]. It was shown that a high level of flame retardancy could be achieved when silk fabric was treated by a reaction mixture of urea and phosphoric acid through pad/dry process [9]. However, the treated silk had limited laundering durability. The flame retardant agent under the commercial name "Pyrovatex CP" which is N-hydroxymethyl (3-dimethylphosphono) propionamide (HDPP) was applied to induce flame retandancy on silk [10,12]. This compound needs formaldehyde, which is one of human carcinogens [13], as the bonding agent. Recently, the use of formaldehyde-free flame retardant finishing process was developed [11]. The treated silk shown improved flame reatadancy with limited laundering durability. Although varying degrees of flame retardancy were obtained, the durability is difficult to solve. It is even more problematic when the textiles are from natural origins. The development of satisfactory, durable flame retardant silk is indeed challenging and the alternative eco-friendly processes have to be considered.

Plasma treatment is a potential technique to impart flame retardant properties to textiles. The reactive species in the plasma interact with the surface atoms or molecules and modify the surface properties without affecting bulk properties. Recently, it was reported that microwave plasma had been employed in the flame retardant finishing process [8,14]. However, low pressure plasma systems need to operate under vacuum which, in turns, add the cost and complexity to the process. Atmospheric pressure plasma source is an alternative system. A few different designs have been developed and employed to modify the surface of materials [15–18]. The system is promising to industrial application since the vacuum system is eliminated.

In this work we utilized an atmospheric pressure plasma jet to graft phosphorus-based flame retardant agent onto silk. The treated silk fabrics were submitted to 45° flammability test. The incorporation of phosphorus was studied via quantum simulations and Energy-Dispersive X-ray spectroscopy (EDS). The durability of the treatment was evaluated.

2. Experimental

2.1. Materials

Silk fabric (Grazie $^{\text{TM}}$) of a density 52.9 g/m 2 was provided by Tanapisarn Pty. Ltd. (Bangkok, Thailand). It has a warp density and a

0257-8972/\$ – see front matter © 2010 Elsevier B.V. All rights reserved. doi:10.1016/j.surfcoat.2010.02.044

^{*} Corresponding author. Plasma and Beam Physics Research Facility, Physics and Materials Science Department, Science Faculty, Chiang Mai University 50200, Thailand. *E-mail address:* dherawan@chiangmai.ac.th (D. Boonyawan).

weft density of 129 and 99 per inch respectively. The air penetration resistance was $98.4 \, \mathrm{cm^3/cm^2 \cdot s}$ indicating that the silk has high air resistance. The fabric was cut into $5 \, \mathrm{cm} \times 17 \, \mathrm{cm}$ samples. Non-durable flame retardant compound under the trade name "Ciba® Pyrovatim® PBS" was supplied by Huntsman (Thailand) Ltd. (Samutsakorn, Thailand). The finishing solution was prepared by mixing the compound with distilled water at 50% wt/wt. Before the treatment, the samples were immersed in acetone for $5 \, \mathrm{min}$ and air dried.

2.2. Methods

2.2.1. Plasma jet system

A self-made plasma jet system used in this experiment is shown schematically in Fig. 1. The inner hollow electrode covered with a quartz tube was centred at the axis of the outer electrode. The inner electrode was connected to a 50 kHz, 0–10 kV voltage source whereas the outer electrode was grounded. Argon were used as a plasma gas with adjustable flow rate from 2 to 10 L/min. The plasma jet was monitored by using a S2000 fibre optics spectrometer (Ocean Optics Inc, USA). The fibre optics probe was placed at right angle to the jet axis at a distance of 5 mm away. The emission spectrum of the plasma was collected at 0.3 nm resolution.

2.2.2. Flame retardant compound grafting

Ar plasma jet was initiated at 8 kV with 4 L/min. These parameters were kept constant for all of the Ar treatments. The sample surfaces was pre-activate for 5 min with Ar plasma. The distance between the nozzle and the sample was set at 5 mm. After Ar pre-treatment, the samples were immersed in the finishing solution of PBS for 10 s and air dried at 60 °C for 10 min. Graft polymerization was performed with Ar plasma for 5 min. These samples were designated as A-PBS-AR silk. The samples were finally immersed in ethanol to remove the residual un-grafted molecules and dried in air at room temperature. For comparison, samples without Ar pre-treatment, directly immersed in the PBS solution were prepared and designated as PBS silk.

2.2.3. Washing stability testing and flame retardancy testing

To evaluate the laundering durability of the flame retardancy, the samples were washed according to TIS-121 (3–1975) in an 1 g/L solution of commercial non-ionic detergent and tap water and at 35 °C for 30 min. The samples were air dried and stored in a desiccator until required. Flammability tests were performed by means of a selfmade 45° tester, according to ASTM D1230. Burning behavior and flame spread rate were recorded.

2.2.4. Surface characterization and chemical composition analysis

Scanning electron microscopy (SEM) and energy dispersive x-ray spectroscopy (EDS) were used to examine the surface of the samples and well as the chemical composition before and after the washing

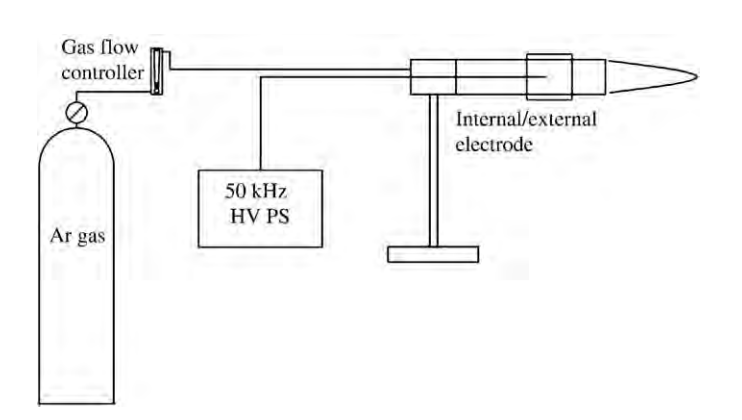


Fig. 1. Schematic view of self-made plasma jet system.

process. The SEM used in this work was a JSM 633S (Jeol, Japan) equipped with EDS.

Additionally, Fourier transform infrared spectroscopy (FTIR) was done to extract the chemical bonding on the surface of the samples. The IR spectra were obtained by using a Nicolet 6700 FTIR spectrophotometer (Bruker, Germany) operated in attenuated total reflectance (ATR) mode. The spectra were collected by averaging 64 scans at a resolution of $4 \, \mathrm{cm}^{-1}$ from $400-4000 \, \mathrm{cm}^{-1}$.

2.2.5. Molecular dynamic (MD) simulation of silk structure

To study the chemical bonding between PBS and the silk structure, MD simulation was performed. The simulation to predict the IR spectrum of silk after the incorporation of PBS was carried out to envisage the interactions. Silk model was generated using repeating glycine-alanine unit as discussed in the previous study [19]. Material Studio 4.3 software was used to build the model and perform energy minimization and MD simulations of the macroscopic structure of silk polymer containing 5 chains of 10-unit glycine-alanine in a periodic box of 30×30×30 Å³ using COMPASS forced field. Energy minimization was carried out to eliminate the potential energy which might arise as a result of the interaction with the neighboring chains with conjugate gradient method. After the minimized cell was obtained, the simulated annealing with Metropolis Monte Carlo (MC) method of Sorption module was designed to simulate the interaction between PBS and the silk model. The cut off distance was set at 12.5 Å for micro canonical ensemble. Trajectories from the MC simulation were collected for radial distribution analysis.

To predict the IR spectrum of silk after plasma treatment process, quantum calculation of silk model compound modified by PBS predicted product from MD simulation was performed using GAUSSIAN 03[20]. B3LYP/6-31G (d) level of density functional theory (DFT) was used to calculate optimized structure and IR frequencies.

3. Results and discussion

3.1. Ar plasma jet diagnostic

The emission spectrum of the Ar plasma jet measured at the sample position which is 5 mm from the jet nozzle is shown in Fig. 2. It can be seen that the spectrum in the wavelength range of 250–850 nm was dominated by excited argon (Ar I) peaks. In addition, reactive radical peaks including hydroxyl (OH) and atomic oxygen were found at 308.9 nm and 777.1 nm, respectively. Ambient species, such as N_2 , were also observed. The presence of these radicals was undesirable

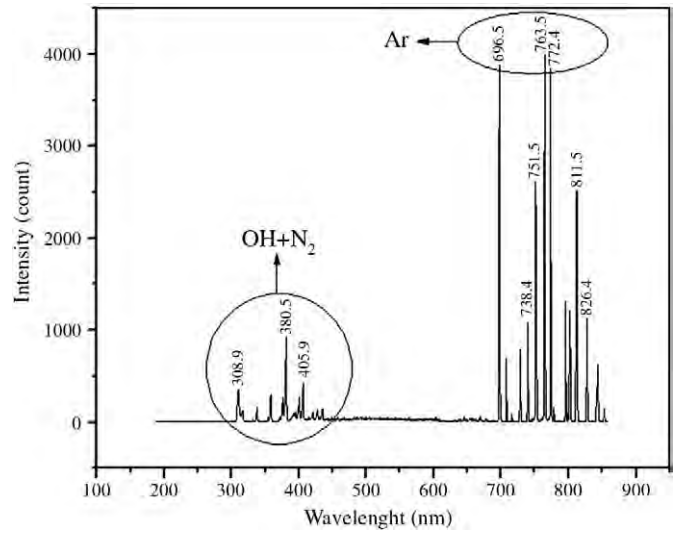


Fig. 2. Ar plasma emission spectrum at sample position from plasma jet.

C. Chaiwong et al. / Surface & Coatings Technology xxx (2010) xxx-xxx

since they might react with the surface of the samples. However, the emergence of these species could be controlled by the system parameters. For example, the OH band was drastically suppressed if the discharge voltage increased. The Ar flow rate was one of the parameters that affects the presence of radical species. It was found that excited N_2 peaks appeared more intense than OH radicals if the Ar flow rate was over 6 L/min.

3.2. Flammability test

Fig. 3 shows the burning behavior of the silk samples. The samples prepared with different procedures were tested. In the case of untreated silk, the sample ignited instantly with a rapid flame spread of 1.43 cm/s. The flame extended to the entire sample without burning smoke. For the sample directly immersed in PBS solution (PBS silk), the ignition character was identical to that of the untreated sample but the flame spread terminated immediately. The sample did not exhibit the afterglow. Burning smoke, as a consequence of char formation, was observed. The char formation is an indication of phosphorus containing residue on the surface of the sample [8]. The compound decomposed to polyphosphoric acid when heated and

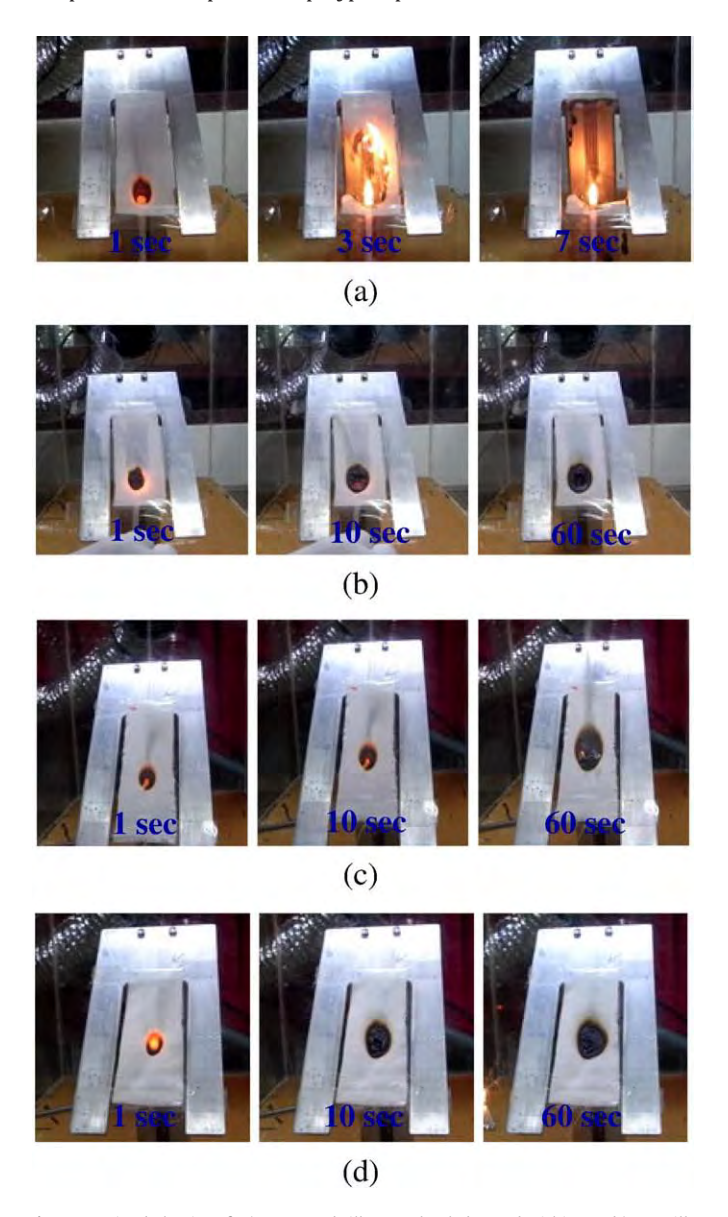


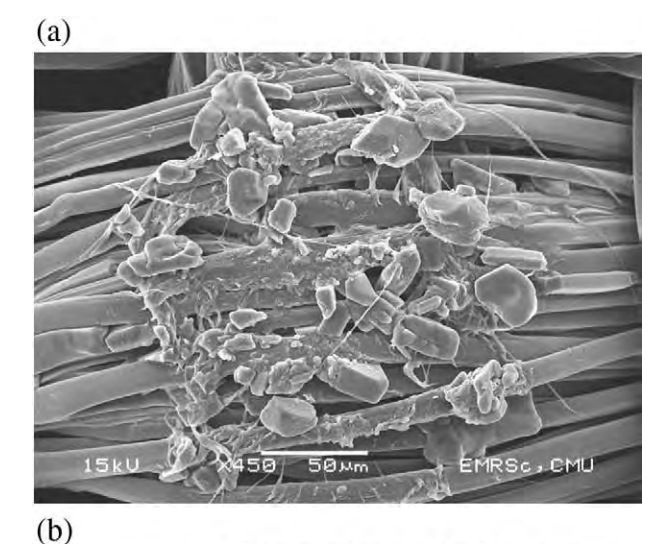
Fig. 3. Burning behavior of; a) untreated silk, completely burned within 7 s; b) PBS silk; c) washed Ar-PBS-Ar silk and; d) ethanol wash only.

formed a viscous surface layer. This layer prevents oxygen to reach the silk fiber. As a consequence the fiber decomposition is inhibited.

After the washing process the burning behavior of the PBS silk was similar to that of the untreated sample. Some burning smoke was observed. This is due to the fact that PBS is water soluble, thus it can be removed from the silk during the washing process. The smoke indicated that some PBS remained in the silk. In contrast, the Ar-PBS-Ar silk behaved differently. Its flame spread rate was higher than the PBS sample. However, the flame vanished immediately without the afterglow. The char formation was observed. The burning smoke was dramatically reduced to the amount that is close to the untreated sample. Since burning smoke mainly comes from the residual PBS on the surface of the sample, it can be said that most of the PBS molecules were grafted homogeneously into the silk molecular chains by the Ar plasma. Washing process might take away the un-grafted PBS molecules from the silk structure but the majority remained intact in the silk structure. Hence, with adequate level of grafted PBS molecules, silk samples can generate char to prevent flame spread without excess burning smoke.

3.3. Surface and chemical composition analysis

By comparing the SEM micrographs of the PBS silk (Fig. 4(a)) and the washed Ar-PBS-Ar silk Fig. 4(b), the grafting of PBS can be observed. As shown in Fig. 4(a), PBS particles deposited locally on the knot of the silk yarn. The surface topography along the yarn was relatively smooth. In contrast, the yarn of the washed Ar-PBS-Ar silk was rough and uniformly covered with the PBS particles. It is evident that the durable flame retardant property of silk can be obtained via Ar plasma grafting.



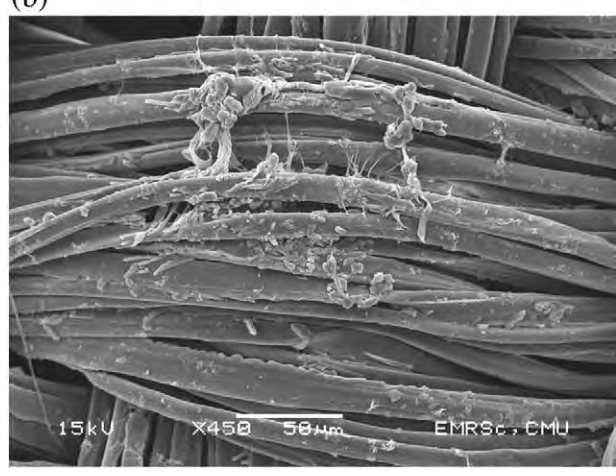


Fig. 4. SEM micrograph of; a) PBS silk and; b) washed Ar-PBS-Ar silk.

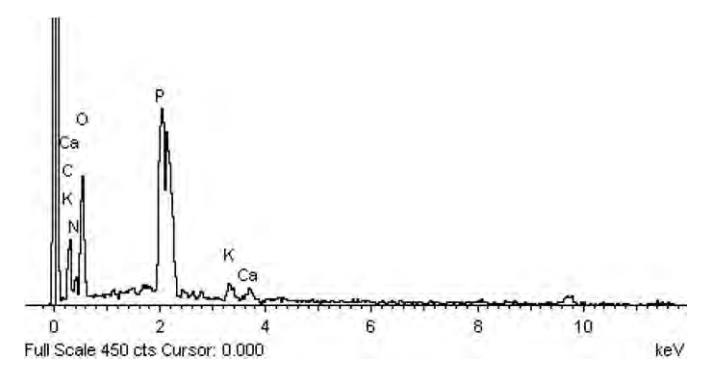


Fig. 5. The EDS spectrum of washed Ar-PBS-Ar silk (Au peak was not subtracted.).

Fig. 5 shows the EDS spectrum obtained from the deposit on the yarn knot of the PBS silk. The spectrum showed evidence of phosphorus arising from PBS compound. Peaks of silk compositions, such as N, C, and O, were revealed. Calcium is one of the fingerprints of natural silk. Quantitative analysis of phosphorus content in the samples was done by means of EDS. The phosphorus content in the Ar-PBS-Ar was found to be 11% weight higher than that in the PBS silk, whose phosphorus content was 7% weight. This high level of phosphorus content in the Ar-PBS-Ar silk remained constant after the washing process. The results clearly indicate that in order to achieve durable flame retardant property, graft polymerization is necessary. The Ar plasma jet used in this work allowed us to bind covalently the flame retardant compound to the silk fabric. One can say that after the washing process, the Ar-PBS-Ar sample was similar to the ordinary silk with addition flame retardant property.

The washed Ar-PBS-Ar silk sample has been characterized by ATR-FTIR in comparison with the untreated as shown in Fig. 6. Graft-polymerization via Ar plasma was indicated by the presence of bands at 1196 cm⁻¹ (C–O stretching vibration), 1078 cm⁻¹ and 919 cm⁻¹ (P–O–C stretching vibration). The PO stretching vibration that indicates the PBS compound overlapped within the C–O band. The IR peak intensity changes seem relatively low indicated the very thin layer of graft-PBS on silk surface from plasma treatment.

3.4. MD simulation results

The interactions between PBS and silk was investigated through MC simulation using model shown in Fig. 7. The most probable structure from MC simulation indicated that the reactive oxygen atom

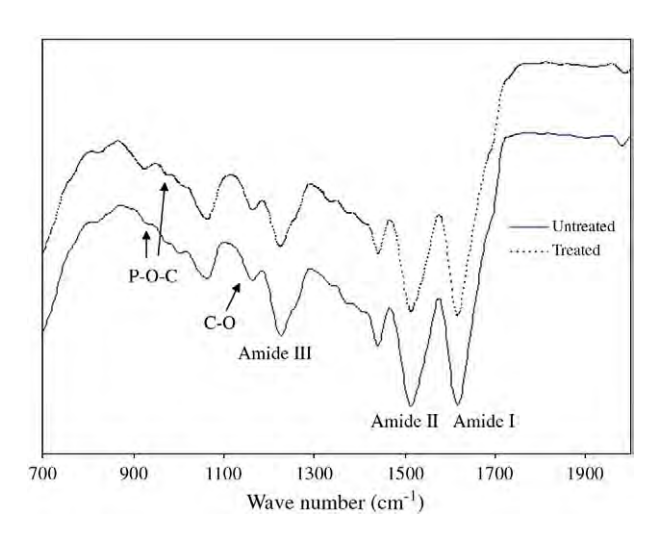


Fig. 6. ATR-FTIR spectra of untreated and washed Ar-PBS-Ar silk.

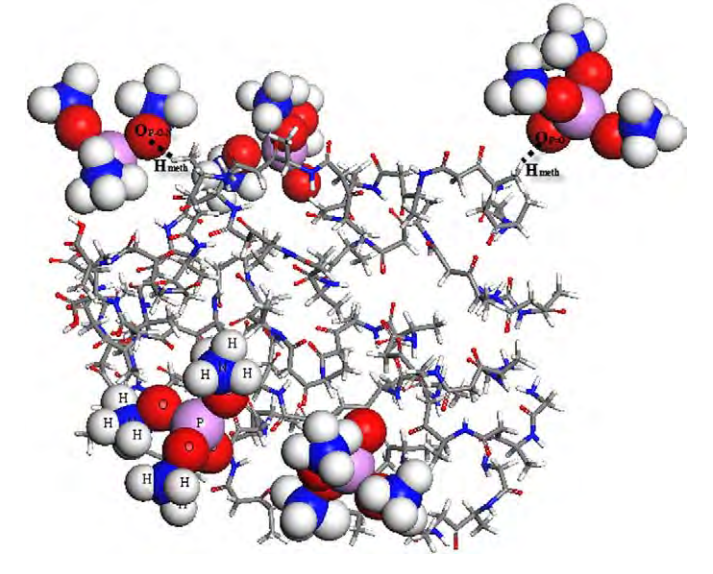


Fig. 7. Complex structure of silk model and PBS molecules system from Monte Carlo Simulated Annealing, dash line indicate strong interaction of P O and P–O–N in PBS with methyl group in silk at distance 2.50–2.60 **Å**.

in P O and P-O-N part of PBS molecule tend to react with silk polymer surface at methyl group of alanine unit.

The radial distribution function (RDF) plot (Fig. 8) of H_{meth} – $O_{O\,P}$ and H_{meth} – O_{P-O-N} represent P O and P–O–N in PBS surrounding methyl group in silk, RDF calculated from collected trajectories suggest that the distribution of PBS around silk was contributed from strong interaction of P O and P–O–N in PBS with methyl group in silk. The graph infers that H_{meth} – $O_{O\,P}$ dominate intermolecular interaction in term of hydrogen bonding from strongest electrostatic interaction of partial negative oxygen and partial positive hydrogen with shell of interaction at 3.25 Å. On the other hand, H_{meth} – O_{P-O-N} interaction is mostly diffuse with radius around 4–9 Å. Therefore P O group of PBS should react with methyl group of alanine residue in silk.

Product of PBS reacting with silk was deduced using above mentioned evident as shown in Fig. 9 in comparison with silk model. The use of calculations level at B3LYP/6-31G(d) show C O stretching at 1777 and 1844 cm $^{-1}$, the stretching of C–O bond presents at 1196 cm $^{-1}$ while group of N–H bending and C–N stretching was found in range of 1200–1700 cm $^{-1}$ for both untreated and PBS silk. The P–O–C stretching vibration at 1078 cm $^{-1}$ and medium peak of P–O–C stretching vibration at 919 cm $^{-1}$ were found correlated well with previous studies [21,22] .

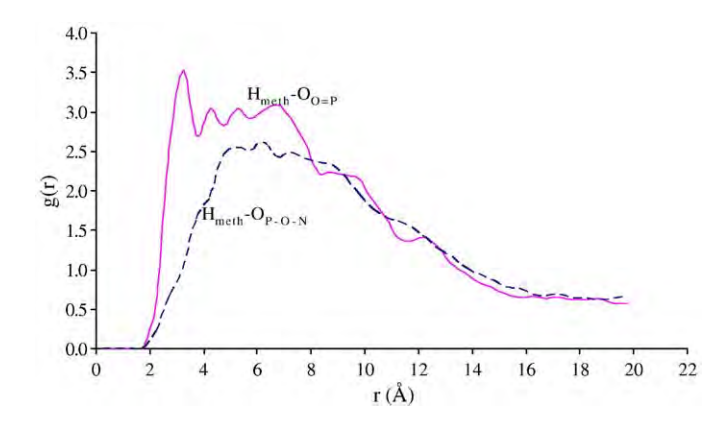


Fig. 8. Radial distribution function of $H_{meth}-O_{O=P}$ and $H_{meth}-O_{P-O-N}$ represent P=O and P-O-N in PBS surrounding methyl group in silk.

C. Chaiwong et al. / Surface & Coatings Technology xxx (2010) xxx-xxx

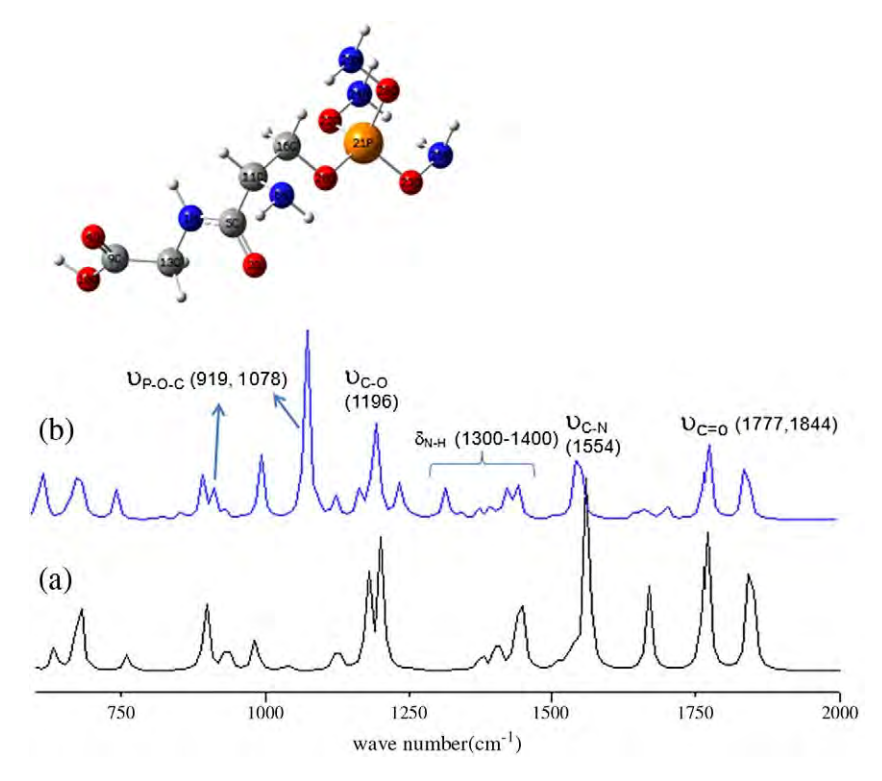


Fig. 9. Vibration spectrum of silk and propose product after treated structure calculated by using B3LYP/6-31G(d); a) untreated silk and; b) PBS silk.

4. Conclusions

The flame retardant property of silk fabrics induced by grafting of flame retardant compound using Ar plasma jet has been investigated. It has been shown that Ar plasma grafting is a necessary procedure to achieve the durable flame retardant property. Ar plasma grafting conferred endurable flame retardant property to silk fabric. The good washing stability could be attributed to the presence of phosphorus that was covalently bound to the silk structure. The MD simulations affirmed the covalent bonds between phosphorus and molecular chains of silk since the predicted IR spectrum agree well with the measured one.

References

- [1] I.S. Wichman, Prog. Energ. Combust. 29 (2003) 247.
- [2] H. Yang, C.Q. Yang, Polym. Degrad. Stabil. 88 (2005) 363.
- [3] S. Gaan, G. Sun, J. Anal. Appl. Pyrol. 78 (2007) 371.
- [4] W. Wu, C.Q. Yang, Polym. Degrad. Stabil. 92 (2007) 363.
 [5] A.R. Horrocks, D. Price, Camb. Woodh. Publ. Limit. (2001), ISBN:1855734192.
- P.R.S. Reddy, G. Agathian, A. Kumar, Radiat. Phys. Chem. 72 (2005) 511.
- W. Wu, C.Q. Yang, Polym. Degrad. Stabil. 91 (2006) 2541.
- M.J. Tsafack, J. Levalois-Grützmacher, Surf. Coat. Technol. 201 (2006) 2599.
- [9] W.B. Achwal, C.R. Mahapatrao, P.S. Kaduska, Colourage 6 (1987) 16.
- [10] T. Kako, A. Katayama, Nippon Sanshigakul Zasshi. 64 (1995) 124.
- [11] J. Guan, C.Q. Yang, G. Chen, Polym. Degrad. Stabil. 94 (2009) 450.

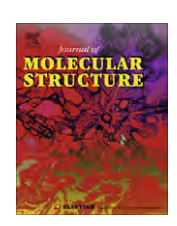
- [12] J. Guan, G.Q. Chen, Fire Mater. 30 (2006) 415.
- P. H. S. U.S. Department of Health and Human Services, National Toxicology Program, Public Health Service, National Toxicology Program, 2009.
- M.J. Tsafack, J. Levalois-Grützmacher, Surf. Coat. Technol. 200 (2006) 3503.
- C. Cheng, Z. Liye, R.-J. Zhan, Surf. Coat. Technol. 200 (2006) 6659.
- J. Schafer, R. Foest, A. Quade, A. Ohl, K.-D. Weltmann, J. Appl. Phys. 194010 (2008). X. Guimin, Z. Guanjun, S. Xingmin, M. Yue, W. Ning, L. Yuan, Plasma Sci. Technol.
- [18] K. Osaki, S. Fujimoto, O. Fukumasa, Thin Solid Films Proceedings of the Joint International Plasma Symposium of the 6th APCPST, the 15th SPSM and the 11th Kapra Symposia, vol. 435, 2003, p. 56.
- P. Khomhoi, W. Sangprasert, V.S. Lee, P. Nimmanpug, Chiang Mai J. Sci. 37 (1)
- M.J. Frisch, G.W. Trucks, H.B. Schlegel, G.E. Scuseria, M.A. Robb, J.R. Cheeseman, J.A. Montgomery, Jr., T. Vreven, K.N. Kudin, J.C. Burant, J.M. Millam, S.S. Iyengar, J. Tomasi, V. Barone, B. Mennucci, M. Cossi, G. Scalmani, N. Rega, G.A. Petersson, H. Nakatsuji, M. Hada, M. Ehara, K. Toyota, R. Fukuda, J. Hasegawa, M. Ishida, T. Nakajima, Y. Honda, O. Kitao, H. Nakai, M. Klene, X. Li, J.E. Knox, H.P. Hratchian, J.B. Cross, V. Bakken, C. Adamo, J. Jaramillo, R. Gomperts, R.E. Stratmann, O. Yazyev, A.J. Austin, R. Cammi, C. Pomelli, J.W. Ochterski, P.Y. Ayala, K. Morokuma, G.A. Voth, P. Salvador, J.J., V.G. Zakrzewski, S. Dapprich, A.D. Daniels, M.C. Strain, O. Farkas, D.K. Malick, A.D. Rabuck, K. Raghavachari, J.B. Foresman, J.V. Ortiz, Q. Cui, A.G. Baboul, S. Clifford, J. Cioslowski, B.B. Stefanov, G. Liu, A. Liashenko, P. Piskorz, I. Komaromi, R.L. Martin, D.J. Fox, T. Keith, M.A. Al-Laham, C.Y. Peng, A. Nanayakkara, M. Challacombe, P.M.W. Gill, B. Johnson, W. Chen, M.W. Wong, C. Gonzalez, J.A. Pople, Gaussian 03, Revision C. 02, Gaussian, Inc., Wallingford, CT, (2004).
- S. Zanini, C. Riccardi, M. Orlandi, C. Colombo, F. Croccolo, Polym. Degrad Stabil. 93 (2008) 1158.
- [22] X.P. Zou, E.T. Kang, K.G. Neoh, Surf. Coat. Technol. 149 (2002) 119.

ELSEVIER

Contents lists available at ScienceDirect

Journal of Molecular Structure

journal homepage: www.elsevier.com/locate/molstruc



Sulfur hexafluoride plasma surface modification of Gly-Ala and Ala-Gly as *Bombyx mori* silk model compounds: Mechanism investigations

W. Sangprasert a, V.S. Lee a, D. Boonyawan b, K. Tashiro c, P. Nimmanpipug a,*

- ^a Department of Chemistry, Faculty of Science, Chiang Mai University, Chiang Mai 50200, Thailand
- ^b Department of Physics, Faculty of Science, Chiang Mai University, Chiang Mai 50200, Thailand
- ^c Department of Future Industry-Oriented Basic Science and Materials, Graduate School of Engineering, Toyota Technological Institute, Tempaku, Nagoya 468-8511, Japan

ARTICLE INFO

Article history:
Received 20 August 2009
Received in revised form 5 October 2009
Accepted 16 October 2009
Available online 20 October 2009

Keywords: Bombyx mori silk Plasma treatment DFT Transition state searching

ABSTRACT

Low-pressure plasma has been used to improve the hydrophobicity of Thai silk. In this study, Glycine–Alanine (GA) and Alanine–Glycine (AG) were chosen to represent model compounds of Bombyx mori silk. Single crystals of the simplified model compounds were characterized by polarizing microscopy and X-ray diffraction. The space groups of $P2_12_12_1$ and $P2_1$ were found for AG and GA, respectively. The initial structures for calculation were obtained from the experimental crystal structures. Density functional theory at the BHandHLYP levels was used to investigate possible mechanisms of fluorine radicals reacting with AG and GA in the SF₆ plasma treatment. The results indicate that hydrogen atoms of silk model compounds were most likely to be abstracted from the alanine residue.

© 2009 Elsevier B.V. All rights reserved.

1. Introduction

During the past several decades, of SF₆ plasma has been employed to improve the hydrophobic properties of Thai silk [1–3]. Natural fibres are in general delicate and cannot be treated under extreme conditions. Plasma processing of textiles should thus be performed through low-pressure RF discharges of suitable gases. The resulting water absorption properties have been found to depend upon the treatment time, radio frequency (RF) power and gas pressures [2].

Thai silk, which is derived from the silk moth *Bombyx mori*, has a heavy chain that consists mainly of glycine (44%) and alanine (30%) [4–8]. The crystal structure of silk fibroin has been examined by several research groups using the constrained least-squares refinement [9]. The simplest model consistent with the X-ray scattering pattern is Gly-Ala or Ala-Gly [8]. Although these structures were solved earlier by Tranter et al. and Naganathan and Venkatesan [10–16], the Gly-Ala structure is polymorphic, indicating the flexibility and the potential of possible alternate structures.

Low-pressure plasma treatment is an environmental friendly process used for modification of wettability, shrink resistance, interfacial adhesion, hydrophilicity and dyeing properties of polymeric materials [17–22]. The main species of such plasmas have been delineated by Picard, who indicated three kinds of energetic species reacting on the polymer surface: neutral molecules, ions,

* Corresponding author. E-mail address: piyaratn@gmail.com (P. Nimmanpipug). and an electron density [23]. The studies of Joubert and Frank suggested that the reaction mechanism at the material surface in a plasma system was a two-step process for energetic species of fluorine reacting with the polymer surface [24,25].

In 2001, Selli et al. proposed a reaction mechanism for the silk surface treated with SF₆ plasma. The reaction is initiated by very active species present in the plasma, such as ions, radicals, electrons and photons, most probably via a two-step replacement of hydrogen atoms. Using XPS, the ratios of F/C, O/C and N/C were determined [26]. The F/C ratio steadily increased with an increase of treatment time and pressure, while the O/C and N/C ratios exhibited no change following exposure to plasma. In 2001, Selli et al. reported hydrophobicity improvement of silk achieved by SF₆ plasma treatment as reflected in the water repellence property measured by water contact angle [26,1,2]. In addition, a molecular model of B. mori silk and the fluorine atoms after the plasma treatment was investigated from the fundamental quantum mechanical level. Ouantum mechanical calculations were applied to investigate the surface state of the plasma treated silk, using model compounds with similar chemical structure as that of B. mori silk. The most plausible structures of fluorine radicals were extracted to examine the chemical reaction $CH + F^- \rightarrow CF + H^-$ [27]. To understand the mechanism of fluorine atoms in an SF₆ plasma reacting with the silk surface, computational methods such as DFT have the potential to produce very accurate results at low cost [27–30].

One way to study complicated polymer structures is to use model compounds of polymeric crystalline structures. Tashiro et al. reported that both poly-*para*-phenyleneisophthalamide

(PPTA) and poly-*meta*-phenyleneisophthalamide (PMIA) crystal structures can be well represented by computer simulations using the software Polymorph Predictor [31–34]. The present study thus aims to investigate the water repellent properties of *B. mori* silk, using model compounds and computer simulation. The model compounds Gly-Ala (GA) and Ala-Gly (AG) were employed in order to investigate the chemical modification of the silk surface resulting from the SF₆ plasma treatment process. Single crystals of the silk model compounds were prepared and their 3D structures elucidated. In parallel, from a theoretical point of view, QM calculations using the DFT method were used to investigate adsorption, interaction and possible mechanisms for the interaction of GA and AG with the fluorine radical (F).

2. Materials and methods

2.1. The plasma process

Powder of the simplified model compounds, $NH_2CH_2CON-HCH(CH_3)COOH$ and $NH_2CH(CH_3)CONHCH_2COOH$ (GA and AG), were purchased from Sigma–Aldrich. The powdered forms were pressed into pellets with a hydraulic force of 10 and 7 N, respectively [28]. The pellets were exposed to SF_6 plasma, which was produced by an inductively coupled RF discharge at 13.56 MHz, as

described elsewhere [3]. The RF generator, a Dressler model HPG1365, was connected to an antenna through a matching network. The diameter of the quartz chamber was 10 cm and the length was 16 cm. The operating gas, SF₆, was fed through a needle valve for operating pressure adjustment. The base pressure of the system was 1.6 mTorr.

The treatment conditions were optimized via adjustment of three parameters: pressure, RF power and treatment time. The optimum conditions were chosen in respect to the water absorption time. The hydrophobicity was studied through a contact angle of a 10 μ L water droplet on the treated sample.

2.2. Recrystallization and characterization

Single crystals of GA and AG were recrystallized using a mixture of water and dimethylsulfoxide as a solvent, followed by evaporation at room temperature. The obtained single crystal was first evaluated by using a microscope with a polarizing attachment, up to $40 \times$ magnification. The crystal was sealed with epoxy adhesive to prevent degradation from moisture during the X-ray. The crystal structure of AG was obtained by single crystal X-ray diffraction (NONIUS: FR590) operated at 50 kV tube voltage and 30 mA tube current, Mo K α radiation with diffraction angle 2θ , a scanning rate of 2° /min using the MAXUS software [35]. The crystal

Fig. 1. H-abstraction of fluorine radical SF₆ plasma reacting with the silk model compounds (GA and AG).

structure of GA was obtained by single crystal X-ray diffraction (Rigaku/MSC and Rigaku Corporation. 2004) operated under the same conditions, using the Crystal Structure 3.7.0, Single Crystal Structure Analysis Software.

2.3. Quantum mechanics (QM) calculation

Molecular conformations reported from untreated singles crystals via X-ray crystallographic data were used to represent the

reactants of reactions under plasma treatment. The ground state molecular minimization and transition state optimization reported here were performed using the GAUSSIAN-03 programs, while the Material Studio 4.3 program package [36,37] was used for transition state location with spin unrestricted calculations. The reaction pathway of silk model compounds treated with plasma ions was investigated using Beck-Lee Yang Parr (BLYP) functional of the Generalize Gradient Approximation (GGA) in DMol3 module of the Material Studio program (Fig. 1). The linear synchronous tran-

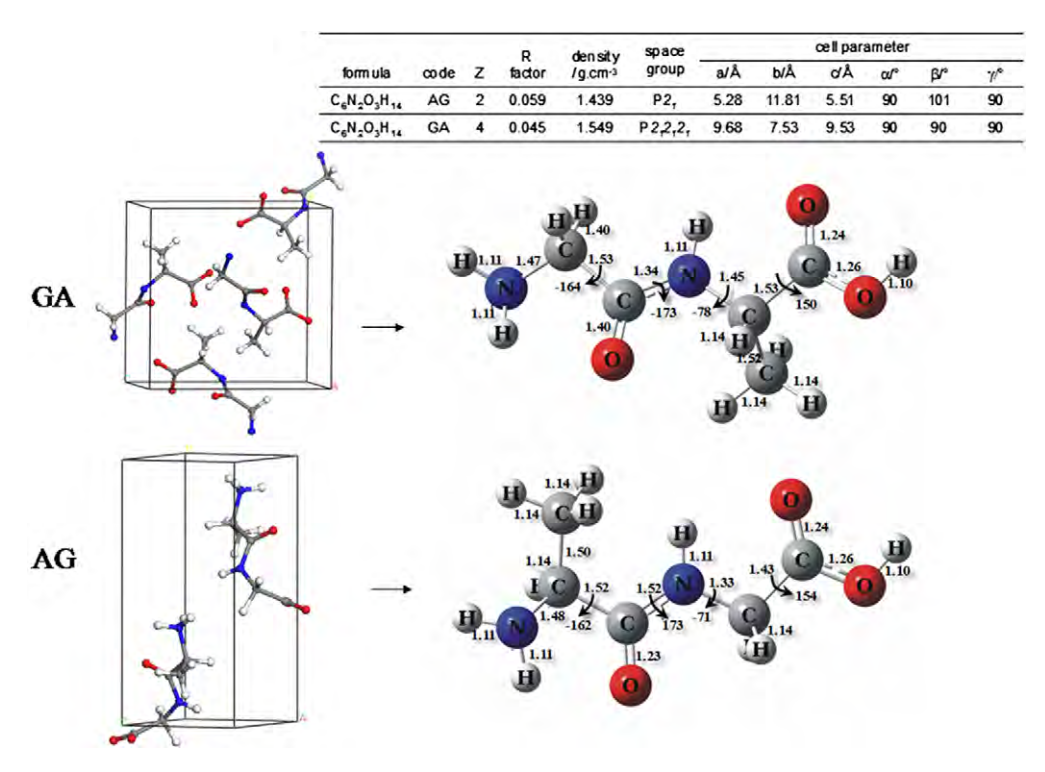


Fig. 2. The crystal structures of untreated GA and AG and corresponding cell parameters using single crystal X-ray diffraction technique.

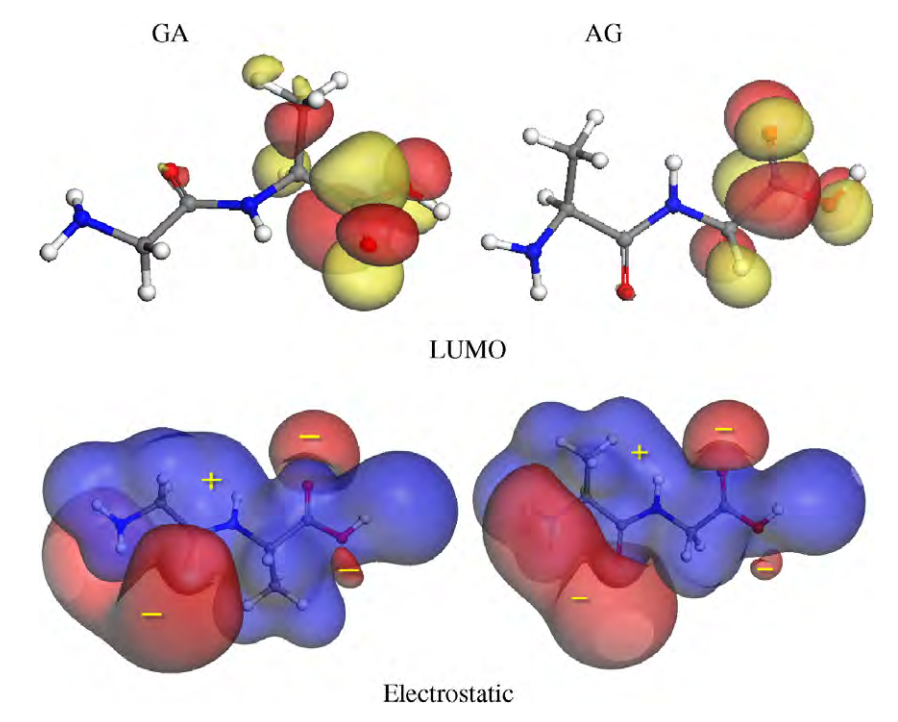


Fig. 3. (a) Initial silk model compound structures, (b) profiles of HOMO and LUMO and (c) electrostatic profiles of GA and AG.

sit (LST) and quadratic synchronous transit (QST) methods were used to study the transition state. A Fermi smearing of 0.005 Hartree was used to improve computational performance. Frequency analysis at the same level determines the nature of the stationary points and each transition state with one imaginary frequency. To fulfill the exchange term in calculations for radicals, hybrid DFT

methods with high content of the orbital exchange Beck-half-and-half-Lee Yang Parr (BHandHLYP) level [38,39] of density functional theory with aug-cc-pVDZ basis set was used to calculate the energy of each stationary structure. The obtained transition state structures were confirmed through intrinsic reaction coordinate (IRC) methods with 2 Å forward and reverse distances.

Table 1The relevant energy values of the species, the activation energies and the thermodynamic state functions involved in six reactions. All energies presented in kcal/mol.

Compounds	E ⁽⁰⁾ Total	$E_{\rm ZPE}$	H ²⁹⁸	G^{298}	Compounds	E ⁽⁰⁾ Total	$E_{\rm ZPE}$	H ²⁹⁸	G^{298}
ւ-Ala-Gly	-333516.81	102.85	109.24	81.57	Gly-Ala	-333508.62	102.01	108.29	80.81
F radical	-62580.97	_	1.48	-9.30	F radical	-62580.97	-	1.48	-9.30
IMr1	-396087.26	103.45	110.65	80.44	IMr1	-396077.87	101.99	109.20	78.83
IMr2	-396080.89	103.44	111.12	79.83	IMr2	-396123.43	106.76	114.60	82.27
IMr3	-396114.14	105.15	112.98	80.55	IMr3	-396120.39	106.39	114.42	81.33
TS1	-395998.68	97.39	104.61	74.06	TS1	-396042.93	98.67	105.81	75.69
TS2	-396039.20	98.19	105.74	74.61	TS2	-396100.20	99.94	107.69	76.67
TS3	-396103.06	99.79	107.63	76.00	TS3	-396110.13	101.08	108.71	77.41
IMp1	-396128.24	102.56	110.45	77.15	IMp1	-396131.44	103.19	110.87	79.28
IMp2	-396088.58	102.03	109.39	78.70	IMp2	-396164.49	105.56	113.50	81.22
IMp3	-396132.93	103.74	111.69	79.29	IMp3	-396131.49	103.19	110.87	79.28
P1	-333110.27	94.65	100.90	73.08	P1	-333101.76	94.99	101.34	73.39
P2	-333121.29	95.48	102.12	73.32	P2	-333111.22	95.14	101.93	73.07
P3	-333115.54	96.05	102.81	73.83	P3	-333105.71	95.29	101.92	73.36
HF	-63014.49	5.88	7.96	-4.41	HF	-63014.49	5.88	7.96	-4.41
AG	Path 1	Pa	th 2	Path 3	GA	Path 1		Path 2	Path 3
Activation energy	82.51		36.43	5.71	Activation ener	gy 31.62		16.40	4.94
H reaction	-28.83	-4	40.12	-33.11	H reaction	-28.26		-36.98	-31.33
G reaction	-32.90	-4	42.85	-36.01	G reaction	-30.32		-39.94	-34.00

IMr, intermediate reactant; IMp, intermediat product; TS, transition state; P, product; HF, hydrogen fluoride; $E_a = E_{TS} - E_{IMr}$; $\Delta H_{reaction} = \sum [H(T) + E]_{product} - \sum [H(T) + E]_{reactant}$; $\Delta G_{reaction} = \sum [G(T) + E]_{product} - \sum [G(T) + E]_{reactant}$.

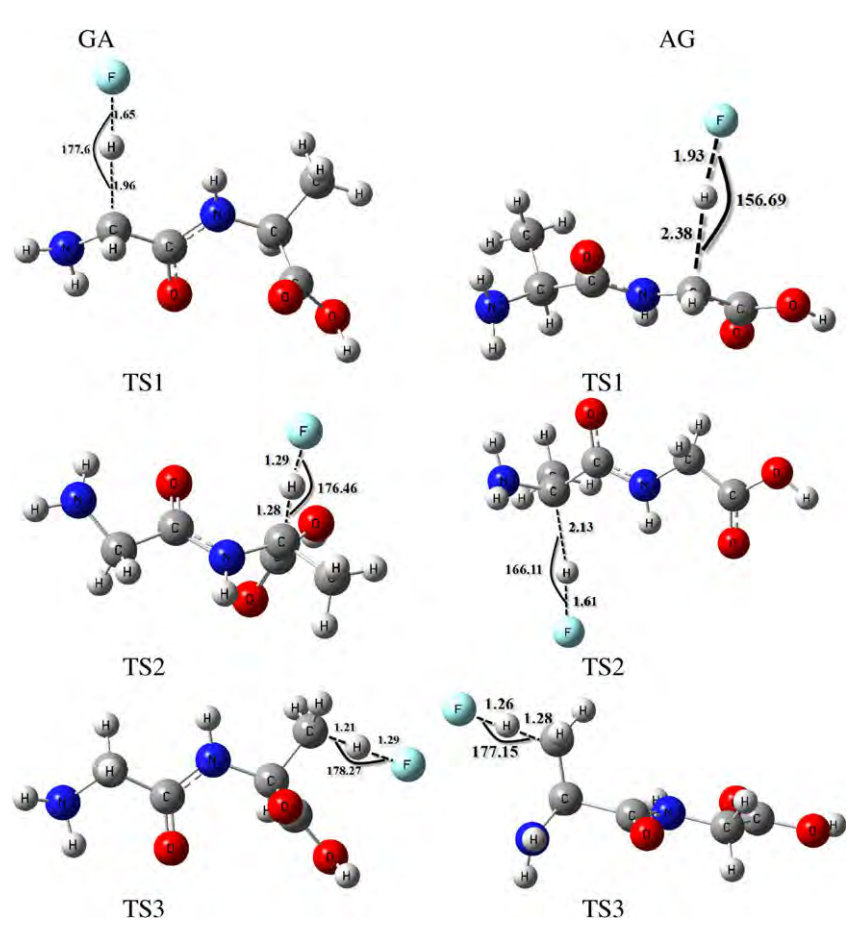
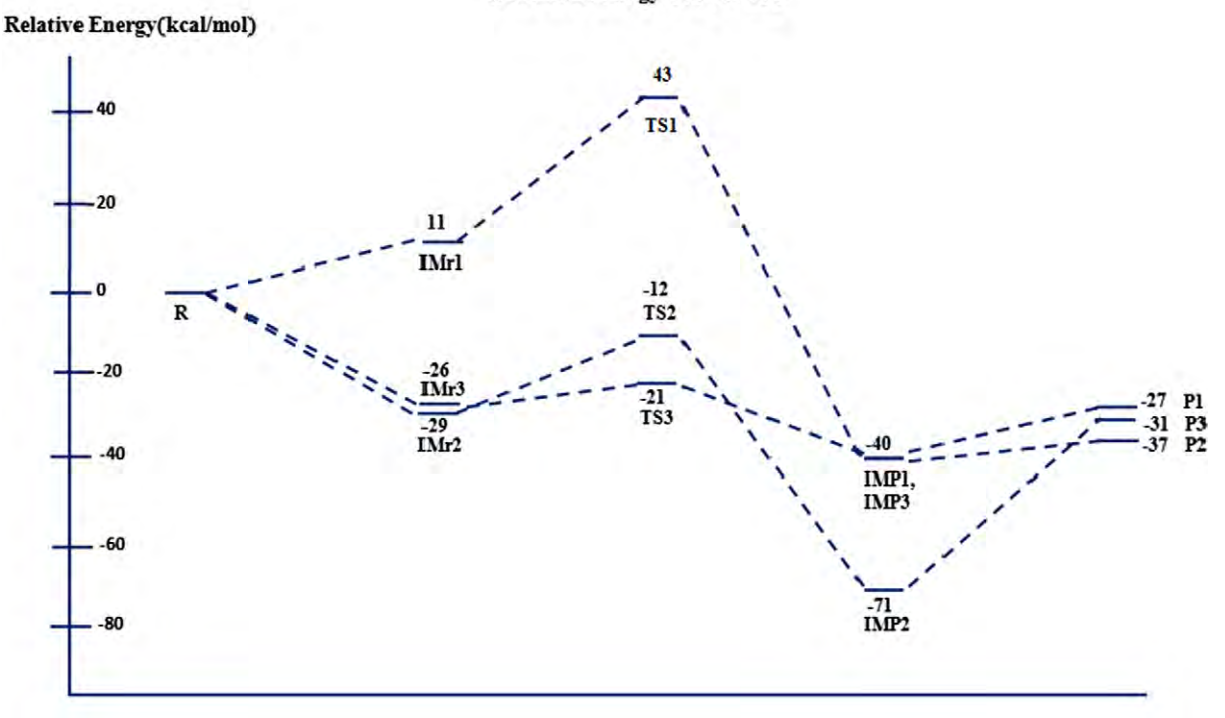


Fig. 4. Transition state structures for all six reactions.

Minimum Energy Path of GA



Path Coordinate

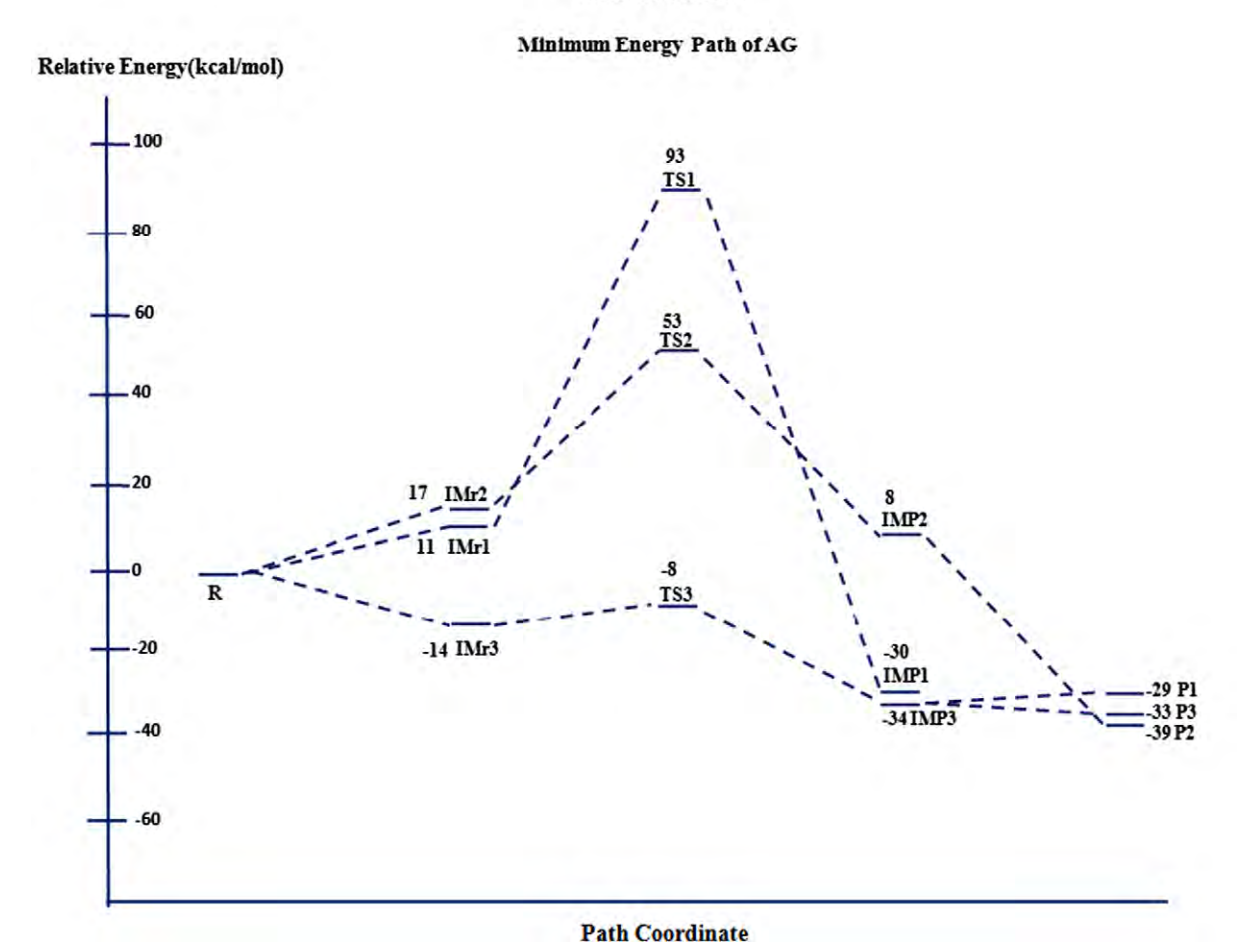


Fig. 5. Energy profiles of six hydrogen abstraction reactions.

3. Results and discussion

3.1. Wettability effect of plasma treated silk and its model compounds

The untreated samples absorbed 10 μ L water droplets immediately, while the treated samples each took time to absorb the water droplets. For each set of experimental conditions, the hydrophobicity increased after treating the sample with SF₆ plasma.

For treated pellets of both silk model compounds AG and GA, silk powder had higher water repellence than AG; the contact angles of silk and AG were 131° and 61°, respectively.

3.2. Crystal structure extraction and the plasma treatment reaction mechanism

Single crystals of the simplified model compounds, GA and AG, of *B. mori* silk were prepared using the evaporation method described previously. The obtained single crystals were examined under a microscope with a polarizing attachment. The single crystals had an almost rectangular shape and were capable of polarizing incoming light.

The data extracted from X-ray scattering in terms of bond lengths and torsion angles are shown in Fig. 2. The crystal structure derived from the X-ray diffraction pattern of the AG compound was a monoclinic crystal system with volume of 337.27(7) ų, and cell dimensions of a = 5.28 Å, b = 11.81 Å, c = 5.51 Å, and $\beta = 101^{\circ}$ in the space group $P2_12_12_1$. The GA crystal structure was found to be orthorhombic with a space group of $P2_1$ with a volume of 695.3(5) ų and cell dimensions of a = 9.68 Å, b = 7.53 Å, and c = 9.53 Å.

The minimized molecular structures of the reactants for GA and AG from untreated single crystal X-ray crystallographic data in a trans conformer of the model compound were essentially the same as a β -pleated conformation of protein [11,16]. Considering LUMO and the electrostatic potential energy profile (Fig. 3) of the model compounds, an F radical in the SF₆ plasma should react with an unoccupied orbital at the methyl group of Alanine part of silk model compounds with partial positive charges.

To investigate the reaction mechanisms, the locations of stationary points were characterized by vibrational frequencies; all reactants, products, and intermediates have real frequencies, and the TSs have only one imaginary frequency. The nature of the TSs has been confirmed by the mode of the imaginary frequency and by IRC calculations.

The potential energy barrier of the AG/GA + F reaction calculated at the UBHandHLYP/aug-cc-pVDZ level is presented in Table 1, which lists total energies of reactants, TS, and reaction products, as well as the activation energy (E_a). Here, we focus on the reactions of the fluorine radicals reacting with GA and AG. The abbreviations of species corresponding to the minimal transition states in Table 1 are as follows: paths 1–3 indicate reactions at three different carbon atoms (Fig. 1) of AG and GA, respectively.

A summary of all ZPE corrected energies is given in Table 1. The table presents the calculated TS values and ZPE, as well as some geometric parameters of molecules optimized using UBHandHLYP methods (Fig. 4). The extracted crystal structure shown in Fig. 2 for GA has torsion angles of -164° , -173° , -78° and 150° . Similarly, in AG the torsion angles are -162° , 173° , -71° , 154° . The imaginary frequency values at each TS geometry indicated stretching motion corresponding to plausible bond breaking. The imaginary frequency at the TS, corresponding to an antisymmetric motion of the bridging hydrogen atom along the C···H···F axis, are 2073, 2157 and $1627 \, \mathrm{cm}^{-1}$ for TS of the GA carbon atom and 1444, 2107 and $1888 \, \mathrm{cm}^{-1}$ for TS of the AG carbon atom at three different carbon atoms. In Fig. 5, TS2 and TS3 of GA had energy lower

than the reactants while simultaneously having a higher energy than the IMr. Similarly, TS3 of AG not only had lower energy than the reactants, but also had a higher energy than the IMr; thus the activation energy was calculated from transition state and IMr. From the previous discussion, the activation energies of each hydrogen abstraction of GA reacting with the fluorine radical were 31.62, 16.40 and 4.94 kcal/mol for the TS1, TS2 and TS3 respectively. The corresponding reaction energies of the fluorine radical and AG were 82.51, 36.43 and 5.71 kcal/mol for TS1, TS2, and TS3. The coordinates of TS1 for both model compounds are less favorable. Regarding the mechanism of the hydrogen abstraction from the GA molecule by fluorine radicals, the transition state structures for the fluorine radical extracting the hydrogen of the GA molecule are shown in Fig. 4. The C1-H distance of TS1 is 1.96 Å and the F-H distance is 1.65 Å. The F-H-C1 angle is 177.60°. The C2–H distance of TS2 is 1.28 Å while the C–H distance of the GA molecule is 1.087 Å long. The forming distance of H-F is 1.29 Å (0.937 Å in HF itself) and the F-H-C2 angle is 176.46°. For the TS3 structure, the C3-H distance is 1.21 Å while the remaining C-H distances are 1.098 Å long. The H-F distance is 1.29 Å in the TS3 transition state. The F-H-C3 angle is 178.27°. Similarly, for AG reacting with fluorine radicals, the breaking C1-H bond of TS1 is stretched by 2.38 Å and the forming F-H bond is 1.92 Å. The F-H-C1 angle is 156.69°. The distance of C2-H in TS5 is 2.14 Å (the C–H bond of AG molecule is 1.088 Å) while the fluorine radical to hydrogen distance is 1.60 Å and the F-H-C2 angle is 166.12°. From the TS3 structure, the distance of C3-H is 1.28 Å. The H-F distance is 1.26 Å and the F-H-C3 angle is 177.15° in the transition state. According to the calculations in Table 1 and Fig. 5, not only do the ΔH of path 2 and path 3 show a strongly exothermic reaction, they also have a greater Gibbs free energy than path 1. From the barrier, thermodynamic state function and transition coordinate structure, the hydrogen abstraction mostly occurs at the alanine residue.

4. Conclusions

In order to carry out quantitative analysis concerning the relationship between structure and physical properties of Thai silk, AG and GA model compounds were introduced to simulate essential features of the parent macromolecule using molecular structures obtained from X-ray crystal structure analysis. The space groups of P2₁2₁2₁ and P2₁ were found for AG and GA, respectively. Molecular conformations of GA and AG from untreated single crystal X-ray crystallographic data were essentially the same as from the β-pleated conformation of the protein. The molecular structures were used to propose a hydrogen abstraction reaction pathway utilizing density functional theory calculations. The results from the contact angle measurement and water absorption time confirmed that the wettability of both silk and its model compounds are lower after SF₆ plasma treatment. According to the calculations, the lowest activation energies for the hydrogen abstraction of both GA and AG for the F radical reaction were 4.94 and 5.71 kcal/mol respectively, at the alanine residue. Therefore, the hydrogen abstraction reactions of the alanine residue should be the preferable pathway in the plasma treatment process.

Acknowledgements

W.S. acknowledge financial support of the Center for Innovation in Chemistry (PERCH-CIC). The authors express grateful acknowledgement to the support of the Thailand Research Fund (TRF), and facilities provided by Computational Simulation and Modeling Laboratory (CSML), Commission on Higher Education, Thailand Center of Excellent in Physics (ThEP center), Thailand. We thank

Associate Professor Palangpon Kongsaeree, Department of Chemistry, Faculty of Science, Mahidol University, Thailand for X-ray structure analysis of AG. The software resource is courtesy of Computational Nanoscience Consortium (CNC) Nanotechnology (NANOTEC), Thailand for the access to the Material Studio Version 4.2 program package.

Appendix A. Supplementary data

Supplementary data associated with this article can be found, in the online version, at doi:10.1016/i.molstruc.2009.10.025.

References

- K. Satreerat, T. Hodak, B. Supasai, K. Paosawatyanyong, V. Kamlangkla, J. Pavarajarn, Applied Surface Science 254 (2008) 4744–4749.
- [2] P. Chaivan, N. Pasaja, D. Boonyawan, P. Suanpoot, T. Vilaithong, Surface & Coatings Technology 193 (2005) 356–360.
- [3] P. Suanpoot, K. Kueseng, S. Ortmann, R. Kaufmann, C. Umongno, P. Nimmanpipug, D. Boonyawan, T. Vilaitong, Surface & Coatings Technology 202 (2008) 5543–5549.
- [4] R.S. Dhavalikar, Journal of Scientific and Industrial Research 21 (C) (1962) 261– 263.
- [5] M.L. Gulrajani, Review Progress Colouration 22 (1992) 79-89.
- [6] S. Nishikawa, S. Ono, Proceeding of Mathematics and Physics 7 (1913) 131.
- [7] R. Brill, Liebigs Annalen de Chemie 434 (1923) 204.
- [8] R.E. Marsh, B.R. Corey, L. Pauling, Biochimica et Biophysica Acta 16 (1955) 1–34.
 [9] Y. Takahashi, M. Gehoh, K. Yuzuriha, International Journal of Biological Macromolecules 24 (1999) 127–138.
- [10] M.P. Bhate, J. Woodard, C.M.A. Mehta, Journal of the American Chemical Society 131 (2009) 9579–9589.
- [11] M.H.J. Koch, G. Germain, Acta Crystallographica Section B 26 (1970) 410-417.
- [12] T.C. Tranter, Acta Crystallographica 6 (1953) 805-806.
- [13] T.C. Tranter, Nature 177 (1956) 37-38.
- [14] P.S. Naganathan, K. Venkatesan, Acta Crystallographica Section B 28 (1972) 552–556.
- [15] M.S. Tafazzoli, K. Amini, Magnetic Resonance in Chemistry 46 (2008) 370-376.
- [16] K. Okuyama, R. Somashekar, K. Noguchi, S. Ichimura, Biopolymers 59 (2001) 310-319.
- [17] R. Molina, P. Jovancic, D. Jocic, E. Bertran, P. Erra, Surface and Interface Analysis 35 (2003) 128–135.
- [18] J.C. Jin, J.J. Dai, Journal of Textile Research 23 (2) (2002) 9-10.

- [19] S.I. Moon, J. Jang, Journal of Materials Science 33 (1998) 3419-3425.
- [20] C. Riccardi, R. Barni, E. Selli, G. Mazzone, M.R. Massafra, B. Marcandalli, G. Poletti, Applied Surface Science 211 (2003) 386–397.
- [21] M.S. Kin, T.J. Kang, Textile Research Journal 72 (2) (2002) 113-120.
- 22] C. Riccardi, R. Barni, P. Esena, Solid State Phenomena 107 (2005) 125-128.
- [23] A. Piccard, G. Turban, B. Grolleau, Applied Physics 19 (1986) 991-1005.
- [24] D.E. Frank, Pure and Applied Chemistry 62 (1990) 1699-1708.
- [25] O. Joubert, J. Pelletier, C. Fiori, T.A. Nguyen Tan, Journal of Applied Physics 67 (9) (1990) 4291–4296.
- [26] E. Selli, C. Riccardi, M.R. Massafra, B. Marcandalli, Macromolecule Chemistry Physicals 202 (2001) 1672–1678.
- [27] P. Nimmanpipug, L.V. Sanghiran, S. Janhom, P. Chaivan, D. Boonyawan, K. Tashiro, Macromolecular Symposia 264 (2008) 107–112.
- [28] P. Khomhoi, Theoretical Study of the Functionalization of Bombyx mori Silk Surface Treated, M.S. Thesis, Chiang Mai University, Chiang Mai, 2008.
- [29] Y. Han, J. Wang, D. Cheng, C. Liu, Industrial & Engineering Chemistry 45 (2006) 3460–3467.
- [30] Y. Han, J. Wang, D. Cheng, C. Liu, Energy & Fuels 18 (2004) 148-153.
- [31] P. Nimmanpipug, K. Tashiro, Y. Maeda, O. Rangsiman, Journal of Physical Chemistry 106B (2002) 6842–6848.
- [32] K. Tashiro, P. Nimmanpipug, O. Rangsiman, Journal of Physical Chemistry 106B (2002) 12884–12895.
- [33] P. Nimmanpipug, K. Tashiro, O. Rangsiman, Journal of Physical Chemistry 107B (2003) 8343–8350.
- [34] P. Nimmanpipug, K. Tashiro, O. Rangsiman, Journal of Physical Chemistry 193 (2005) 356–360.
- [35] S. Maskay, C.J. Gilmore, C. Edwards, N. Stewart, K. Shankland, Bruker Nonius, Netherlands, MacScience, Japan, The University of Glasgow, 1999.
- [36] M.J. Frisch, G.W. Trucks, H.B. Schlegel, G.E. Scuseria, M.A. Robb, J.R. Cheeseman, J.A. Montgomery Jr., T. Vreven, K.N. Kudin, J.C. Burant, J.M. Millam, S.S. Iyengar, J. Tomasi, V. Barone, B. Mennucci, M. Cossi, G. Scalmani, N. Rega, G.A. Petersson, H. Nakatsuji, M. Hada, M. Ehara, K. Toyota, R. Fukuda, J. Hasegawa, M. Ishida, T. Nakajima, Y. Honda, O. Kitao, H. Nakai, M. Klene, X. Li, J.E. Knox, H.P. Hratchian, J.B. Cross, V. Bakken, C. Adamo, J. Jaramillo, R. Gomperts, R.E. Stratmann, O. Yazyev, A.J. Austin, R. Cammi, C. Pomelli, J.W. Ochterski, P.Y. Ayala, K. Morokuma, G.A. Voth, P. Salvador, J.J. Dannenberg, V.G. Zakrzewski, S. Dapprich, A.D. Daniels, M.C. Strain, O. Farkas, D.K. Malick, A.D. Rabuck, K. Raghavachari, J.B. Foresman, J.V. Ortiz, Q. Cui, A.G. Baboul, S. Clifford, J. Cioslowski, B.B. Stefanov, G. Liu, A. Liashenko, P. Piskorz, I. Komaromi, R.L. Martin, D.J. Fox, T. Keith, M.A. Al-Laham, C.Y. Peng, A. Nanayakkara, M. Challacombe, P.M.W. Gill, B. Johnson, W. Chen, M.W. Wong, C. Gonzalez, J.A. Pople, Gaussian-03, Revision C.O.2, Gaussian Inc., Wallingford, CT, 2004.
- [37] Accelrys Software Inc., Materials Studio, Release 432, Accelrys Software Inc., San Diego, 2007.
- [38] C. Lee, W. Lee, R.G. Parr, Physical Review B 37 (1988) 785.
- [39] A.D. Becke, Journal of Chemical Physics 98 (1993) 1372.